THE UNIVERSITY OF CHICAGO

MOLECULAR CARTOGRAPHY OF THE MOUSE *IN TOTO* REVEALS MECHANISMS OF SYSTEMIC INFLAMMATION

A DISSERTATION SUBMITTED TO
THE FACULTY OF THE DIVISION OF THE BIOLOGICAL SCIENCES
AND THE PRITZKER SCHOOL OF MEDICINE
IN CANDIDACY FOR THE DEGREE OF
DOCTOR OF PHILOSOPHY

INTERDISCIPLINARY SCIENTIST TRAINING PROGRAM:
IMMUNOLOGY

BY

DENIS CIPURKO

CHICAGO, ILLINOIS
DECEMBER 2024

Copyright © 2024 by Denis Cipurko

All Rights Reserved

To my family, whose sacrifices and unwavering support have made this journey possible.

TABLE OF CONTENTS

LIST OF FIGURES vi

LIST OF ABBREVIATIONS vii

ACKNOWLEDGMENTS x

ABSTRACT xiii

1 INTRODUCTION 1
1.1 The mouse as the mammalian model of choice for biomedical research 1
1.1.1 The advantages of the mouse model for genetic and translational research 1
1.1.2 Previous efforts to map the cellular and genetic architecture of the mouse body 4
1.2 The technological evolution of spatial transcriptomics methods 8
1.2.1 Relevance of spatial cell type organization and gene expression in biology and disease 8
1.2.2 The landscape of *in situ* hybridization-based spatial transcriptomics technologies 11
1.2.3 RNA sequencing methods preceding array-based spatial transcriptomics 16
1.2.4 The emergence of spatial transcriptomics into the repertoire of RNA sequencing methods 18
1.2.5 The landscape of current spatially barcoded spatial transcriptomics technologies 20
1.2.6 The interplay of spatial proteomics and transcriptomics 24
1.3 The organism-wide inflammatory response in sepsis 27
1.3.1 Epidemiology and clinical definitions of sepsis 27
1.3.2 Molecular mechanisms of sepsis 28
1.3.3 The role of cytokines in sepsis 30
1.3.4 The impact of sepsis on innate immune cells 32
1.3.5 Impact of sepsis on lymphocytes 33
1.3.6 Central transcription factors in the sepsis response 34
1.3.7 Non-immune proteins in sepsis pathophysiology 35
1.3.8 Diverse mechanisms organ dysfunction and damage in sepsis 36
1.3.9 Spatial omics approaches in sepsis research 37

2 REPURPOSING LARGE-FORMAT MICROARRAYS FOR SCALABLE SPATIAL TRANSCRIPTOMICS 41
2.1 Abstract 41
2.2 Introduction 42
2.3 Materials and Methods 44
2.4 Results 59

2.4.1 On-slide assembly of spatially barcoded, mRNA capture probes on custom microarrays . . . 59
2.4.2 Array-seq yields high quality spatial transcriptomics data . . . 69
2.4.3 Benchmarking Array-seq against the widespread commercial platform Visium . . . 70
2.4.4 Array-seq enables high-throughput spatial transcriptomics in two and three dimensions . . . 76
2.4.5 Spatial transcriptomics analysis of whole-mount, human spleen section 87
2.5 Discussion . . . 90

3 SPATIOMOLECULAR CARTOGRAPHY OF THE MOUSE *IN TOTO* REVEALS MECHANISMS OF SYSTEMIC INFLAMMATION . . . 95
3.1 Abstract . . . 95
3.2 Introduction . . . 96
3.3 Materials and Methods . . . 99
3.4 Results . . . 106
3.4.1 Spatial transcriptomics of whole-mouse sections with Array-seq . . . 106
3.4.2 Array-seq accurately captures tissue subregions across the mouse body 110
3.4.3 Organism-wide mapping of mouse cell types . . . 115
3.4.4 Spatiomolecular mapping of systemic inflammation . . . 121
3.4.5 Whole-mouse spatial profiling reveals PLA2G5 as a harmful factor in sepsis . . . 130
3.4.6 Organism-wide analysis reveals PLA2G5's role red blood cell homeostasis during sepsis . . . 137
3.4.7 PLA2G5 acts as a self-venom during sepsis by mediating intravascular hemolysis . . . 138
3.5 Discussion . . . 145

4 DISCUSSION . . . 147
4.1 Array-seq overcomes hurdles of current spatial transcriptomics methods . . . 147
4.2 Application of spatial transcriptomics to multi-omics and targeting of non-polyadenylated RNA species . . . 152
4.3 Conclusion . . . 154
4.4 Future Questions . . . 155

REFERENCES . . . 158

LIST OF FIGURES

1.1 Landscape of array-based spatial transcriptomics methods 21
1.2 Hallmarks of sepsis 40

2.1 On-slide assembly of spatially barcoded mRNA capture probes using microarrays 62
2.2 Sequence level overview of the on-slide assembly procedure yielding mRNA capture probes 63
2.3 Array-seq accurately captures region-specific expression patterns in tissues . . . 64
2.4 Reproducibility of Array-seq data from mouse main olfactory bulb sections . . . 66
2.5 mRNA diffusion and spatial cell type assignment analyses 68
2.6 Side-by-side comparison of Array-seq and Visium data using adjacent mouse kidney sections 72
2.7 Extended comparison of Array-seq and Visium mouse kidney spatial transcriptomics data 75
2.8 Spatial marker gene expression analyses in mouse kidney sections 77
2.9 Array-seq enables the three-dimensional profiling of spatial transcriptomes . . . 80
2.10 Three-dimensional Array-seq analysis of serial mouse kidney sections 81
2.11 Multi-tissue, spatial transcriptomics profiling using Array-seq 83
2.12 Reproducibility of Array-seq for multi-organ section profiling 84
2.13 Spatial enrichment of gene ontology gene sets in Array-seq profiles 86
2.14 Array-seq profiling of a whole-mount section from a human spleen organ 88
2.15 Array-seq analysis of a whole-mount, human spleen section 89
2.16 Comparison between Array-seq and sequencing-based, spatial transcriptomics methods 94

3.1 Transfer enables whole mouse sections with high histological quality 107
3.2 Array-seq analysis of whole-mouse section 108
3.3 Whole mouse Array-seq data quality metrics 109
3.4 Organ-level analysis of whole mouse Array-seq data 111
3.5 Organ subregion clustering and marker gene analysis 113
3.6 Cell type mapping of whole mouse Array-seq data 117
3.7 Reproducibility of organism-wide cell type annotation 119
3.8 Specific cell type annotation of whole mouse sections 120
3.9 Organism-wide Array-seq analysis of a mouse endotoxemia model 122
3.10 Agreement of LPS-induced gene expression changes in Array-seq and bulk RNA-seq 124
3.11 Cell type and gene expression changed in a mouse endotoxemia model 126
3.12 Analysis of transcription factor regulated gene expression changes during sepsis 128
3.13 Identification of PLA2G5 as a harmful factor in sepsis 132
3.14 Spatial transcriptomics analysis of *Pla2g5* in the gut 134
3.15 Blocking PLA2G5 rescues mice from sepsis 135
3.16 Impact of PLA2G5 on serum cytokine and lipid levels during sepsis 139
3.17 PLA2G5 induces intravascular hemolysis during sepsis 140
3.18 PLA2G5 hydrolyzes phospholipids of damaged erythrocyte membranes 142

LIST OF ABBREVIATIONS

AKI acute kidney injury

ARDS acute respiratory distress syndrome

ATAC-seq assay for transposase-accessible chromatin and sequencing

bp base pair

cDNA complementary deoxyribonucleic acid

CLP cecal ligation and puncture

CITE-seq cellular indexing of transcriptomes and epitopes by sequencing

CODEX CO-Detection by indEXing

DAMP damage-associated molecular patterns

DSP digital spatial profiling

DNB DNA nanoball

H&E hematoxylin and eosin

HSP heat shock protein

IFN interferon

IL interleukin

ISG interferon-stimulated gene

ISH *in situ* hybridization

ISS *in situ* sequencing

FACS fluorescence-activated cell sorting

FFPE formalin-fixed paraffin-embedded

FISH fluorescence *in situ* hybridization

LPS lipopolysaccharide

MERFISH multiplexed error-robust fluorescence in situ hybridization

MOB main olfactory bulb

mRNA messenger RNA

NGS next-generation sequencing

nt nucleotide

OSOM outer stripe of outer medulla

PAMP pathogen-associated molecular patterns

PCR polymerase chain reaction

PFA paraformaldehyde

PLA proximity ligation assay

poly(A) polyadenosine

ROI region of interest

ROS radical oxide species

RCA rolling circle amplification

RT reverse transcription

SAA serum amyloid A

scRNA-seq single-cell RNA sequencing

SOFA sequential organ failure assessment

ST spatial transcriptomics

TF transcription factor

TGF-β transforming growth factor beta

Tregs regulatory T cells

UMI Unique Molecular Identifier

ACKNOWLEDGMENTS

There are many individuals and groups who I would like to thank for their contribution in the work described in this thesis. I would like to start by thanking my advisor, Dr. Nicolas Chevrier for his outstanding guidance and mentorship. When I arrived in the lab, I lacked many of the research skills and knowledge needed to be successful in an immunology and molecular engineering lab. Despite this, he put considerable faith in me by giving me an ambitious project, believing together we could execute it. During both setbacks and breakthroughs in my research, he did not hesitate to meet with me any time I needed to formulate new plans, interoperate data, and encouraged me to persevere. Nicolas' unwavering support and expertise have been instrumental in my development as a scientist. He has challenged me to think critically and approach problems with diligence and rigor. It was an honor and pleasure to work with Nicolas; I could not have asked for a better advisor.

I would like to thank my committee members, Savas Tay, Marcus Clark, Tao Pan, and Andrew Ferguson for their support and guidance. They were instrumental in directing the focus of my project and mapping my goals throughout my time in lab. I was grateful to have the support and generosity of individuals during my graduate research.

I would like to thank the past and current member of the Chevier lab for their continuous insights and always being there when I needed help. In particular to Michihiro Takahama, who I was able to work with closely on multiple projects, and whose work on the mechanisms of sepsis and PLA2G5 tied into my own. His training, expertise, and unparalleled hard work was a major determinant in my success. To Madison Plaster, Katerina Cheronis, Surya Pandey for their help in training me with mouse experiments and tissue collections. To Ling Mei and Tatsuki Udea for their help in Array-seq optimization experiments. To Fabian Hernandez for data collection and analysis contributions not shown in this thesis, but are valuable to my research projects. To Adil Mohammed, who has been a valued office-mate and whose conversations about science and non-science-related topics have always been

enlightening and enjoyable.

I would like to thank individuals outside of our laboratory who provided valuable input and assisted me with various aspects of my research; the researchers and staff at the University of Chicago Genomics Core, Single Cell Immunophenotyping Core (Mustafa Abasiyanik), the Animal Resources Center (Ani Solanki), the Research Computing Center, Integrated Light Microscopy Core (Khalil Rodriguez, Christine Labno, and Shirley Bond), Human Tissue Resource Center (Sarah Rose, Ellen Panetto, Brittany Grantham), whose generosity of their time and schedule was imperative to this work. Steven Dudek at the University of Illinois at Chicago for sharing PLA2G5 knockout mice for this work. Lastly, I would like to thank Ashwini Patil at Combinatics Inc who was imperative to the integration of single cell RNA-seq into large datasets and made this analysis feasible.

I would like to thank my undergraduate mentors, Dali Liu and Daniel Becker for opening their labs to me and enabling me to experience independent research. Their mentorship, wisdom, and passion for science were central to my decision to pursue a MD/PhD.

I would also like to thank the many friends I have met through these programs, especially Arpit Panda, Sukarn Chokkara, Sudhamsh Tippireddy, and members of the Pritzker entering class of 2019, who have filled my life with joy and meaning these past five years.

I would like to express my heartfelt gratitude to my family, whose unwavering support has been a cornerstone throughout my journey. Your generosity and selflessness throughout my life have made me who I am today. Your resilience and kindness have been a continual source of inspiration to me. To my stepdad, your encouragement and joy in celebrating my successes have always uplifted me and pushed me forward. To my sister, who is the yin to my yang, your companionship and thoughtful conversations have helped me maintain perspective. And to my late father who never doubted in me and who I hope I have made proud. I feel incredibly fortunate to have you all nearby, allowing me to visit often and draw on your support and love. Your collective love and support have been a driving force, and

for that, I am eternally grateful. You have made this journey not just possible, but also deeply rewarding and meaningful.

ABSTRACT

The mouse model has been at the forefront of biomedical research and discovery for over a century, significantly advancing our understanding of disease. However, a fundamental gap persists in our comprehension of the complete spatial cellular and transcriptional profile of the mouse body in both health and disease, which hinders a comprehensive understanding of disease mechanisms and molecular dysfunction. Here, we describe Array-seq, a novel method that repurposes classical oligonucleotide microarrays for spatial transcriptomics profiling, achieving an 11.31 cm^2 area coverage with 30 µm resolution. We demonstrated that the large surface area of Array-seq slides enables the generation of spatial transcriptomes at high throughput by profiling multi-organ sections, in three dimensions by processing serial sections from one sample, and across whole human organs using spleen sections. Additionally, we developed a novel sectioning method using adhesive film to transfer whole mouse sections to Array-seq slides, preserving the high histological quality of such large and heterogeneous sections. This enables spatial transcriptomics analysis and mapping of organs, tissue subregions, and cell types of the adult mouse model. By applying this technology to an endotoxemia mouse model of sepsis, Array-seq identified spatial patterns of inflammation-associated genes and cell type changes across the mouse body. This identified PLA2G5 as a critical mediator in the pathogenesis of the disease, operating as a "self-venom" that disrupts red blood cell integrity and iron metabolism. Our work developing Array-seq demonstrates a versatile tool for spatial transcriptomics, addressing key limitations in the field by offering high-throughput capabilities, large-scale spatial mapping, and integration with histology. This technology presents a new path forward for profiling diseases at scale, providing broader contexts for disease investigation and therapeutic profiling.

CHAPTER 1

INTRODUCTION

1.1 The mouse as the mammalian model of choice for biomedical research

1.1.1 The advantages of the mouse model for genetic and translational research

The mouse model has long been at the center of biological and biomedical research, offering unparalleled insights into genetics, development, and disease. The utility of the mouse as a model organism is rooted in its genetic, physiological, and anatomical similarities to humans, making it an indispensable tool for studying human biology and disease mechanisms (Talmadge et al., 2007; Perlman, 2016). Mice are small, economically viable, breed prolifically, and have a short lifespan, allowing for rapid generation turnover and time-efficient studies. Moreover, the extensive knowledge accumulated over more than a century of mouse research provides a robust framework for scientific inquiry and experimental manipulation.

The sequencing of both the human and mouse genomes has revealed a high degree of genetic similarity between the two species, with approximately 85% of mouse genes sharing homology with human genes (Birney Ewan et al., 2002; Dietrich et al., 1996). This genetic similarity, coupled with the ability to manipulate the mouse genome with advanced molecular tools, enables researchers to model human diseases with high fidelity. Beyond genetic similarities, physiological similarities further enhance the mouse's utility as a model organism. This includes similar embryological development, and functionally and structural homologous organ systems such as circulatory, reproductive, digestive, hormonal, and nervous systems (Canales and Walz, 2019; Bockamp et al., 2002).

The mouse immune system, while not identical, shares key similarities with the human

immune system, making them suitable for studying immunological diseases and responses. Both species possess innate and adaptive immunity with analogous cell types and mechanisms, such as T cells, B cells, macrophages, and dendritic cells (Mestas and Hughes, 2004). However, there are notable differences, such as variations in immune cell populations and responses to pathogens, which must be considered when extrapolating findings to human biology (Zschaler et al., 2014; Canales and Walz, 2019). These similarities and differences make mice well-suited for studying a wide array of biological processes and diseases, from cancer to autoimmune disorders (Mestas and Hughes, 2004).

The accumulated library of mouse strains is another reason the mouse model is a staple in biological research. Independent research labs and companies such as Jackson Laboratory maintains over 10,000 genetically defined strains of mice, including inbred lines, knockout models, and humanized mice, providing a comprehensive resource for the scientific community (Davisson, 2020). The ability to generate and maintain pure, inbred lines is crucial for ensuring experimental reproducibility and understanding the genetic basis of disease (Morse III, 2007). Mice can be genetically manipulated to mimic virtually any human disease or condition, and the precise mutations underlying these diseases can be introduced into mice to yield more accurate and useful data (Mestas and Hughes, 2004).

The mouse common genetic manipulation used in mice is gene knockout technology, involving the complete inactivation of a gene, have been instrumental in elucidating the roles of numerous genes in development, physiology, and disease (Bouabe and Okkenhaug, 2013). More advanced techniques, such as CRISPR-Cas9, allow for precise and efficient modifications of the mouse genome can be used to create knockouts, introduce point mutations, and generate knock-in models where specific gene sequences are inserted into the genome (Wang et al., 2016; Pickar-Oliver and Gersbach, 2019). Additionally, floxed genes and the Cre-lox system provide another layer of genetic manipulation, enabling cell type-specific and temporal control of gene expression. This system allows researchers to activate or deactivate genes

in specific cell types, providing insights into cell type dependent gene function in health and disease (Ventura et al., 2004). These genetic manipulations have profound implications for understanding biological processes and the role of specific genes in diseases. Knockout models, for example, have been essential in identifying critical genes involved in various diseases, including cancer, cardiovascular diseases, and neurological disorders (Yin et al., 2014; Ventura et al., 2004). Furthermore, the use of floxed genes in conjunction with the Cre-lox system has allowed for the study of gene function in specific tissues and at particular developmental stages, shedding light on processes such as neural development, immune responses, and metabolic regulation (Skarnes et al., 2011; Xu et al., 2015; Herzig et al., 2001).

Despite the versatility, convenience, and general homology of the mouse model to study human biology and disease, there are notable differences that must be accounted for when deciding to use them for research (Perlman, 2016). There are metabolic differences such as having different complements of cytochrome P450 enzymes, making toxicity of treatments difficult to predict for translational research (Guengerich, 2008). While globally similar, mice have some differences in organ systems to human systems. Because mice have evolved with different diets, they have differences in their digestive system, such as having a different small intestine to large intestine ratio, a prominent cecum, and not having an appendix (Kararli, 1995). Furthermore, their circulatory system is different due to smaller size. They have lower hemoglobin oxygen affinity, which is compensated by their size and a roughly 5-fold increase in heart rate (Saraiva and Sposito, 2014). Furthermore, there are notable differences in the mouse and human immune systems. For example, mouse blood leukocytes predominantly consist of neutrophils (50-70% in human vs 10-25%), while human blood has lymphocytes as the predominant leukocyte population (Mestas and Hughes, 2004). There are also differences in cytokines. Humans have IL-8 as a neutrophil chemoattractant factor, while there is no IL-8 analogue in mice; they use CXCL1 and CXCL2 instead (Pease and Williams, 2006). They also have differences in the humoral immune system. Mice have subclasses of IgG (IgG1,

IgG2a, IgG2b, and IgG3) that have different affinities for Fc receptors and complement proteins compared to their human counterparts (Bruhns, 2012).

Therefore, while mice serve as an excellent model for many aspects of human biology and disease due to their genetic and physiological similarities, the observed differences in metabolism and physiology may necessitate the use of complementary methods. Mice are invaluable tools in research due to their rapid reproduction, ease of genetic manipulation, and well-characterized biology, which have led to countless breakthroughs in understanding fundamental biological processes and disease mechanisms (Perlman, 2016). Validation of findings using human tissue samples and clinical data is crucial to ensure translational relevance. Clinical human tissue samples, in vitro human cell cultures, and organoids are platforms for studying human-specific cellular responses and tissue architecture (Clevers, 2016). Organoids, which mimic the three-dimensional structure of human tissues, offer insights into complex interactions that are difficult to replicate in two-dimensional cell cultures (Clevers, 2016; Corsini and Knoblich, 2022). However, organoids can lack certain systemic interactions present in whole organisms. Human cell cultures, while easier to manipulate and observe, may not fully recapitulate the multicellular environment of tissues. Therefore, combining these approaches with the versatility of mouse models creates a comprehensive framework for biomedical research, enhancing the accuracy and applicability of scientific discoveries.

1.1.2 Previous efforts to map the cellular and genetic architecture of the mouse body

The utility and ubiquity of the mouse model in biomedical research have created a need to comprehensively characterize cell types and gene expression in adult mouse tissues. With the advent of next-generation sequencing (NGS) technology, gene expression atlases have become essential tools for decoding the complexity of gene regulation and cellular heterogeneity

across various tissues and developmental stages. Organism-wide atlases were first generated using bulk RNA sequencing (bulk RNA-seq), which provided high-throughput sequencing of entire transcriptomes, followed by single-cell RNA sequencing (scRNA-seq) and spatial transcriptomics technologies. While technological advances in bulk RNA-seq and scRNA-seq have been coupled with increased throughput and lower costs, spatial transcriptomics still faces challenges related to limited capture areas and high costs.

Bulk RNA-sequencing (RNA-seq) was the first NGS method introduced, enabling high-throughput sequencing of the entire transcriptome. This approach has been crucial for gaining biological insights into organ function and gene expression regulation. The first comprehensive bulk RNA-seq of mouse organs was through the functional annotation of the mammalian genome 5 (FANTOM5) (Andersson et al., 2014). The FANTOM5 performed single-molecule cDNA sequencing from most mouse organs and dozens of cell lines. However, cDNA sequencing methods did not allow for multiplexing of samples and bridge amplification of cDNA transcripts, leading to laborious data acquisition and relatively low sequencing data quality. Future efforts to expand bulk RNA-seq capabilities led to the development of PME-seq, a method that integrates sample barcodes in library preparation with Illumina sequencing to increase multiplexing of samples. This technique enabled the parallel sequencing of a greater number of samples, providing a more comprehensive view of gene expression across tissues (A whole-tissue RNA-seq toolkit for organism-wide studies of gene expression with PME-seq) (Pandey et al., 2020). Using PME-seq, researchers were able to sequence 17 organs in both healthy mice and those infected with virus strains with vaccinating (modified Vaccinia Ankara) and pathogenic (Western Reserve) properties (Kadoki et al., 2017). This study not only offered a more comprehensive map of the whole mouse organ-wise transcription but also uncovered a multi-organ network of tissue-resident memory T cells that functionally adapt to their environment to stop viral spread across the organism (Kadoki et al., 2017). Another study using PME-seq profiled up to 15 organs in mice dur-

ing an endotoxemia model and during single and pairwise injections of cytokines (Takahama et al., 2024). This research revealed the organism-wide transcriptomic response during sepsis and demonstrated that the pairwise effects of tumor necrosis factor plus interleukin IL-18, interferon-γ, or IL-1β suffice to mirror the impact of sepsis across tissues. These findings underscore the importance of measuring the transcriptome of the mouse to understand biology and disease, and how increased multiplexing and efficiency of NGS methods enable the assessment of multiple treatment conditions, uncovering underlying mechanisms of disease (Takahama et al., 2024). While bulk RNA-seq can deconvolute enriched immune programs present in tissues, it does not provide direct cellular measurements, making identifying cellular mechanisms of disease more challenging.

This limitation was addressed through the application of scRNA-seq to profile mouse organs. The Mouse Cell Atlas (MCA) offered a comprehensive scRNA-seq resource for mouse tissues, covering critical organs including the brain, heart, lungs, liver, kidneys, and reproductive organs (Han et al., 2018). The Tabula Muris project, published in the same year, generated a single-cell transcriptomic atlas of 20 mouse organs and tissues, including the brain, heart, lungs, liver, kidneys, spleen, and bone marrow. The data were collected using both microfluidic droplet-based and FACS-based scRNA-seq technologies, providing a robust resource for studying gene expression across diverse cell types and tissues (Schaum et al., 2018). Expanding on the Tabula Muris, the Tabula Muris Senis project extends the analysis to aging mice, profiling 23 tissues from young and old mice. This atlas provides insights into the aging process and its impact on cellular and molecular functions across tissues, highlighting age-related changes in gene expression and cellular composition (Consortium, 2020). However, these scRNA-seq atlases lack spatial information and therefore offer limited insight into the organization of cell types in the context of the tissues collected and their potential communication axes.

To address this limitation, spatial transcriptomics atlases have been developed, integrat-

ing spatial context with high-resolution gene expression data to map the organization and interactions of cells within their native tissue environments. While no organism-wide adult mouse ST atlas has been complied to date, there has been studies that map the spatial transcriptome of most individual mouse organs (Moses and Pachter, 2022). Currently, the mouse body has only been profiled with spatial transcriptomics during the embryonic stages. The first ST embryonic dataset was generated on day 10 mouse embryos using DBiT-seq. However, the relatively large size of the embryo necessitated the use of the 50 µm channel width, reducing the data resolution (Liu et al., 2020). Sci-Space profiled the day 14 mouse embryo using diffusion of spotted barcoded nucleotides into cells withing tissue sections prior to scRNA-seq (Srivatsan et al., 2021). While this yielded single cell transcriptomics data, the center-to-center distance of spots was ~220 µm which only roughly approximates cellular localization within the embryo sections. Lastly, the mouse organogenesis spatiotemporal transcriptional atlas (MOSTA), generated during the initial demonstration of Stereo-seq generated an atlas of mouse embryogenesis (Chen et al., 2022). This nanometer-resolution ST alas integrated spatial transcriptomics at different stages in development and in three dimensions with scRNA-seq to elucidate gene expression dynamics during development, offering insights into regulatory mechanisms driving tissue differentiation and organ formation (Chen et al., 2022). Efforts to profile adolescent or adult mouse sections have been hindered by the lack of spatial transcriptomics methods with sufficiently large capture areas and the absence of robust histological techniques for generating high-quality whole-mouse sections. This limitation restricts our ability to understand the spatial genetic architecture of the adult mouse in a single experiment, which is essential for minimizing batch effects and ensuring accurate expression differences between tissues and cell types. Additionally, it hampers our capacity to profile organism-wide diseases across the entire mouse body, leaving significant gaps in our knowledge of pathophysiological mechanisms. Therefore, there is a need to develop both a new spatial transcriptomics method with a large capture area and histological techniques for

generating large heterogeneous tissues is crucial for advancing our understanding of spatial biology of the mouse model in health and disease.

1.2 The technological evolution of spatial transcriptomics methods

1.2.1 Relevance of spatial cell type organization and gene expression in biology and disease

The function of biological tissues is intricately tied to both the specialized roles of the individual cell types they comprise and their spatial organization within the tissue architecture. Each cell type within a tissue performs specific functions, contributing collectively to the tissue's physiological role. However, beyond cellular functions, the arrangement and interaction of these cells in three-dimensional space are crucial. Tissue organization dictates how cells communicate (Yáñez-Mó et al., 2015), how mechanical forces are transmitted (Vining and Mooney, 2017), and how nutrients and signals are distributed throughout the tissue (Adil et al., 2021). Thus, understanding both cellular function and tissue organization is essential for unraveling the complex mechanisms underlying tissue function and dysfunction in health and disease (Tian et al., 2023).

Spatially coordinated biological functions are exemplified in all organs in the mouse and human body. For example, the liver is characterized by zonation of pericentral and periportal hepatocytes within lobules (Cunningham and Porat-Shliom, 2021). This spatial arrangement is crucial for the liver's metabolic and synthetic activities which are coordinated in relation to the flow of blood through the lobule. Pericentral hepatocytes are located around the central vein, where blood from the hepatic arteriole and portal vein merges. There, they are exposed to blood that is relatively depleted in oxygen and rich in nutrients and toxins (Chen et al., 2023b). In contrast, periportal hepatocytes reside closer to the portal triads, where oxygen-rich blood from the hepatic artery and nutrient-rich blood from the portal vein enter the

lobule. This positioning allows periportal hepatocytes to engage in processes such as glucose uptake, detoxification, and bile production, which are crucial for metabolic homeostasis and detoxification (Kozuki et al., 2023). The spatial organization of these hepatocyte populations is further elucidated by the distinct patterns of gene expression, which drive their specialized metabolic activities and responses to the hepatic microenvironment (Halpern et al., 2017; Ben-Moshe et al., 2019).

In another example, the kidney is characterized by distinct structural units, including the cortex and medulla, each housing specialized cell types essential for its function (Smith, 1951). This spatial arrangement is crucial for the kidney's ability to filter blood, reabsorb essential nutrients, and excrete waste. In the renal cortex, the proximal tubule cells are primarily responsible for reabsorbing glucose, amino acids, and electrolytes from the filtrate (Murer et al., 2000). Conversely, the renal medulla contains the loop of Henle and collecting ducts, where cells are adapted for concentrating urine and regulating water balance (Knepper et al., 2015). The spatial organization of these renal cell populations is further elucidated by their distinct gene expression profiles. For instance, genes involved in active transport and metabolism are highly expressed in the proximal tubules, reflecting their role in nutrient reabsorption. In contrast, genes related to osmoregulation and water transport are predominant in the cells of the loop of Henle and collecting ducts, aligning with their function in urine concentration (Haug et al., 2024; Hinze et al., 2021). This spatially resolved gene expression is essential for the coordinated activities of the kidney, ensuring efficient filtration and homeostasis (Wu et al., 2024; Jain and Eadon, 2024).

Aberrations in spatial phenotypes are prevalent in all diseases, driving disease pathophysiology by altering tissue structure, function, and cellular interactions. The pathophysiology and heterogeneity of solid tumors in cancer are particularly notable for their spatial complexity and diverse cellular composition. Solid tumors consist of cancer cells and a complex stroma that includes fibroblasts, immune cells, endothelial cells, and extracellular matrix

components. This cellular diversity and organization exhibit distinct spatial patterns that influence tumor behavior and response to treatment (Junttila and De Sauvage, 2013; Hanahan and Weinberg, 2011). For instance, the hypoxic regions typically found at the tumor core are often associated with aggressive cancer phenotypes, resistance to therapy, and poor prognosis. These regions are characterized by the stabilization of hypoxia-inducible factors, which regulate the expression of genes involved in angiogenesis, metabolism, and survival pathways (Semenza, 2012; Vaupel and Mayer, 2007). Moreover, the tumor microenvironment also plays a significant role in the spatial organization of gene expression. For example, tumor-associated macrophages (TAMs) which adopt an M2-like phenotype that supports tumor growth and metastasis through the secretion of cytokines and growth factors, thereby creating a protumorigenic niche (Qian and Pollard, 2010; Mantovani et al., 2017; Moncada et al., 2020). Advances in spatial transcriptomics have enabled the detailed mapping of gene expression within tumors, providing insights into the spatial heterogeneity and organization of different cell types. For example, Aurora et al. demonstrated that leading a edge gene signature is associated with worse clinical outcomes while tumor core gene signature is associated with improved prognosis (Arora et al., 2023). Therefore, understanding the spatial dynamics of gene expression in tumors is crucial for developing effective treatments, as it allows for the identification of specific cellular and molecular targets that are relevant to the distinct regions within the tumor (Andersson et al., 2020; Ren et al., 2023).

While perhaps the most prominent example, cancer is not the only disease that exhibits spatially relevant changes; conditions such as sepsis and colitis also demonstrate significant spatial heterogeneity in tissue responses and cellular interactions (Singer et al., 2016; Parigi et al., 2022). These diseases, like cancer, involve complex interactions between cell types and their microenvironments, and involve distinct patterns of gene expression that are critical for disease progression and response to treatment (Hotchkiss et al., 2013; Garrido-Trigo et al., 2023). In sepsis, the liver microenvironment undergoes profound changes, particularly

involving Kupffer cells, which are the resident macrophages of the liver. A recent study has shown that extracellular cold-inducible RNA-binding protein (eCIRP) secreted by adjacent hepatocytes promotes the inflammatory polarization of Kupffer cells to the M1 phenotype through the TLR4 pathway, resulting in the overproduction of pro-inflammatory cytokines such as IL-6 and TNF-α, which exacerbate liver injury (Shimizu et al., 2024). This polarization contributes to a cycle of inflammation and tissue damage, highlighting the critical role of Kupffer cells in the pathogenesis of septic liver injury. Therefore, understanding the spatial organization of gene expression is essential for comprehending the underlying biology and pathology of diseases, providing crucial insights that can inform the development of more effective therapeutic strategies.

1.2.2 The landscape of in situ hybridization-based spatial transcriptomics technologies

The efforts to identify and visualize the spatial distribution of gene expression have spanned decades, resulting in spatial transcriptomics (ST) methods with continually expanding scale and throughput. The earliest examples, whose modern counterparts are still frequently used, rely on *in situ* hybridization, involving the binding and imaging of labeled oligonucleotide probes complimentary to the target transcript or genomic region. The initial methods for visualizing the spatial distribution of transcripts began in 1969 with the use of radioactive labeling, followed by fluorescent labeling of specific RNA species through hybridization with complementary probes (Harrison et al., 1973; Rudkin and Stollar, 1977). The next innovation in ST came with the use of multiplexed fluorescently labeled cDNA probes, where combinations of three fluorescent probes enabled simultaneous imaging and visualization of individual transcript molecules of 6 distinct RNA species in a single cell (Levsky et al.,

2002)[1]. The advent of super-resolution microscopy enabled the development of smFISH (single molecule FISH) in 2012, which utilized cDNA probes labeled with multiple types of fluorescent molecules at different segments of the probes. This design allowed for increased multiplexing (up to 32 RNA species) and the visualization of individual transcript molecules (Lubeck and Cai, 2012).

The next phase of ISH-based methods was accompanied by a dramatic increase in the number of target transcripts capable of being analyzed. Firstly, in 2014, smFISH was improved upon through the use of sequential rounds of probe hybridizations, stripping (using DNAse), and imaging. Each round of probes carries the same sequence, but labeled with a different fluorophore. This altered method, called seqFISH, negated the requirement of super-resolution microscopy, and enabled exponential scaling of target molecules based upon the number of unique fluorophores and the number of rounds of hybridization (Lubeck et al., 2014). However, this approached also increases the duration of the experiment due to the increased required cycles of hybridization and imaging. In 2015, another technology when enabled highly multiplexed detection of RNA transcripts is, smFISH technique is multiplexed error-robust FISH (MERFISH) (Chen et al., 2015). This method involved the use of multiple probes, specifically designed for different sequences along the length of the transcript, flanked by readout encoding sequences. The readout encoding sequences can be hybridized (1) or not (0) by a fluorescent labeled complimentary probe. Sequential rounds of imaging and probe addition creates a binary sequence which is encoded to a specific gene transcript identity. The method also included error-correction by incorporating a Hamming distance ≥ 4 to minimize misidentification of transcripts. The original method enabled localization of 140 unique transcript identities within a cell (Chen et al., 2015). Subsequent application of MERFISH technology has increased the surface area coverage of tissue sections such as

1. The preeminent goal of ISH-based methods before the modern era was elucidating intracellular localization of RNA species to gain insight into cellular biology. Furthermore, the trade-off of imaging resolution and field-of-view was also a factor in the imaging and analysis of a small number of cells rather than on tissue sections.

the mouse kidney, liver, and hypothalamic preoptic region of the mouse brain (Liu et al., 2023a; Moffitt et al., 2018) with limited gene targets ($<$ 500 transcript targets)[2]. However, detection efficiency has been a challenge in scaling beyond 1000 target transcripts despite commercialization through of the method through Vizgen and multiple adaptations of the method (Moses and Pachter, 2022; Wang et al., 2018a).

Another approach which emerged in the same period as seqFISH and MERFISH is *(*in situ) sequencing (ISS). The original method involves a ligation reaction of a padlock probe, where a ligase enzyme joins the ends of the padlock probe primer only if both bind to the target RNA (Ke et al., 2013). Non-matching probes are washed away, and s rolling circle amplification (RCA) is performed, which generates multiple copies of the target sequence to enhance signal strength, and therefore detection sensitivity. Finally, the RCA product can be identified by the transcript template though sequencing by ligation (SBL). Future versions of this method employed similar uses of padlock probes, but utilized more sensitive and efficient sequencing methods; FISSEQ and STARmap leveraged SOLiD sequencing on 8102 gene transcripts (Lee et al., 2014; Wang et al., 2018b) while BAR-seq used sequencing by synthesis (which is the method of choice for current Illumina sequencers) on 68 gene transcripts but covering a large portion of the mouse motor and auditory cortex.

Another category of ISH ST methods is Digital Spatial Profiling (DSP), which includes technologies such as GeoMx and Zip-seq. GeoMx DSP utilizes photocleavable oligonucleotide tags linked to antibodies or RNA probes (Merritt et al., 2020). After probe hybridization and antibody binding, these tags are released upon exposure to light, allowing for the multiplexed readout of proteins or RNAs in specific regions of interest (ROIs) of between 1 and 5000 cells within tissue samples. The cleaved oligonucleotides can be aspirated, PCR ampli-

2. These technologies typically rely on tissue sections, typically around 10 µm thick, which can be either fresh frozen or FFPE (formalin-fixed paraffin-embedded). Fresh frozen tissue sections are more commonly used due to the degradation of RNA in FFPE-fixed tissues, particularly affecting hybridization-based ST methods. The process involves embedding the tissue in a medium and sectioning it using either a microtome or a cryomicrotome. The process entails embedding the tissue in a medium and then sectioning it using either a microtome for standard sections or a cryomicrotome for frozen sections.

fied, indexed to differentiate between oligonucleotides from separate ROIs, and sequenced. Zip-seq follows a similar protocol, however the oligonucleotide tags lined to antibody or hybridization probes are accompanied by covalently conjugated to an 'anchor' sequence that can be separated from the remained of the probe through an initial photoclevage even in a region of the tissue (Hu et al., 2020). A spatial encoding "zip" barcode can then by hybridized to the probe. Repeated unmasking of the anchors and addition of zip barcodes can create a grid of spatially encoded probes which can then be photocleaved, collected, and sequenced to generate spatially mapped transcriptomic and proteomic data. A major advantage of DSP methods the ability to quantitatively measure both protein and RNA species (Merritt et al., 2020). Furthermore, DSP decreased data output file sizes and shortened acquisition time relative to all other ISH ST methods, requiring only a single round of hybridization and/or antibody binding with GeoMx. However, the major limitation of DSP methods is the selection of ROIs from the larger tissue section, preventing data collection from a full sample and therefore potentially excluding insightful biological measurements. Furthermore, the ROIs are not at cellular resolution, preventing a complete understanding of cell type organization and communication across space. The original GeoMx paper reported 100 µm x 100 µm ROI while Zip-seq demonstrated a minimum grid resolution of 10 µm x 10µm (Merritt et al., 2020; Hu et al., 2020). Despite the shortcomings, DSP technologies have gained wide-spread adoption through commercialization through GeoMx by Nanosring and Xenium by 10x Genomics.

Perhaps the most promising demonstrations for the continued growth in scale and number of transcript targets of ISH based ST methods is the recent generation of mouse brain atlases. Shin *et. al.* used STARmap to generate 3-dimensional datasets of the mouse brain (both sagittal and coronal), and spinal cord, totaling a mapping of 1.09 million high-quality cells using 1,099 target transcripts (Shi et al., 2023). Zhang *et. al.* used MERFISH to also generate 3-dimensional datasets of the coronal and sagittal mouse brain, totaling ap-

proximately 10 million cells with a panel of more than 1,100 genes. Both studies generated nanometer-resolution cell atlases of the mouse brain which will contribute to future functional investigations of neural circuits and their dysfunction in health and disease. Furthermore, recent publications have also proposed novel approaches for the design of *in situ* ST experiments in order to minimize the trade-off between resolution and throughput during image data collection. Borm *et. al.* developed Enhanced ELectric Fluorescence in situ Hybridization (EEL FISH), in which electrical current is passed through a glass coverslip coated with an optically transparent and electrically conductive layer of indium tin oxide (ITO), which is modified with oligo(dT) and positively charged poly(D-lysine) to capture RNA both by hybridization and by electrostatic attraction (Borm et al., 2023). The tissue can then be digested leaving only the captured RNA on the surface. Target probe hybridization and fluorescence decoding can proceed with standard sequential hybridization or ISS methods. The process of drawing RNA molecules to the surface of the ITO slide decreases the necessary z-stack planes for robust data acquisition. Moreover, tissue clearance also removed autofluorescent lipofuscin from the imaging region, enabling shorter exposure times. EEL FISH enabled data generation from a 440 gene panel in 58 hours, which was a reduction from previous methods which report data acquisition times of days to weeks (Codeluppi et al., 2018; Moffitt et al., 2018).

Taken together, ISH based ST methods offer advantages to spatially-barcoded based ST methods, including single-molecule resolution, reliable measurement of subcellular localization of RNA transcripts, less lateral RNA diffusion, and robust cell segmentation. However, seqFISH and ISS methods hold a minority share of methods used in ST papers despite being the first instantiations of ST and undergoing multiple of iterations of improvements. This is in part due to the need for complicated home-built fluidic systems (for methods that have not been commercialized), long imaging time, terabytes of imaging data, and expensive probes. This speaks to the importance of cost and ease of use in the adoption of ST methods. This is

exemplified in the emergence and relative dominance of DSP methods. Despite the apparent shortcomings of DSP technologies, their use in scientific studies outnumber all other ISH-based ST methods (Moses and Pachter, 2022) shortly after their introduction. This suggests that lower experiment duration, cost, and computational requirements are important factors for the adoption, and therefore impact of ST technologies.

1.2.3 RNA sequencing methods preceding array-based spatial transcriptomics

The evolution of next-generation RNA sequencing technologies has significantly increased the throughput and coverage of transcriptome measurements, allowing for more comprehensive and detailed analysis of gene expression. This progression has been transformative, enabling the identification of previously undetectable cellular heterogeneity and uncovering complex molecular mechanisms underlying various biological processes and diseases. Starting with bulk RNA sequencing (RNA-seq) and advancing to single-cell RNA sequencing (scRNA-seq), each iteration has addressed the limitations of its predecessors, ultimately paving the way for the development of spatial transcriptomics. Initially, bulk RNA-seq provided a comprehensive overview of gene expression levels across entire tissue samples. This method involves the extraction of RNA from a heterogeneous mixture of cells within a tissue, followed by reverse transcription to synthesize cDNA from the RNA template. The cDNA is then amplified using PCR and subsequently sequenced using next-generation sequencing (NGS) technologies (Wang et al., 2009; Mortazavi et al., 2008). This approach allowed researchers to quantify gene expression, discover new transcripts, and identify differential gene expression across various conditions (Wang et al., 2009; Mortazavi et al., 2008; Wolf et al., 2018).

Bulk RNA-seq has inherent limitations due to the averaging of gene expression signals from all cells in the sample, which masks the contributions of individual cell types and obscures cellular heterogeneity (Marioni et al., 2008; Sandberg, 2014). This averaging effect limits the ability to detect rare cell types and specific cellular responses to environmental

changes, thereby providing only a generalized view of gene expression. To overcome these limitations of bulk RNA-seq, scRNA-seq was developed, enabling the analysis of gene expression at the resolution of individual cells. A significant challenge in scRNA-seq was the isolation of single cells from complex tissues. This was addressed by employing advanced techniques such as microfluidics, which compartmentalizes individual cells into droplets, droplet-based systems that allow high-throughput single-cell isolation, and fluorescence-activated cell sorting, which sorts cells based on fluorescence labeling (Zheng et al., 2017; Kolodziejczyk et al., 2015; Trapnell et al., 2014). In scRNA-seq, high-throughput sequencing of the cDNA libraries allows for the profiling of thousands of individual cells, providing detailed insights into cellular diversity, differentiation pathways, and the discovery of rare cell types (Zheng et al., 2017; Kolodziejczyk et al., 2015; Trapnell et al., 2014).

Several popular scRNA-seq methods have been developed, each building on the strengths of previous techniques while addressing their limitations. The first scRNA-seq methods that gained wide adoption was SMART-seq Switching Mechanism at the 5' end of the RNA Transcript sequencing (SMART-seq), which provides full-length transcript coverage, enabling the detection of alternative splicing and the identification of novel transcripts. This technique uses FACS sorting of cells into droplets, oligo-dT primers to capture polyadenylated RNA and template switching to add adapter sequences for PCR amplification (Picelli et al., 2013, 2014). However, this method relied on substantial manual pipetting of reagents into droplets, limiting the scalability of the methods. The next major method was Drop-seq, which used microfluidic droplets to encapsulate single cells with barcoded beads, enabling high-throughput single-cell RNA sequencing. This method significantly reduces the cost and complexity of library preparation, making scRNA-seq more accessible (Macosko et al., 2015). 10x Genomics Chromium system further refines this approach by improving the efficiency and scalability of cell encapsulation and barcoding, allowing for the sequencing of tens of thousands of cells in a single experiment (Zheng et al., 2017).

ScRNA-seq on the field of genomics has enabled researchers to dissect the cellular composition of tissues, uncover novel cell types, and understand the complex dynamics of cellular processes and interactions (Zappia and Oshlack, 2018; Luecken and Theis, 2019; Kelsey et al., 2017). However, scRNA-seq also has limitations, primarily the loss of spatial context. While scRNA-seq provides high-resolution gene expression data, it does not retain information about the spatial organization of cells within their native tissue environment. This spatial information is crucial for understanding tissue architecture and cell-to-cell interactions (Crosetto et al., 2015; Luecken and Theis, 2019; Saliba et al., 2014).

1.2.4 The emergence of spatial transcriptomics into the repertoire of RNA sequencing methods

While ISH ST methods opened possibilities for profiling the spatial distribution of gene expression, they were limitations in the number of transcripts that can be analyzed, rely on existing knowledge of meaningful genes to measure, and are labor-intensive (Chen et al., 2015). Furthermore, they and not compatible H&E-stained sections, the standard research and diagnostic setting of regular histological tissue sections (Lubeck et al., 2014). As a result, it remained outside the category of high-throughput sequencing technologies which were rapidly becoming adopted among scientists.

In 2016, Ståhl *et.al.* introduced a spatially-barcoded ST method[3] , which involves the use of a glass slide coated with immobilized oligonucleotides arranged in a grid of spots (Ståhl et al., 2016) (Fig 1.1a-b). Each oligonucleotide consists of a 5' 18-mer spatial barcode, a 9 bp semi-randomized unique molecular identifier (UMI), and a 3' (dT)20VN sequence. The spatial barcode identifies the location of each spot on the grid, while the (dT)20VN sequence hybridizes with the 3' poly(A) tails of mRNA, serving as a primer for reverse transcription.

3. this method of spatially-barcoded ST will be referred to as simple "ST" for the remainder of this dissertation.

The method begins with the preparation of a cryosection of tissue, which is placed onto the barcoded slide and fixed using methanol or paraformaldehyde (PFA). The tissue is then stained with hematoxylin and eosin (H&E) to visualize histological features. After imaging the stained tissue to record its morphology, the tissue is permeabilized, typically using 0.1% pepsin, to release the mRNA from the cells. The released mRNA molecules hybridize to the oligonucleotide probes on the slide. Reverse transcription is then performed, converting the mRNA into cDNA while preserving the spatial barcodes.

Next, the amplified cDNA is prepared for sequencing by attaching sequencing adapters. High-throughput sequencing is then performed, generating paired-end reads that contain both the spatial barcode and the gene expression information. The spatial barcodes enable the mapping of gene expression data back to the specific locations on the tissue slide where the mRNA was originally captured. This method provides a scalable and straightforward approach to spatially resolve gene expression without the need for fluorescent imaging, making it more suitable for high-throughput applications. Additionally, spatial barcoding can be seamlessly integrated with histological techniques such as H&E staining, providing a comprehensive view of tissue architecture alongside molecular data. The use of poly(A) tail priming ensures that all polyadenylated mRNA species are represented in the analysis, offering a broad and unbiased view of the transcriptome (Ståhl et al., 2016; Salmén et al., 2018). The introduction of this method enabled the integration of spatial information with transcriptome-wide gene expression data and, enhancing the understanding of tissue architecture, cellular interactions, and the spatial organization of molecular processes (Ståhl et al., 2016; Rodriques et al., 2019; Xiaowei, 2021).

1.2.5 The landscape of current spatially barcoded spatial transcriptomics technologies

While the initial demonstration of ST by Ståhl *et.al.* laid the groundwork for the field of high-throughput sequencing-based spatial transcriptomics, it was lacking in technical metrics that impact the quality of the data and potential applications of the technology. These include resolution (the barcoded feature diameter, and feature center-to-center distance), capture area size, and RNA measurement sensitivity (number of UMI per unit area). The initial demonstration of ST had a spot diameter of 100 µm diameter, a center-to-center distance of 100 µm, and a capture area size of 6.2 x 6.2 mm^2. Furthermore, the sensitivity of this method was 6.9 ± 1.5% of single-molecule fluorescent in situ hybridization, which is comparable to the sensitivity of some single cell RNA-seq methods (Grün and van Oudenaarden, 2015). While this method was able to identify tissue domains in mouse MOB and breast cancer, the lower resolution prevented robust inference into gene expression of cell types within the tissues. This original ST method was commercialized in 2019 when 10x Genomics released Visium. The Visium array has a higher resolution (55 µm spot diameter and 100 µm center-to-center distance) and larger capture area (6.5 x 6.5 mm^2). Because it does not require specialized instrumentation for library preparation, provides transcriptome-wide profiling, and utilizes compact data storage and simple data preprocessing, Visium is still the most commonly used ISH or spatially-barcoded ST technology to date (Moses and Pachter, 2022).

Subsequent spatial transcriptomics methods would seek to improve upon all of the metrics, utilizing varied approaches in array design and spatial barcoding of mRNA. The barrier of cellular resolution ST was broken in 2019 with the introduction of Slide-seq and High-Definition Spatial Transcriptomics (HDST) (Rodriques et al., 2019; Vickovic et al., 2019). Rather than immobilizing spatially barcoded oligonucleotides directly on a slide, oligonucleotides were immobilized onto functionalized beads which were then added to the surface of a slide. Slide-seq used 10-µm diameter beads and coated in a monolayer onto a slide,

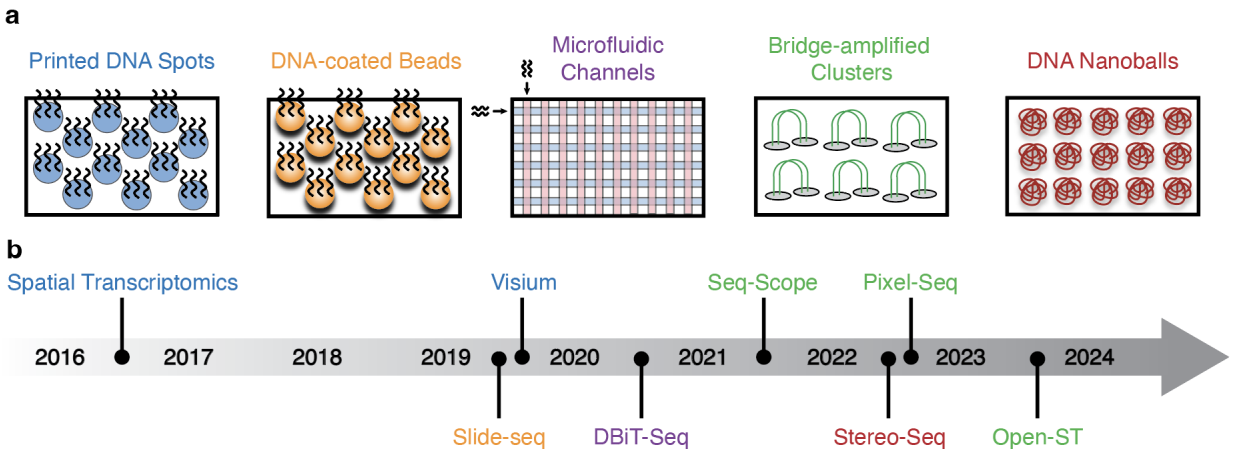


Figure 1.1: Landscape of array-based spatial transcriptomics methods. a, Diagrams of the different spatially barcoded features used in array-based spatial transcriptomics methods. **b,** Timeline of array-based spatial transcriptomics methods, colored by the category of capture probe outlined in **(a)**.

while HDST used 2-µm beads which fit into an etched silica slide (Fig 1.1a-b). The positions of beads were spatially decoded through SOLiD sequencing of the spatial barcodes. While both of these bead-based methods were able to accurately deconvolute cell type signatures for each bead, they notably suffered from lower sensitivity (Stoeckius et al., 2017; Liu et al., 2020). However, a future version of Slide-seq was able to improve sensitivity by over an order of magnitude through improvements in the library preparation protocol (Stickels et al., 2021).

In 2020, deterministic barcoding in tissue for spatial omics sequencing (DBiT-seq), utilized parallel microfluidic channels on a polydimethylsiloxane (PDMS) chip to deliver DNA barcodes to the surface of a tissue slide (Liu et al., 2020). The crossflow of orthogonal barcodes ligates to poly(A) sequences so each spot can be identified with a unique pairwise combination (Fig 1.1a). Notably, this was also the first ST method to quantify both RNA and protein in a tissue section. Proteins were quantified via the use of polyadenylated barcoded oligonucleotides conjugated to antibodies like those used in multi-omics single cell RNA sequencing reported previously (Stoeckius et al., 2017). This method also had a minimum of 10 µm channel width and reported the highest sensitivity of any ST method to that

point (Liu et al., 2020).

Cho *et. al.* developed a subcellular resolution ST method involving solid-phase amplification of randomly barcoded single-molecule oligonucleotides using the Illumina sequencing platform (Cho et al., 2021). Custom designed oligonucleotides containing PCR/read adaptor sequences and a semi-random spatial barcode sequence, oligo-dT, are loaded into a MiSeq flowcell. This oligonucleotide library is amplified on, generating clusters or "polonies", each of which is derived from a single "seed" molecule (Fig 1.1a). Following cleavage of the bridge products at an inserted restriction enzyme site, the protective coating of the flow cell can be removed. The resulting surface can then be cut and used as an ST array. With an average center-to-center distance of 0.6 µm, this was the first method to achieve subcellular resolution with high gene and UMI sensitivity. Other similar methods modifying the Illumina platform such as Nova-ST and Open-ST were recently developed utilizing the larger NovaSeq flowcell with similar spatial resolution (Poovathingal et al., 2024; Schott et al., 2024). While these methods demonstrate impressive resolution and sensitivity, the capture area size is limited by the dimensions of the flow cell lanes (0.9 mm^2 for Seq-Scope and 12 mm^2 for Open-ST and Nova-ST).

Perhaps the most advanced ST method to date is Stereo-seq, first published in 2022. Stereo-seq combines DNA nanoball-patterned array technology pioneered by the Beijing Genomics Institute (BGI) (Fehlmann et al., 2016), with spatially barcoded DNA nanoballs (DNBs) (Chen et al., 2022) (Fig 1.1a-b). Standard DNB chips have etched spots with approximately 220 nm diameter and a center-to-center distance of 500 or 715 nm. Spatially barcoded DNBs are loaded onto the chip, amplified via RCA, and sequenced by synthesis to record the spatial position of each DNB polony. The initial demonstration of Stereo-seq generated a three-dimensional spatiotemporal atlas of mouse embryogenesis using 200 mm^2 chips (Chen et al., 2022). A later study generated a three-dimensional atlas of the macaque brain cortex using 1500 mm^2 chips (Chen et al., 2023a). This study revealed the distribution

of 264 cell types and their marker genes across the layers of the macaque brain cortex, the largest single-cell resolution ST atlas to date. Stereo-seq offers not only the highest resolution and capture area size but has also demonstrated the highest sensitivity out of all current ST methods (Poovathingal et al., 2024). However, the silicon chip makes imaging of H&E-stained tissue sections infeasible. The Stereo-seq technology was recently commercialized with STOmics offering up to 2 x 3 cm^2 ST chips.

Pixel-seq is a recent ST method that employs a dense array of pixelated capture sites, each linked to a unique barcode (Fu et al., 2022). The high resolution is achieved by reducing the size of the capture sites to subcellular levels, around 1 µm, by utilizing continuous polony gels (Fig 1.1a-b). These gels are made through soft lithography pioneered by Xia *(*et al.) in which PCR amplification of randomly barcoded single-molecule oligonucleotides on a polyacrylamide gel surface, creates discrete clusters or "polonies" (Xia and Whitesides, 1998). The gel stamp used in Pixel-seq is fabricated by casting a polyacrylamide gel onto a microfabricated mold that imprints a high-density array of tiny wells. These wells are filled with barcoded oligonucleotides, which are sequenced *in situ* and transferred to the tissue section through stamping. As with most other high-resolution ST methods, Pixel-seq has only been able to demonstrate capture of RNA in a small capture area (49 mm^2). However, an additional advantage of the methods is the capacity to restamp the polony gels onto multiple tissue sections without significant decreases in sensitivity (Fu et al., 2022).

Despite these advancements in the available ST methods, several challenges remain. While there has been a dramatic increase in the resolution of methods, the size of capture areas remains generally low, limiting their applicability for larger tissue samples. Additionally, the incompatibility of some methods with H&E staining poses a problem for integrating spatial transcriptomics data with traditional histological analysis, and modern computational applications such inference of clinical diagnosis and prognosis from imaging data (Kather et al., 2020, 2019; Dolezal et al., 2022). Furthermore, several spatial transcriptomics meth-

ods require in situ sequencing to identify the position of barcodes (Fu et al., 2022; Rodriques et al., 2019; Vickovic et al., 2019). This reintroduces the complexity of fluorescent in situ sequencing, which was a notable advancement in spatially barcoded ST technologies. While *in situ* sequencing on a flow cell simplifies this process slightly, it still adds a layer of complexity that can be challenging to implement in standard laboratory settings (Poovathingal et al., 2024; Schott et al., 2024; Cho et al., 2021). Another critical issue is the cost associated with many commercialized ST methods. These factors can limit the accessibility and scalability of spatial transcriptomics, hindering its widespread adoption, especially for smaller laboratories or large-scale studies requiring extensive sample processing.

In conclusion, there is a pressing need for large-scale, cost-effective spatial transcriptomics methods that are simple to implement and do not require *in situ* sequencing. Such advancements would make spatial transcriptomics more accessible and scalable, enabling researchers to generate comprehensive spatial maps of gene expression across previously unreachable large tissue sections such as a whole adult mouse section. This, in turn, could accelerate the understanding of tissue architecture, cellular interactions, and the spatial dynamics of diseases at the organism scale.

1.2.6 The interplay of spatial proteomics and transcriptomics

Spatial proteomics has become a crucial addition to spatial transcriptomics, providing a more comprehensive understanding of protein distribution and interactions within tissues. An integrative approach is essential as proteins often exhibit post-translational modifications and interactions not directly inferred from transcriptomic data (Lundberg and Borner, 2019; Christopher et al., 2022). Furthermore, there is an increasing awareness that transcript levels by themselves are not sufficient to predict protein levels in many scenarios, particularly during disease where RNA species are subject to sudden fluctuations (Liu et al., 2016). Advances in fluorescence imaging, mass spectrometry, and proximity ligation assays have driven

the development of spatial proteomics, enabling detailed visualization and quantification of proteins within their native spatial context (Caprioli et al., 1997; Söderberg et al., 2008).

CO-Detection by indEXing (CODEX) is a leading method in fluorescence-based spatial proteomics. CODEX uses DNA-barcoded antibodies to label multiple proteins simultaneously within tissue sections, allowing for the visualization of up to 60 proteins in a single section at subcellular resolution of approximately 0.5 microns (Goltsev et al., 2018; Angelo et al., 2014). This high multiplexing capability is ideal for comprehensive proteomic analyses in complex tissues, facilitating the study of intricate cellular microenvironments and protein networks (Schulz et al., 2018). The high resolution of CODEX enables detailed mapping of cellular heterogeneity and cell-specific protein expression patterns (Giesen et al., 2014). However, the complexity of the technique, which involves multiple cycles of antibody staining, imaging, and fluorophore inactivation, can be time-consuming and technically challenging (Stack et al., 2014; Redit et al., 2023).

Mass spectrometry imaging (MSI) allows direct measurement of proteins, lipids, and metabolites from tissue sections without the need for labels or antibodies. Techniques like Matrix-Assisted Laser Desorption/Ionization (MALDI) MSI can target hundreds of biomolecules simultaneously with spatial resolution down to 5-20 microns, depending on the instrument and settings (Caprioli et al., 1997). MSI's label-free nature avoids biases introduced by antibody-based detection methods (Chughtai and Heeren, 2010). MSI can analyze a wide range of molecular species, offering a comprehensive view of the tissue microenvironment (Porta Siegel et al., 2018). It is also suitable for large tissue areas, making it useful for studying spatial heterogeneity across entire organs (Eriksson et al., 2013). However, the spatial resolution of MSI is generally lower than that of fluorescence-based techniques like CODEX, and its sensitivity can be influenced by the ionization efficiency of different molecules (Schulz et al., 2018).

Proximity ligation assay (PLA)-based approaches are valuable for studying protein-

protein interactions and post-translational modifications in situ. PLA uses paired antibodies conjugated with oligonucleotides that, when in close proximity, are ligated to form a circular DNA template, which is then amplified and detected using fluorescence microscopy, achieving a resolution of approximately 100 nanometers (Söderberg et al., 2008; Blokzijl et al., 2010). PLA typically targets 10-30 proteins, depending on antibody availability and design (Koos et al., 2014). Its high specificity for detecting protein interactions and modifications provides valuable insights into protein function within tissues. However, the dependence on high-quality antibody pairs and the assay's complexity can pose challenges (Weibrecht et al., 2010).

Spatial proteomics technologies significantly advance our understanding of biological processes and disease mechanisms. In cancer research, these technologies reveal tumor microenvironment heterogeneity, identifying protein expression patterns and interactions that drive tumor progression and therapy resistance (Goltsev et al., 2018; Blokzijl et al., 2010). In inflammatory diseases, spatial proteomics maps immune cell distribution and activation states, offering insights into immune response dynamics (Lundberg and Borner, 2019).

While spatial proteomics offers detailed views of protein distribution and interactions within tissues, it is rarely implemented for proteome-wide profiling and typically does not cover areas larger than 0.5 cm^2 (Lundberg and Borner, 2019). Therefore, it is often the case that spatial transcriptomics is initially used to probe gene expression patterns, followed by spatial proteomics for validation or more detailed investigation at the protein level. This sequential approach allows researchers to integrate transcriptomic and proteomic data for a comprehensive understanding of biological processes.

Alternatively, transcriptomic and proteomic measurements can be generated simultaneously through multi-omics technologies. Recently, methods such as spatial CITE-seq, Spatial Multi-Omics (SM-Omics), and DBit-seq combine oligonucleotide-labeled antibodies with spatial transcriptomics techniques to profile cell surface proteins and RNA in the same

tissue sections (Liu et al., 2023b; Vickovic et al., 2022; Liu et al., 2020). Because the oligonucleotides are polyadenylated and barcoded for each antibody species, they can be captured and processed in parallel to mRNA. This integrated approach significantly enhances the amount of information and throughput obtained from spatial experiments, providing a more comprehensive understanding of tissue architecture and function.

1.3 The organism-wide inflammatory response in sepsis

1.3.1 Epidemiology and clinical definitions of sepsis

Sepsis is the most common cause of death among critically ill patients in non-coronary intensive care units (Mayr et al., 2014) and was deemed a global health priority in 2017 (Rudd et al., 2020). This condition arises when the body's response to an infection becomes dysregulated, leading to widespread inflammation, tissue damage, organ failure, and potentially death. Sepsis is a complex syndrome that involves a combination of pathogenic microorganisms and a host's exaggerated immune response, making it a significant challenge for healthcare systems worldwide (Martin et al., 2006; Angus and Van der Poll, 2013). The incidence of sepsis continues to rise, with an estimated 49 million cases and 11 million sepsis-related deaths annually (Rudd et al., 2020). The high mortality rate and the complexity of managing septic patients necessitate a deeper understanding of its pathophysiology to improve clinical outcomes.

The clinical definition of sepsis has evolved significantly over the years, reflecting advancements in understanding its pathophysiology. Initially described as a systemic inflammatory response to infection, the Sepsis-1 and Sepsis-2 definitions focused on the presence of infection and a systemic inflammatory response syndrome (Bone et al., 1992; Levy et al., 2003). However, these definitions lacked specificity and often led to overdiagnosis (Seymour et al., 2016). The Sepsis-3 definition, introduced in 2016, redefined sepsis as life-threatening organ

dysfunction caused by a dysregulated host response to infection (Singer et al., 2016). This updated definition uses the Sequential (Sepsis-related) Organ Failure Assessment (SOFA) score to identify sepsis, aiming to improve diagnostic accuracy and emphasize the critical role of organ dysfunction in disease progression (Seymour et al., 2016; Evans et al., 2021). This shift underscores the importance of timely recognition and intervention to prevent irreversible organ damage and improve patient outcomes.

1.3.2 Molecular mechanisms of sepsis

The molecular mechanisms of sepsis are intricate and multifaceted, involving the recognition of pathogen-associated molecular patterns (PAMPs) by pattern recognition receptors (PRRs) on innate immune cells. These interactions trigger a cascade of intracellular signaling pathways that culminate in a dysregulated immune response characterized by excessive inflammation, endothelial dysfunction, and coagulopathy, ultimately leading to multiple organ failure and death. At the forefront of sepsis pathophysiology are Toll-like receptors (TLRs), particularly TLR4, which play a crucial role in detecting lipopolysaccharide (LPS) from Gram-negative bacteria. TLR4, upon recognizing LPS, forms a complex with the accessory proteins MD2 and CD14, initiating downstream signaling pathways through the adaptor protein MyD88-dependent and TRIF-dependent pathways (Janeway Jr and Medzhitov, 2002; Akira and Takeda, 2004). The MyD88-dependent pathway leads to the activation of nuclear factor kappa-light-chain-enhancer of activated B cells (NF-κB) and mitogen-activated protein kinases (MAPKs), resulting in the production of proinflammatory cytokines such as TNF-α, IL-1β, and IL-6 (Cohen, 2002; Luster, 2002) (Fig 1.2). The TRIF-dependent pathway, on the other hand, induces the production of type I interferons and the expression of interferon-stimulated genes (ISGs) through the activation of interferon regulatory factor 3 (IRF3) (Kawai and Akira, 2010).

The excessive release of proinflammatory cytokines, often referred to as a "cytokine

storm," is a hallmark of sepsis. TNF-α is one of the earliest and most critical cytokines released, inducing vasodilation and increasing vascular permeability, which contribute to hypotension and tissue edema characteristic of septic shock (Tracey et al., 1987; Fischer et al., 1992). IL-1β and IL-6 further amplify the inflammatory response by promoting the acute phase response, recruiting immune cells to sites of infection, and enhancing the production of additional proinflammatory mediators (Dinarello, 2011; Opal and DePalo, 2000). The acute phase response involves the liver producing acute phase proteins such as C-reactive protein (CRP), serum amyloid A (SAA), and fibrinogen, which play roles in opsonization, complement activation, and coagulation (Gabay and Kushner, 1999). The NLRP3 inflammasome is another critical component in the pathophysiology of sepsis. PAMPs and damage-associated molecular patterns (DAMPs) trigger the assembly of the NLRP3 inflammasome, leading to the cleavage and activation of caspase-1. Activated caspase-1 processes pro-IL-1β and pro-IL-18 into their mature forms, which are then secreted to further propagate the inflammatory response (Lamkanfi and Dixit, 2014; Jo et al., 2016). This amplification loop usually ensures a robust inflammatory response but is the central driver to tissue damage and systemic inflammation during sepsis.

Endothelial dysfunction is also a characteristic of sepsis, contributing to the pathogenesis of multiple organ failure. Proinflammatory cytokines such as TNF-α and IL-1β induce the expression of adhesion molecules (e.g., ICAM-1, VCAM-1) on endothelial cells, promoting the recruitment and extravasation of leukocytes into tissues (Spronk et al., 2004) (Fig 1.2). Additionally, these cytokines disrupt the endothelial barrier function by altering the cytoskeleton and junctional proteins, leading to increased vascular permeability and edema (Esmon, 2005). Endothelial cells also produce nitric oxide (NO) in response to inflammatory stimuli, which causes vasodilation and contributes to the hypotension observed in septic shock (Moncada et al., 1991).

Coagulopathy is another hallmark of sepsis, characterized by disseminated intravascular

coagulation (DIC) and microvascular thrombosis. The inflammatory response activates the coagulation cascade through the expression of tissue factor on endothelial cells and monocytes, leading to the generation of thrombin and fibrin clots (Levi, 2017). Concurrently, the anticoagulant pathways, including antithrombin, protein C, and tissue factor pathway inhibitor (TFPI), are impaired, exacerbating the procoagulant state (Esmon, 2005). The fibrinolytic system is also dysregulated, with elevated levels of plasminogen activator inhibitor-1 (PAI-1) inhibiting fibrinolysis and promoting clot persistence (Levi and van der Poll, 2013). These coagulation abnormalities result in microvascular occlusions that compromise tissue perfusion and contribute to organ dysfunction.

1.3.3 The role of cytokines in sepsis

Cytokines are pivotal in the pathophysiology of sepsis, orchestrating the immune response and mediating the inflammatory cascade. TNF-α is one of the earliest and most critical cytokines released during sepsis, inducing vasodilation and increasing vascular permeability, which contribute to hypotension and tissue edema characteristic of septic shock (Tracey et al., 1987; Fischer et al., 1992) (Fig 1.2). TNF-α has been shown to upregulate adhesion molecules on endothelial cells, facilitating the recruitment of leukocytes to sites of infection and inflammation (Beutler and Cerami, 1988). Elevated levels of TNF-α are associated with worse outcomes in sepsis, underscoring its central role in disease progression (Parrillo et al., 1990).

IL-1β and IL-6 are also key mediators that promote the acute phase response and recruit immune cells to sites of infection. IL-1β induces fever, increases the expression of adhesion molecules on endothelial cells, inflammasome activation, and stimulates the production of acute phase proteins by the liver (Lamkanfi and Dixit, 2012; Dinarello, 2011). IL-6 is a pleiotropic cytokine that, besides promoting the acute phase response, also has anti-inflammatory properties, highlighting its dual role in inflammation (Hunter and Jones,

2015). It has been shown that elevated IL-6 levels correlate with disease severity and mortality in septic patients (Dellinger et al., 2008; Hack et al., 1989).

Type I IFNs, including IFN-α and IFN-β, induce the expression of ISGs, which have antiviral properties and can modulate the function of various immune cells (Stetson and Medzhitov, 2006; de Padilla and Niewold, 2016). It has been shown that type I IFNs can exacerbate inflammation by promoting the activation of inflammatory macrophages and enhancing the production of other proinflammatory cytokines (Schneider et al., 2014; Crayne et al., 2019).

Moreover, IL-10, an anti-inflammatory cytokine, is elevated in sepsis and serves to counterbalance the proinflammatory response. IL-10 inhibits the production of proinflammatory cytokines and reduces the expression of MHC class II on antigen-presenting cells, thereby limiting the immune response (Moore et al., 2001). Despite its protective role, excessive IL-10 production can lead to immunosuppression and increased susceptibility to secondary infections (Couper et al., 2008).

Cytokines can also act synergistically to drive the molecular mechanisms of sepsis pathophysiology. The pairwise effects of TNF-α with IL-18, IFN-γ, or IL-1β have been shown to sufficiently mirror the impact of sepsis across tissues (Takahama et al., 2024). Moreover, TNF-α and IFN-γ co-treatment has been demonstrated to activate the JAK/STAT1/IRF1 axis, leading to increased nitric oxide production and driving caspase-8/FADD-mediated PANoptosis in bone marrow-derived macrophages (Karki et al., 2021). Additionally, the combination of IL-1β and TNF-α has been observed to be more potent than either agent alone in inducing the hemodynamic and hematological changes typical of septic shock (Okusawa et al., 1988). Therefore, the interplay between cytokines creates a feedback loop that exacerbates the inflammatory response, highlighting the need for therapeutic strategies that target multiple cytokines to effectively manage sepsis. Therapeutic interventions such as monoclonal antibodies against TNF-α, IL-1 receptor antagonists, and inhibitors of IL-6 sig-

naling are being explored to modulate the cytokine response in sepsis, but with limited success (Cohen, 2002; Shakoory et al., 2016). However, the challenge remains to balance the suppression of harmful inflammation while preserving the host's ability to fight infections.

1.3.4 The impact of sepsis on innate immune cells

Innate immune cells, such as macrophages, neutrophils, and mast cells/basophils, are significantly impacted during sepsis. Macrophages, which are key players in the initial immune response, are activated through PRRs like TLR4, leading to the production of proinflammatory cytokines and chemokines (Akira and Takeda, 2004; Takeda and Akira, 2003) (Fig 1.2). This activation is crucial for the early defense against pathogens, but dysregulation can contribute to the cytokine storm observed in sepsis (Chen et al., 2023c). It has been shown that macrophages in septic patients exhibit altered metabolism, characterized by a shift towards glycolysis, which supports their proinflammatory functions (Chen et al., 2023c; Angiari et al., 2020).

Neutrophils, the first responders to infection, undergo significant changes in function and lifespan during sepsis. They exhibit enhanced phagocytic activity and the release of neutrophil extracellular traps (NETs), which can trap and kill pathogens but also contribute to tissue damage and organ dysfunction (Brinkmann et al., 2004; Klopf et al., 2021). The excessive formation of NETs has been implicated in the pathogenesis of sepsis-associated acute lung injury and disseminated intravascular coagulation (Caudrillier et al., 2012; Camicia et al., 2014). Furthermore, mast cells and basophils, release histamine, tryptase, and other mediators that exacerbate vascular permeability and inflammation, contributing to the hypotension and edema characteristic of septic shock (Galli et al., 2008; Abraham and St. John, 2010).

These innate immune cells are distributed throughout various organs, such as the lungs, liver, and spleen, and their activation and dysfunction play critical roles in the pathogenesis

of sepsis. For instance, Kupffer cells in the liver can produce large amounts of proinflammatory cytokines, leading to systemic inflammation and liver damage (Crispe, 2009). Similarly, alveolar macrophages in the lungs contribute to the development of acute respiratory distress syndrome (ARDS) by releasing cytokines that increase vascular permeability and attract neutrophils (Matthay et al., 2019). The spleen, an important organ for filtering blood and mounting immune responses, can also be severely affected, with splenic macrophages contributing to systemic inflammation and immune dysregulation (Lewis et al., 2019). Overall, the complex interplay between these various innate immune cells and their responses to sepsis highlights the need for targeted therapies that can modulate their activities without compromising the body's ability to fight infection.

1.3.5 Impact of sepsis on lymphocytes

Lymphocyte apoptosis is a hallmark of sepsis, contributing to the profound immunosuppression observed in septic patients. T cells and B cells undergo apoptosis in response to overwhelming inflammation and direct signaling from cytokines like TNF-α and Fas ligand (FasL) (Hotchkiss et al., 1999, 2001). This apoptosis leads to a depletion of adaptive immune cells, impairing the body's ability to mount an effective immune response against the initial infection and increasing susceptibility to secondary infections (Leentjens et al., 2013; Hotchkiss et al., 2016). Studies have shown that septic patients exhibit significant reductions in $CD4^+$ and $CD8^+$ T cell counts, which correlate with increased mortality (Boomer et al., 2011). Furthermore, the apoptosis of B cells compromises the production of antibodies, further weakening the immune defense (Balk, 2000).

The loss of lymphocytes also disrupts the balance of regulatory T cells (Tregs) and effector T cells, further contributing to immune dysregulation and the persistence of the septic state. Tregs, which normally help maintain immune homeostasis and prevent autoimmunity, can become dysfunctional or depleted during sepsis, exacerbating the uncontrolled inflam-

matory response (Venet et al., 2008; Boomer et al., 2011). This imbalance not only impairs the resolution of inflammation but also increases the risk of secondary infections due to the impaired regulatory function of Tregs (Leentjens et al., 2013). The intricate interplay between pro-apoptotic signals and the immune environment in sepsis highlights the complexity of the disease and the challenges in developing effective immunomodulatory therapies.

1.3.6 Central transcription factors in the sepsis response

Key transcription factors, such as STAT1 and IRF1, play critical roles in regulating the immune response during sepsis. STAT1 is activated by type I and II interferons and is essential for the induction of ISGs, which are involved in antiviral responses and immune regulation (Darnell Jr et al., 1994; Schindler et al., 2007). Activation of STAT1 leads to the transcription of genes that enhance the antimicrobial activity of macrophages and the production of proinflammatory cytokines, which are crucial for controlling infection (Schroder et al., 2004; Lazear et al., 2019). IRF1, another important transcription factor, regulates the expression of genes associated with the inflammatory response, apoptosis, and immune cell differentiation (Taniguchi and Takaoka, 2001; Paun and Pitha, 2007) (Fig 1.2). IRF1 is activated by various cytokines, including IFN-γ and TNF-α, and it plays a pivotal role in the expression of genes involved in the immune response, such as inducible nitric oxide synthase (iNOS) and caspase-1 (Schroder et al., 2004). Studies have shown that IRF1 is crucial for the regulation of the immune response during sepsis, and its dysregulation can lead to either an excessive inflammatory response or immune paralysis (Ivashkiv and Donlin, 2014; Paun and Pitha, 2007).

Other notable transcription factors in sepsis include NF-κB and AP-1.NF-κB is a key regulator of the immune response and is activated by various PAMPs and DAMPs during sepsis (Hayden and Ghosh, 2012; Bonizzi and Karin, 2004). NF-κB controls the expression of a wide range of proinflammatory cytokines, chemokines, and adhesion molecules, and its

activation is essential for the recruitment and activation of immune cells at sites of infection (Lawrence, 2009). AP-1, a transcription factor complex composed of members of the JUN, FOS, and ATF families, also plays a significant role in the immune response during sepsis (Hess et al., 2004). AP-1 is activated by various stress signals and cytokines and regulates the expression of genes involved in inflammation, cell proliferation, and apoptosis (Shih et al., 2011). Studies have shown that AP-1 activity is increased in septic patients and is associated with the expression of proinflammatory cytokines and the induction of apoptosis in immune cells (Hess et al., 2004). Understanding the transcriptional networks involved in sepsis is crucial for unraveling the complex mechanisms underlying the condition, leading to more informed management strategies.

1.3.7 Non-immune proteins in sepsis pathophysiology

The pathophysiology of sepsis involves not only the traditional players of the immune system but also proteins not typically associated with the immune inflammatory response that play significant roles. One example is secreted phospholipase A2 (sPLA2) enzymes, present in mammalian tissues and snake venom, which hydrolyze phospholipids to release fatty acids and fatty acids, playing diverse roles in health and disease (Lambeau and Gelb, 2008). Their functions depend on intrinsic catalytic properties, substrate preferences, and changes in expression across cell types and disease conditions (Murakami et al., 2020). For instance, sPLA2 group V (PLA2G5) exhibits pathogenic and protective roles in macrophages, adipocytes, endothelial cells, bronchial epithelial cells, and cardiomyocytes (Samuchiwal and Balestrieri, 2019; Yamaguchi et al., 2018; Sato et al., 2014; Watanabe et al., 2020; Yano et al., 2011). PLA2G5 is induced by LPS in acute lung injury models, but its role in systemic inflammation such as sepsis remains underexplored (Muñoz et al., 2009). High-Mobility Group Box 1 (HMGB1) is another protein that plays a significant role in the pathophysiology of sepsis. Originally identified as a nuclear protein that binds DNA and regulates transcrip-

tion, HMGB1 can be released extracellularly during tissue injury and infection (Yang et al., 2013). Extracellular HMGB1 acts as DAMP that amplifies the inflammatory response by interacting with receptors such as TLR4 and the receptor for advanced glycation end products (Yang et al., 2013; Wang et al., 2014) (Fig 1.2). Elevated levels of HMGB1 have been associated with poor outcomes in septic patients, and targeting HMGB1 has been proposed as a therapeutic strategy to mitigate the inflammatory response in sepsis (Jiang et al., 2022). Heat shock proteins (HSPs) are another group of proteins that, while traditionally known for their role in protein folding and protection against cellular stress, have been implicated in the immune response during sepsis. HSP70 and HSP90, in particular, can be released into the extracellular space where they function as chaperones. HSP70 has been shown to enhance the production of proinflammatory cytokines and promote the maturation of dendritic cells, while HSP90 stabilizes several proteins involved in the inflammatory signaling pathways (Calderwood et al., 2007; Maloney and Workman, 2002). Additionally, adipokines, such as adiponectin and leptin, are hormones secreted by adipose tissue that play roles in metabolism and immune function. In the context of sepsis, adipokines can influence the immune response and metabolic regulation. Adiponectin has anti-inflammatory properties and can modulate the activity of macrophages and neutrophils, whereas leptin, which generally promotes inflammation, has been shown to be elevated in septic patients and may contribute to the dysregulated immune response observed in sepsis (Fantuzzi, 2005; Naylor and Petri, 2016).

1.3.8 Diverse mechanisms organ dysfunction and damage in sepsis

Sepsis affects multiple organs, leading to a cascade of physiological disruptions that can result in multi-organ failure. The lungs are often the first organs affected, with sepsis frequently leading to ARDS, characterized by increased vascular permeability, alveolar damage, and inflammatory infiltration (Matthay et al., 2019). The kidneys are also highly susceptible,

with sepsis-induced acute kidney injury (AKI) resulting from hypoperfusion, inflammation, and direct cellular toxicity (Bellomo et al., 2012) (Fig 1.2). Cardiovascular dysfunction is another critical aspect of sepsis, with myocardial depression and vasodilation contributing to septic shock and impaired tissue perfusion (Rudiger and Singer, 2013). Hepatic dysfunction and gut barrier disruption further exacerbate systemic inflammation by allowing translocation of bacteria and endotoxins from the gastrointestinal tract into the bloodstream, thus perpetuating the cycle of infection and inflammation (Rao, 2009).

Historically, measurements of sepsis have been primarily conducted using blood samples. While informative, this approach does not provide a complete picture of how individual organs respond to sepsis, emphasizing the need for organ- and tissue-specific studies. The importance of organ impact is highlighted in the most recent definition of sepsis, which underscores the need to understand the responses of different organs to develop more effective treatments (Singer et al., 2016). Current efforts to address organ damage in sepsis include the use of supportive therapies such as mechanical ventilation, renal replacement therapy, and vasoactive drugs, as well as experimental approaches targeting specific pathways involved in organ injury (Angus and Van der Poll, 2013; Dellinger et al., 2008). These interventions are crucial for stabilizing patients and preventing irreversible damage, but further research is needed to develop targeted therapies that can modulate the underlying pathophysiological processes of sepsis and limiting the organ damage associated with mortality.

1.3.9 Spatial omics approaches in sepsis research

Understanding the spatial dynamics of sepsis is crucial for elucidating the mechanisms underlying this complex syndrome. Spatial transcriptomics allows researchers to visualize how different regions within an organ respond to sepsis and identify spatial patterns of gene expression that contribute to disease pathology. By capturing the spatial context of cellular and molecular changes, spatial transcriptomics can reveal critical insights into how different

tissues and organs respond to genetic perturbations, environmental changes, and disease processes. For example, spatial analysis of lung tissues from septic patients has shown that specific regions within the lungs exhibit distinct gene expression profiles associated with different stages of ARDS. It has been observed that alveolar macrophages, when exposed to high levels of TNF-α and IL-1β, produce significant amounts of proinflammatory cytokines and chemokines, leading to localized tissue damage and increased vascular permeability (Matthay et al., 2019; Kasmani et al., 2023). These findings highlight the importance of local immune responses and tissue-specific damage in the progression of ARDS during sepsis. In the kidneys, spatial mapping in a sepsis-induced AKI model revealed that regions such as the renal cortex and medulla show differential immune cell infiltration and gene expression patterns. Specifically, it was been shown that infiltrating neutrophils and macrophages in the renal cortex produce high levels of reactive oxygen species (ROS) and proinflammatory cytokines, contributing to tubular injury and impaired renal function (Kirita et al., 2020). This region-specific information is crucial for understanding the heterogeneous nature of kidney damage in sepsis and for developing targeted therapies.

Spatial information about the distribution of cell types and region-specific effects within organs significantly impacts our understanding of sepsis. Alveolar macrophages in the lungs and Kupffer cells in the liver play critical roles in localized inflammatory responses and systemic cytokine dissemination during sepsis (Matthay et al., 2019; Crispe, 2003). In the liver, Kupffer cells exposed to LPS and DAMPs release high levels of TNF-α and IL-6, leading to hepatocyte apoptosis and liver dysfunction (Crispe, 2003). The spatial distribution of these immune cells and their interactions with other cell types are crucial for the development and progression of multi-organ dysfunction in sepsis. In addition to spatial transcriptomics, other spatially resolved techniques, such as multiplex immunohistochemistry and in situ hybridization, have been employed to study sepsis. These methods allow for the visualization and quantification of protein expression and cellular interactions within

the tissue microenvironment. For instance, multiplex immunohistochemistry has identified changes in the expression of immune checkpoint molecules, such as PD-1 and CTLA-4, in different tissue compartments during sepsis, suggesting potential targets for immunotherapy (Madorsky Rowdo et al., 2015).

In conclusion, sepsis is a multifaceted syndrome characterized by systemic inflammation and multi-organ dysfunction. The molecular mechanisms, clinical definitions, and roles of cytokines and immune cells have been extensively studied, yet much remains to be understood about the spatial dynamics of sepsis. Advances in spatial transcriptomics provide new opportunities to explore the tissue-specific responses to sepsis and uncover the intricate interplay between different cell types and organs. This knowledge is crucial for developing targeted therapies and improving outcomes for patients with sepsis.

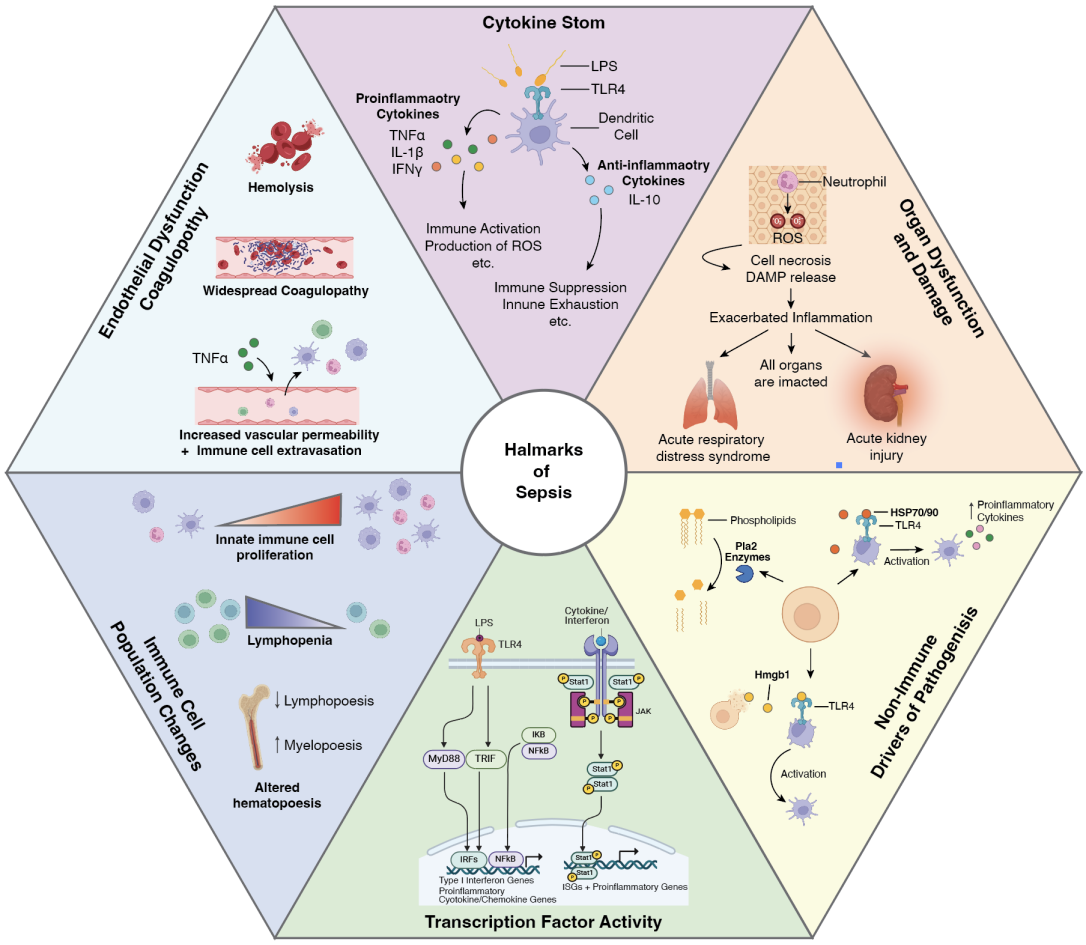


Figure 1.2: Hallmarks of sepsis. Diagram illustrating the pathophysiological features of sepsis, encompassing **Cytokine Storm:** Triggered by LPS and TLR4 signaling, leading to the release of pro-inflammatory and anti-inflammatory cytokines, resulting in inflammation and immune paralysis. **Organ Dysfunction and Damage:** Driven by cell necrosis and DAMP release from neutrophils, leading to exacerbated inflammation and multi-organ impact, including acute respiratory distress syndrome, and acute kidney injury. **Non-Immune Drivers of Pathogenesis:** Several classes of non-immune related proteins contribute to sepsis pathophysiology. The activation of HSP70/90 and HMGB1 through TLR4 signaling, contributes to exacerbating the inflammatory response. Pla group 2 phospholipase activity also contributes to the sepsis response. **Transcription Factor Activity:** LPS-induced TLR4 signaling activates transcription factors such as NF-κB and IRFs, which regulate the expression of pro-inflammatory cytokine and chemokine genes. Interferon- or cytokine-induced Janus kinase (JAK)/STAT signaling regulates the expression of ISGs and pro-inflammatory cytokines. **Immune Cell Population Changes:** Involves decreased lymphopoiesis, increased myelopoiesis, contributing to lymphopenia and innate immune cell proliferation. **Endothelial Dysfunction and Coagulopathy:** Characterized by hemolysis, widespread coagulopathy, increased vascular permeability, and immune cell extravasation, primarily driven by TNF-α.

CHAPTER 2

REPURPOSING LARGE-FORMAT MICROARRAYS FOR SCALABLE SPATIAL TRANSCRIPTOMICS

2.1 Abstract

Spatiomolecular analyses are key to study tissue functions and malfunctions. However, we lack profiling tools for spatial transcriptomics that are easy-to-adopt, low cost, and scalable in terms of sample size and number. Here, we describe a method, Array-seq, to repurpose classical oligonucleotide microarrays for spatial transcriptomics profiling. To generate Array-seq slides, we first obtain microarrays carrying custom-design probes that contain common sequences flanking unique barcodes at known coordinates. Second, we perform a simple, two-step reaction that produces mRNA capture probes across all spots on the microarray and thereby creates Array-seq slides set for spatial transcriptomics. We demonstrate that Array-seq yields spatial transcriptomes with high detection sensitivity and localization specificity using histological sections from mouse tissues as test systems. Moreover, we show that the large surface area of Array-seq slides enables the generation of spatial transcriptomes at high throughput by profiling multi-organ sections, in three dimensions by processing serial sections from one sample, and across whole human organs using spleen sections. Thus, by combining the two workhorses in gene expression measurements from the past three decades – microarrays and next-generation sequencing – we created a simple and flexible platform for spatial transcriptomics which paves the way for spatiomolecular studies of small-to-large specimens at scale.

2.2 Introduction

The architecture of a tissue determines its function and malfunction in health and disease. Therefore, technologies to study the spatial organization of cells and molecules in tissues are fundamental to biomedical research and clinical pathology. Recent advances in the field of spatial transcriptomics (ST) have enabled the sequencing of the transcriptome associated with specific areas of tissue sections (Moses and Pachter, 2022; Lein et al., 2017; Rao et al., 2021; Crosetto et al., 2015). Transcriptome-wide ST methods most commonly rely on mRNA capture via spatially barcoded oligo(dT) probes that are anchored onto a solid substrate. The data obtained by ST profiling is composed of mRNA counts at each of the spots tiling the area of the substrate under the tissue section. Several technologies for ST profiling through mRNA capture on a slide have emerged from academic labs in recent years (Ståhl et al., 2016; Stickels et al., 2021; Vickovic et al., 2019; Liu et al., 2020; Chen et al., 2022; Cho et al., 2021; Fu et al., 2022). However, existing ST methods face limitations ranging from small surface area, lack of compatibility with H&E staining, low throughput, and high costs. In addition, the spread of these methods beyond their institutions of origin has been impeded by significant barriers to adoption including the need for special instrumentation, expertise, and custom-built reagents. One notable exception is that of the first platform developed for spatial transcriptomics, now Visium, which has become widespread thanks to commercialization and ease of use (Ståhl et al., 2016; Salmén et al., 2018). However, this platform remains limited by its small surface area, low resolution, and high cost. Taken together, these gaps in ST technologies preclude broad adoption across fields and detailed spatiomolecular analyses across many tissue samples, small or large, for basic and clinical research.

To fill these gaps in spatiomolecular profiling methods, we hypothesized that classical oligonucleotide microarrays could be repurposed for spatial transcriptomics. Oligonucleotide microarrays have profoundly influenced the fields of genomics and molecular biology by en-

abling high-throughput analysis of gene expression and genetic variations. The foundational work for microarray technology began in the early 1990s, drawing upon the solid-phase synthesis of oligonucleotides (Caruthers et al., 1987; Beaucage and Caruthers, 1981). The initial development of DNA microarrays utilized photolithographic techniques, enabling the light-directed synthesis of custom oligonucleotides directly on a glass slide (Fodor et al., 1991; Pease et al., 1994). This method allowed for the integration of thousands of unique oligonucleotide probes on a single slide. Each probe represented a specific gene sequence, thereby enabling high-throughput analysis of gene expression. Microarrays have been widely used to measure changes in gene expression (Schena et al., 1995), genomic DNA sequence and structure (Chee et al., 1996), or protein-DNA interactions (Ren et al., 2000). However, the oligonucleotide length (~25- to 85-mer) and its 3' tethering to the glass slide precludes using off-the-shelf arrays for spatial transcriptomics because they cannot carry 5' anchored probes with oligo(dT) for mRNA capture. In addition, the chemistry for oligonucleotide synthesis on arrays is not compatible with the addition of random bases needed for quantifying mRNA molecules using unique molecular identifiers (UMIs) (Islam et al., 2014). That being said, finding ways to repurpose microarrays into ST-compatible slides would be attractive in theory due to several advantageous characteristics of this platform. First, the synthesis of custom-design barcodes at pre-determined x, y coordinates can be done on demand using in situ synthesis of oligonucleotides by an ink-jet printing method based on phosphoramidite chemistry (Hughes et al., 2001). On the contrary, most existing ST tools rely on the random dispersion of barcoded sequences across the two-dimensional plane of a substrate (Stickels et al., 2021; Vickovic et al., 2019; Chen et al., 2022; Cho et al., 2021; Fu et al., 2022). Therefore, these ST methods require additional sequencing steps prior to the spatiotranscriptomic profiling of tissue sections to determine the spatial localization of barcodes, which compounds with other barriers to adoption and increase time and costs. Second, over two decades of technology development and refinement by many academic and industrial groups have led to

the emergence of robust array printing technologies that enable the rapid, high-accuracy, and on-demand synthesis of microarrays with custom sequences at low costs. Third, microarrays use glass slides of the standard microscope format, which makes them compatible with H&E staining and standard imaging instrumentation.

Here, we transformed custom-sequence microarrays into ST slides using a simple, two-step reaction yielding spatially barcoded probes for in situ mRNA capture in tissue sections. Using large-format arrays, our method produced Array-seq slides carrying 974,016 spots of 30 µm in diameter (36.65 µm center-to-center distance) across 11.31 cm^2 in total surface area, thereby providing a high degree of flexibility in terms of the size and number of samples that can be profiled on a single slide. We demonstrated that Array-seq generated high quality data using mouse and human tissues in two- and three-dimensional configurations. We thus created a highly scalable ST platform poised to propel the broad adoption and application of spatiomolecular profiling across basic and clinical fields of inquiry.

2.3 Materials and Methods

Mice

Female C57BL/6J mice (6- to 8-weeks old) were obtained from the Jackson Laboratories (stock 000664). Animals were housed in specific pathogen-free conditions at The University of Chicago, and all experiments were performed in accordance with the US National Institutes of Health Guide for the Care and Use of Laboratory Animals and approved by The University of Chicago Institutional Animal Care and Use Committee.

Access to human tissue and ethics oversight

The human spleen sample was obtained from a patient with metastatic high-grade serous carcinoma of Mullerian origin. The surgical intervention involved a splenectomy. The splenic

parenchyma was negative for carcinoma. The donor sample was collected at the University of Chicago Medical Center (UCMC) with informed consent from the donor family. Deidentified tissue sample collection and subsequent experiments were approved by the University of Chicago Biological Sciences Division/UCMC Institutional Review Board (IRB = 21-0707). The human spleen sample was collected within 1 hour of resection, placed in a plastic bag, frozen in a dry ice hexane bath for 3 minutes and stored at -80°C until use.

Custom oligonucleotide microarray design

Spatial barcodes were designed using the DNABarcodes R package (Buschmann, 2017). For 18-mer barcodes used for the initial gel-based optimizations of on-slide probe assembly, we first generated 9-mer barcodes with a minimum Hamming distance of 3, no self-complimentary sequences, no consecutive base repetition ≥ 3, and with a 50% GC content. Resulting barcodes were duplicated and concatenated in all possible 2-way combinations, creating a pool of over 6.5 million, 18-mer barcodes which maintained the minimum Hamming distance of 3 as in the original set. Barcode sequences were filtered to maximize sequencing performance using the following criteria: (1) does not begin with AC or CC, (2) does not end with GG, and (3) no consecutive base repetition ≥ 3. After filtering, we obtained 5,069,490 unique barcode sequences from which a random set of 974,016 barcodes was selected. For 12-mer barcodes used for all Array-seq ST profiling experiments, we followed a similar procedure as described above for the 18-mer barcodes without the concatenation step. We first generated an initial pool of all possible 12-mer barcodes with a GC content between 40 and 60%, yielding 10,272,768 independent barcodes. Barcode sequences were then filtered to maximize sequencing performance using the following criteria: (1) no individual base present in more than half of the entire barcode sequence, (2) no base repeated consecutively 4 times or greater, (3) no base repeated three times with additional occurrences of the same base 2 bases away from the repeat in either direction, (4) no 4-base stretches of As and/or Ts or

Gs and/or Cs in the first 4, middle 4, or last 4 bases of the 12-mer barcode. After filtering, we obtained 6,814,344 unique barcode sequences which were further filtered to only include a pool of barcode with a minimum Hamming distance of 2, and no self-complementarity, yielding a pool of 1,048,608 barcode sequences from which a random set of 974,016 barcodes not starting with AC or CC was selected.

On-slide, mRNA capture probe assembly

Custom large-format microarrays were attached to an adaptor with 1- or 8-well chambers (Electron Microscopy Sciences, 63484-31 or 63484-25). Anchor 1 (5'-CCCTACACGACGCTC TTCCGATCT-3') and Anchor 2-UMI-(dT)30VN (5'- /5Phos/GTAAAACGACGGCCAGN NNNNNNNNNNTTTTTTTTTTTTTTTTTTTTTTTTTTTT*T*T*V*N-3')
(500 nM each) were hybridized to probes on the array in duplexing buffer (IDT, 11-01-03-01). After adding soluble oligos into array chambers, we sealed the arrays (Electron Microscopy Sciences, 63484-80) and incubated the gasket with solution for 1 hour at 45°C on an in situ hybridization (ISH) adapter (Techne, EAR99) in a thermocycler (Mastercycler X50a, Eppendorf, 6313000018). After hybridization, arrays were washed using a three-step procedure with the following buffers consecutively for 1 min each chamber on the array: 0.1% Tween20 in 1X PBS, 0.01% Triton X100 in 1X PBS, and 1X PBS. Next, we prepared an extension-ligation reaction mix consisting of 1X T4 Ligase Buffer (NEB, M0202L), 0.2 mg/mL BSA (Sigma, B8667- 1.25ML), 50 mM KCl (Millipore Sigma, P3911), 100 µM dNTPs (NEB, N0447), 5 mM ATP (NEB, P0756L), 0.05 U/µL Phusion High-Fidelity DNA Polymerase (NEB, M0530L), and 30 U/µL T4 DNA ligase (NEB, M0202L). The extension-ligation reaction mix was added into each chamber on the array, the chamber was sealed, and the array was incubated overnight at 37°. After extension-ligation, arrays were washed using the three-step procedure detailed above. Lastly, to remove unligated Anchor 2-UMI-dT oligonucleotides, the array was incubated for 10 minutes at 58°C in 25 mM NaCl and 25 mM

Tris-HCl (pH = 7.4). The array was washed using the three-step procedure detailed above, washed briefly with nuclease free water, detached from the chamber, air dried, and stored at 4°C in a sealed, opaque 50-mL conical tube (Thermo Fisher Scientific, 50-550-489) until use. We note that our gap-fill reaction yields 3 oligonucleotide species (see lane c of the gel in Fig 2.1c): (i) a fully assembled capture probe (107-mer), (ii) an Anchor 2-UMI-dT oligo, and (iii) an overextended Anchor 1 oligo. The inclusion of the last wash step at 58°C for 10 min in the procedure detailed above leads to the removal of the unwanted Anchor 2-UMI-dT oligo (see lane d of the gel in Fig 2.1c). The wash step does not fully remove the overextended Anchor 1 species, which is not a problem because these oligos do not interfere with mRNA capture, cDNA synthesis, or library construction since they are likely to be progressively removed during wash steps such full length cDNA cleanup with zymo columns and post-PCR cleanups with SPRI beads. We estimated that the remaining overextended Anchor 1 oligos likely decrease the theoretical, maximum mRNA binding capacity of Array-seq slides by ~25%.

Polyacrylamide gel electrophoresis (PAGE) analysis

On-slide probe assembly was carried out as described in the previous section using the 18-mer barcode arrays (SureSelect DNA Capture Array (1M) design, (Agilent, G3358A, Design ID = 086624) and hybridized with Anchor 1 and modified Anchor 2 with a 17-bp UMI sequence (5'-/5Phos/GTAAAACGACGGCCAGNNNNNNNNNNNNNNNNTTTTTTTTTTTTTTTT TTTT TTTTTTTT*T*T*V*N-3') to facilitate the identification of the various oligo species resulting from our on-slide, gap-fill reaction. Following ST probe assembly, oligonucleotide products were eluted from the microarray with 0.1M KOH (Sigma, P4494-50ML). Oligonucleotide eluates were neutralized by adding 0.2X volume of 1M Tris-HCl (pH = 7.4) (Bioworld, 21420063-1) and purified using Oligo Clean & Concentrator columns (Zymo, D4060). Purified oligonucleotide samples were mixed with an equal volume of Novex TBE-Urea Sample

Buffer (2X) (Thermo Fisher Scientific, LC6876) and heated at 70°C for 3 minutes. Samples and the 20/100 Ladder (IDT, 51-05-15-02) were loaded on a Novex 15% TBE-Urea Gel (Thermo Fisher Scientific, EC68855BOX) and ran at 200V for 75 minutes using the XCell SureLock Mini-Cell gel electrophoresis system (Thermo Fisher Scientific, EI0001) in 1X Novex TBE Running Buffer (ThermoFisher Scientific, LC6675). Gels were stained with 1X SYBR Gold Nucleic Acid Gel Stain (Thermo Fisher Scientific, S11494) in 1X TBE Running Buffer for 10 minutes and imaged on the ChemiDoc MP Imaging System (Bio-Rad). Gel band intensities were quantified using ImageJ (https://imagej.net/ij/index.html).

Ligation bias analysis

Ligation bias analysis. To quantify potential ligation biases during the extension-ligation reaction on the array for mRNA capture probe assembly, we calculated the averages of total UMI counts per spot across all the spots whose spatial barcodes ended with the same last single or two bases. For these analyses, we used the Array-seq data from tissue section (replicate 1) of the main olfactory bulb (MOB) system of the mouse brain shown in Fig 2.3.

Nuclei per spot analysis

Array-seq slides were hybridized with a fluorescently labeled Anchor 1 (5'-/5Cy5/CCCTACA CGACGCTCTTCCGATCT-3') as described above. After hybridization, arrays were washed with nuclease-free water and dried at room temperature. Tissue sections were placed on fluorescently labeled slides and fixed in 100% methanol at described above. Sections were subsequently stained for 10 min at room temperature with 1 µg/mL DAPI (Fisher Scientific, NC0804630). Sections were washed with nuclease-free water, dried at room temperature, and imaged at 20X magnification using an Olympus VS2000 slide scanner. Resulting fluorescent images capturing spots (Cy5) and nuclei (DAPI) were analyzed using Qupath-0.2.3 (https://qupath.github.io/). Nuclei and spots were detected using the Cell Detection tool in

Qupath and the centroids for each nucleus and spot object were exported for downstream processing in R. A nucleus was assigned to a spot by calculating the minimum Euclidean distance between each nucleus and all spots. Resulting distributions of the numbers of nuclei per spots for each tissue type were plotted using the ggplot packages (https://ggplot2.tidyverse.org/).

Histological sectioning

Mice were euthanized with CO2 and organs were harvested, fresh-frozen in OCT (Tissue-Tek, 4583) on powdered dry ice, and stored at -80°C until further use. Frozen tissues were sectioned (10- µm thickness) using a cryomicrotome (Leica CM3050S) and placed on Array-seq slides pre-chilled in the cryostat chamber prior to downstream histology analysis and spatial transcriptomics profiling. For serial sectioning used to perform 3D ST analyses, consecutive mouse kidney sections were placed onto Array-Seq slides while skipping ~100 µm between each section that was profiled. In mouse sections intended for comparison between Array-Seq and Visium, immediately adjacent kidney sections were placed onto each ST slide. The human spleen sample was taken from -80°C storage, immediately placed in a freezing frame containing SCEM (SECTION-LAB Co. Ltd.), and frozen into a dry ice hexane bath. The frozen human spleen was sectioned using a cryomacrotome (Leica CM3600XP).

Tissue section fixation, H&E staining, and imaging for Array-seq

Tissue sections on Array-seq slides were thawed at 37°C for 1 minute and fixed for 30 minutes at -20°C in 100% methanol (Sigma-Aldrich, 32213). Following fixation, slides were dried for 1 minute at room temperature, and incubated with 2 U/ µL Ribolock (Thermo Fisher Scientific, EO0382) in 5X SSC (Sigma, S6639-1L) for 5 minutes at room temperature. Hematoxylin (Sigma-Aldrich, MHS16-500ML) and eosin (Sigma-Aldrich, HT110216-500ML) were filtered through a 0.22-µm sterile filter (Foxx Life Sciences, 371-2215-OEM) before use. After the SSC buffer was removed from the slide surface, sections were stained for 3 minutes

at room temperature with hematoxylin, washed in nuclease free water, and stained for 1 minute at room temperature with eosin diluted 1:10 in 0.45 M Tris-Acetic acid buffer, pH = 6.0 (Sigma-Aldrich, GE17-1321-01 and A6283). The slide was washed in nuclease-free water and kept at room temperature until dry and imaged at 20X magnification using an Olympus VS2000 slide scanner.

Tissue section permeabilization and in situ reverse transcription for Array-seq

Array-seq slides with H&E-stained sections were attached to an adaptor with 1- or 8-well chambers (Electron Microscopy Sciences, 63484-31 or 63484-25). For permeabilization and reverse transcription, we followed procedures previously described by others12 with modifications as described below. Tissue sections were permeabilized with 0.1% pepsin (Sigma, P7000-25G) in 0.1 M HCl (Cole-Parmer, EW-88011-96) at 37°C. Permeabilization times were optimized by low-depth sequencing of Array-seq libraries using MiSeq (Illumina). Human spleen and mouse MOB were permeabilized for 20 minutes, and all other tissues were permeabilized for 15 minutes. After permeabilization, sections were washed once with 0.1X saline-sodium citrate (SSC) buffer. After removing the wash buffer, reverse transcription mix consisting of 1X Maxima Reverse Transcriptase Buffer (ThermoFisher Scientific, EP0753), 0.2 mg/mL BSA (Sigma, B8667-1.25ML), 0.5 mM dNTPs (NEB, N0447L), 3 µM of template switching oligonucleotide (TSO) (5'-/5MeisodC// iisodG//iMe-isodC/CCCTACACGACGC TCTTCCrGrGrG-3'), 2 U/µL Ribolock, and 10 U/µL Maxima H Minus Reverse Transcriptase (Thermo Fisher Scientific, EP0753) was added to each well and incubated overnight at 42°C. The array was washed once with 0.1X SSC and incubated for 1 hour at 37°C using a tissue removal buffer containing Proteinase K (Qiagen, 19131) at 1:8 dilution in buffer PKD (Qiagen, 1034963). The array was washed once with 0.1X SSC and incubated for 1 hour at 37°C with an Exo1 mix containing 1X Exonuclease reaction buffer and 1 U/µL Exonuclease 1 (NEB, M0293L). The array was washed with 0.1X SSC followed by buffer EB, and full-

length cDNAs were eluted from the array by incubating for 10 minutes at room temperature in 0.1 M KOH (Sigma, P4494-50ML). Eluted cDNAs were transferred into a 1.5- or 15-mL tube (depending on size and number of tissues/chambers) and neutralized by adding 0.2X volume of 1M Tris-HCl (pH=7.4) (Bioworld, 21420063-1).

Array-seq library preparation and sequencing

We followed procedures described by others (Soumillon et al., 2014) with modifications as described below. cDNAs were purified using a DNA Clean & Concentrator-5 kit (Zymo Research, D4013) and amplified using single-primer PCR with the following primer: 5'-/5Biosg/CCCTACACGACGCTCTTCC-3' using the KAPA HiFi HotStart ReadyMix (Roche, KK2601) in a 50-µL reaction volume and with the following cycling conditions: 1 cycle at 95°C for 3 min; 8 cycles at 98°C for 20 sec, 60°C for 20 sec, 72°C for 3 min; and 1 cycle at 72°C for 5 min. Amplified cDNAs were cleaned up using 0.6X volume of magnetic SPRISelect beads (Beckman Coulter, A63880) and quantified using the Qubit dsDNA High Sensitivity Assay Kit (ThermoFisher Scientific, Q32851) and a TapeStation D5000 high sensitivity DNA Screentape kit (Agilent). 100 ng of amplified cDNA was tagmented using Tagment DNA TDE1 Enzyme and buffer (Illumina, 20034197) for 5 min at 55°C and amplified by PCR using the following forward primer: 5'- AATGATACGGCGACCACCGAGATCTA-CACTCTTTCC
CTACACGACGCTCTTCCG*A*T*C*T-3' and Illumina i7 reverse primers (Illumina, FC-121-1011) with the following cycling conditions: 1 cycle at 98°C for 30 sec; 8 cycles at 98°C for 10 sec, 63°C for 30 sec and 65°C for 30 sec; and 1 cycle at 65°C for 5 min. Libraries were cleaned up using 0.8X volume of magnetic SPRISelect beads followed by gel purification using 2% E-Gel EX Agarose Gels (Thermo Fisher Scientific G402002) and MinElute columns (Qiagen, 28604), and quantified with the Qubit dsDNA High Sensitivity Assay Kit (Thermo Fisher Scientific Q32851). Resulting libraries were sequenced on the NextSeq 550 or 2000

platforms (Illumina) with 38 bases for read 1, 8 bases for i7 barcodes, and 42 bases for read 2.

Visium spatial transcriptomics

Following sectioning, mouse kidney sections were mounted onto a Visium Spatial Gene Expression library preparation slide (10X Genomics) and samples were processed to generate spatial transcriptomics sequencing libraries according to the manufacturer's instructions. Resulting libraries were sequenced on the NextSeq 2000 platform (Illumina), with 28 bases for read 1, 10 bases for the sample index, and 50 for read 2.

Tissue harvest for bulk RNA-seq

Mouse tissues (liver, kidney, brain) were harvested, frozen and stored as previously described.37,38 Mice were anesthetized with 2,2,2-tribromoethanol (250- 500 mg/kg) and perfused transcardially with PBS containing 10 mM EDTA (to avoid signal contamination from blood in tissues). Immediately after perfusion, tissues were placed in RNA-preserving solution (5.3 M ammonium sulfate, 25 mM sodium citrate, 20 mM EDTA) and kept at 4°C overnight prior to transfer at -80°C for storage.

Whole-tissue RNA extraction

Whole-tissue RNA extraction was performed as described previously (Pandey et al., 2020; Kadoki et al., 2017). Briefly, tissues stored in RNA-preserving solution were thawed and transferred to 2 mL tubes containing 700-1500 µL (depending on tissue) of PureZOL (Bio-Rad, 7326890) or homemade Trizol-like solution (38% phenol, 0.8 M guanidine thiocyanate, 0.4 M ammonium thiocyanate, 0.1 M sodium acetate, 5% glycerol). Tissues were lysed by adding 2.8-mm ceramic beads (OMNI International, 19-646) and running 1-3 cycles of 5-45 s at 3500 rpm on the PowerLyzer 24 (Qiagen). For liver, brain, and small intestine

samples, tissues were lysed with 3-5 mL using M tubes (Miltenyi biotec, 130-096-335) and running 1-4 cycles of the RNA_02.01 program on the gentleMACS Octo Dissociator (Miltenyi biotec). Next, lysates were processed in deep 96-well plates (USA Scientific 1896-2000) by adding chloroform for phase separation by centrifugation, followed by precipitation of total RNA in the aqueous phase using magnetic beads coated with silane (Dynabeads MyOne Silane; TermoFisher Scientific 37002D), buffer RLT (Qiagen 79216), and ethanol. Genomic DNA contamination was removed by on-bead DNase I (ThermoFisher Scientific AM2239) treatment at 37 °C for 20 min. After washing steps with 80% ethanol, RNA was eluted from beads. This RNA extraction protocol was performed on the Bravo Automated Liquid Handling Platform (Agilent). Sample concentrations were measured using a Nanodrop One (Thermo Scientific). RNA quality was confirmed using a Tapestation 4200 (Agilent Technologies).

Whole-tissue RNA sequencing

For each tissue sample, full-length cDNA was synthesized in 20 µL final reaction volume containing the following: (1) 10 µL of 10 ng/µL RNA; (2) 1 µL containing 2 pmoles of a custom RT primer biotinylated in 5' and containing sequences from 5' to 3' for the Illumina Read 1 primer, a 6-bp sample barcode (up to 384), a 10-bp unique molecular identifier (UMI), and an anchored oligo(dT)30 for priming; and (3) 9 µL of RT mix containing 4 µL of 5X RT buffer, 1 µL of 10 mM dNTPs, 2 pmoles of template switching oligo (TSO), and 0.25 µL of Maxima H Minus Reverse Trascriptase (Thermo Scientific, EP0753). First, barcoded RT primers were added to RNA, which were then denatured at 72°C for 1 min and snap cooled on ice. Second, the RT mix was added, and plates were incubated at 42°C for 120 min. For each library, double stranded cDNA from up to 384 samples were pooled using DNA Clean & Concentrator-5 columns (Zymo Research, D4013), and residual RT primers were removed using exonuclease I (New England Biolabs, M0293). Full-length

cDNAs were amplified with 5 to 8 cycles of single-primer PCR using the Advantage 2 PCR Kit (clontech 639206) and cleaned up using SPRIselect magnetic beads (Beckman Coulter B23318). cDNA was quantified with a Qubit dsDNA High Sensitivity Assay Kit (ThermoFisher Scientific 32851) and 50 ng of cDNA per pool of samples was tagmented using the Tagment DNA Enzyme I (Illumina 20034197) and amplified using the NEBNext Ultra II Q5 Master Mix (NEB, M0544L). Libraries were gel purified using 2% E-Gel EX Agarose Gels (ThermoFisher Scientific G402002), quantified with a Qubit dsDNA High Sensitivity Assay Kit (ThermoFisher Scientific Q32851) and a Tapestation 4200 (Agilent Technologies), and sequenced on the NextSeq 550 platform (Illumina).

Sequence alignment and generation of spatial gene expression matrix

Fastq files from Array-seq and Visium sequencing experiments were generated using BaseSpace DRAGEN Analysis v1.3.0 (Illumina). For both platforms, the spatial barcodes and UMIs are contained in the Read 1 sequence (Array-seq spatial barcode: 1-12 bases, Array-seq UMI: 29-38 bases; Visium spatial barcode:1-16, Visium UMI: 17-28) while the Read 2 sequence contains cDNA information. To generate spatial count matrices, fastq files were processed using STARsolo from the STAR package version 2.7.10a (https://github.com/alexdobin/STAR/blob/master/docs/STARsolo.md). Reads were aligned to the mm10 mouse or CRCh38 human reference genome, spatial barcode demultiplexed against the whitelist of the reverse complement sequences of the 974,016 Array-seq spatial barcodes or 4,992 Visium barcodes (using the Exact option), and unique molecular identifiers (UMIs) were collapsed (using the 1MM_CR option for error correction).

Alignment of spatial data with H&E image

To filter the Array-seq data to only include spots under the tissue, we followed similar procedures described by others (Liu et al., 2020) with modifications as described below. In brief,

the STARsolo output count matrices were read into Python 3.8.5 (http://www.python.org) with Scanpy (Wolf et al., 2018) and stored in an AnnData object together with the spatial coordinates of each barcoded spot on the slide. The spot coordinates and UMI counts were used to generate a scalable vector graphic (svg) image composed of points matching the x, y positions of each barcoded spot which were colored based on UMI counts. The svg image was converted to a png format using the Wand package (https://github.com/emcconville/wand) and manually aligned with the H&E image of the same section using Illustrator (Adobe). The x and y positions, height, and width of the aligned images were recorded. Next, we detected tissue sections in H&E images using the scikit-image package (Van der Walt et al., 2014). The spatial transcriptomics data was imported, scaled to match the corresponding pixel coordinated of the H&E image, and filtered to remove spots not under the detected tissue. For H&E images containing multiple sections, each detected tissue sample was labeled. The annotation of organs and replicates were mapped to the object labels, the individual section H&E images were cropped, and the spot spatial data was rescaled. Lastly, to filter spots under tissue, we kept spots overlapping with pixels coordinates containing tissue objects. Visium datasets were filtered for spots under tissue and aligned to H&E images by joining the tissue positions list csv, generated by the Spaceranger v1.2.0 software (10X Genomics), to the AnnData object generated from the STARSolo count matrix.

Clustering and differential gene expression analysis

For spatial gene expression analysis using Scanpy, resulting count matrices were further filtered to keep (1) genes with at least 20 UMIs across all spots, and (2) spots with more than 120 UMIs in total. For clustering, data was normalized, log10 transformed, and clustered using principal component analysis (PCA), k-nearest neighbors (k-NN) identification, and the Leiden clustering algorithm (Traag et al., 2019). Our mouse MOB data was also clustered using the algorithms GraphST v1.0.020 and BayesSpace v1.5.121 in R-4.1.0 (http://www.R-

project.org). For differential expression analysis, we used the tl.rank_genes_groups() function in Scanpy. To map tissue subregions to spatial cluster obtained with the Leiden algorithm, we used the top 15 differentially expressed genes from each cluster for manual annotation. For plotting, spatial count or clustering data were overlaid on the greyscale H&E image using Seaborn (https://seaborn.pydata.org/). For plotting MOB marker spatial distribution along the x-axis, we used the scipy's gaussian_kde() function to compute the smoothed spatial distribution of each gene.

Spatial assignment of cell types

To deconvolute the cell types present at each spot, we used the following packages: CARD v1.0.0 (Conditional Auto Regressive-based Deconvolution), Spacexr/RCTD v2.2.1 (Cable et al., 2022), and cell2location v0.1.3 (Kleshchevnikov et al., 2022). As reference, we used publicly available single-cell RNA-seq data for the mouse MOB (Tepe et al., 2018) and kidney tissues (Kirita et al., 2020). For the MOB reference data, we excluded some clusters of granule cells, transition neurons, and olfactory nerve cells which led to confounding integration results across the three algorithms listed above. For kidney datasets, cell type proportions for each spot were calculated using the CARD deconvolution function with the ST (Array-seq or Visium) and single-cell RNA-seq count matrices as input, and results were plotted using the Seaborn package.

mRNA diffusion analysis

We quantified the numbers of UMIs detected under the tissue section versus those detected outside of the tissue section as described by others. We manually selected a field of view surrounding MOB Array-seq replicates and labeled spots as under or adjacent to the tissue section without filtering based on minimal reads per spot. To estimate diffusion in Visium, we performed a similar analysis using publicly available mouse MOB data

(https://www.10xgenomics.com/datasets/adult-mouse-olfactory-bulb-1-standard-1).

Benchmarking Array-seq and Visium sequencing statistics and analysis

For a direct comparison of Array-seq and Visium using 4 pairs of immediately adjacent kidney sections, we normalized sequencing depth so each tissue would have equivalent UMIs/mm^2 of tissue over the capture area. To this end, we manually outlined the tissue area for each Array-Seq and Visium section using QuPath v0.2.3. The reads for each of the fastq files were then scaled to have equivalent UMIs/mm^2, and sequencing metrics were measured using STARSolo. All clustering, cell type annotation, and differential gene expression was performed using the full sequencing data, without any prior downsampling.

Three-dimensional mouse kidney Array-seq data analysis

Each section was processed for image to ST data alignment as described above. H&E images from each section were cropped, and the spot spatial data was rescaled. To align H&E images, we used a computational approach involving detecting tissue, then identifying the optimal overlap of the tissue using the following calculation following a combination of rotations and vertical and horizontal translations. Following alignment of the first two sections, the transformation was applied to the second H&E image and ST data. The next tissue in the z-axis was then aligned to the previously transformed section. After alignment, all raw count matrices were merged, normalized, clustered, and analyzed for differential expression as described above.

Spatial gene ontology enrichment

Gene sets from the Gene Ontology Biological Process 2024 were read into python using GSEApy (Fang et al., 2023). Enrichment of each gene set was calculated using scanpy's tl.score_genes() function. Scores for each spot for gene sets with a minimum score of at least

1 were saved with the metadata. For manually selected genesets, the average enrichment score was calculated for each tissue subregion and average enrichment scores were normalized relative to the highest scoring subregion.

Chemokine ligand-receptor analysis

For visualizing spatial ligand-receptor (L-R) dynamics in the human spleen, we used the COMMOT package on a selected subset of the tissue (Cang et al., 2023). Selected chemokine L-R interactions were inferred using Commot's tl.spatial_communication() function using a distance threshold of 150. L-R pair communication directionality was calculated with the tl.communication_direction() function using k = 5. Vectors for interaction magnitude and directionality were plotted and overlayed onto the H&E image.

Spatial Transcriptomics Cost analysis

. Values for method cost were those stated in the articles of origin for each method. Array-seq costs were calculated based on the costs of individual reagents and supplied needed to implement our method (see full list of reagents and associated pricing in Table S1). Visium cost was based on the list price for a 4-capture area, single slide kit from a quote obtained on August 7, 2023 (Dual index and accessories not included). Curio Bioscience (Seeker) cost was based on a cost estimate provided by a sales representative on Feb. 28, 2024. STOmics cost (2x3 cm format) cost was based on a cost table provided by a sales representative on Mar. 27, 2024.

Sensitivity analysis across existing ST methods

Array-seq MOB sequencing data sensitivity was benchmarked against publicly available spatial transcriptomics data from MOB tissue sections, or other tissues when MOB was not found (Table S2). To normalize the mean UMI counts per unit area, we divided the mean

counts in the dataset by the number of spots per μm^2 (based on the stated values of total spots and capture area size in the articles) or by the number of μm^2 in the data bin size (Seq-Scope).

Whole-tissue RNA-seq data analysis

Sequencing read files were processed to generate UMI (unique molecular identifier) count matrices using the python toolkit from the bcbio-nextgen project version 1.1.5 (https://bcbio-nextgen.readthedocs.io/en/latest/). In brief, reads were aligned to the mouse mm10 transcriptome with RapMap (https://github.com/COMBINE-lab/RapMap). Quality control metrics were compiled with a combination of FastQC (http:bioinformatics.babraham.ac.uk/projects/fastqc/), Qualimap, MultiQC (https://github.com/ewels/MultiQC). Samples were demultiplexed using barcodes stored in Read 1 (first 6 bases) and raw UMI count matrices were computed using UMIs stored in Read 1 (bases 7 to 16) (https://github.com/vals/umis). Differential expression (DE) analysis was done using custom scripts in R (http://www.R-project.org). Raw count matrices were filtered to keep genes with at least 20 counts per million (cpm) or 5 UMIs in 2 samples and normalized across

2.4 Results

2.4.1 On-slide assembly of spatially barcoded, mRNA capture probes on custom microarrays

We designed custom oligonucleotide microarrays with spatially barcoded sequences flanked by common sequences that enable the on-slide assembly of mRNA capture probes necessary for ST profiling (Fig 2.1a and Methods). Custom microarrays were synthesized with 3'-anchored oligonucleotides (52- or 58-mer in total length) carrying Spatial Barcodes (12- or 18-mer) unique to each spot and flanked by two sequences, Anchors 1 (24-mer) and 2

(16-mer), which were common across all spots on the array (Fig 2.1b, left panel, and Fig 2.2a). We initially used 58-mer oligos to facilitate the identification of the various oligonucleotide species generated during the optimization of our method for on-slide probe assembly. Subsequently, arrays carrying 52-mer oligos with 12-mer Spatial Barcodes were used for all spatial transcriptomics profiling experiments to decrease next-generation sequencing cycle requirements (88 cycles in total). The Anchor 1 sequence, tethered to the glass slide by its 3' end, matches the first 24 bases of the Illumina Read 1 sequencing primer, and serves as a primer for both cDNA amplification and Illumina sequencing (Fig 2.2a). The 16-mer Anchor 2 sequence matched the commonly used M13 forward (M13F) primer, chosen because (1) it is short which limited the number of repetitive bases that are sequenced between the spatial barcode and UMI (unique molecular identifier) sequences, and (2) its melting temperature) was compatible with downstream cleanup steps to remove incorrectly assembled spatial probes (Fig 2.2a). For spatial barcodes, we designed 974,016 unique 12-mer sequences (hamming distance ≥ 2) while minimizing self-dimerization and interactions with the two Anchor sequences (Methods).

Next, to assemble ST probes on the microarray, we first hybridized arrays with two oligonucleotides: (a) a partial Illumina Read 1 sequence (Anchor 1), and (b) a probe for mRNA capture containing the reverse complement of Anchor 2, UMIs, and an oligo(dT) (Fig 2.1b and S1a). Second, we performed an on-slide, extension-ligation reaction (or "gap-fill") using a DNA polymerase to synthesize the reverse complement of the spatial barcode at the 3' end of the hybridized Anchor 1, and a DNA ligase to attach the newly synthesized barcode to the phosphorylated, 5' end of Anchor 2 (Fig 2.1b and S1a). The conditions for the gap-fill reaction were optimized using a DNA polymerase, Phusion, shown to have minimal strand displacement activity (Chen et al., 2018), which would lead to the unwanted stripping of annealed Anchor 2 before ligation (Fig 2.1c). Moreover, we maximized ligation efficiency while minimizing ligation biases towards specific sequences (Fig 2.2b-c). Third, after gap-

filling, we sought to remove unligated Anchor 2-UMI-dT oligonucleotides from the array to avoid a sink effect for tissue mRNAs which would decrease sensitivity. Unligated Anchor 2-UMI-dT oligonucleotides are hybridized on array probes by the M13F sequence only (16-mer with Tm = 50.7°C), whereas correctly ligated spatial probes (Anchor 1-Spatial barcode-Anchor 2-UMI-oligo(dT30)VN) are hybridized to the full length of each probe sequence (58-mer with mean Tm = 71.3 °C and SD= 0.5°C). We thus washed off unligated Anchor 2-UMI-dT oligonucleotides using a temperature, 58°C, between these two melting points, yielding fully assembled mRNA capture probes at >75% purity (Fig 2.1c).

After on-slide assembly, each capture probe on the array included a spatial barcode for localization, UMIs for quantification, and an oligo(dT) for capturing poly-adenylated transcripts (Fig 2.1b). Resulting ST-compatible arrays carried 974,016 spots of 30 µm in diameter (36.65 µm center-to-center distance) arranged in 1,068 rows and 912 columns across 11.31 cm^2 in total surface area usable for ST profiling. Each spot on the array carried a unique spatial barcode sequence at known x and y coordinates. Thus, our custom sequence design followed by on-slide probe assembly yielded Array-seq slides compatible with downstream in situ reverse transcription to perform spatial transcriptomics profiling (Fig 2.2a). To estimate how many cells were captured per spot on an Array-seq slide, we counted the number of nuclei in tissue sections that overlap with each spot across 10 mouse organ types (Fig 2.1d-e). Array-seq spots overlapped with median numbers of nuclei ranging from 2 and 3 for muscle and brain and 15 and 19 for bone marrow and spleen (Fig 2.1e). All other tissue types tested displayed median numbers of nuclei per spot ranging from 5 (brown fat, liver, heart, lung) to 7 (colon) and 8 (kidney) (Fig 2.1e). One Array-seq slide can therefore capture up to ~2 to 20 million cells depending on the tissue type and the number and size of the tissue sections to analyze.

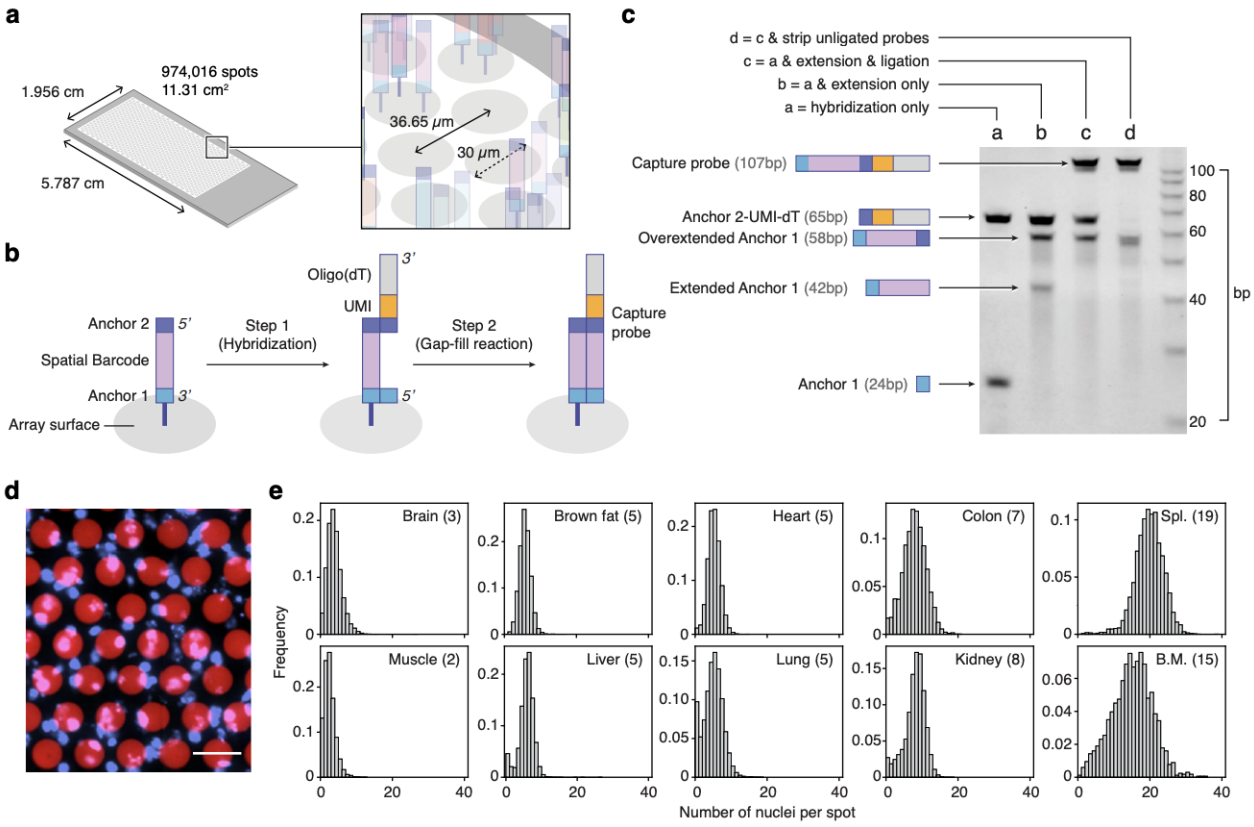


Figure 2.1: On-slide assembly of spatially barcoded mRNA capture probes using microarrays. **a,** Schematic diagram of a custom sequence, large-format microarray comprising 974,016 spots of 30 µm in diameter that are arranged in 1,068 rows and 912 columns across 11.31 cm^2 in surface area. Each spot on the array carries a unique spatial barcode sequence. **b,** Overview of the on-slide assembly of mRNA capture probes by hybridization of indicated oligos (Step 1) followed by an extension-ligation or "gap-fill" reaction (Step 2). **c,** Polyacrylamide gel electrophoresis (PAGE) analysis of the oligonucleotide products obtained after the indicated on-slide assembly procedures in lanes a through d. **d,** Representative fluorescence image of an area from a mouse brain section placed on an Array-seq slide hybridized with constant Cy3-labeled probes. Blue indicates the DAPI nuclear stain of the brain section. Scale bar, 50 µm. **e,** Histograms of the numbers of DAPI-positive nuclei per spot for indicated mouse organs.

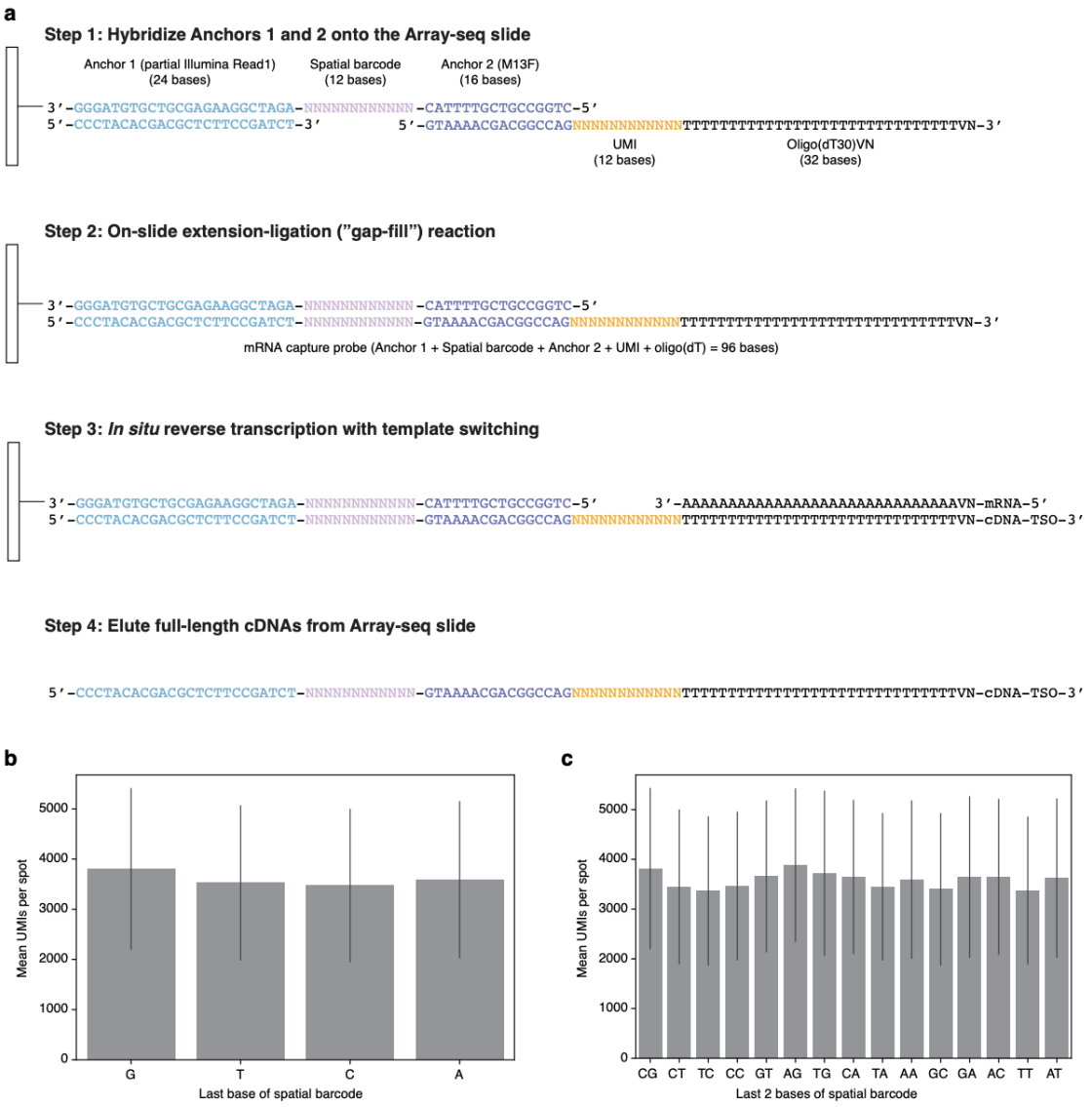


Figure 2.2: Sequence level overview of the on-slide assembly procedure yielding mRNA capture probes. a, Custom sequence oligonucleotide microarrays containing two common sequences (Anchors 1 and 2) and a spatial barcode sequence unique to each spot on the array are hybridized with indicated oligonucleotides (Step 1). On-slide extension-ligation using a DNA polymerase and a DNA ligase yields a fully assembled mRNA capture probe containing a sequencing adaptor, a spatial barcode, UMIs, and an oligo(dT) sequence (Step 2). In situ reverse transcription in tissue sections placed on an Array-seq slide generates full-length cDNAs with a template switching oligo (TSO) sequence in 3’ (Step 3). Full length cDNAs are eluted from the slides and processed for RNA sequencing library construction (Step 4). **b-c,** Ligation bias analysis after extension-ligation of mRNA capture probes. Bar plots showing the number of UMIs captured by spot across an Array-seq slide after grouping and normalizing by the last single **(b)** or two **(c)** bases of the spatial barcode sequence. Error bars, SD (n = 2767 to 3771 spots in **b**, and n = 647 to 1144 spots in **c**).

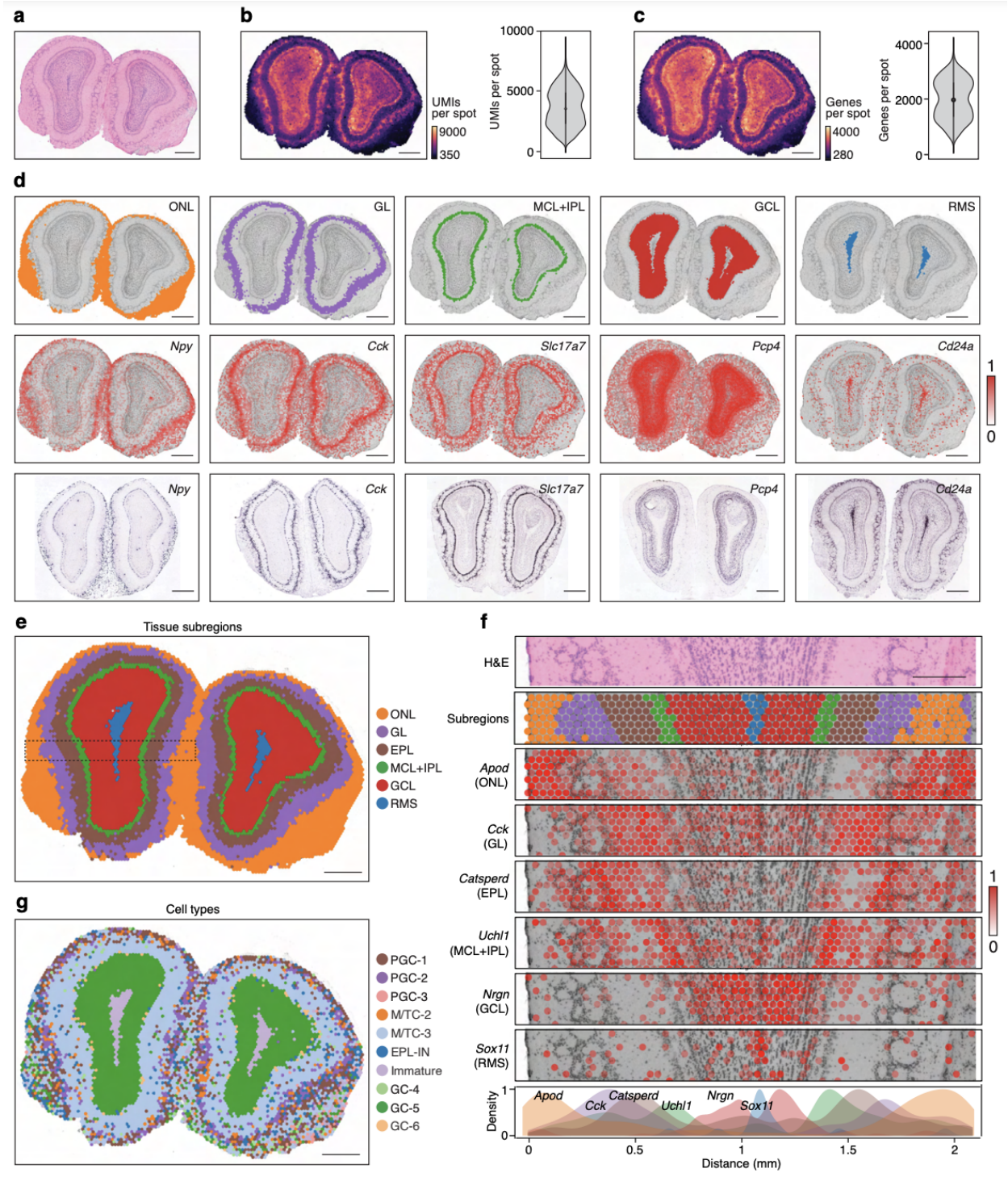


Figure 2.3: Array-seq accurately captures region-specific expression patterns in tissues. a, H&E image of a section (10 µm) from the main olfactory bulb (MOB) system of the mouse brain profiled by Array-seq.

Figure 2.3: **b-c,** Numbers of genes **(b)** and UMIs **(c)** detected per spot across the tissue section visualized as spatial plots (left panels) and violin plots (right panels). **d-e,** Unsupervised clustering highlights the histological layers of the MOB tissue (**d**, top, and **e**), as confirmed by the spatial expression (**d**, middle) and in situ hybridization (**d**, bottom; images from the Allen Brain Atlas database) of indicated gene markers. ONL, Olfactory Nerve Layer; GL, Glomerular Layer; EPL, External Plexiform Layer; MCL, Mitral Cell Layer; IPL, Internal Plexiform Layer; GCL, Granule Cell Layer; RMS, Rostral Migratory Stream. **f,** Magnified image of the MOB inset shown in **e** (dashed line). From top to bottom: H&E; subregion annotations; scaled expression of indicated gene markers overlaid on a grayscale H&E image; and line plots showing gene expression smoothed using kernel density estimation (y axis) of indicated genes across the selected tissue area (x axis). **g,** Cell type assignments across spots on the Array-seq slide for the indicated MOB cell types. Cell types with the highest percentage in inferred proportion per spot were assigned to each spot. PGC, periglomerular cell; M/TC, mitral and tufted cell; EPL-IN, external plexiform layer interneuron; GC, granule cell. Scale bars: **a-e** and **g**, 500 µm; **f**, 200 µm.

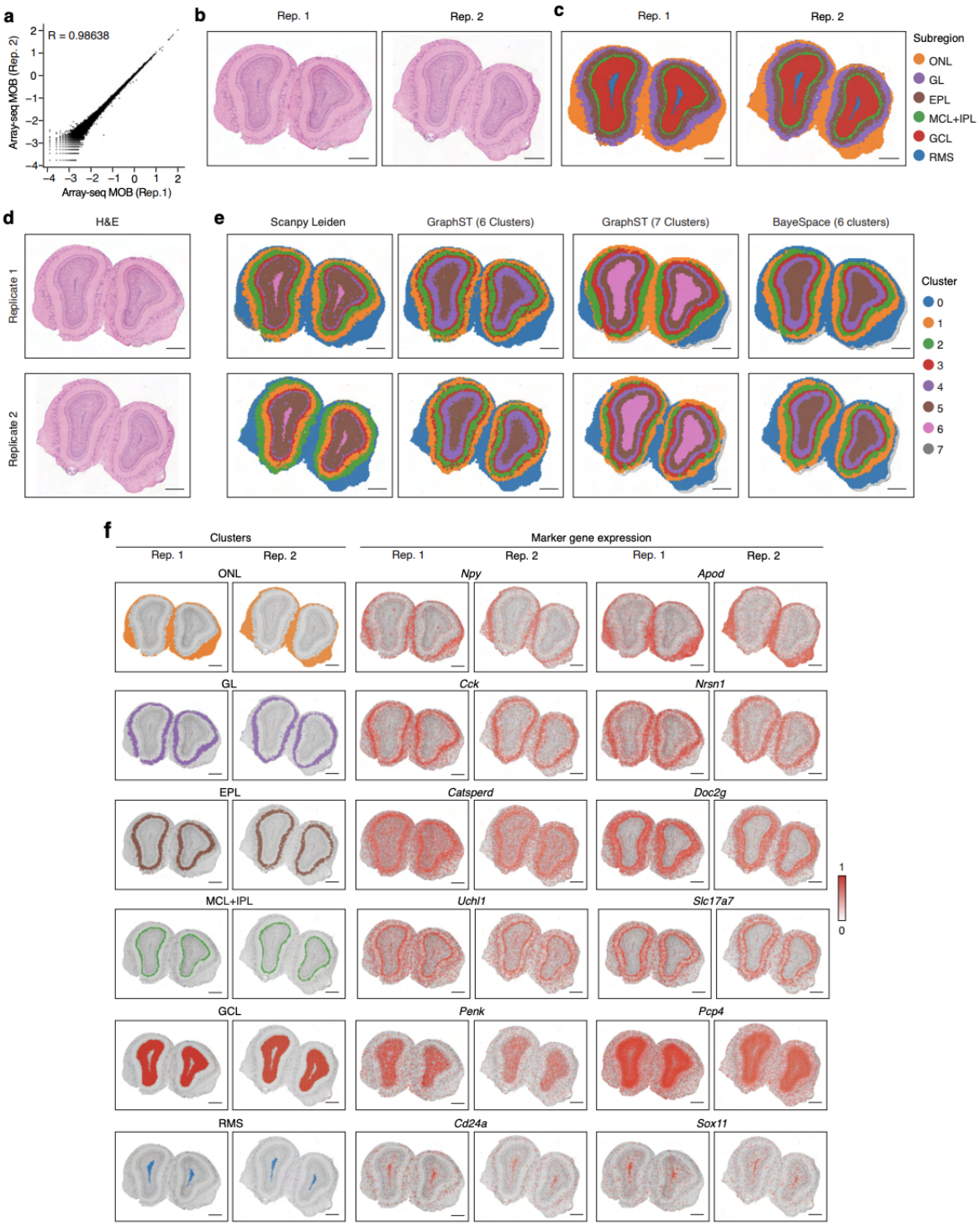


Figure 2.4: Reproducibility of Array-seq data from mouse main olfactory bulb sections. a, Correlation (Pearson's coefficient) between Array-seq replicates 1 and 2 from two sections obtained from two independent mouse main olfactory bulb (MOB) tissues. Shown are the normalized log10 UMI counts which were averaged across all spots for each gene across both replicates.

Figure 2.4: **b** and **d,** H&E images of independent MOB tissue sections which were placed onto separate gasket chambers of the same Array-seq slide. **c** and **e,** Unsupervised clustering highlights the histological layers of the MOB tissue using the Leiden algorithm (**c**, showing clusters annotated by tissue subregions) or indicated algorithms for comparative analyses (**e**, showing raw clustering results across methods). ONL, Olfactory Nerve Layer; GL, Glomerular Layer; EPL, External Plexiform Layer; MCL, Mitral Cell Layer; IPL, Internal Plexiform Layer; GCL, Granule Cell Layer; RMS, Rostral Migratory Stream. **f**, Spatial plots of indicated MOB tissue subregions (left panels) and scaled expression of subregion-specific marker genes (right panels) overlaid on grayscale H&E images. Scale bars, 500 µm.

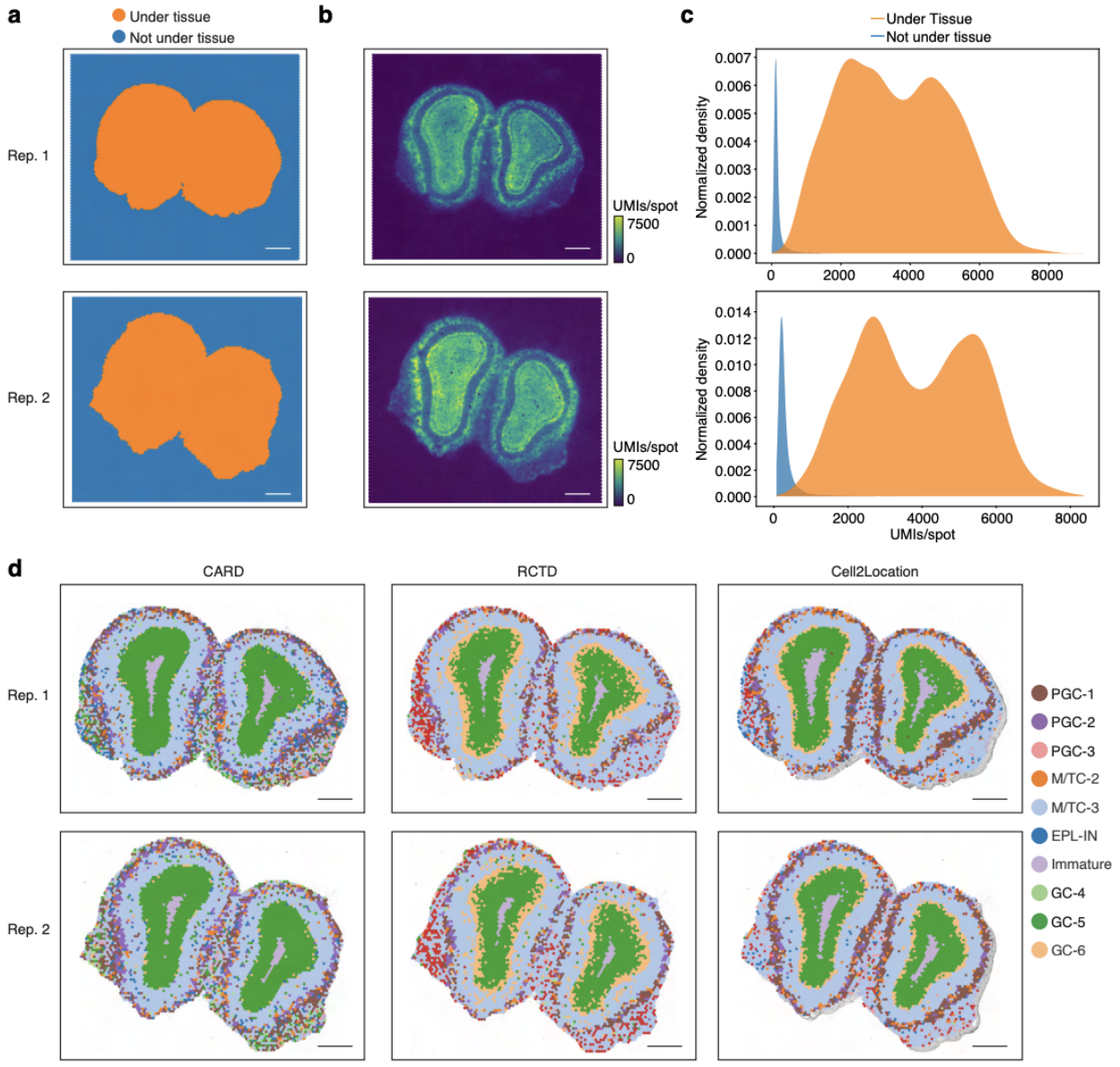


Figure 2.5: mRNA diffusion and spatial cell type assignment analyses. a, Images highlighting the spots of the Array-seq slide that were under (orange) or outside (blue) of the two main olfactory bulb (MOB) sections which were profiled. **b,** Spatial plots of total unique molecular identifiers (UMIs) detected per spot across both MOB Array-seq data sets. **c,** Density plots (smoothed by kernel density estimation) of the distributions of UMIs per spot detected under (orange) and outside (blue) of the tissue sections. **d,** Cell type assignments across spots on the Array-seq slide for the indicated MOB cell types using indicated (top labels) algorithms. Cell types with the highest percentage in inferred proportion per spot were assigned to each spot. EPL-IN, external plexiform layer interneuron; GC, granule cell; M/TC, mitral and tufted cell; PGC, periglomerular cell. Scale bars, 500 µm.

2.4.2 Array-seq yields high quality spatial transcriptomics data

To test Array-seq, we first profiled the main olfactory bulb (MOB) system of the mouse brain, a tissue of choice for the benchmarking of ST methods due to its small size and well-defined morphological layering (Ståhl et al., 2016; Stickels et al., 2021; Vickovic et al., 2019; Chen et al., 2022). Since Array-seq slides are generated from a standard microscopy slide substrate, tissue sectioning, fixation, and staining can be done with standard reagents and slide scanners. Following tissue permeabilization, library preparation, and sequencing of MOB, we detected 3582.2 UMIs ± 1553.8 SD and 1971.5 genes ± 709.4 SD per spot on the array, whose patterns of intensity reflected the histological feature of the tissue section as observed by H&E imaging (Fig 2.3a-c). We observed similar numbers in an independent MOB section with 3492.1 UMIs ± 1437.9 SD and 1968.9 genes ± 682.7 SD per spot and a high degree of correlation between our two MOB datasets (Pearson's correlation coefficient 0.986) (Fig 2.4a). Next, we applied unsupervised clustering to the MOB data using the Leiden algorithm (Traag et al., 2019), which identified clusters corresponding to all known layers of the MOB tissue (Fig 2.3d-e and Fig 2.4b-c). Using different clustering algorithms led to similar results recapitulating all the layers of the MOB from the olfactory nerve layer (ONL) to the granule cell layer (GCL), although only the Leiden algorithm correctly identified the inner-most, rostral migratory system (RMS) layer (Fig 2.4d-e) (Long et al., 2023; Zhao et al., 2021). Moreover, the spatial distribution of marker genes for MOB tissue layers agreed with in situ hybridization data published by others (Fig 2.3d, bottom) (Lein et al., 2007), and with histological regions defined by our H&E imaging data (Fig 2.3f and Fig 2.4f).

Next, we examined the potential diffusion of mRNA molecules outside of their physical location of origin by computing the percentage of UMIs captured under the tissue section versus outside of it. We found that an average of 3581.7 UMIs per spot were detectable under the tissue compared to 168.76 outside of that area across both MOB datasets combined, suggesting that on average 4.5% of the total UMIs detected were not under the tissue and

likely resulting from diffusion (Fig 2.5a-c). For comparison, a MOB dataset generated on the Visium platform showed 5.4% of UMIs being detected by mRNA capture probes localized outside of the tissue section, suggesting similar diffusion rates across Array-seq and Visium platforms (Methods). Furthermore, the spatial containment of marker genes for each histological layer of the MOB was well preserved and closely followed the anatomical regions defined by H&E and unsupervised clustering (Fig 2.3f).

Lastly, we sought to test the spatial assignment of cell types across the histological layers of the MOB tissue. We used conditional autoregressive-based deconvolution (CARD) to infer the cell type composition for each Array-seq spot under the two MOB sections (Ma and Zhou, 2022). We used publicly available single-cell RNA-seq data from the MOB tissue as reference for spatial cell type assignments (Tepe et al., 2018). We found that the cell types annotated across spots were correctly assigned to specific MOB layers (Fig 2.3g). For example, immature migrating adult-born neurons localized specifically to the RMS layer and a subset of granule cells (GC-5) in the GCL region (Fig 2.3g). We also found that the results obtained for cell type calling across each Array-seq spot were comparable across various algorithms, including CARD, Robust Cell Type Decomposition (RCTD), and Cell2Location (Fig 2.5d) (Ma and Zhou, 2022; Cable et al., 2022; Kleshchevnikov et al., 2022). Taken together, Array-seq generates spatiotranscriptomic profiles that detect genes, cell types, and histological regions at high resolution.

2.4.3 Benchmarking Array-seq against the widespread commercial platform Visium

We benchmarked Array-seq against the well-established, commercial platform Visium (10X Genomics). We reasoned that Visium is the most appropriate platform for a side-by-side performance comparison with Array-seq because out of all existing ST methods, Visium and Array-seq are the only ones which are easy to access and implement without the need

for special instrumentation, slides, or expertise, and both are compatible with H&E on the same section. Array-seq slides provided an 8.1-fold increase in spot density (861.2 vs 106.2 spots/mm^2) (Fig 2.7a-b), a 216.8-fold increase in total number of spots on the slide (974,016 vs 4,992 spots) (Fig 2.7c), and a 26.7-fold increase in total active surface area (11.31 cm^2 vs 0.42 cm^2). We profiled four sets of two immediately adjacent mouse kidney sections by dividing each pair of sections between Array-seq and Visium slides and using comparable sequencing depth across samples and platforms. On average, we obtained a total of 193,357,436 mapped reads ± 29,929,596 SD (n = 4) for Array-seq and 230,739,959 ± 107,06,663 SD (n = 4) for Visium, leading to 5.39 mapped reads/μm^2 spots in Array-seq and 7.64 mapped reads/μm^2 spots in Visium. Moreover, a downsampling analysis revealed similar degrees of sequencing saturation and gene detection across both platforms at the sequencing depth used in our experiments (Fig 2.7d). We obtained spatial transcriptomics data from an average of 30,579 spots ± 3,740 SD (n = 4) for Array-seq and 3,447 spots ± 430 SD (n = 4) for Visium using the four pairs of adjacent kidney sections (Fig 2.7e). While Visium captured more UMIs (25,820.6 ± 1,322.6 SD) and genes (4,918.8 ± 93.4 SD) per spot than Array-seq (2,563.5 UMIs ± 390.7 SD and 1,292.1 genes ± 119.7 SD) due to the larger size spot diameter (55 µm in Visium vs 30 µm in Array-seq), normalizing those numbers per square micron revealed a similar detection sensitivity between the two methods with 3.10 UMIs/μm^2 ± 0. 06 SD and 0.55 genes/μm^2 ± 0.01 SD for Visium and 2.28 UMIs/μm^2 ± 0.28 SD and 1.09 genes/μm^2 ± 0.08 SD for Array-seq (Fig 2.7f-h).

Next, we performed unsupervised clustering of the eight kidney tissue sections that were profiled in total across both platforms.

Clustering identified spatial areas matching known histological regions of the kidney for both methods, albeit at a higher resolution in Array-seq due to the higher density and smaller diameter of spots on our spatial slides (Fig 2.6a-b and Fig 2.7i-j). For example, finer tissue structures such as the renal urothelium or the renal cortex, enriched in the

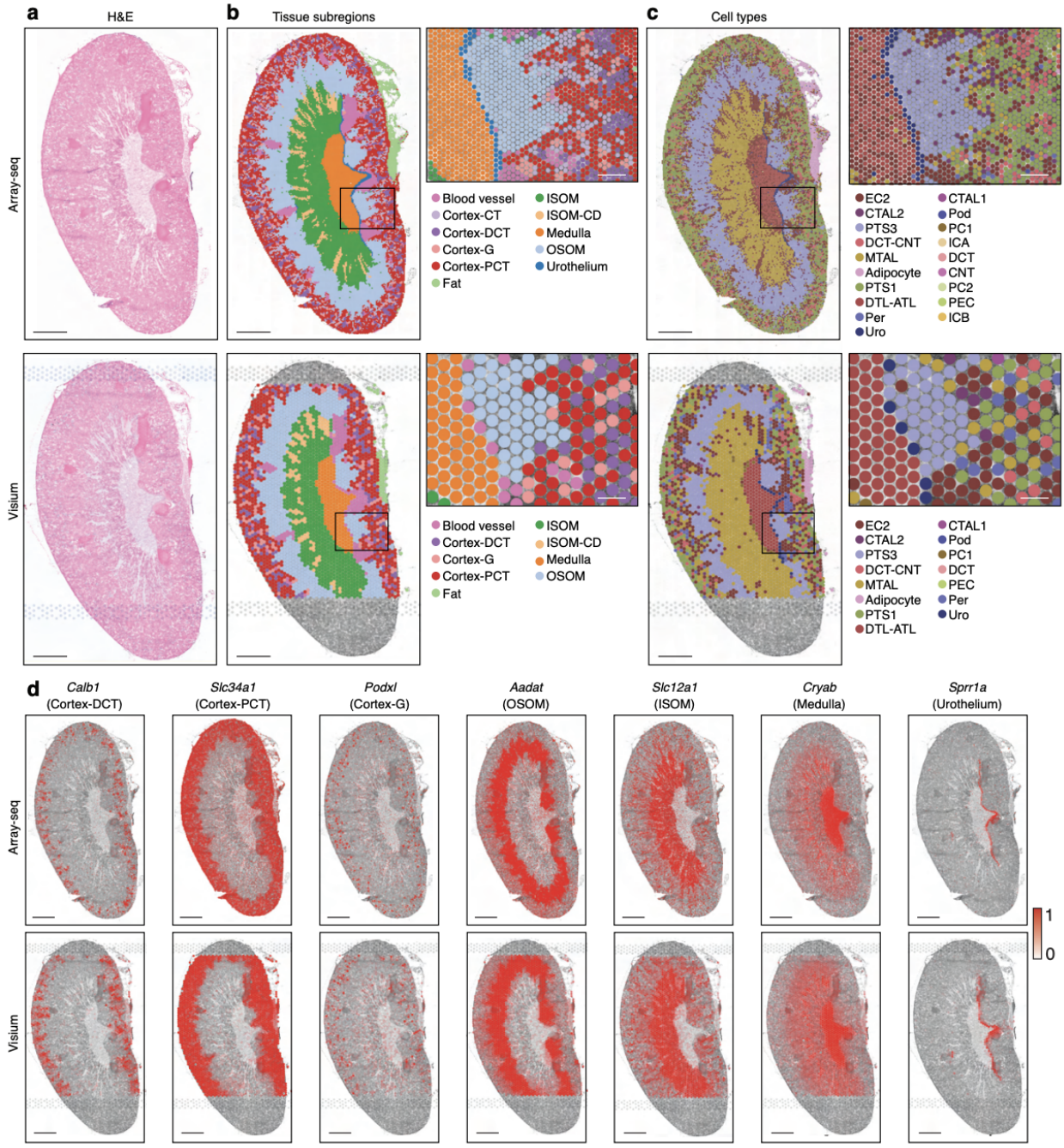


Figure 2.6: Side-by-side comparison of Array-seq and Visium data using adjacent mouse kidney sections. **a,** H&E image of immediately adjacent section from a mouse kidney placed onto Array-seq (top) and Visium (bottom) slides. **b-c,** Annotation of kidney tissue subregions (**b**) and cell types (**c**) for Array-seq (top) and Visium (bottom) datasets (left).

Figure 2.6: Cell types with the highest percentage in inferred proportion per spot were assigned to each spot. Insets (dashed lines) indicate the localization of the magnified images shown in b and c. Subregions: CT, Connecting tubule; DCT, Distal Convoluted Tubule; G, Glomerulus; PCT, Proximal Convoluted Tubule; ISOM, Inner Stripe of Outer Medulla; CD, Collecting Duct; OSOM, Outer Stripe of Outer Medulla. Cell types: ATL, thin ascending limb of loop of Henle; CNT, connecting tubule; CTAL, thick ascending limb of loop of Henle in cortex; DCT, distal convoluted tubule; DTL, descending limb of loop of Henle; EC, endothelial cells; ICA, type A intercalated cells of collecting duct; ICB, type B intercalated cells of collecting duct; MTAL, thick ascending limb of loop of Henle in medulla; PC1 and 2; principle cells; PEC, parietal epithelial cells; Per, pericytes; Pod, podocytes; PTS1 and 3, S1 and S3 segments of proximal tubule; Uro, urothelium. **d,** Scaled expression of differentially expressed marker genes for indicated subregion (columns) in Array-Seq (top) and Visium (bottom) data. Scale bars: **a-d**, 1 mm; insets shown in **b-c**, 200 µm.

glomerular segment of the nephron, were more consistently detectable and well defined in Array-seq than in Visium (Fig 2.6a-b and Fig 2.7i-j). To further our analysis, we tested the spatial assignment of the cell type composition for each spot using the CARD algorithm with publicly available single cell RNA-seq data from mouse kidneys (Kirita et al., 2020). In agreement with the clustering analysis, we found that Array-seq outperformed Visium in its ability to find and correctly assign cell types at high resolution, including for cell types which were inferred to be present in small number of spots, such as podocytes (0.025% of total spots), connecting tubule cells (0.02%), or distal convoluted tubule cells (0.03%) (Fig 2.6c and Fig 2.7i and S4k).

We then performed gene expression analyses to identify subregion-specific gene markers and to compare the spatial distribution of those marker genes across both platforms. The spatial distribution of differentially expressed marker genes for kidney tissue regions matched the zoning expected based on the H&E analysis for both methods although with higher resolution, as expected, for Array-seq (Fig 2.6d and Fig 2.8a). The top differentially expressed marker genes between kidney tissue regions agreed across both methods (Fig 2.8b). Moreover, our results suggested that the spatial distributions of genes, including highly expressed genes such as *Cryab* (renal medulla) or *Aadat* (OSOM), showed a high degree of specificity for their expected histological regions, suggesting that spatial patterns of gene expression showed little to no alteration due to mRNA diffusion prior to capture on the slide (Fig 2.6d and Fig 2.8a). Lastly, we confirmed that the mRNA expression profiles obtained with both methods correlated significantly with whole-kidney RNA-seq data (Fig 2.8c). Taken together, Array-seq outperforms the gold-standard platform for ST profiling, Visium, in metrics such as spot density and diameter and total surface area, while maintaining similar levels of sensitivity (e.g., genes detected per surface area) and specificity (e.g., expected spatial localization of marker genes).

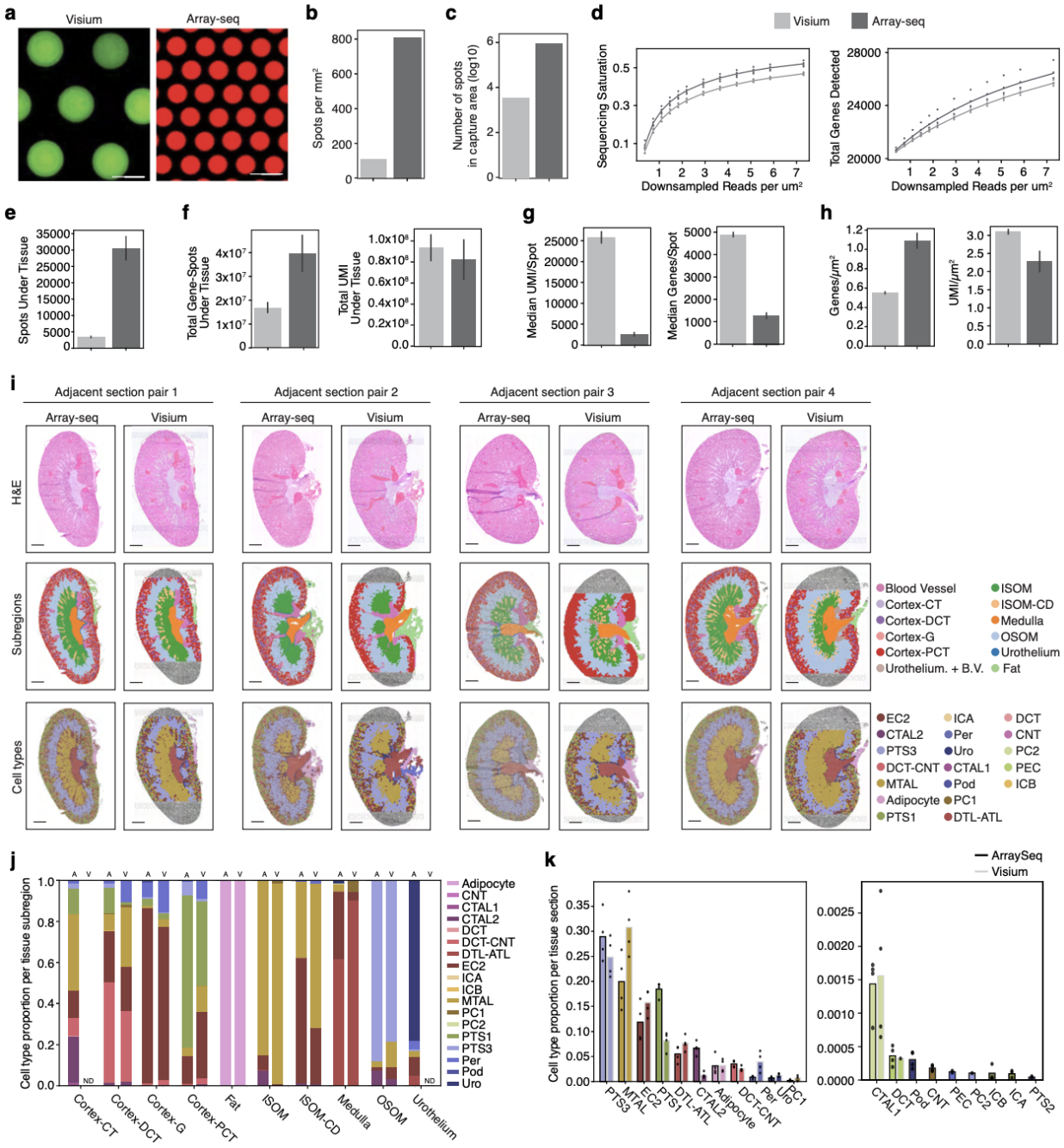


Figure 2.7: Extended comparison of Array-seq and Visium mouse kidney spatial transcriptomics data. a, Spot coverage (18.8% for Visium vs 60.1% for Array-seq). Scale bars, 50 μm. **b-c,** Bar plots of the number of spots per mm^2 (**b**) and total active area (**c**) on indicated platforms.

Figure 2.7: **d**, Downsampling analysis showing changes in sequencing saturation (left) and total genes detected across the entire section (right) using kidney section data from Array-seq (dark gray) and Visium (light gray) platforms. **e-h,** Bar plots of the numbers of spots under kidney tissue sections (**e**), total genes and UMIs detected (**f**), median genes and UMIs detected per spot (**g**), and genes and UMIs detected per μm^2 of tissue on top of the capture area (**h**). Numbers were calculated using data that were downsampled to similar levels of sequencing depth. Error bars, SD (n = 4 per platform). **i,** H&E images (top) overlaid with annotations of tissue subregions (middle) and cell type assignments to spots (bottom) across replicates and platforms (columns). Subregions: CT, Connecting tubule; DCT, Distal Convoluted Tubule; G, Glomerulus; PCT, Proximal Convoluted Tubule; ISOM, Inner Stripe of Outer Medulla; CD, Collecting Duct; OSOM, Outer Stripe of Outer Medulla. Cell types: ATL, thin ascending limb of loop of Henle; CNT, connecting tubule; CTAL, thick ascending limb of loop of Henle in cortex; DCT, distal convoluted tubule; DTL, descending limb of loop of Henle; EC, endothelial cells; ICA, type A intercalated cells of collecting duct; ICB, type B intercalated cells of collecting duct; MTAL, thick ascending limb of loop of Henle in medulla; PC1 and 2; principle cells; PEC, parietal epithelial cells; Per, pericytes; Pod, podocytes; PTS1 and 3, S1 and S3 segments of proximal tubule; Uro, urothelium. Scale bars, 1 mm. **j-k,** Bar plots of the proportions of cell types assigned to tissue subregions (**j**, section pair 1 only) and total spots (**k**, section pairs 1-4) under tissue sections for both platforms (A or black line, Array-seq; or gray line, Visium). Dots (**k**) indicate individual replicate kidney sections.

2.4.4 Array-seq enables high-throughput spatial transcriptomics in two and three dimensions

We tested the performance of Array-seq for the three-dimensional (3D) profiling of spatial transcriptomes using the mouse kidney as a test system (Fig 2.9a). The surface area of an Array-seq slide (11.31 cm^2) allows for the analysis of serial mouse kidney sections in parallel on the same slide. To test this, we generated eight, 10-µm thick sections by performing serial sectioning of a mouse kidney and analyzing one section every ~80-120 µm across a total of ~800 µm of tissue depth, thereby covering ~10% of the total kidney volume (Fig 2.9b-c). We selected an area of the kidney tissue that captured the major histological regions of the organ across all sections collected as shown by H&E imaging analysis (Fig 2.9b-c). The histological features of the 3D kidney volume observed by H&E were correctly recapitulated by unsupervised clustering analysis of the Array-seq data on the same tissue sections (Fig

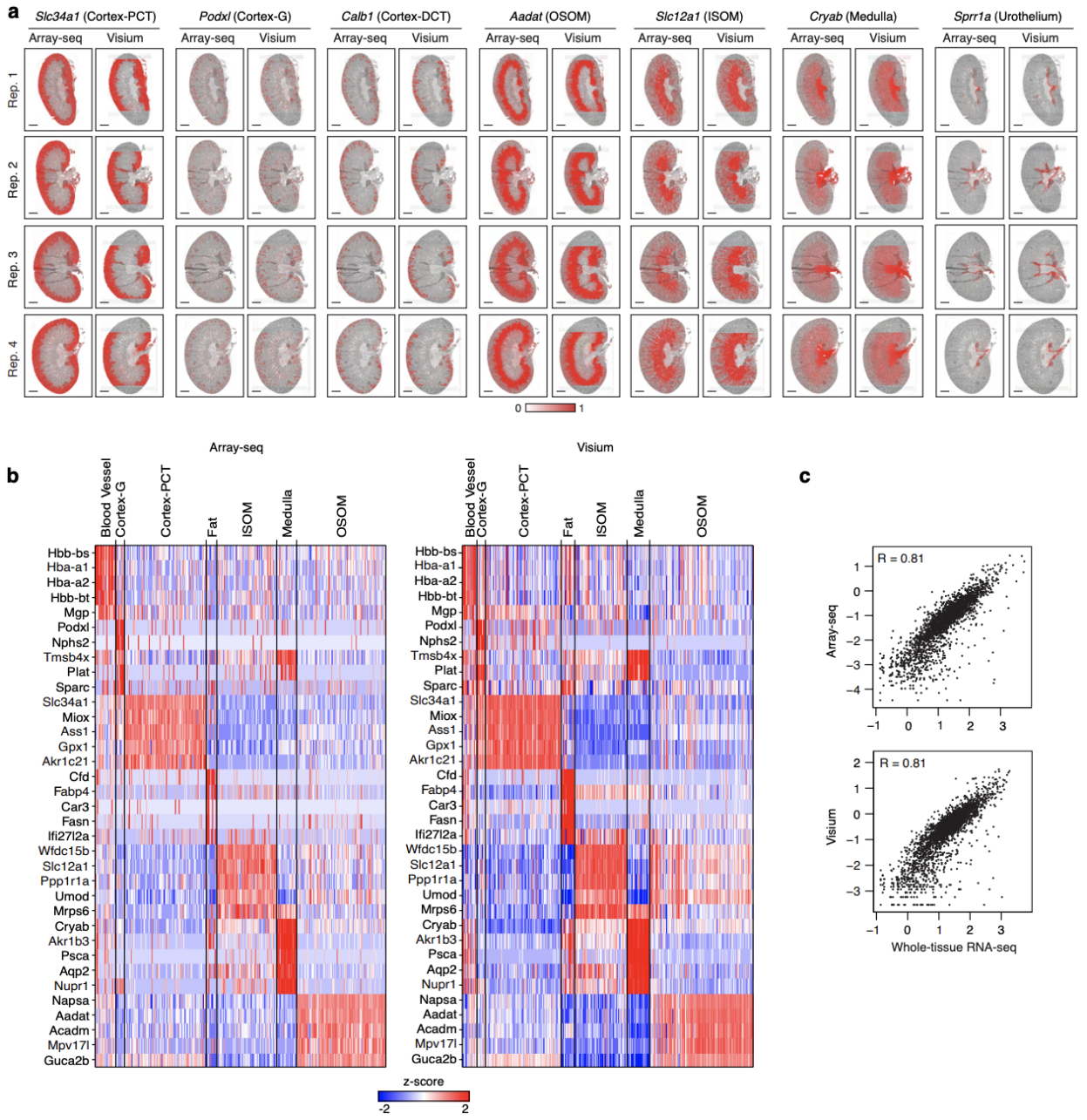


Figure 2.8: Spatial marker gene expression analyses in mouse kidney sections. a, Scaled expression of indicated marker genes overlaid on grayscale H&E images of matching kidney sections for indicated tissue subregions and platforms (columns). PCT, Proximal Convoluted Tubule; G, Glomerulus; DCT, Distal Convoluted Tubule; ISOM, Inner Stripe of Outer Medulla; ISOM, Inner Stripe of Outer Medulla. Scale bars: 1 mm. **b,** Heatmaps of differentially expressed (DE) genes (rows) for spots (columns) corresponding to indicated kidney tissue subregions (top). Shown are the top five DE genes obtained with Array-seq data and plotted for both Array-seq (left) and Visium (right) datasets. Values are z-scores of log10 normalized unique molecular identifier (UMI) counts.

Figure 2.8: c, Correlation (Pearson's coefficient) between Array-seq and Visium kidney gene expression and whole-kidney, bulk RNA-seq data. Shown are the normalized log10 unique molecular identifier (UMI) counts which were averaged across all spots and replicates (n = 4) for indicated spatial platform (Y axis) or across independent replicates (n = 4) for bulk, whole-tissue RNA-seq (X axis).

2.9d-e and Fig 2.10a-d). The surface area covered by each tissue subregion varied according to the depth of a given section within the kidney. For example, we observed an increase in proximal convoluted tubule-enriched regions of the renal cortex (Cortex-PCT) and a decrease in the outer stripe of the outer medulla (OSOM) subregions as quantified by the proportion of spot matching to these histological regions across the z stack (Fig 2.9d and Fig 2.10e). Furthermore, the spatial distribution of marker genes for each of the tissue subregions identified by unsupervised clustering and confirmed by histology closely aligned with their expected regional expression (Fig 2.9f-g and Fig 2.10f).

Next, we sought to assess the performance of our method for measurements of multi-tissue spatial transcriptomes (Fig 2.11a). To do so, we profiled 8 mouse tissue sections on a single Array-seq slide, including brain (n = 2), liver (n = 3), and kidney (n = 3) tissues (Fig 2.11b). Each spatial profile correlated significantly amongst replicates (Fig 2.12a) and with whole-tissue RNA-seq from matching tissue types (average Pearson's correlation coefficient 0.794 ± 0.030 SD for n = 8 tissue sections) (Fig 2.12b). Unsupervised clustering across all 8 sections correctly identified known tissue subregions for each organ type (Fig 2.11c and Fig 2.12c). For example, our clustering data recapitulated the major brain subregions and the expected spatial zonation of periportal and pericentral hepatocytes within liver lobules (Fig 2.11c). These observations were further corroborated by the spatial expression patterns of marker genes for tissue subregions, such as *Mobp*, *Pcp2*, and *Nrep*, found in the fiber tracts, the granular layer, and the molecular layer of the cerebellar cortex regions of the brain, respectively, or *Cyp2f2*, *Cyp2e1*, and *Glul*, found in the periportal and pericentral zones of the liver (Fig 2.11d-e and Fig 2.12d). Lastly, spatial gene set enrichment analyses correctly assigned the biological functions of an organ to its expected histological locations, such as fluid transport, regulation of systemic arterial pressure, and gluconeogenesis in the kidney renal medulla, distal convoluted tubule-enriched renal cortex, and proximal convoluted tubule-enriched renal cortex, respectively (Fig 2.13a-b). Similarly, we observed that

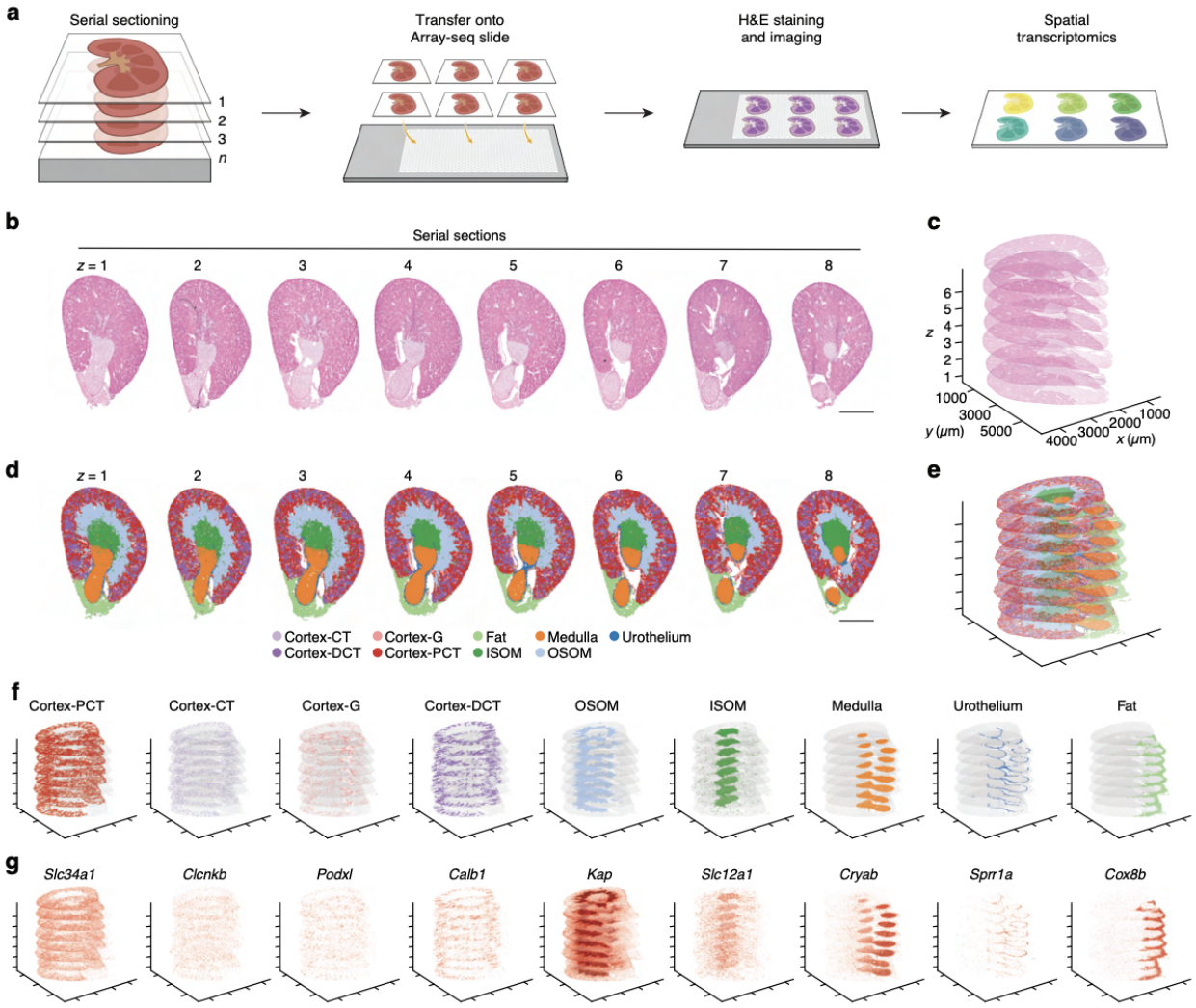


Figure 2.9: Array-seq enables the three-dimensional profiling of spatial transcriptomes. **a,** Schematic overview of the experimental workflow. **b-c,** H&E images of eight mouse kidney sections (10 µm each) placed onto an Array-seq slide and shown in two dimension (**b**) and aligned in a Z-stack (**c**). 100 µm were skipped in between each section. d-e, Unsupervised clustering highlights the histological subregions of the kidney as shown in two (**d**) and three dimensions (**e**). CT, Connecting tubule; DCT, Distal Convoluted Tubule; G, Glomerulus; PCT, Proximal Convoluted Tubule; ISOM, Inner Stripe of Outer Medulla; OSOM, Outer Stripe of Outer Medulla. **f-g,** Z-stack of H&E images (grayscale) from serial kidney sections that are overlaid with indicated tissue subregions (**f**) and marker genes (**g**, scaled expression). Scale bars: **b** and **d**, 1 mm.

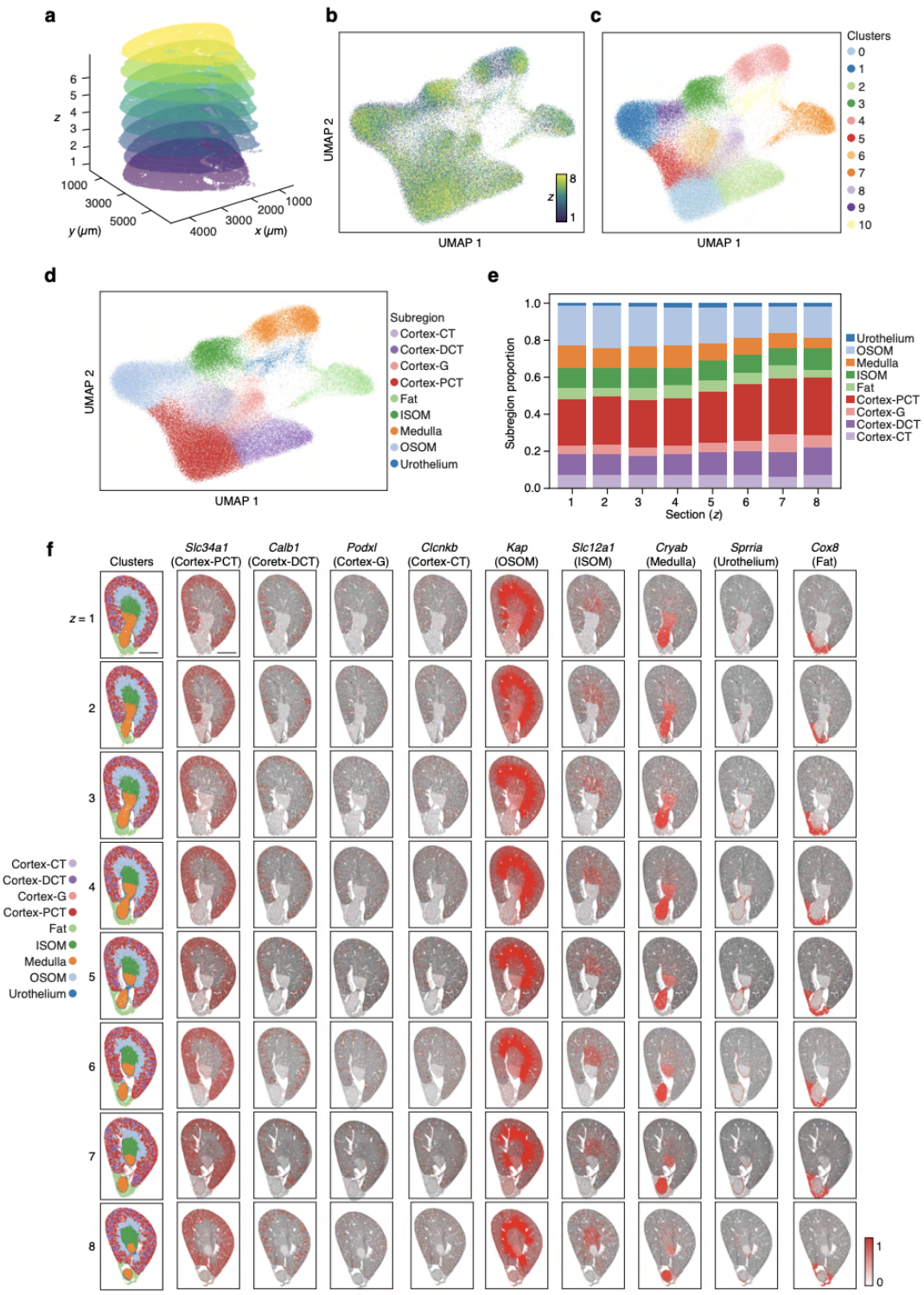


Figure 2.10: Three-dimensional Array-seq analysis of serial mouse kidney sections. a, H&E images of eight mouse kidney sections (10 µm each) aligned in a Z-stack and colored according to z positions within the stack. 100 µm were skipped in between each section.

Figure 2.10: b-d, Uniform Manifold Approximation and Projection (UMAP) plots of all spots from Array-seq profiles aggregating all eight serial kidney sections and colored by z position (**b**), Leiden clusters (**c**), or manually annotated clusters matching kidney tissue subregions (**d**). CT, Connecting tubule; DCT, Distal Convoluted Tubule; G, Glomerulus; ISOM, Inner Stripe of Outer Medulla; ISOM, Inner Stripe of Outer Medulla; PCT, Proximal Convoluted Tubule. **e,** Bar plots of the proportion of spots annotated as belonging to indicated kidney tissue subregions (y axis) for each tissue section (x axis). **f,** Spatial plots of indicated kidney tissue subregions (leftmost panels) and subregion marker genes (scaled expression) overlaid on grayscale H&E images. Consecutive kidney sections are shown from top (z = 1) to bottom (z = 8). Scale bars, 1 mm.

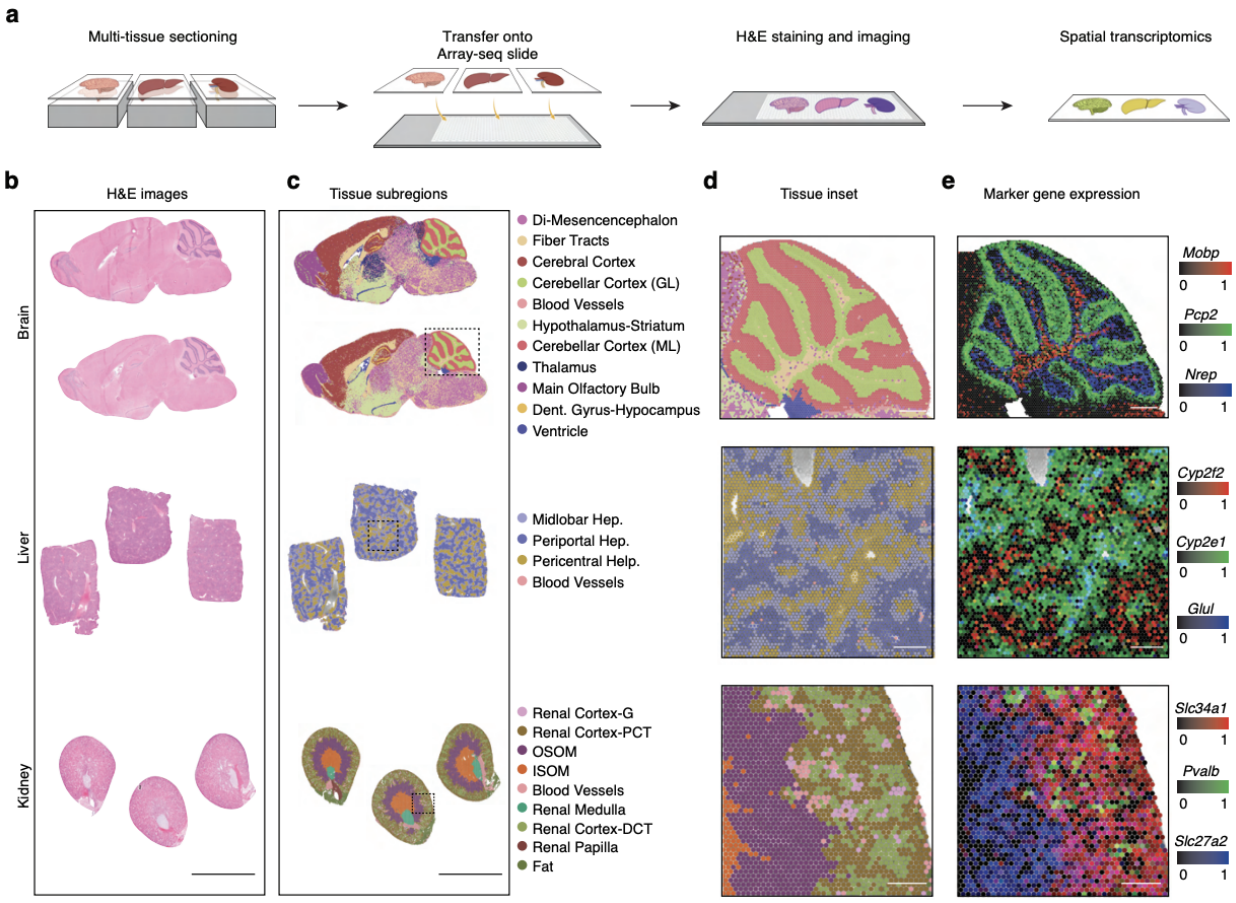


Figure 2.11: Multi-tissue, spatial transcriptomics profiling using Array-seq. a, Schematic overview of the experimental workflow. **b,** H&E images of tissue sections from mouse brain (top; n = 2), liver (middle; n = 3), and kidney (bottom; n = 3) organs which were placed onto a single Array-seq slide. **c,** Unsupervised clustering highlights the histological subregions of each organ type. Brain: GL, Granular Layer; ML, Molecular Layer; Dent., dentate. Liver: Hep., hepatocyte. Kidney: DCT, Distal Convoluted Tubule; G, Glomerulus; PCT, Proximal Convoluted Tubule; ISOM, Inner Stripe of Outer Medulla; OSOM, Outer Stripe of Outer Medulla. **d-e,** Magnified images of indicated insets (dashed lines in **c**) for brain (top), liver (middle), and kidney (bottom) showing tissue subregions (**d**) and scaled expression for indicated marker genes (**e**). Scale bars: **b-c**, 5 mm; **d-e**, 250 µm.

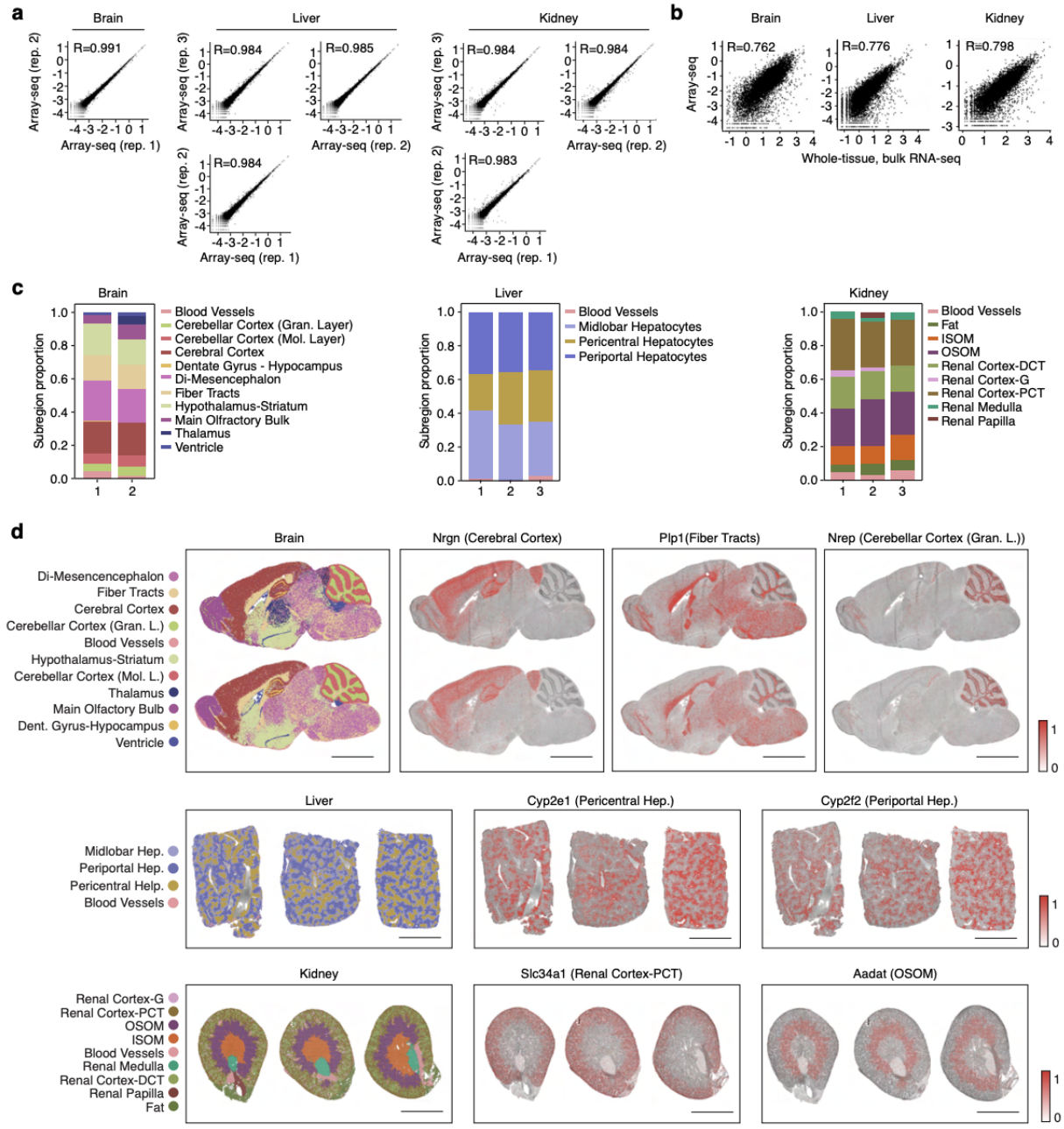


Figure 2.12: Reproducibility of Array-seq for multi-organ section profiling. a-b, Correlation (Pearson's coefficient) between replicate Array-seq profiles (**a**), or between average Array-seq and bulk RNA-seq datasets (**b**) for indicated mouse tissue types. In **a**, shown are the normalized log10 unique molecular identifier (UMI) counts which were averaged across all spots for each gene across each replicate. In **b**, Shown are the normalized log10 unique molecular identifier (UMI) counts which were averaged across all spots for Array-seq data (n = 2 for brain and 3 for liver and kidney sections) (y axis) or across independent organ samples (n = 4) for bulk, whole-tissue RNA-seq data (x axis).

Figure 2.12: **c,** Bar plots of the proportion of the total Array-seq spots under tissue sections which matched indicated tissue subregions. Bars (x axis), replicate sections for each organ type. For brain: Gran. Layer, Granular Layer; Mol. Layer, Molecular Layer. For kidney: DCT, Distal Convoluted Tubule; G, Glomerulus; PCT, Proximal Convoluted Tubule; ISOM, Inner Stripe of Outer Medulla; ISOM, Inner Stripe of Outer Medulla. **d,** Spatial plots of indicated tissue subregions (leftmost panels) and subregion marker genes (scaled expression) overlaid on grayscale H&E images. Scale bars, 2 mm

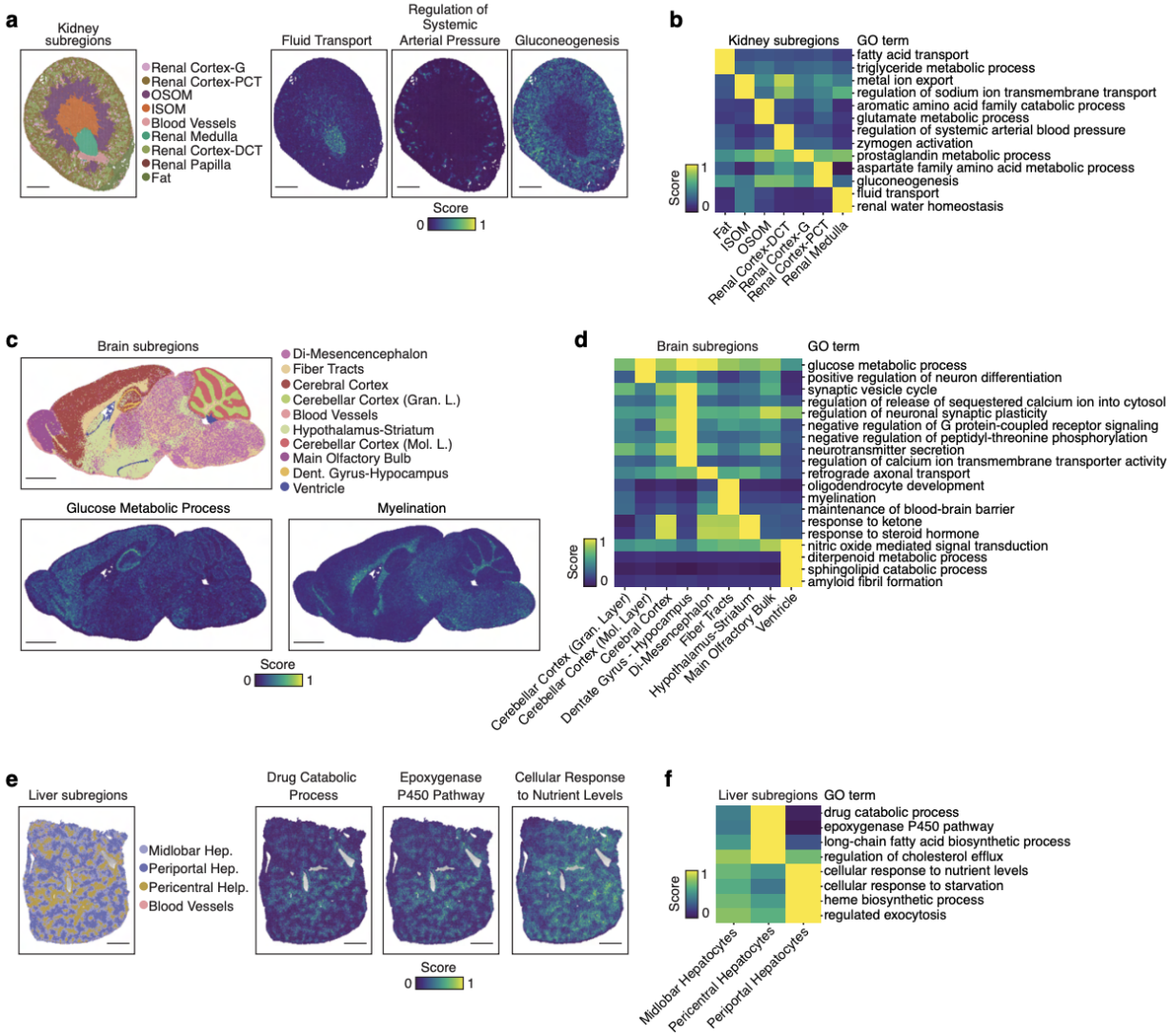


Figure 2.13: Spatial enrichment of gene ontology gene sets in Array-seq profiles. **a, c, e,** Spatial plots of indicated tissue subregions (left) and normalized enrichment score of indicated gene sets (right) in representative kidney (**a**), brain (**c**), and liver (**e**) sections. For brain: Gran. L., Granular Layer; Mol. L., Molecular Layer; Dent., dentate. For kidney: DCT, Distal Convoluted Tubule; G, Glomerulus; PCT, Proximal Convoluted Tubule; ISOM, Inner Stripe of Outer Medulla; ISOM, Inner Stripe of Outer Medulla. Scale bars, 2 mm. **b, d, f,** Heatmap of enriched Gene Ontology (GO) terms (rows) in indicated tissue subregions (columns) in representative kidney (**b**), brain (**d**), and liver (**f**) sections. Values are row normalized enrichment scores.

sets of genes linked to specific tissue functions were enriched in the expected spatial regions of the brain and liver as well (Fig 2.13c-f).

These results thus suggested that scaling up the number of tissues processed per Array-seq slide did not alter data quality. The large surface area of Array-seq slides enabled the generation of spatial transcriptomes at high resolution and throughput, including in three dimensions.

2.4.5 Spatial transcriptomics analysis of whole-mount, human spleen section

While a large surface area is useful for comparing many conditions or sample types, it could also, in theory, enable the analysis of whole-mount sections from larger tissues. To test this, we obtained fresh human spleen tissue which we processed for Array-seq profiling (Fig 2.14a). We generated whole-mount, longitudinal sections using a cryomacrotome due to the large surface area covered by the human splenic tissue (~12 cm^2) (Fig 2.14b, left panel). H&E staining followed by imaging of human spleen sections readily revealed the known histological structures of spleen, including the red pulp interspersed with a patchwork of white pulp nodules or trabecular vessels (Fig 2.14b, middle panel). The spleen tissue covered a total of 750,640 spots, covering 77% of the array surface. Clustering of the spatial transcriptomic data obtained from the same splenic section as imaged by H&E correctly identified the red pulp, white pulp, and marginal zones (Fig 2.14b, right panel, and Fig 2.15a-c). The expression of key marker genes for splenic immune cell types, such as *CD68*, *FCGR3A*, *CSFR1*, and *ITGAX* for macrophages, *CD79A*, *CD19*, *IGHD*, and *CD22* for B cells, and *CD3D*, *CD3E*, *CD69*, and *SELL* for T cells, were spatially restricted to the histological regions known to contain these cell types (Fig 2.14c, Fig 2.15d-f).

Next, we examined the spatial expression patterns of pairs of chemokines and their matching receptors which are key to the maintenance of splenic tissue architecture and the organization of immune cell positioning in the spleen. For example, we examined the expression of

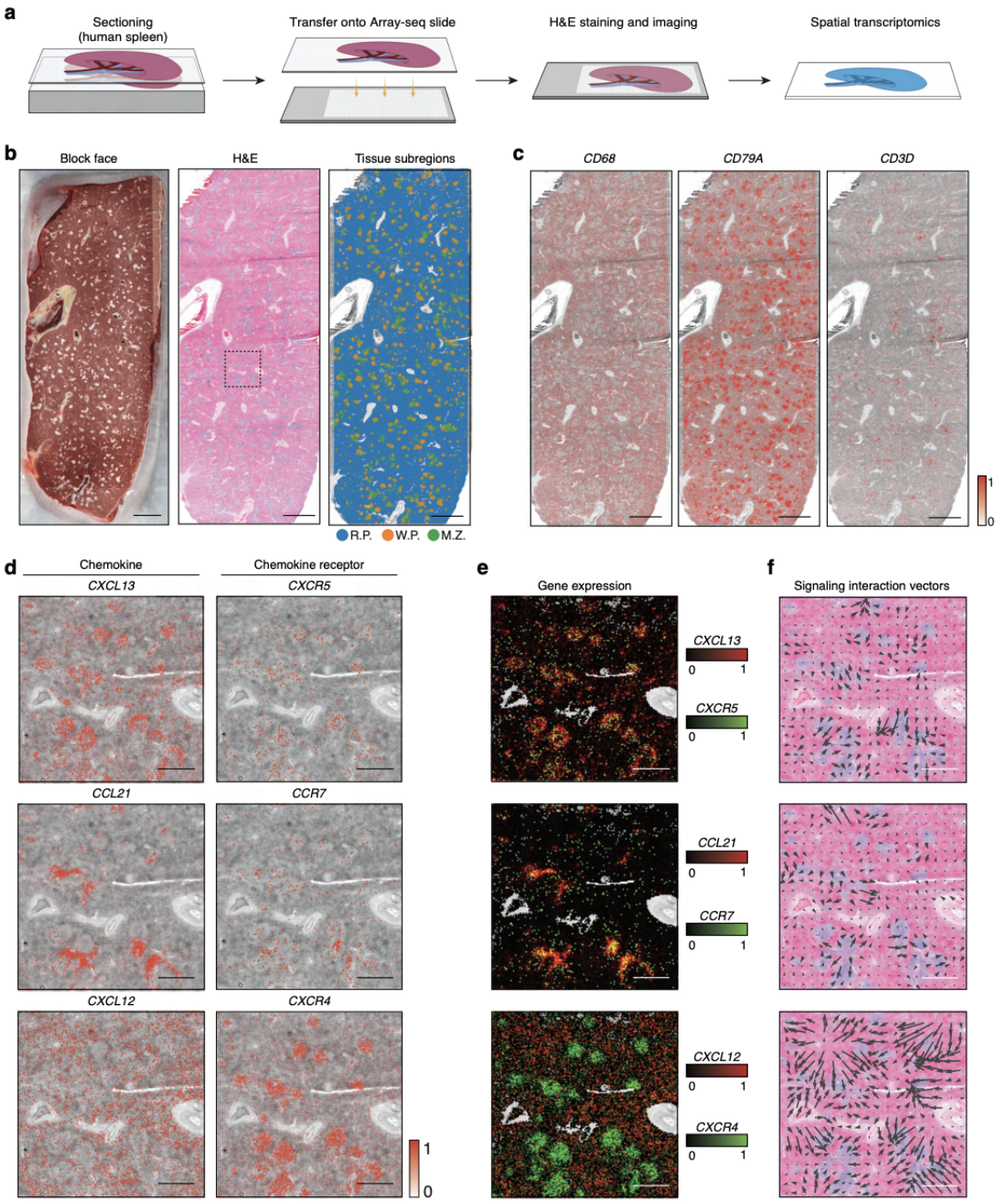


Figure 2.14: Array-seq profiling of a whole-mount section from a human spleen organ. a, Schematic overview of the experimental workflow. **b,** Images of the block face of an embedded, longitudinally sectioned human spleen (left), the H&E image from a section immediately adjacent to the block face view (middle), and manually annotated unsupervised clusters of the Array-seq data obtained on the same section as shown by H&E (right). M.Z., Marginal Zone; R.P., Red Pulp; W.P., White Pulp.

Figure 2.14: c-d, Scaled expression of indicated marker genes for macrophages (CD68), B cells (CD79A), and T cells (CD3D) (**c**) and for chemokine ligand (left) and chemokine receptor (right) pairs (**d**). Gene expression values were overlaid on the grayscale H&E image of the same section. **e,** Scaled expression values of ligand (red) receptor (green) for indicated chemokine ligandreceptor pairs. **f,** Signaling directions of the indicated chemokine ligand-receptor pairs which were inferred computationally using the COMMOT package. Scale bars: **b-c**, 5 mm; **d-f**, 1 mm.

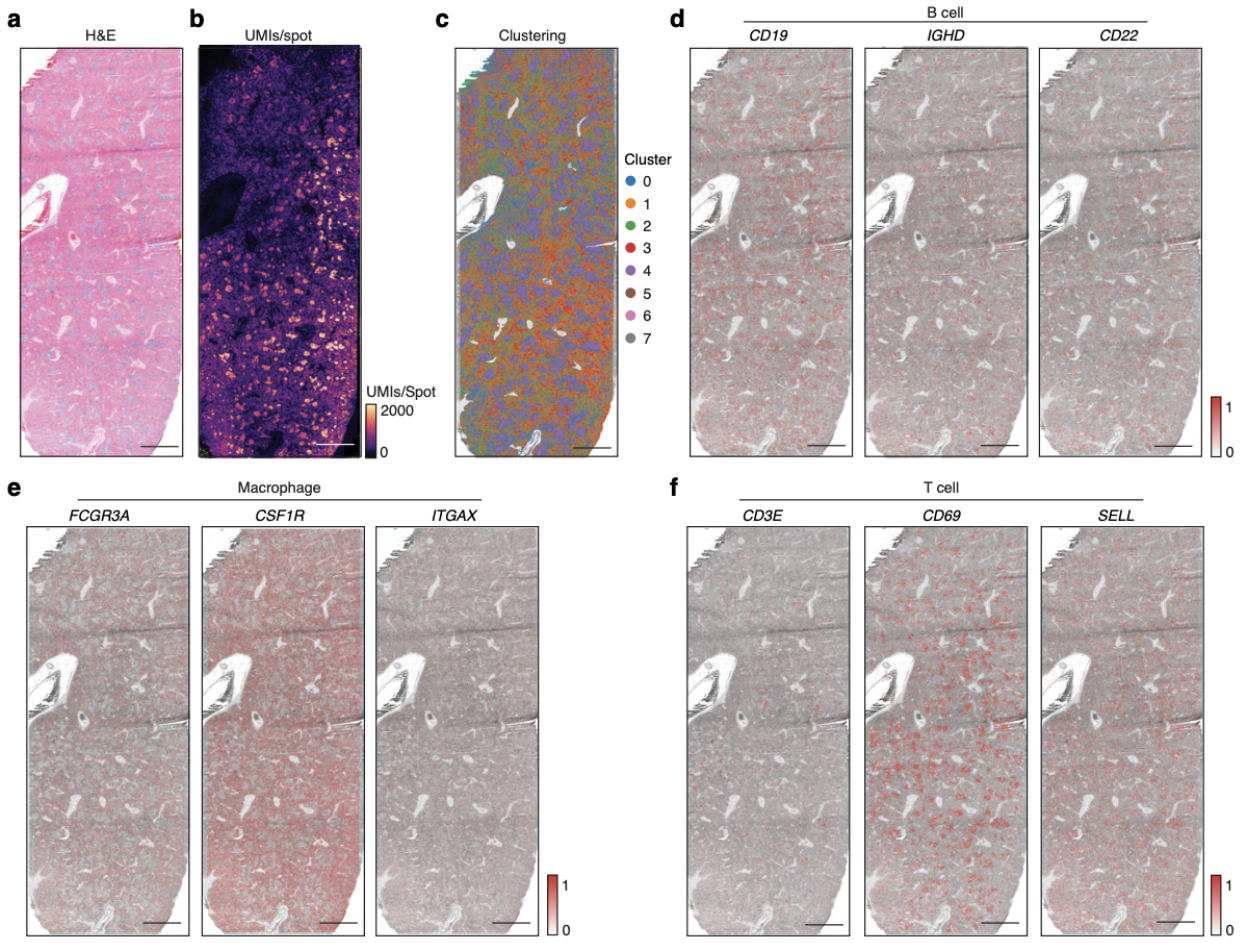


Figure 2.15: Array-seq analysis of a whole-mount, human spleen section. a, H&E image of a whole-mount, human spleen section mounted onto an Array-seq slide. **b-f,** Spatial plots of total unique molecular identifiers (UMIs) per spot (**b**), unsupervised, Leiden clustering results (**c**), and scaled gene expression for indicated marker genes for B cells (**d**), macrophages (**e**), and T cells (**f**). Scale bars, 5 mm.

CXC-chemokine ligand 13 (*CXCL13*), which is a ligand for the *CXCR5* receptor and helps construct B cell follicles in the human spleen (Alexandre and Mueller, 2023). We found that *CXCL13* and *CXCR5* mRNAs overlapped in their spatial expression at B cell follicles (Fig 2.14d-e). Next, we plotted the expression of CC-chemokine ligand 21 (*CCL21*) which contributes to the attraction and survival of CC-chemokine receptor 7 (*CCR7*)-expressing, naïve T cells in the T cell zone of the spleen (Alexandre and Mueller, 2023). Our data also revealed the colocalized expression patterns of the *CCL21* and *CCR7* mRNAs in the T cell zones which are adjacent to the larger B cell follicles in the human splenic tissue (Fig 2.14d-e). Lastly, our data correctly recapitulated the expected expression patterns of the CXCL12-CXCR4 axis (Alexandre and Mueller, 2023). We found *CXCL12* to be expressed in the red pulp and contributing to the attraction of $CXCR4^+$ B cells to the red pulp, as predicted the computational inference of spatial signaling directionality (Fig 2.14d-f) (Cang et al., 2023). Therefore, we found that the spatial distributions of individual genes encoding chemokines and chemokine receptors agreed with their expected localization within the splenic tissue (Fig 2.14d-f). Overall, Array-seq allows for the spatial profiling of histological sections covering the entirety of the active surface area for mRNA capture, thereby paving the way for whole-mount analyses of tissues and organisms whose sections fit within a dozen cm^2.

2.5 Discussion

By combining the two workhorses in gene expression from the beginning of the 21st century – microarrays and next-generation sequencing – we created a simple, large-format platform for spatial transcriptomics. Our method pushes the boundaries of spatial profiling by enabling the processing of small-to-large samples ranging from murine tissues to whole-mount human organs as shown in this work or whole-mouse sections, as we recently demonstrated (Takahama et al., 2024). We also showed that Array-seq enables the three-dimensional profiling

of tissue samples by processing large numbers of serial sections from the same tissue block. Notably, Array-seq is scalable thanks to its large format and low cost, easy to adopt without special expertise or instrument, compatible with H&E staining – the gold standard for clinical pathology diagnosis – and readily applicable to all fields of basic and clinical research. Thus, the Array-seq platform is poised to contribute to the spatial omics revolution by enabling spatiomolecular studies at scale and facilitating technology adoption across research communities. The total surface of active area for mRNA capture of on Array-seq slide is 11.31 cm^2, which is 26.7-fold larger than the only widespread method for ST profiling, Visium. Therefore, Array-seq slides provided a high degree of flexibility in the size and number of samples which can be profiled per slide, while keeping costs low thanks to cheap microarray manufacturing. We estimated that, at full occupancy, a single Array-seq slide could capture up to ~2 to 20 million cells depending on the tissue type and the number and size of the tissue sections to analyze (Fig 2.1d-e). Our method therefore provides high-throughput profiling capabilities which are needed to address questions requiring large numbers of samples such as time series, functional perturbations, drug responses, animal or patient cohorts, or three-dimensional analyses as demonstrated on mouse kidney tissue (Fig 2.9). For example, Array-seq opens the door to functional spatiomolecular studies whereby molecular, cellular, or tissue-level perturbations can be coupled with downstream ST profiling. Our method also enables cohort-level studies of patient samples by making the profiling of hundreds of specimens on dozens of Array-seq slides feasible and affordable to yield information with high clinical value.

Where does Array-seq fit within the landscape of existing methods for spatiomolecular profiling? Here, we benchmarked Array-seq against Visium because it is the only other ST tool to date which also combines all the following characteristics of our method: compatible with histology analysis (H&E) on the same tissue section, and easy to adopt and access without the need for special instrumentation, expertise, or custom-built reagents. Going

further, we compared the characteristics of Array-seq to those of other existing ST methods which also rely on mRNA capture on a slide followed by cDNA sequencing. First, the total surface of active area for Array-seq slides was 1 to 4 logs larger than all existing methods for sequencing-based spatial profiling (Fig 2.16a-c), with perhaps the exception of a recent implementation of the Stereo-seq method on macaque brain sections (Chen et al., 2023a). Second, the resolution of Array-seq (30 µm spots with 36.65 µm center-to-center distances between spots) was 8.1-fold higher spots/mm^2 than Visium, but lower than methods with higher resolution such as DBiT-seq and Slide-seq (10 µm), HDST (2 µm), Pixel-seq (1 µm), Seq-Scope (0.63 µm), and Stereo-seq (0.22 µm) (Fig 2.16a). However, methods with a physical resolution on the substrate below 10 µm, such as Stereo-seq, Pixel-seq, and Seq-Scope, require spatial binning of the data for most downstream analyses and visualization due to the sparsity of count data, suggesting that the effective difference in resolution between Array-seq and these methods at the spatial data level is less pronounced than what the physical properties of spots across methods suggest. Third, existing ST methods other than Visium have not been adopted outside of their institutions of origin due to complex requirements in instrumentation, expertise, and custom reagents, making these methods difficult to implement by independent labs (Fig 2.16a) (Moses and Pachter, 2022). Fourth, multiple methods are not compatible with H&E staining on the same tissue section as the one used for ST profiling due to the use of substrates other than glass for the mRNA capture slide (Fig 2.16a). Array-seq is compatible with simultaneous H&E analysis, which is, in our view, a critical pre-requisite for any ST platform aiming to integrate with existing clinical workflows and research. Fifth, the sensitivity of Array-seq, as measured by the number of UMIs per µm^2, was comparable to other ST methods (Fig 2.16d). We anticipate that further optimizations of Array-seq slide assembly will likely yield higher sensitivity by removing the remaining overextended Anchor 1 products and thereby increasing the number of functional capture probes per spot (Fig 2.1c). Lastly, the cost of Array-seq is lower than all other

methods reported to date and, for example, by a decrease of >100-fold when comparing to Visium (Fig 2.16e and Tables S1-2). We estimated that the cost of sequencing nearly all ~1M spots on one Array-seq slide at a depth of 5,000-10,000 raw sequencing reads per spot (i.e., ~5-10B reads total) would cost $3,550 to $7,100 using present day next-generation sequencers (i.e., ~$314 to $628 per cm^2 using a NovaSeq X Series 10B Reagent Kit with 100 cycles). Array-seq thus lies at a unique position when compared to existing ST platform thanks to its unique large surface area, ease of adoption by any lab, and lowest cost.

In conclusion, Array-seq is thus readily deployable to address fundamental questions across all fields of basic and translational biomedical research. We foresee that the open-source nature of Array-seq, which relies on cheap, well-established microarray technology, will help democratize and enhance the reach of spatiomolecular profiling. Future developments of the Array-seq platform will enable the multi-modal analysis of whole or targeted transcriptomes and proteomes in fresh and fixed samples, as shown for other spatiomolecular profiling tools (Liu et al., 2020, 2023b; Vickovic et al., 2022). Moreover, we anticipate that future modifications of the technology will help increase its resolution by, for example, modifying microarray printers to decrease spot diameters or combining sample expansion protocols with current Array-seq slides (Fan et al., 2023). The throughput of the method can also be readily increased using automation procedures facilitated by the format of Array-seq slides which is that of standard microscopy slides. Array-seq will thus enable the spatial cartography of mammalian and non-mammalian organisms and organs at scale – without the need for the preselection of small regions that may bias the analysis of tissue architecture.

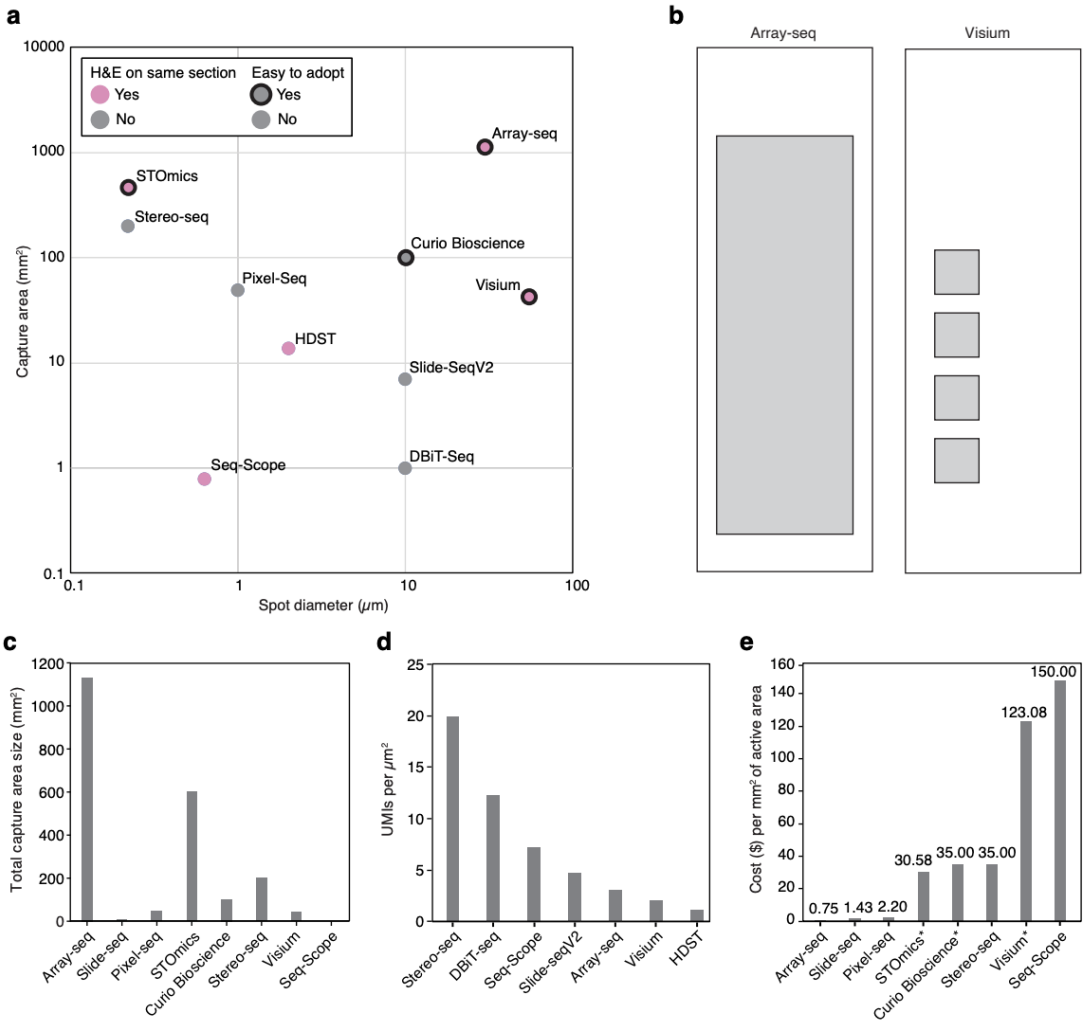


Figure 2.16: Comparison between Array-seq and sequencing-based, spatial transcriptomics methods. **a,** Dot plot showing the total surface area available for spatial profiling (Y axis) and the diameter of the barcoded spots, beads, or DNA species arranged on the slides or substrates used for mRNA capture (X axis). Pink dots indicate that a method is compatible with H&E imaging on the same section that is used for spatial profiling. Easy-to-adopt indicates methods which can be readily deployed without the need for special expertise, instrumentation, and reagents. **b,** Diagram of Array-seq (left) and Visium (right) slides showing the mRNA capture area sizes and positions (grey) at scale. **c-d,** Bar plots of the cost per mm^2 of active area (**c**), the total surface area available for mRNA capture (**d**), and the sensitivity computed in total unique molecular identifiers (UMIs) detected per μm^2 (**e**) for indicated methods (bars). In **c**, the numbers indicate the dollar amounts for each method based on values reported by the developers of each method or from commercial quotes, and the asterisks indicate that library preparation cost were included in the values shown. In **e**, the sensitivity analysis was performed using publicly available, preprocessed datasets for each method on MOB tissue, except for Seq-Scope (mouse liver) and DBiT-seq (mouse embryo).

CHAPTER 3

SPATIOMOLECULAR CARTOGRAPHY OF THE MOUSE *IN TOTO* REVEALS MECHANISMS OF SYSTEMIC INFLAMMATION

3.1 Abstract

The detailed understanding of systemic diseases such as sepsis has been hampered by the lack of tools capable of integrating molecular data with spatial tissue context at a whole-organism scale. Addressing this, our study leverages a novel implementation of Array-seq, a large-format spatial transcriptomics platform, enabling the spatial mapping of gene expression while retaining histological integrity across adult mouse sections. This enables spatial transcriptomics analysis of the mouse model at the level or organ, tissue subregion, and cell types. By applying this technology to a endotoxemia mouse model of sepsis, Array-seq identified spatial patterns of inflammation-associated genes and cell type changes across the mouse body. We have also identified PLA2G5[1] as a critical mediator in the pathogenesis of the disease, operating as a "self-venom" that disrupts red blood cell integrity and iron metabolism. The inhibition of PLA2G5 via genetic and antibody approaches mitigated the deleterious effects of sepsis in mice, highlighted by restored splenic red pulp macrophage counts and iron homeostasis. This study marks a significant step in the convergence of molecular biology and spatial genomics, providing an in-depth understanding of systemic inflammation and opening new avenues for research into other complex diseases.

1. Most *in vivo* and *in vitro* experiments relating to PLA2G5 were performed by Michihiro Takahama, a previous postdoctoral researcher in the Cheverier lab. He was also principally involved in delineating the molecular mechanisms of PLA2G5 during sepsis.

3.2 Introduction

The mouse model has been at the center of biological scientific discoveries for almost a century, playing a pivotal role in our understanding of genetics, development, and disease. This model's genetic, physiological, and anatomical similarities to humans make it an indispensable tool in biomedical research (Canales and Walz, 2019; Perlman, 2016). Understanding the transcriptomic architecture of the mouse is crucial for comprehending normal physiology and disease mechanisms. Efforts to map the mouse transcriptome using bulk RNA sequencing (RNA-seq) have provided valuable insights into gene expression profiles across tissues but lack the resolution to discern individual cell types (Wang et al., 2009; Mortazavi et al., 2008). More refined approaches, such as single-cell RNA sequencing (scRNA-seq), exemplified by projects like the Mouse Cell Atlas (MCA) and Tabula Muris, have significantly advanced our knowledge by revealing cellular heterogeneity and identifying rare cell populations (Consortium, 2020; Han et al., 2018).

However, spatial information is necessary for a complete understanding of biological systems. Spatially dependent cell-to-cell communication and tissue interfaces play critical roles in dictating biological function and disease pathophysiology, adhering to the principle that structure determines function (Crosetto et al., 2015; Lubeck et al., 2014). For instance, understanding the spatial organization of cells within tissues can illuminate how microenvironments influence cell behavior and how disruptions in these spatial relationships contribute to disease processes (Ståhl et al., 2016; Rodriques et al., 2019).

The best approach for capturing this spatial context is through barcode-based spatial transcriptomics. Imaging-based methods, such as multiplexed fluorescence in situ hybridization (FISH), enable high-resolution spatial information but are limited in the number of transcripts they can target and generate large datasets that require substantial computational resources for processing and analysis (Chen et al., 2015, 2016). In contrast, barcode-based technologies offer transcriptome-wide coverage without the burden of extensive imaging data,

relying only on brightfield imaging of the histological sections (Ståhl et al., 2016; Rodriques et al., 2019). Several barcode-based spatial transcriptomics methods have recently been developed, each with its strengths and limitations. For example, Slide-seq, 10x Genomics Visium, and STOmics Stereo-seq have made significant strides in spatial transcriptomics but are limited in the size of the capture area they can analyze (Rodriques et al., 2019; Stickels et al., 2021; Chen et al., 2022). However, the recent spatial transcriptomics method Array-seq has the capture area size required for whole-mount adult mouse sections and integration with hematoxylin and eosin (H&E) for visualizing gene expression in the context of histological staining. This large-format spatial transcriptomics methods allows for efficient organism-wide analysis of spatial gene expression and cell type organization in healthy and diseased mice.

Sepsis is a canonical organism-wide disease characterized by systemic inflammation, often triggered by an infection that leads to a dysregulated immune response, resulting in widespread tissue damage, organ failure, and potentially death (Rudd et al., 2020; Singer et al., 2016; Hotchkiss et al., 2016). The pathophysiology of sepsis involves a complex interplay between pro-inflammatory and anti-inflammatory pathways, endothelial dysfunction, and coagulopathy, making it a major cause of morbidity and mortality worldwide (Cecconi et al., 2018; van der Poll and Opal, 2008). Intravascular hemolysis is a severe, well-established complication of sepsis and other disorders such as sickle cell disease, malaria infection, or beta-thalassemia (Schaer et al., 2013). In homeostatic conditions, damaged red blood cells are removed from the circulation through phagocytosis by macrophages in the spleen and liver. However, in disease conditions such as sepsis, intravascular hemolysis leads to the destruction of red blood cells and the release of free hemoglobin, heme, and iron into the circulation (Rother et al., 2005). These degradation products lead to toxic effects for the vasculature and tissues through, for example, oxidative stress and the amplification of damaging inflammatory signals (Gozzelino et al., 2010; Su et al., 1999). In addition, the plasma

levels of free hemoglobin, heme, and iron have each been linked with increased mortality in sepsis (Adamzik et al., 2012). However, the molecular mechanisms underlying hemolysis during sepsis remain unclear with candidate mechanisms including the coagulation and complement systems or the direct membrane effects of lipopolysaccharide (Larsen et al., 2010). As a result, we lack suitable targets to decrease hemolysis in sepsis.

The past two decades has broadened our understanding of the biology of the PLA2 family of phospholipase enzymes as both secreted and cellular PLA2 enzymes have been linked to a wide array of homeostatic and pathological processes across tissues (Murakami et al., 2020), prompting the search for inhibitors of these enzymes as potential therapies (Quach et al., 2014). Secreted phospholipase A2 (sPLA2) enzymes are found in mammalian tissues and snake venom. sPLA2 enzymes hydrolyze the glycerol backbone of phospholipids to release fatty acids and lysophospholipids and have been collectively involved in a vast array of biological functions in health and disease (Murakami et al., 2020; Lambeau and Gelb, 2008). Each sPLA2 enzyme's pleiotropic functions result from both its intrinsic catalytic properties and substrate preferences and its changes in expression across cell types, tissues, and disease conditions (Murakami et al., 2020). For example, sPLA2 group V (PLA2G5) has several local pathogenic and protective roles linked to various cell types, including macrophages, adipocytes, endothelial cells, bronchial epithelial cells, and cardiomyocytes (Samuchiwal and Balestrieri, 2019; Yamaguchi et al., 2018; Sato et al., 2014; Watanabe et al., 2020; Yano et al., 2011). PLA2G5 has also been shown to be induced by lipopolysaccharide (LPS) in a model of acute lung injury (Muñoz et al., 2009). However, the expression and function of PLA2G5 during systemic inflammation such as sepsis has not been studied in mice or humans.

3.3 Materials and Methods

Mice

Female C57BL/6J mice (6- to 8-weeks old) were obtained from the Jackson Laboratories (stock 000664). Animals were housed in specific pathogen-free conditions at The University of Chicago, and all experiments were performed in accordance with the US National Institutes of Health Guide for the Care and Use of Laboratory Animals and approved by The University of Chicago Institutional Animal Care and Use Committee.

Sepsis induction

For LPS endotoxemia, mice were injected intraperitoneally with either lethal (10-15 mg/kg) or sublethal (3-5 mg/kg) doses of LPS derived from Escherichia coli O55:B5 (Sigma-Aldrich) diluted in PBS. Dosing was established for each lot of LPS by in vivo titration.

Histological sectioning and transfer of whole mount mice

Mice were euthanized with CO2 then massaged with a depilatory agent (NAIR ^{TM}) until all hair was removed. Mice were then placed in a plastic bag and frozen in a dry ice hexane bath for at least 3 minutes and moved to -80°C for no longer than 3 months. Mice were taken from -80°C storage, immediately placed in a freezing frame containing SCEM (SECTION-LAB Co. Ltd.) and placed into a dry ice hexane bath until all of the media was frozen. Frozen tissues were sectioned (10-µm thickness) using a cryomacrotome (Leica CM3600XP). Once an appropriate cross-sectional blockface profile was obtained (all major organs described in the paper are visible the gross tissue block), we applied transfer film to the surface of the block and applied gentle pressure with the transfer film application tool (SECTION-LAB Co. Ltd.). The next section would then be adhered to the transfer film (Fig S.). The section was then placed onto a glass slide or prepared Array-seq slide pre-cooled to -20°C,

and flattened with the transfer film application tool. Another glass slide was then placed on top of the section, creating a "sandwich" and warmed at room temperature until the section visible thawed. The glass slides and section were then rapidly cooled to -80°C after being placed on a flat metal block, during which the section would freeze without ice crystal formation, damaging the cellular structures in the section. The top glass slide was removed and the section on the Array-seq slide was submerged in a 95% n-hexane bath pre-cooled to -20°C on a stir plate (VWR, 10153-314) with a stir bar (VWR, 74950-296) spinning at 800 rpm overnight. During this time, the adhesive on the transfer film would dissolve, leaving the section on the Array-seq slide. Following transfer, the section was transferred to two pre-cooled 95% n-hexane washes for 1 hour each. Finally, the section was removed from the wash solution and left at -20°C for 2 minutes for residual hexane to evaporate.

Spatial assignment of cell types with CellKb

To systematically test the spatial assignment of cell types across whole-mouse sections, we used the CellKb database to infer the cell type composition for each Array-seq spot under whole-mouse sections. CellKb contains a curated collection of cell-type specific gene signatures from publicly available single-cell RNA-seq experiments. Each gene signature is assigned a tissue and cell type using standardized Uberon Ontology and Cell Ontology terms, respectively. By using single-cell RNA-seq data covering ~60M cells, we obtained 18,745 gene signatures covering 495 cell types across 16 mouse tissue types in total (Methods) (https://www.cellkb.com). For each spot, 500 spot-specific genes with the highest positive log fold change compared to all other spots were calculated. This ranked gene list was compared to all gene signatures from a specific tissue in CellKb using a rank-based method. For each spot-specific gene list, the rank-based method assigned a match score to every gene signature in CellKb based on a) the number of overlapping genes with the gene signature, b) the ranks of the overlapping genes, c) the rank differences of the overlapping

genes, and d) the number of genes in the gene signature. Based on the scores of the top 100 matching gene signatures, the proportion of each cell type per spot was calculated as follows: Proportion of cell i:

$$P_i = (M_i - \overline{M}) + \left(0.1 \times \left[\overline{M} \times (n_i - 1)\right]\right)$$

where,

M_i = match score of the first matching marker gene set of cell type i

$\overline{M}$ = average match score of the top 20 matching marker gene sets

n_i = number of matching marker gene sets of cell type i in the top 20

Top 3 positive cell type proportions, P_i, are normalized to such that their sum is 1 and assigned to the spot. We also classified the cell types into core and broad cell types to facilitate some of the downstream analyses and visualizations of the spatial data. Cell types were manually assigned to core and broad groups based on the parent cell types in the Cell Ontology annotations.

Recombinant cytokine injections

C57BL/6J mice were injected intravenously with 2.5 µg of recombinant TNF, IL-1β, IL-6, IL-10, IL-18, or IFN-γ used alone (6 singles) or in pairwise combinations (15 pairs).

Neutralizing antibody and drug treatment

For neutralizing antibody, C57BL/6J mice were injected intraperitoneally with 50 µg of anti-PLA2G5 (clone MCL-3G1, Cayman Chemical) neutralizing antibody, or mouse IgG1 isotype control (Clone MOPC-21, BioXCell BE0083) in 100 µl of PBS 1 hour prior to LPS injection.

Recombinant PLA2G5 injections

C57BL/6J mice were injected intravenously with 10 µg of recombinant PLA2G5 (Cayman chemical, 10009563).

Blood analysis

Mouse whole blood was harvested by cardiac puncture and plasma and serum were isolated using lithium heparin coated Microtainer blood collection tubes (BD 365965) and Microtainer blood collection tubes (BD 365978), respectively. For flow cytometric, bead-based immunoassays, serum was diluted and processed using the LEGENDplex Mouse Macrophage/Microglia Panel (BioLegend 740846) kit. Data were acquired on the NovoCyte flow cytometer (Acea Biosciences/Agilent) and analyzed using the LEGNEDplex software v8 (BioLegend). To measure tissue injury marker levels in sera or plasma, samples were processed by In Vivo Animal Core, University of Michigan, with the following kits for BUN (BioAssay Systems DIUR-100), ALT (Cayman Chemical 700260), and troponin-I (Life Diagnostics CTNI-1-HS) levels according to the manufacturer's instructions, or with a Vet Axcel blood chemistry analyser (Alfa Wasserman). Total plasma heme was measured with the 3,3',5,5' tetramethylbenzidine (TMB) peroxidase assay and oxyhemoglobin with a Nanodrop One (Thermoscientific) instrument.

Spleen histology

Tissue processing, embedding, sectioning, and immunohistochemistry using H&E and Periodic Acid Schiff were performed by the Human Tissue Resource Center at the University of Chicago. To stain ferric iron in tissue sections, spleens were frozen in OCT using dry ice, sectioned (10 µm) using a cryostat (Leica CM1850) and stained with Perl's Prussian blue (Sigma-Aldrich, P3289) and neutral red (Sigma-Aldrich, 72210). Section images were obtained using the Slideview VS200 Research Slide Scanner (Olympus).

In vitro erythrocyte lysis assay

Mouse whole blood was spun at 1,000 g, the plasma and buffy coat were removed, and red blood cells were washed three times in Hepes-buffered saline. Subsequently, a portion of erythrocytes was incubated with 100 µM CaCl2 in Hepes-buffered saline for 3 min at 37°C. Calcium ionophore (Cayman Chemical, A23187) was added to a final concentration of 4 µM, and the cells were further incubated for 10 min at 37°C to induce membrane phospholipid (PS) scrambling. After that, 2 mM EDTA was added to stop the reaction. In the presence or absence of 100 nM of varespladib, hypertonic solution (100 mM NaCl), or hypotonic solution (water-diluted Hepes-buffered saline), PS-exposing or untreated erythrocytes (109 cells/mL) were incubated with 5, 50, or 500 ng/mL of human recombinant PLA2G5 (Cayman chemical, 10009563) for 1 h at 37°C in Hepes-buffered saline with 2 mM of calcium for the activity of PLA2G5. Hemolysis was measured by determining the amount of oxyhemoglobin in the supernatant of erythrocyte suspensions after centrifugation at 4,000 g. The absorbance at 414 nm in the supernatant of erythrocyte suspensions was measured using Nanodrop (Thermoscientific) and compared to that of a hemolyzed aliquot of the same erythrocyte suspension treated with Triton X-100.

Lipidomics analysis of colon tissues

The procedures for lipidomics analysis using high-performance liquid chromatography coupled with electrospray tandem mass spectrometry (LC-ESI-MS/MS) were described previously (Yamamoto et al., 2017). Briefly, C57BL/6J were injected intraperitoneally with 50 µg of anti-PLA2G5 neutralizing antibodies in 100 µl of PBS 1 hour prior to LPS injection. Twelve hours after LPS injection, mice were anesthetized with 2,2,2-tribromoethanol (250-500 mg/kg) and perfused transcardially with PBS containing 10 mM EDTA. Immediately after perfusion, colon tissues were extensively washed in PBS and frozen by liquid nitrogen and kept at -80°C until the following procedures. Tissues were mechanically homogenized

with the Precellys 24 homogenizer (Bertin Technologies, Montigny-le-Bretonneux, France) in methanol containing internal standards (500 pmol/sample of d4-labeled EPA, d5-labeled PGE2, LPC with a 17:0 fatty acyl chain (LPC17:0), and PC with two 14:0 fatty acyl chains (PE14:0-14:0)) and then incubated overnight at -20°C. For extraction of phospholipids and lysophospholipids, one-tenth of tissue lysates were added to 10 volumes of 20 mM Tris-HCl (pH 7.4) and were extracted using the method of Bligh and Dyer (PMID = 13671378)66. For extraction of oxygenated fatty acid metabolites, nine-tenths of the tissue lysates were added to water (final methanol concentration of 10% (v/v)), and the lipids were extracted using an Oasis HLB cartridge (Waters, Milford, MA, USA). The samples were applied to a Kinetex C18 column (Kinetex C18, 2.1 x 150 mm, 1.7 µm particle; Phenomenex, Inc., Torrance, CA, USA) connected with ESI-MS/MS on a liquid chromatography (NexeraX2 system; Shimadzu Co., Kyoto, Japan) coupled with a 4000Q-TRAP quadrupole-linear ion trap hybrid mass spectrometer (AB Sciex, Framingham, MA, USA). For analyses of free fatty acids (FFAs), lysophospholipids (LPLs) and phospholipids, the samples were applied to the column and separated by a step gradient with mobile phase A (acetonitrile/methanol/water =1/1/1 (v/v/v) containing 5 mM phosphoric acid and 1 mM ammonium formate) and mobile phase B (2-propanol containing 5 µM phosphoric acid and 1 mM ammonium formate) at a flow rate of 0.2 mL/min at 50°C. For analyses of oxygenated fatty acid metabolites, the samples were applied to the column and separated using a step gradient including mobile phase C (water containing 0.1% acetic acid) and mobile phase D (acetonitrile/methanol = 4/1 (v/v)) at a flow rate of 0.2 mL/ min at 45°C. Identification of phospholipids, LPLs, FFAs, and oxygenated PUFAs (polyunsaturated fatty acids) metabolites was conducted by multiple reaction monitoring (MRM) transition, and quantification was performed based on the peak area of the MRM transition and the calibration curve obtained with an authentic standard for each compound (Yamamoto et al., 2015).

Lipidomics analysis of erythrocytes

T he procedures for lipidomics analysis using high-performance liquid chromatography coupled with electrospray tandem mass spectrometry (LC-ESI-MS/MS) were described above. Mouse whole blood was spun at 1,000 g, the plasma and buffy coat were removed, and red blood cells were washed three times in Hepes-buffered saline. Subsequently, a portion of erythrocytes was incubated with 100 µM CaCl2 in Hepes-buffered saline for 3 min at 37°C. Calcium ionophore (Cayman Chemical, A23187) was added to a final concentration of 4 µM, and the cells were further incubated for 10 min at 37°C to induce membrane phospholipid (PS) scrambling. After that, 2 mM EDTA was added to stop the reaction. PS-exposing or untreated erythrocytes (109 cells/mL) were incubated with or without 100 ng/mL of human recombinant PLA2G5 (Cayman chemical, 10009563) for 1 h at 37°C in Hepes-buffered saline with 2 mM of calcium for the activity of PLA2G5. The samples were kept at -80°C until the following procedures.

Plasma transfer

Whole blood was harvested by cardiac puncture from donor Pla2g5$^{+/+}$ or Pla2g5$^{-/-}$ mice injected with LPS 12 hours prior to bleeding animals. Plasma was isolated using lithium heparin coated Vacutainer tubes (BD) and incubated with or without PLA2G5 neutralizing antibody for 4 hours at 4°C. Plasma treated with PLA2G5 neutralizing antibody was transferred intravenously (100 µl) to recipient C57BL/6J mice. Plasma oxyhemoglobin in recipient mice was measured 16 hours after plasma transfer.

3.4 Results

3.4.1 Spatial transcriptomics of whole-mouse sections with Array-seq

We sought to measure the spatial distribution of the transcriptome across whole-body histological sections from a 6-week-old mouse on a C57BL/6J genetic background (Fig 3.1a). We chose the mouse strain and age because they are widely used in experimental mouse models (Mukherjee et al., 2022). First, we developed a method for the histological sectioning of whole mice is compatible with downstream spatiomolecular profiling of the transcriptome. We sectioned whole, fresh-frozen mice using a cryo-macrotome and an adhesive film to support resulting whole-body sections (Fig 3.2a and Methods) (Morodomi et al., 2019; Kawamoto and Kawamoto, 2014, 2021). The resulting whole-mouse sections maintained the finest histological structures with little to no damage across tissues, including the eye, the intestinal mucosa, the spleen, and bone marrow (Fig 3.2b-g). Next, we transferred histological sections onto glass slides while maintaining RNA integrity by modifying our film transfer method (Fig 3.2h and Methods) (Kawamoto and Kawamoto, 2021). Second, we transferred whole-body sections onto Array-seq slides which we recently developed as a large-format platform for the spatiomolecular profiling of histological sections (Fig 3.1a) (Takahama et al., 2024). Array-seq slides, which are repurposed from oligonucleotide microarrays, carried 974,016 spots of 30 µm in diameter (36.65 µm center-to-center distance) arranged in 1,068 rows and 912 columns across 11.31 cm^2 in total surface area usable for spatial transcriptomics of whole mouse sections. Each spot on the array carries copies of a single-stranded DNA probe with a unique spatial barcode sequence at known x and y coordinates, a unique molecular identifier (UMI), and a poly-(dT) sequence for poly adenylate mRNA capture.

Next, we combined our tools for large-format sectioning and spatial transcriptomics to profile whole-mouse sections from two independent animals. Each section was stained with hematoxylin and eosin (H&E) and imaged prior to Array-seq profiling, thereby allowing us

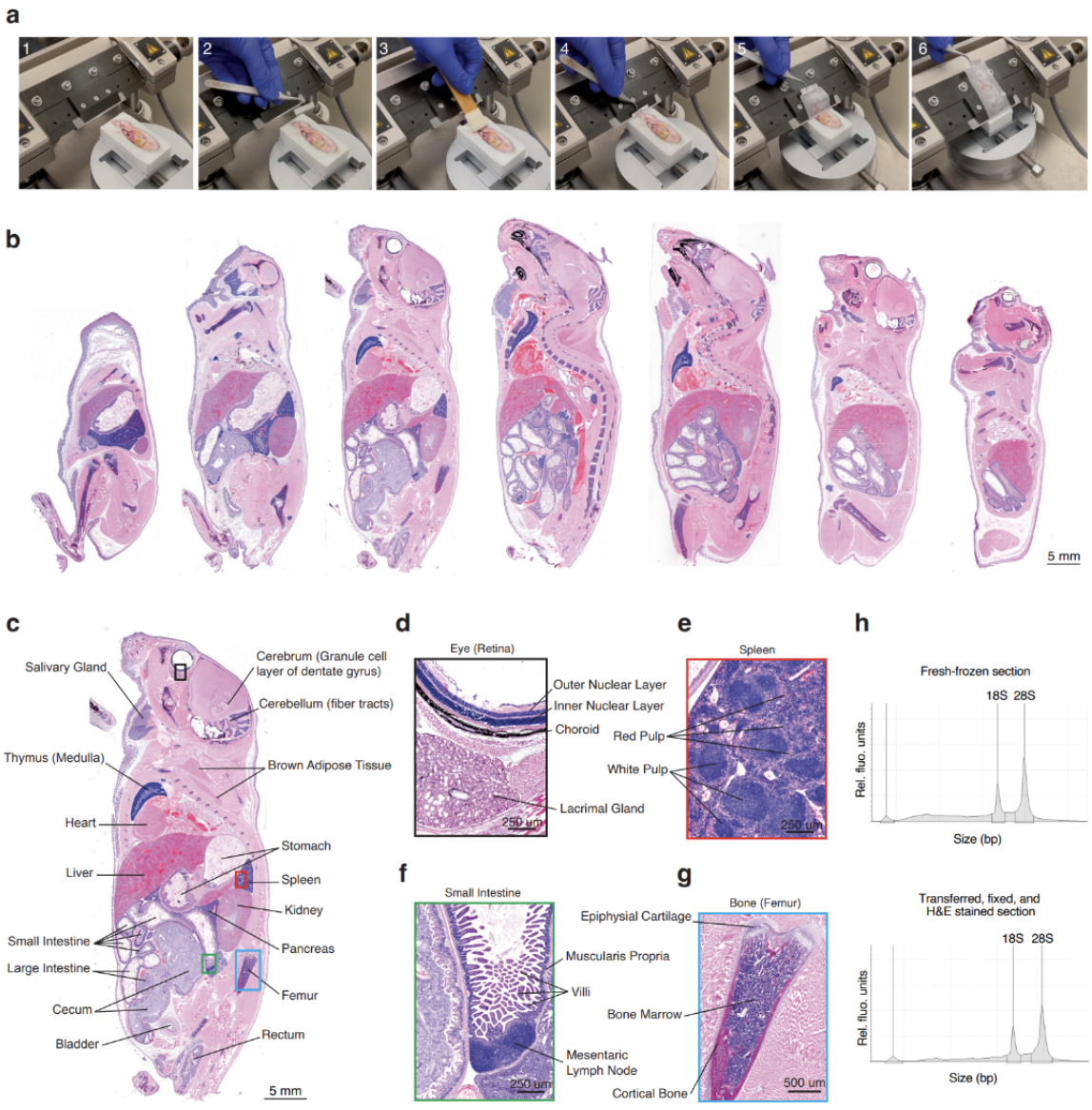


Figure 3.1: Transfer enables whole mouse sections with high histological quality. **a,** Images showing the use of transfer film during sectioning. Transfer film is placed on the surface of a block face (image 1-2) then secured to the film and removed air bubbles with the applicator tool (image 3). The following section is adhered to the transfer film (images 4-6), generating a section with high histological quality. **b,** Sections generated from a single 6-week-old mouse at different z-planes. Optimal sections for spatial transcriptomics are those with major organs well represented in the z-plane (Z = 3). **c,** Z-plane image 3 from (**b**) with annotation of major organs and anatomical/histological structures. **d-g,** Zoomed regions of the whole mouse H&E image in (**c**) depicting smaller anatomical/histological structures in the eye (**d**), spleen (**e**), small intestine (**f**), and bone (**g**). **h,** RNA quality of mouse thymus before (top) and after (bottom) transfer as RNA size distribution from TapeStation. Scale bars, **b-c**, 5 mm; **d-f**, 250 µm; **g**, 500 µm.

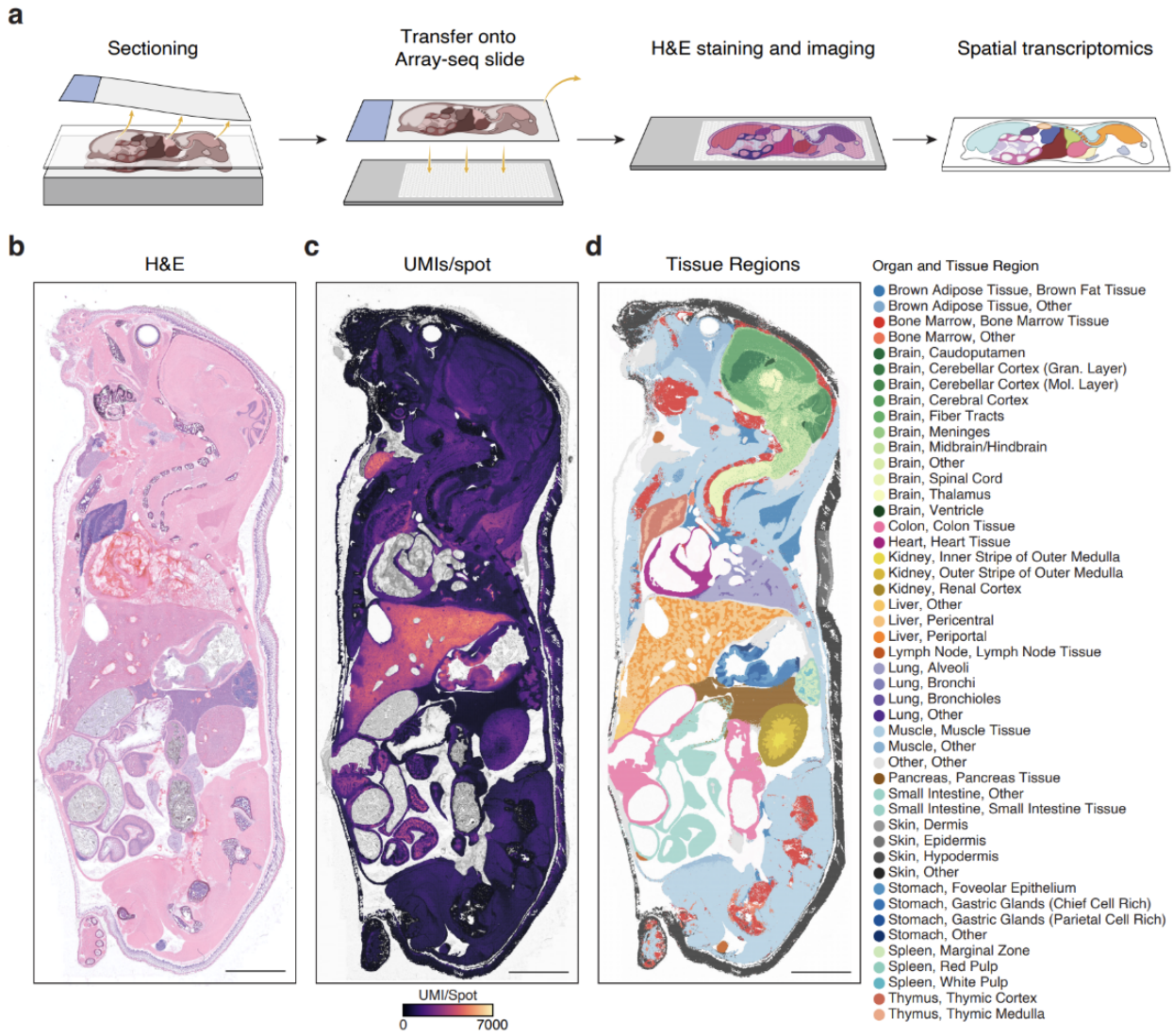


Figure 3.2: Array-seq analysis of whole-mouse section. **a,** Schematic overview of a whole mouse spatial transcriptomics experiment. Transfer film is applied to a block face once an appropriate cross section is reached. The following section is adhered to the transfer film and transferred to an Array-seq slide (Methods). The section is then fixed, stained, and subjected to a standard spatial transcriptomics workflow. **b,** Image of a 6-week old whole mouse after transfer and H&E staining. **c,** Spatial plot of Array-seq spots colored by the number of UMIs detected. **d,** Spatial plot of spot organ and subregion annotation of unsupervised clustering followed by manual annotation. Scale bars, 5 mm. Panel **d** was generated by Ashwini Patil.

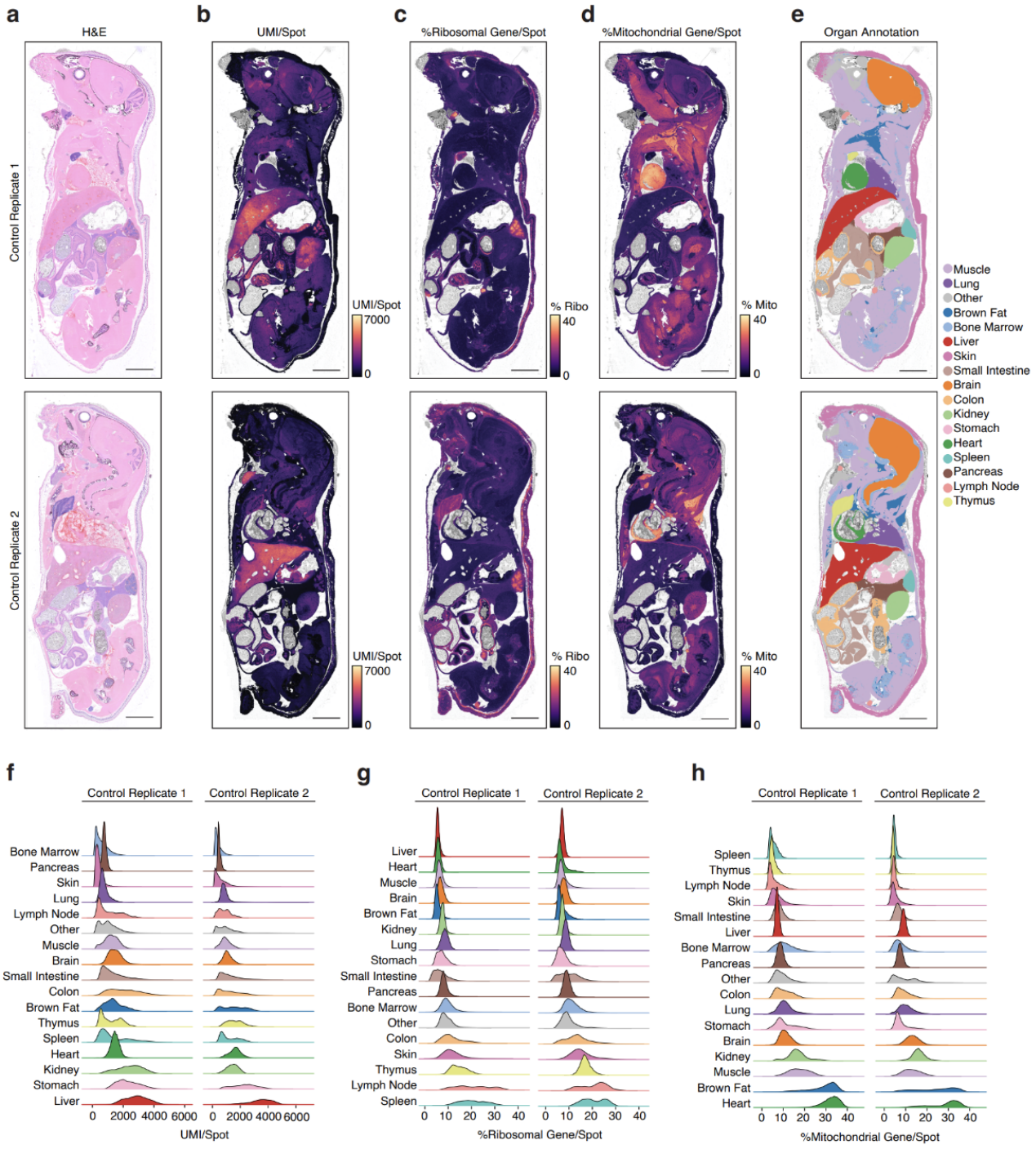


Figure 3.3: Whole mouse Array-seq data quality metrics. a-e, Two 6-week old mouse H&E sections (rows) (**a**) with corresponding spatial transcriptomics data showing spot organ annotation (**b**), UMI counts (**c**), percent of UMI mapped to ribosomal (**d**) or mitochondrial (**e**) genes. **f-h,** KDE plot of (**f**) UMI/spot, (**g**) percent of UMI mapped to ribosomal or (**h**) mitochondrial genes for each individual organ (y axis) for of two control whole mouse replicates. Scale bars, 5 mm.

to compare histological and molecular readouts (Fig 3.1b and Fig 3.3a). The total surface area of each whole-mouse section covered 588,299 and 610,689 spots per Array-seq slide for replicate 1 and 2, respectively. We detected 660.5 genes ± 331.1 SD and 1237.9 UMIs ± 876.8 SD per spot on average across both replicates and all tissues represented across whole-mouse sections. The spatial patterns of expression intensity measured by total UMIs and ribosomal and mitochondrial genes per spot reflected the expected variations in RNA content across organs (Fig 3.1c and Fig 3.3b-h). For example, we found the highest number of UMIs per spot in the liver tissue whereas the bone marrow and skin displayed the lowest (Fig 3.3b-h). In addition, mitochondrial RNA content was highest in heart and fat, which is expected given their high metabolic activities (Fig 3.3b-h). Taken together, by combining histological and spatial profiling innovations, we generated spatiomolecular maps of whole-mouse sections at 30-µm resolution.

3.4.2 Array-seq accurately captures tissue subregions across the mouse body

We asked if our whole-mouse profiles could correctly identify organ types and their histological subregions by performing unsupervised clustering and manual cluster annotation. We found that clustering of our spatiotranscriptomic data correctly identified the main organ types of the body (Fig 3.3e), which was further validated by examining the spatial expression patterns of known organ-specific marker genes (Fig 3.4a-b). Each organ-specific spatial profile correlated significantly amongst independent whole-mouse sections (average Pearson's correlation coefficient 0.968 ± 0.0129 SD for n = 16 tissues) and with bulk RNA-seq from matching tissue types (average Pearson's correlation coefficient 0.790 ± 0.0405 SD for n = 12 tissues) (Fig 3.4c-d).

Moreover, we obtained clusters that accurately recapitulated the histological features and tissue subregions detectable by H&E staining across all organs tested (Fig 3.2d and Fig S4a). The agreement between histological features and clustering data was further

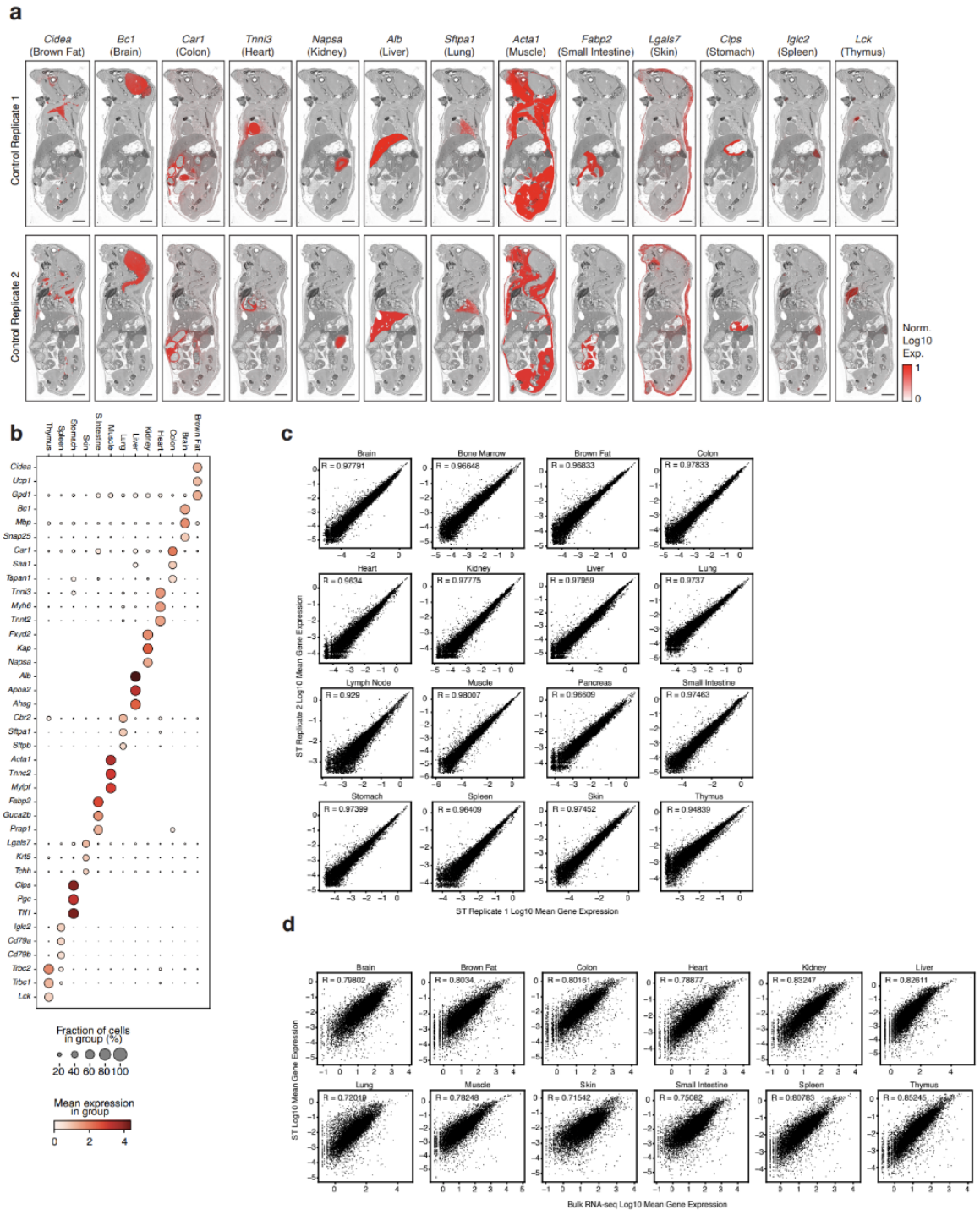


Figure 3.4: Organ-level analysis of whole mouse Array-seq data. a, Spatial plots of normalized log10 gene expression of a marker gene for each indicated organ (columns) for two whole mouse section replicates (rows). **b,** Dot plot of three marker genes (x axis) for each of the selected organs (y axis). Spot size scales according to the percent of spots which have at least one UMI count of that gene in the organ subset.

Figure 3.4: **c,** Correlation (Pearson's coefficient) between organ subsets of replicate Array-seq profiles and **d**, between average of organ subsets and bulk RNA-seq datasets. In **c**, shown are the normalized log10 unique molecular identifier (UMI) counts which were averaged across all spots for each gene across each replicate. In **d**, organ bulk RNA-seq counts were averaged across replicates (n=3-4) and log10 transformed. Scale bars, 5 mm.

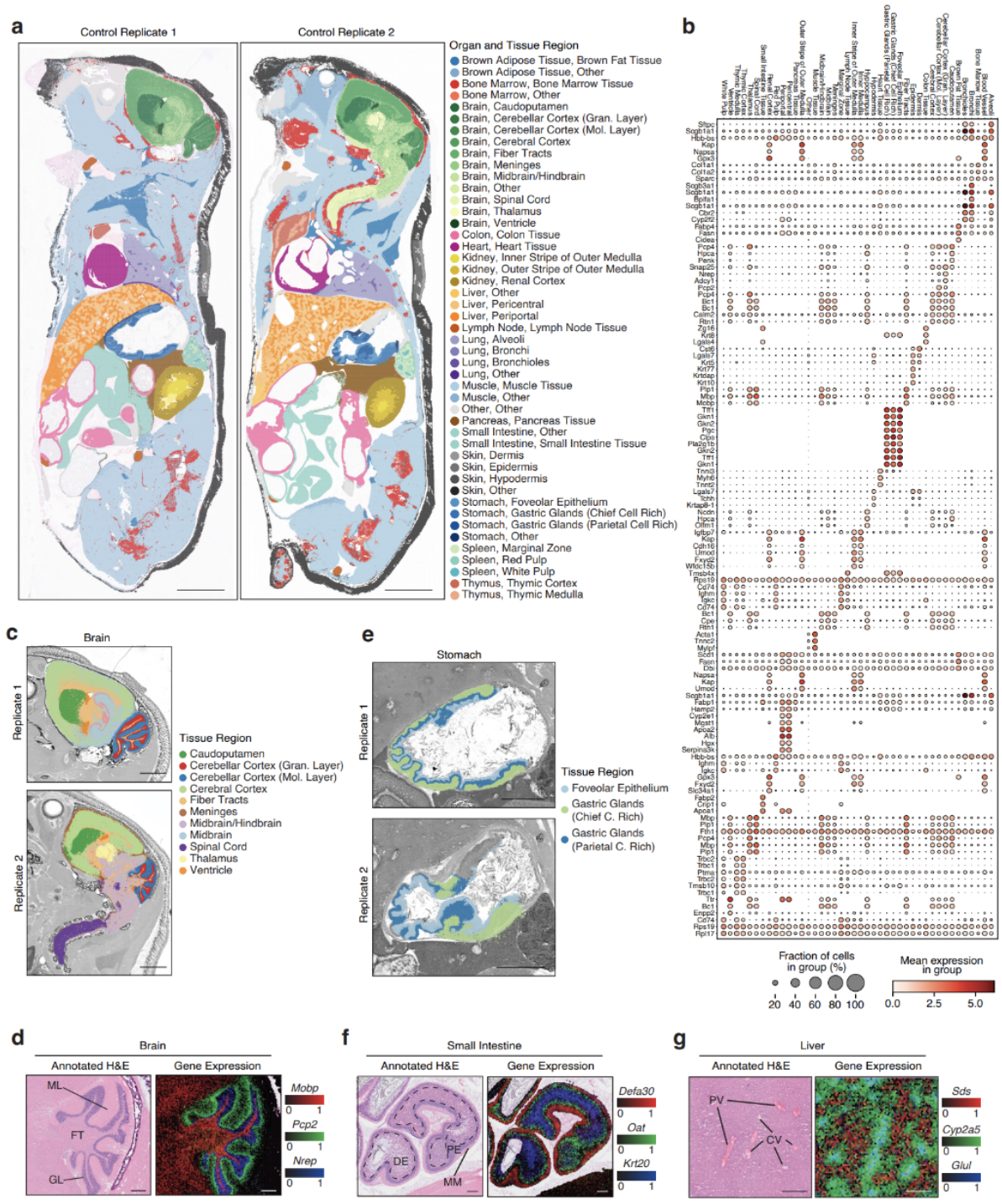


Figure 3.5: Organ subregion clustering and marker gene analysis. a, Spatial plots of subregion annotation across two whole mouse replicates. **b-c,** Spatial plots of subregion annotation for b, brain and c, stomach for each replicate(rows). **d,** Dot plot of three marker genes (x axis) for each of the selected subregions (y axis). Spot size scales according to the percent of spots which have at least one UMI count of that gene in the subregion subset.

Figure 3.5: e-g, H&E image (left) and spatial plot of the expression of 3 genes (right), normalized log2 transformed counts were mapped to red, green, or blue values, then combined. Scale bars, **a**, 5 mm; **b-c**, 2.5 mm. **e-g**, 1 mm. Panel **a** was generated by Ashwini Patil.

corroborated by the spatial expression of known marker genes across tissue subregions (Fig 3.5b). For example, in the mouse forebrain, our data correctly identified subregions such as the caudoputamen, cerebral cortex, fiber tracts, and ventricles (Fig 3.5c). Our data also identified the layers of cerebellum as shown by the distribution of the genes *Mobp*, *Pcp2*, and *Nrep* which are specific for the fiber tracts, granular layer, and molecular layer, respectively (Fig 3.5d). In the gastrointestinal tract, we observed the foveolar epithelium and different functional regions of the gastric glands of the stomach, including parietal cell and chief cell rich regions, responsible for HCl and pepsinogen secretion, respectively (Fig 3.5e) (Sáenz and Mills, 2018). We also correctly detected the spatial distribution of marker genes of the tissue layers composing the small intestine with *Defa30* for muscularis mucosa, *Oat* for proximal enterocytes, and *Krt20* for distal enterocytes (Fig 3.5f). Lastly, in liver, the expression of marker genes *Sds*, *Cyp2a5*, and *Glul* mirrored the transition from periportal to pericentral hepatocytes in liver lobules (Fig 3.5g). We thus showed that the spatial transcriptomics profiles of whole-mouse sections accurately captured the histological subregions of all the mouse tissues.

3.4.3 Organism-wide mapping of mouse cell types

We aimed to define the distribution of cell types across all the organs present in our whole-body sections from mice. To systematically test the spatial assignment of cell types across whole-mouse sections, we developed a computational method to infer the cell type composition for each Array-seq spot under whole-mouse sections. First, we used published single-cell RNA-seq profiles that were curated into a publicly available database, CellKb, to build a reference dataset of ~60M single cells spanning 16 mouse tissue types (https://www.cellkb.com) (Patil and Patil, 2020). Using our reference single cell dataset, we defined cell-type-specific gene sets covering 495 cell types encompassing all tissue types present in our whole-mouse sections (Methods). In addition, we classified these 495 cell types into 30 core and 79 broad

cell types to facilitate some of the downstream analyses and visualizations of the spatial data.

Second, we used our cell-type-specific gene sets to estimate computationally the cell type composition of each spot across our two whole-mouse spatial profiles covering 1,195,065 spots in total across two Array-seq slides. Out of the 495 cell types interrogated, we found 333 (67.3%) and 342 (69.1%) cell types being represented in total for each of the two sections tested. Skeletal muscle cells were the most represented in our computational annotation of spots, covering 44.18% (259,641/587,691) and 32.57% (197,802/607,374) of all spots in replicate 1 and 2, respectively, which was expected based on the H&E analysis of the whole-body sections used for Array-seq profiling (Fig 3.6a and Fig 3.7a-b). After muscle cells, hepatocytes and gut epithelial cells were detected in 8.9% and 7.8% (specialized epithelial cells) of all spots (Fig 3.6a and Fig 3.7a-b). Notably, cell types present in relatively low abundance across the body-wide sections were also detected accurately, including osteocytes (0.2%) in bone such as the skull and spine and hip bones, or endothelial cells (<0.1%) in brain, brown fat, colon, heart, kidney, liver, lung, muscle, pancreas, skin, and thymus (Fig 3.6a and Fig 3.7a-b). All hematopoietic cell types combined represented ~12.27% of all the spots (146,646/1,195,065) across both Array-seq slides combined, including 6.12% in lymphoid organs (thymus, spleen, and bone marrow) and 6.15% in non-lymphoid tissues at steady state (Fig 3.6a and Fig 3.7a-b). Furthermore, our cell type analysis recapitulated the expected cell type composition of each organ (Fig 3.7b). For example, the most abundant broad cell types in brown fat, heart, and kidney were adipocytes (98.41%, 30,948/31,449 of organ-specific spots), cardiac muscle cells (94.69%, 18,840/19,897), and renal epithelial cells (86.52%, 27,455/31,733), respectively (Fig 3.7b). Collectively, the types of T cells in our reference annotation data (48/495 total cell types) were detected in abundance in lymph node (29.13%, 998/3,426), spleen (37.42%, 3,678/9,828), and thymus (64.82%, 6,663/10,280), as well in non-lymphoid tissues such as colon (17.15%, 6,661/38,844) and skin (12.51%,

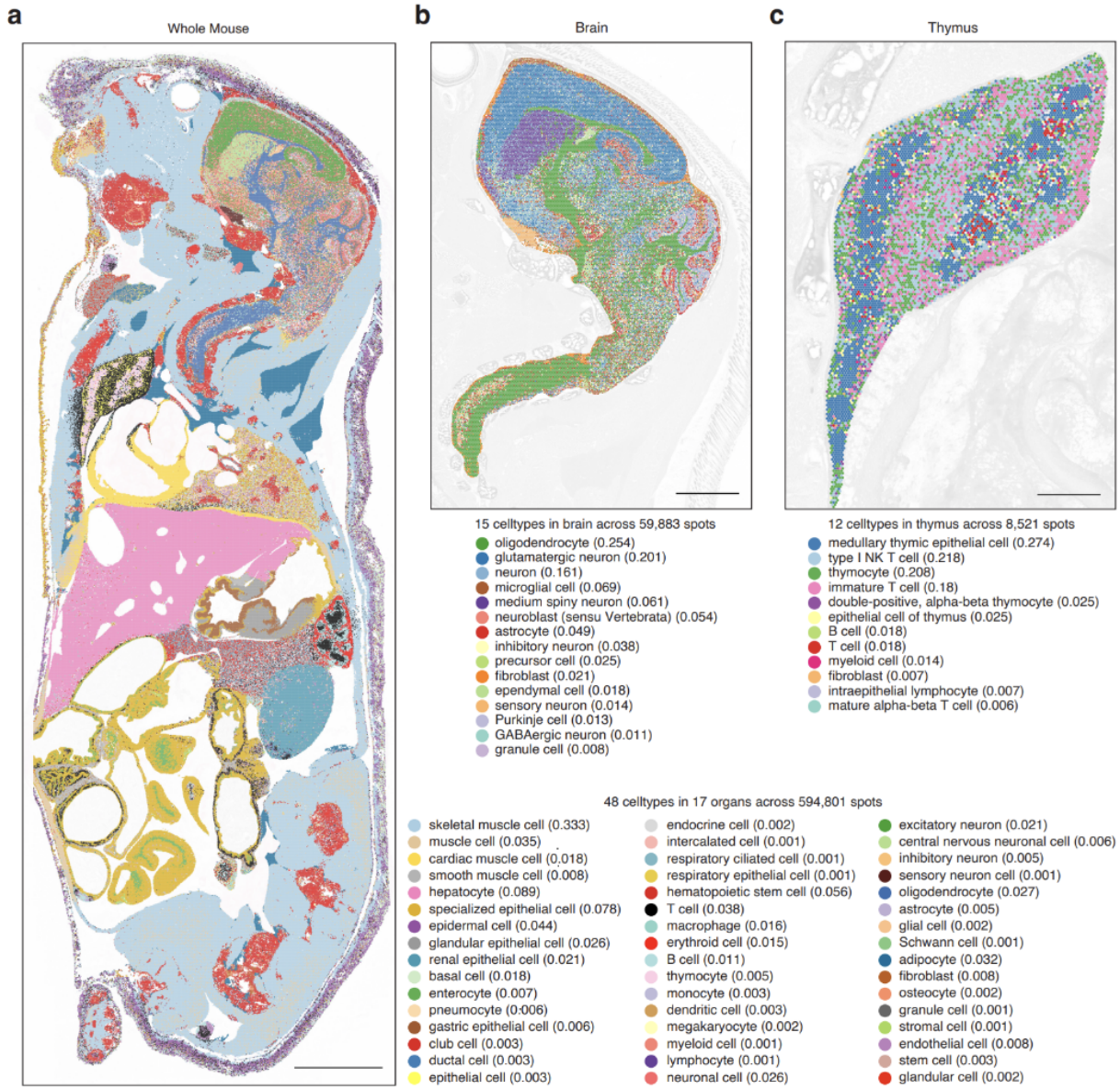


Figure 3.6: Cell type mapping of whole mouse Array-seq data. a, Array-seq spots annotated according to the cell type with the highest signature proportion, overlayed on a grey-scaled image of the corresponding whole mouse section. The legend (bottom right) indicated 48 cell types/cell type categories were identified in the whole mouse section and the proportion of spots which were identified broad cell types. **b,** Spatial plot of specific cell type annotation of the mouse brain subset and **c,** thymus subset. Scale bars: **a**, 5mm; **b-c**, 2.5 mm. Panels **a-c** were generated by Ashwini Patil.

15,104/120,754), and encompassed a total of 27 T cell subsets out of the 48 present in our reference (Fig 3.7b). Panels **a-c** were generated by Ashwini Patil.

Lastly, the spatial distribution of cell types annotated across Array-seq spots were correctly assigned to histological subregions of tissues. For example, in the cerebellar cortex of the brain, the Purkinje cell layer, which is ~100 µm or 10-cell thick in our sections, was accurately detected between the granular and molecular layers of this subregion of the brain (Fig 3.6b) (Bonnan et al., 2021). These observations were corroborated by the the spatial expression pattern of the marker gene *Calb1* which is expressed in Purkinje cells (Fig 3.8b-c). In thymus, the spatial assignment of cell types to spots reflected the known localization of T cells as they mature (Fig 3.8c). For example, immature, double positive (DP) thymocytes, which express *Rag1*, were found specifically in the thymic cortex, as expected based on prior knowledge (Fig 3.6b and Fig 3.8d) (Klein et al., 2014). Moreover, our data detected high levels of *Ccr9* and its chemokine ligand *Ccl25* in the cortex where DP thymocytes are found (Fig 3.8e). These observations matched known processes during the positive selection of thymocytes which are retained in the thymic cortex by CCL25 produced by cortical thymic epithelial cells (Klein et al., 2014). After positive selection, thymocytes decrease expression of *Ccr9* and increase *Ccr7*, leading them towards *Ccl21a*-expressing, medullary thymic epithelial cells prior to becoming single positive CD8 or CD4 thymocytes (Kozai et al., 2017). These processes were accurately captured by our spatial data (Fig 3.8e).

Taken together, our analyses yielded a body-wide map of the composition and localization of mouse cell types across histological regions that included fine layers of few cells in thickness. We also showed that integrating the spatial distribution of cell types and genes encoding intercellular signaling molecules such as chemokines enabled the reconstruction of functional cell-cell interactions in space.

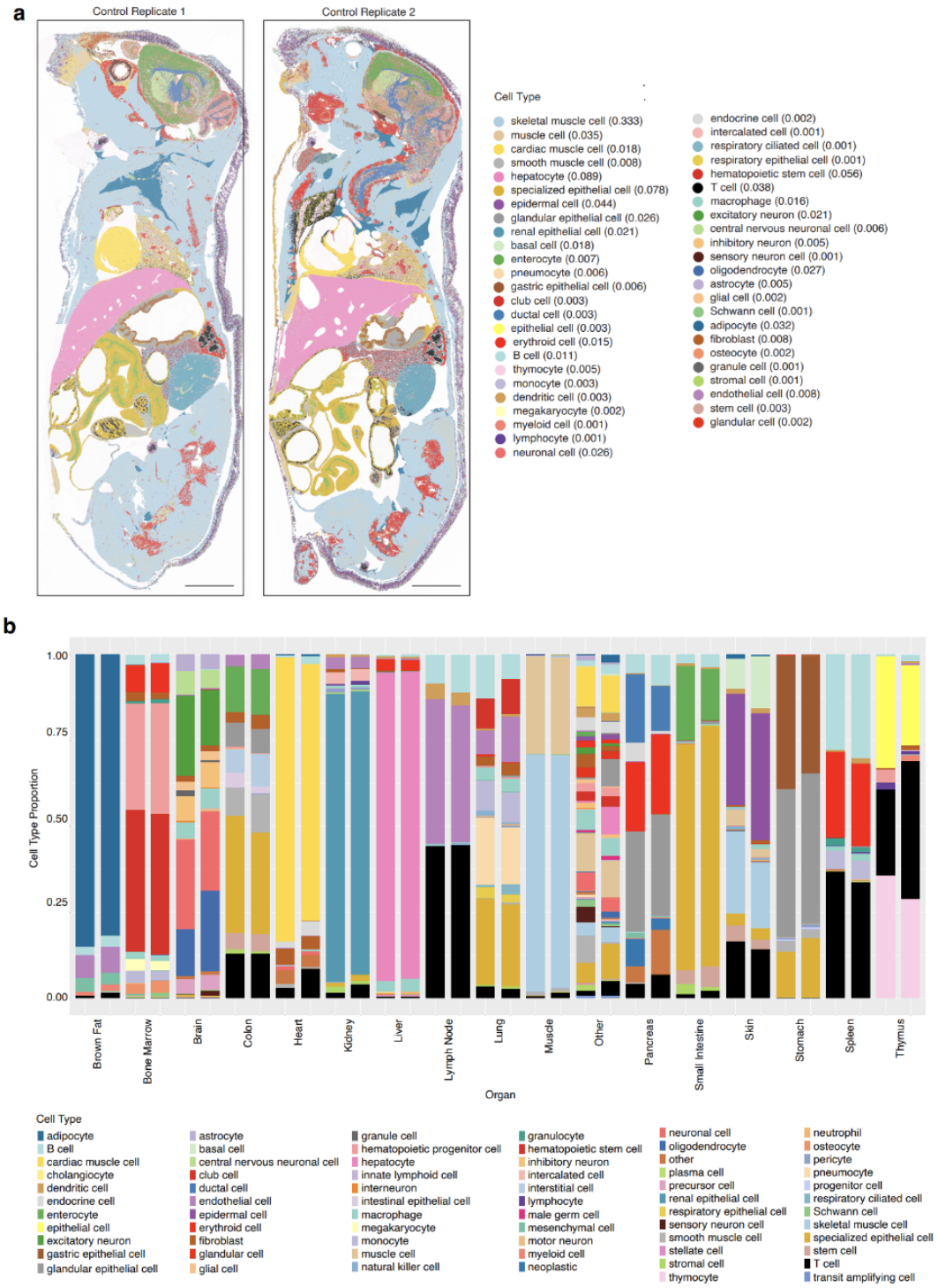


Figure 3.7: Reproducibility of organism-wide cell type annotation. a, Spatial plots of broad cell type annotation across two whole mouse replicates. **b,** Stacked bar plot of cell type proportion in each organ subset (x-axis) from two mouse replicates (left and right for each organ label). Scale bars: 5 mm. Panels **a-b** were generated by Ashwini Patil.

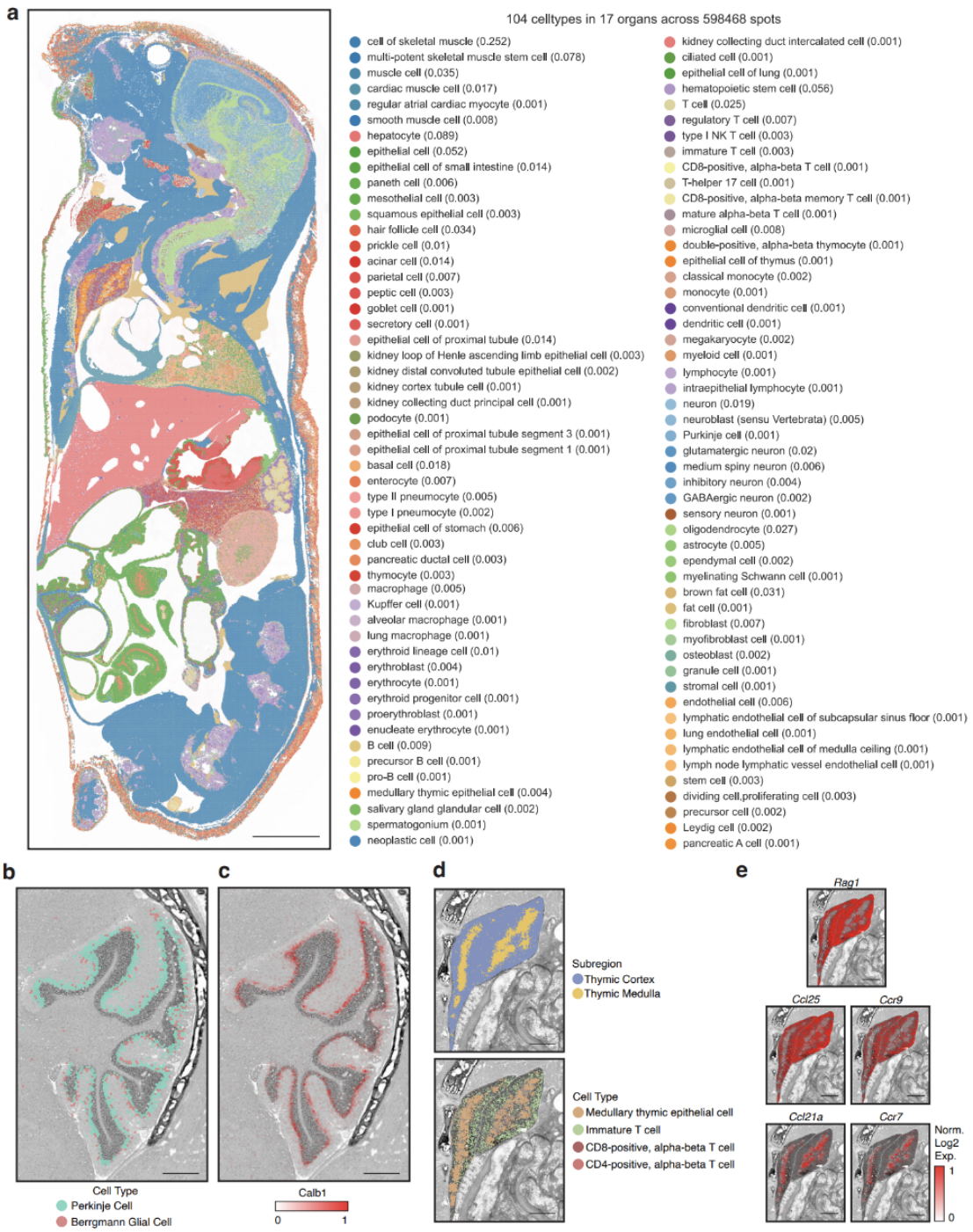


Figure 3.8: Specific cell type annotation of whole mouse sections. a, Spatial plots of specific cell type annotation across Array-seq whole mouse dataset. **b-c,** Spatial plots of mouse cerebellum annotated by (**b**) Purkinje cells and Bergmann glial cells, and (**c**) *Calb1* expression. **d-e,** Spatial plots of mouse thymus annotated by (**d**) subregion (top), select cell types (bottom), and (**e**) select marker genes. Scale bars: **a**, 5 mm; **b-e**, 1mm. Panel **a** was generated by Ashwini Patil.

3.4.4 Spatiomolecular mapping of systemic inflammation

We used our whole-mouse spatial profiling method to study the response to systemic inflammation using a mouse model of endotoxemia, whereby LPS is injected intra-peritoneally to mimic systemic bacterial inflammation (Fig 3.9a). We mapped the spatial transcriptomes of whole-mouse sections from mice injected with a sublethal dose of LPS (5 mg/kg) for 12 hours or left untreated as control (Takahama et al., 2024). Each mouse had been sectioned to capture similar histological regions and tissues across the body. We used unsupervised clustering of whole mouse sections followed by manual annotations to assign organ types across all four sections (Fig 3.10a). Moreover, we re-clustered each organ type independently to label tissue subregions across all four sections. We found both organs and subregions to be similarly represented across sections, suggesting that the datasets were suitable for differential expression analysis between identical anatomical sites of mice injected with LPS or left untreated as control (Fig 3.10a). We identified a total of 5,315 genes that were differentially regulated between LPS and control whole-mouse sections across 45 tissue subregions encompassing 16 organ types (Fig 3.9b). Next, we compared the genes identified as differentially expressed upon LPS injection by spatial transcriptomics to those found by whole-tissue, bulk RNA-seq. We found a strong correlation between bulk and spatial datasets in terms of the identify of LPS-regulated genes and the magnitude of the detected changes in expression across all 16 tissues tested (Fig 3.10b). Genes found to be differentially regulated in spatial but not bulk and vice versa were likely reflecting the intrinsic differences between the two measurement types and their respective statistical methods for the analysis of gene expression changes across samples and conditions (Methods).

We calculated the cell type composition across each of the Array-seq spots covering the control and LPS mouse sections (Methods). The tissue-level compositions and spatial distributions of cell types were broadly similar across control and LPS sections, although several differences could be detected across most if not all tissues (Fig 3.11a). Our data

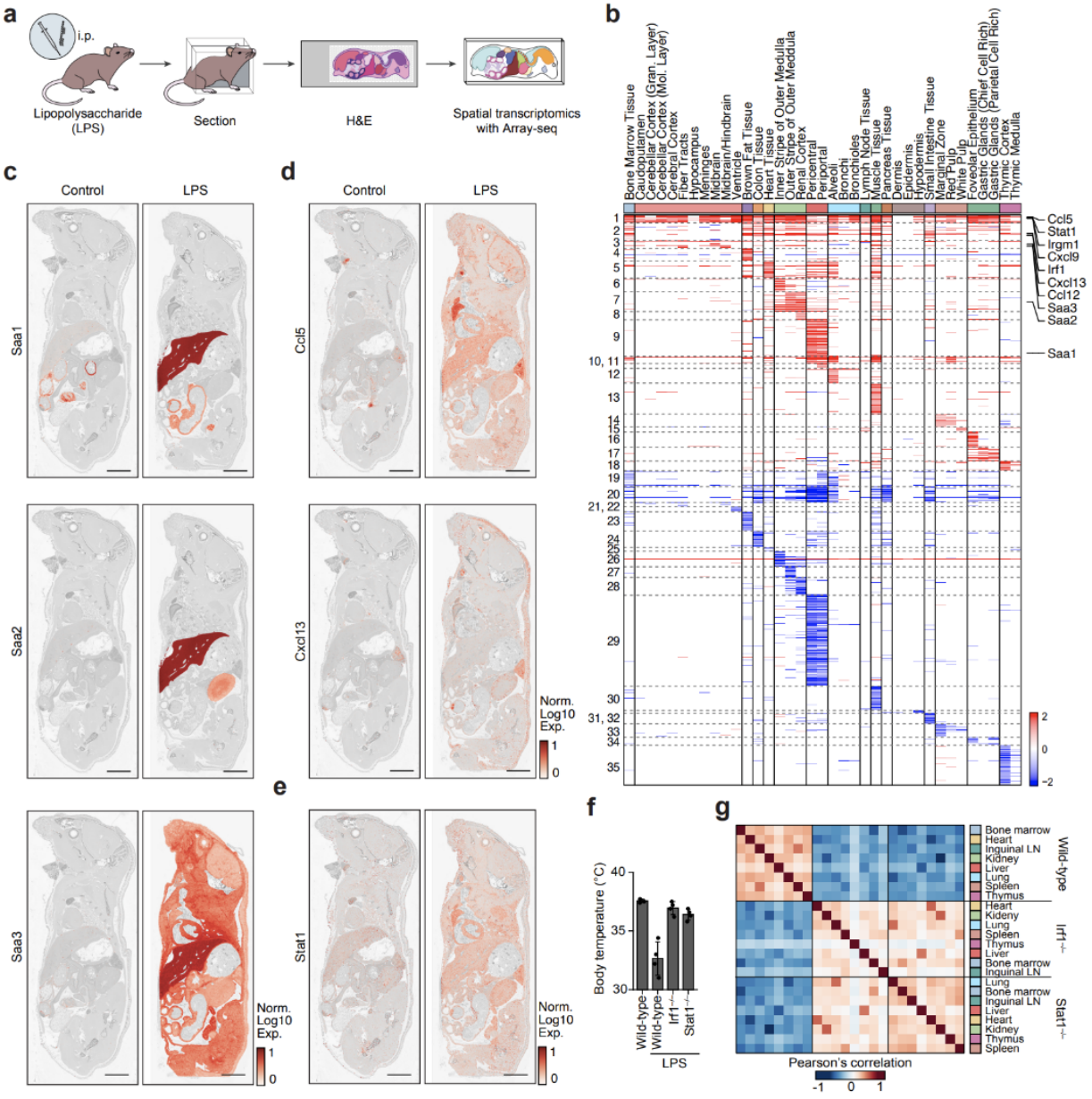


Figure 3.9: Organism-wide Array-seq analysis of a mouse endotoxemia model. **a,** Schematic overview of the experimental workflow for whole-mouse sectioning followed by large-format spatial transcriptomics. **b,** Heatmap of differentially expressed genes (rows) from spatial transcriptomic mRNA profiles ordered by k-means clustering (dashed lines) and organ (top, colors) and tissue subregion (top, label) at 12 hours after sublethal LPS injection. Values are log2 fold-changes relative to matching tissues from untreated mice (FDR-adjusted p-value < 0.01; n $= 2$). **c-e,** Spatial plots of a representative control (left) and LPS (right) of normalized log2 expression of (**c**) serum amyloid A genes (**d**) chemokine genes and (**e**) *Stat1*.

Figure 3.9: f, Measurements of rectal temperature in mice of indicated genotypes at 12 hours post-sublethal LPS injection (5 mg/kg) or in untreated controls. Error bars, SD (n = 4). **g,** Similarity (Pearson's correlation coefficient) between whole-tissue mRNA profiles from mice of indicated genotypes at 12 hours post-sublethal LPS injection (5 mg/kg). Scale bars, 5mm. The experiments shown in **f-g** were conducted, and the figures were generated, by Michihiro Takahama.

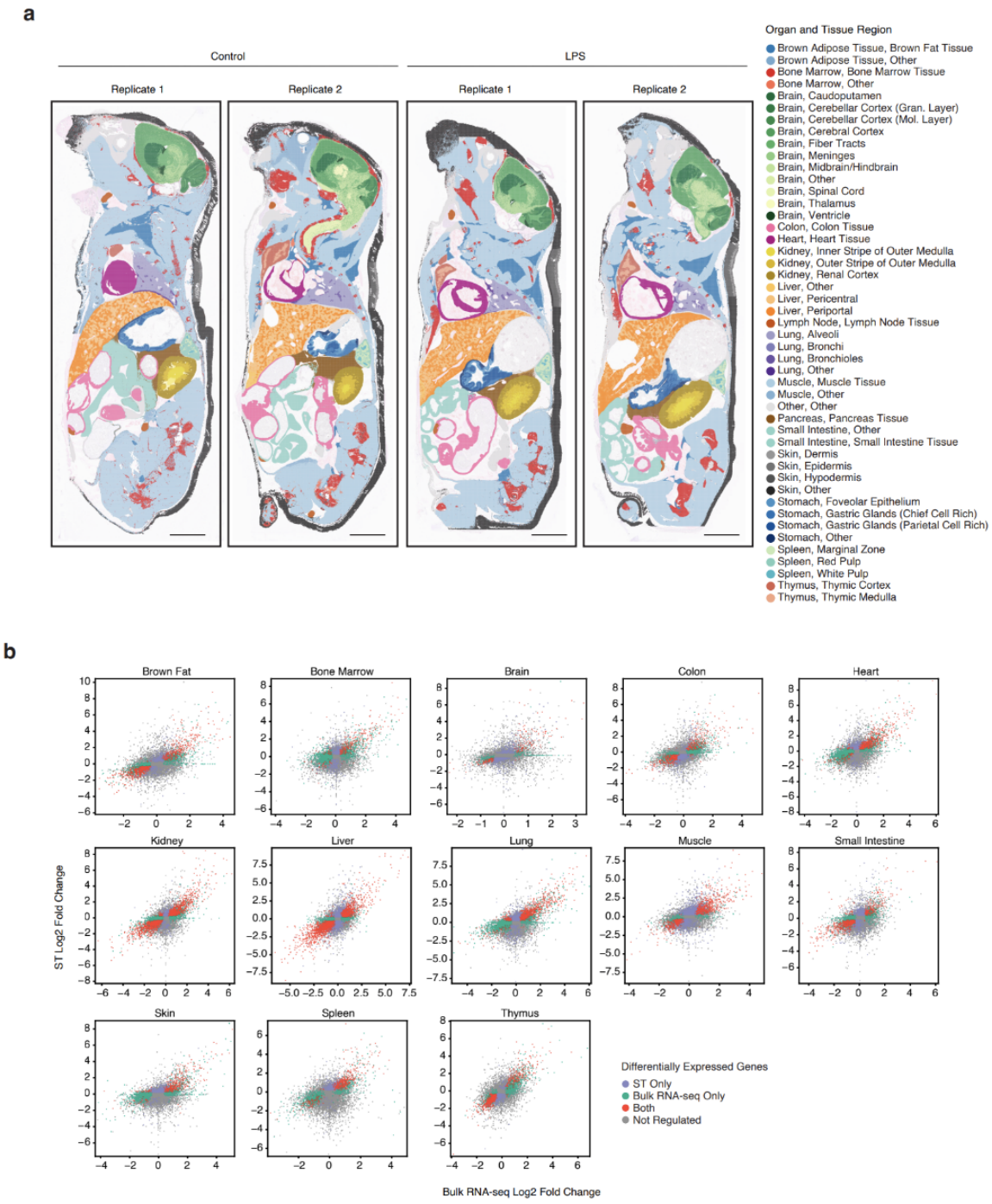


Figure 3.10: Agreement of LPS-induced gene expression changes in Array-seq and bulk RNA-seq. a, Spatial plots of organ annotation across two untreated and two LPS-treated whole mouse replicates.**b,** Log2 fold change of each gene in organ bulk RNA-seq (x-axis) and Array-seq pseudobulk (y-axis). Each gene is colored according to which dataset the gene was differentially expressed in LPS relative to control. Scale bars, 5 mm. Panel **a** was generated by Ashwini Patil.

also revealed previously unreported changes in the spatial distribution of immune cell types across the body during systemic inflammation such as a multi-tissue increase in mast cells (Fig 3.11b), which may help explain the negative effects of these cells in tissue injury (Cai et al., 2011). Non-hematopoietic cells displayed significant composition and spatial changes across various tissues, such as changes in epithelial and endothelial cell types of several tissues including lung, kidney liver, or brain (Fig 3.11c). We also observed several changes in hematopoietic cell types reflected known effects of endotoxemia on the body, such as a decrease in B lymphocytes, as shown by the expression of the *Cd79a* gene in spleen (Fig 3.11b-d). Concomitantly, the proportions of macrophages and neutrophils in the spleen increased as shown by the higher levels of their respective marker genes *Marco* and *S100a8* (Fig 3.11d-f).

Next, we examined the spatial expression of genes linked to systemic inflammation such as acute phase proteins, chemokines, and interferon-stimulated genes (ISGs). The expression of genes encoding serum amyloid A (SAA) protein 1, 2, and 3 – common biomarkers of systemic inflammatory conditions – were all strongly upregulated in the liver, while *Saa1* was also found in the gut, *Saa2* in kidney, and *Saa3* in virtually all tissues of the body (Fig 3.9c). Several chemokines also displayed spatially restricted expression patterns during endotoxemia, such as *Ccl5* and *Cxcl9* (broadly upregulated), *Ccl12* (brain only), and *Cxcl13* (mostly in the marginal zone of the spleen and the basal layer of the skin) (Fig 3.9d and Fig 3.12a-b). Lastly, we found several ISGs with spatially restricted or broadly distributed expression patterns upon LPS injection. For example, *Irgm1* was strongly induced in kidney and multiple other tissues, including liver, lung, or heart (Fig 3.12c), which may help explain the reported protective effects of this protein against LPS-induced shock (Bafica et al., 2007).

Furthermore, we examined the spatial expression patterns of transcription factors (TFs) involved in ISG regulation, namely Stat1 and Irf1. We focused on these two TFs because: (i) both TFs were widely upregulated across organs and tissue subregions albeit with some

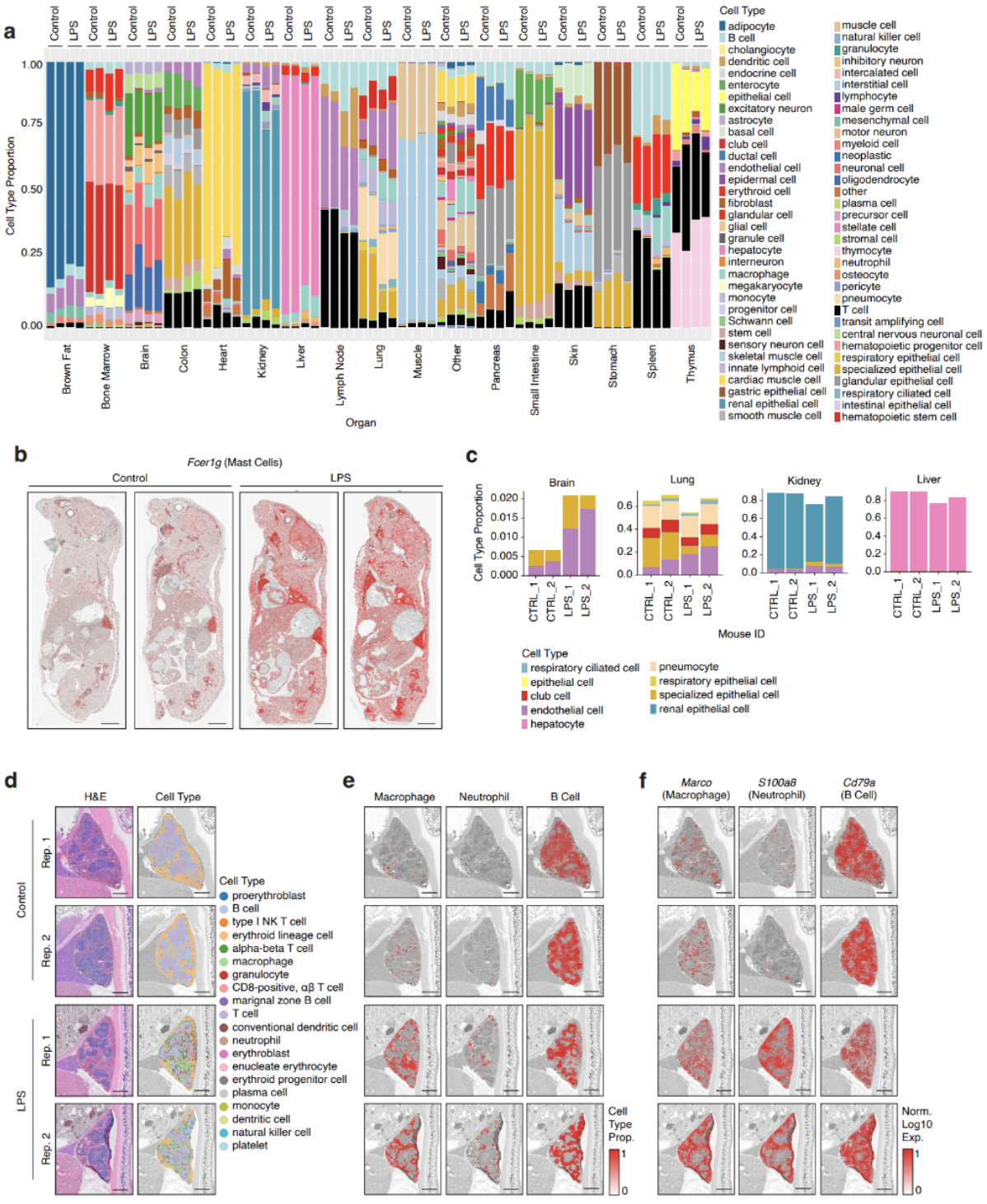


Figure 3.11: Cell type and gene expression changed in a mouse endotoxemia model. a, Stacked bar plot of cell type proportion in each organ subset (x-axis) from two control and two LPS mouse replicates (top x-axis label). **b,** Spatial plot of normalized log2-transformed counts of *Fcer1g*.

Figure 3.11: c, Stacked bar plot of annotated spot counts for endothelial and epithelial cell types in the brain, lung, kidney, and liver. **d-f,** Cell type and gene expression changes in the mouse spleen during sepsis. **d,** Zoom of H&E stained spleen (left) and cell type annotation (right) of control and LPS mouse replicates (rows). These spleen zooms were overlayed with spatial plots of (**e**) cell type proportion of macrophages, neutrophils, and B-cells, and (**f**) associated marker genes for cell types in **e**. Scale bars: **b**, 5 mm; **d-f**, 1 mm. Panel **a** was generated by Ashwini Patil.

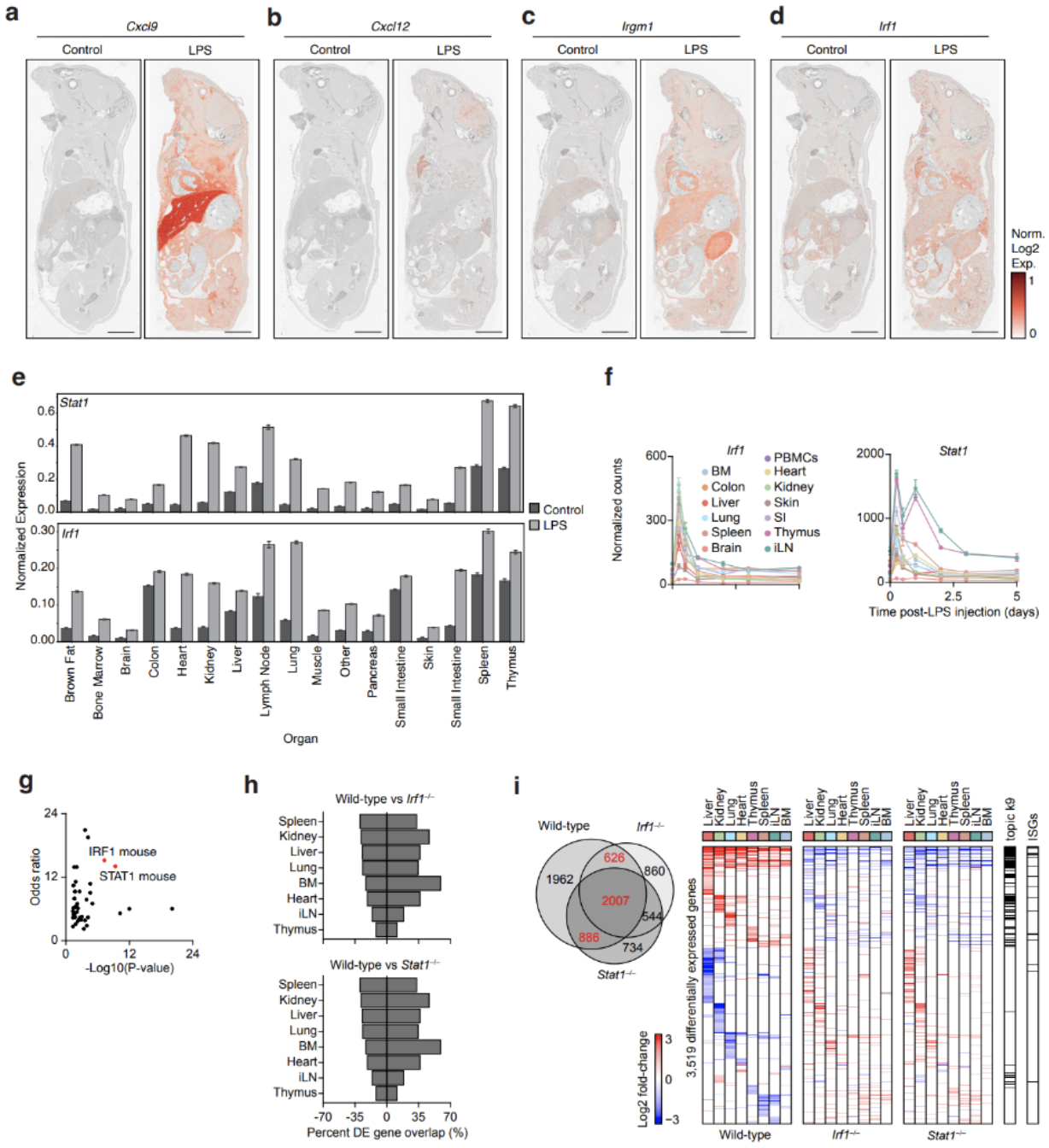


Figure 3.12: Analysis of transcription factor regulated gene expression changes during sepsis. a-d, Spatial plots of sepsis associated marker genes. **e,** Mean expression of log2 gene expression of Stat1 (top) and Irf1 (bottom) in Array-seq data. Data are shown as pooled replicate means (n=2) ± SEM of spot values. **f,** Bulk RNA-seq time-course expression of Irf1 and Stat1 in organs from LPS-injected mice. LN, lymph node; SI, small intestine. Means ± SEM are shown (n = 3-4). **g,** Plot of odds ratio and −Log10 P-value of enrichment of genes regulated by transcription factors.

Figure 3.12: h, Percent of differentially expressed in wild type (WT) treated with PBS and the indicated genotype mice treated with LPS relative to WT mice treated with LPS. Values were separated by upregulated (right) and downregulated (left) genes. **i,** Venn diagram (left) of differentially expressed genes in wild type (WT) treated with PBS and the indicated genotype mice treated with LPS relative to WT mice treated with LPS. Heatmap (right) of differentially expressed genes (rows) from whole-tissue mRNA profiles ordered organ types (top, colors) at 12 hours after sublethal LPS injection (left), and indicated genotypes treated with LPS relative to 12 hours after sublethal LPS injection (middle, right) with annotations of interferon stimulated genes (right, black annotation). Values are log2 fold-changes relative to matching organs from untreated controls for wild-type (FDR-adjusted p-value < 0.01, absolute fold change > 2; n $= 4$). P < 0.05 (*). Scale bars, 5 mm. The experiments shown in **f-i** were conducted, and the figures were generated, by Michihiro Takahama.

differences in tissue specificities (Fig 3.9e and Fig 3.12e-f); (ii) they were predicted computationally to be the TFs regulating the ISGs regulated in our data (Fig 3.12g); and (iii) even though they are well-known regulators of ISGs (Bonelli et al., 2019; Hu et al., 2021), the target genes of these two TFs across tissues have not been mapped. To test the functional roles of these two TFs in endotoxemia, we injected a sublethal dose of LPS into Irf1$^{-/-}$ and Stat1$^{-/-}$ mice. We found that LPS did not lead to a decrease in body temperature in Irf1$^{-/-}$ and Stat1$^{-/-}$ mice as seen in wild-type mice (Fig 3.9f), in agreement with published data (Fu and Wang, 2023; Zhang et al., 2024). Moreover, genetic deletions of Irf1 and Stat1 abrogated the organism-wide ISG response driven by LPS (Fig 3.9g and Fig 3.12h-i). The LPS-induced genes regulated by IRF1 and STAT1 across organs overlapped for the most part, although some tissue-specific effects were also observed, such as in liver, kidney, and lung (Fig 3.12i). Thus, our results demonstrated that whole-body profiling enables the detailed spatial analysis of the molecular and cellular changes driving systemic inflammatory processes.

3.4.5 Whole-mouse spatial profiling reveals PLA2G5 as a harmful factor in sepsis

We asked if the spatiomolecular profiles from whole-mouse sections could identify novel regulators of systemic inflammation. After examining the spatial expression patterns of proteins known to be secreted and upregulated by LPS in non-lymphoid tissues, we focused on the secreted phospholipase PLA2G5. We found *Pla2g5* transcripts to be significantly upregulated in the colon and small intestine and downregulated in the heart and spleen at 12 hours post-LPS injection (Fig 3.13a-b). To identify the cell types in which Pla2g5 mRNAs were upregulated in the gut, we used the CARD deconvolution method (Ma and Zhou, 2022) with publicly available mouse tissue single-cell RNA-seq data (Consortium, 2020) as a reference to estimate the cell-type composition for each spot of the arrays used for spatial

transcriptomics profiling. Our analysis identified colon goblet cells and secretory cells as the cell types in which the expression of the *Pla2g5* gene is upregulated during endotoxemia (Fig 3.14a-b). *Pla2g5* was strongly upregulated in the colon and small intestine within 6 to 12 hours post-LPS injection and returned to baseline within 2 to 3 days (Fig 3.13c and Fig 3.15a). In addition, heart and spleen *Pla2g5* mRNA levels were downregulated upon LPS injection and returned to control levels by day 5 post-sepsis induction (Fig 3.15a). In steady state conditions, heart and spleen were the two tissues with the highest levels of *Pla2g5* gene expression out of 17 tissue types profiled using both whole-mouse spatial transcriptomics (Fig 3.13a-b) and whole-tissue RNA-seq (Fig 3.15b). Notably, *Pla2g5* mRNA levels were also upregulated in the colon after cecal ligation and puncture (CLP) (Fig 3.15c), which is considered the gold standard model for sepsis due to its high clinical relevance (Rittirsch et al., 2009; Sjaastad et al., 2020).

Next, to test if PLA2G5 plays a role in the pathogenesis of endotoxemia and CLP sepsis, we first injected mice with PLA2G5-neutralizing or isotype control antibodies 1 hour prior to a challenge with a lethal dose of LPS. We found that neutralization of PLA2G5 with antibodies (Muñoz et al., 2000) significantly increased survival and prevented body temperature loss upon lethal LPS challenge (Fig 3.13d and Fig 3.15d). Second, we found that Pla2g5$^{-/-}$ mice did not exhibit a significant loss in body temperature and survived both lethal LPS and CLP sepsis challenges whereas their wild-type counterparts did not (Fig 3.13e-f and Fig 3.15e-f). Moreover, we found that both genetic deletion and neutralization of PLA2G5 led to a decrease in the serum levels of renal, liver, and cardiac injury markers – blood urea nitrogen (BUN), alanine aminotransferase (ALT), and troponin I, respectively – during sepsis (Fig 3.13g and Fig 3.15g). We did not observe differences in other systemic metabolic parameters such as blood glucose, triglyceride, and cholesterol levels upon PLA2G5 blockade during sepsis (Fig 3.15h). Lastly, both genetic deletion and neutralization of PLA2G5 led to decreased signs of histopathology in kidney, liver, heart and lung tissues during sepsis (Fig

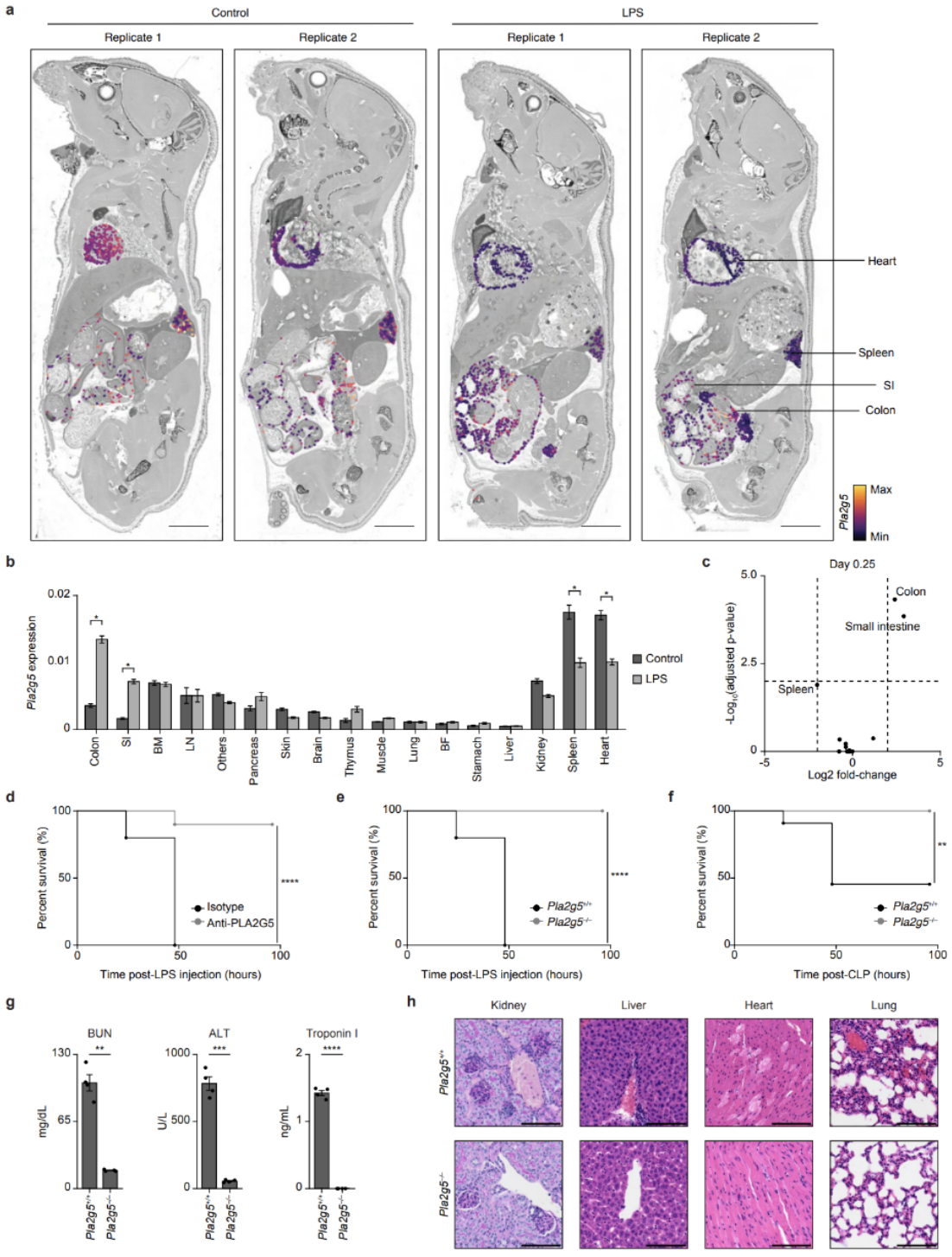


Figure 3.13: Identification of PLA2G5 as a harmful factor in sepsis. a, Spatial plot of Pla2g5 overlaid on a greyscale H&E staining. Shown are whole-mount sections and ST data from 5-weeks old mice injected with a sublethal dose of LPS (5 mg/kg) or left untreated as control. BF, brown fat; LN, lymph node; BM, bone marrow.

Figure 3.13: b, Average expression of Pla2g5 across all ST array spots covering indicated tissues sampled in sections from A and B. Means ± SEM are shown. **c,** Volcano plot for Pla2g5 expression at 6 hours post-LPS injection across all 12 organs (circles) from **a**. (This is from the time course plots of expression of *pla2g5* in the different organs) **d-f,** Survival curves of mice upon LPS (**d-e**) or CLP (**f**) sepsis using PLA2G5 neutralizing or mouse IgG1 isotype control antibodies (Isotype) (**d**) or indicated mouse genotypes (**e-f**) (n = 10-11) **g,** Serum levels of indicated organ injury markers at 24 hours post-injection of LPS in indicated mouse genotypes. Means ± SEM are shown (n = 4-5). **h,** Histological analysis of kidney (PAS staining) and liver, heart, and lungs (H&E staining) at 24 hours post-sublethal LPS injection from Pla2g5$^{+/+}$ (top) or Pla2g5$^{-/-}$ (bottom) mice. Scale bars, 100 µm. The experiments shown in **c-h** were conducted, and the figures were generated, by Michihiro Takahama.

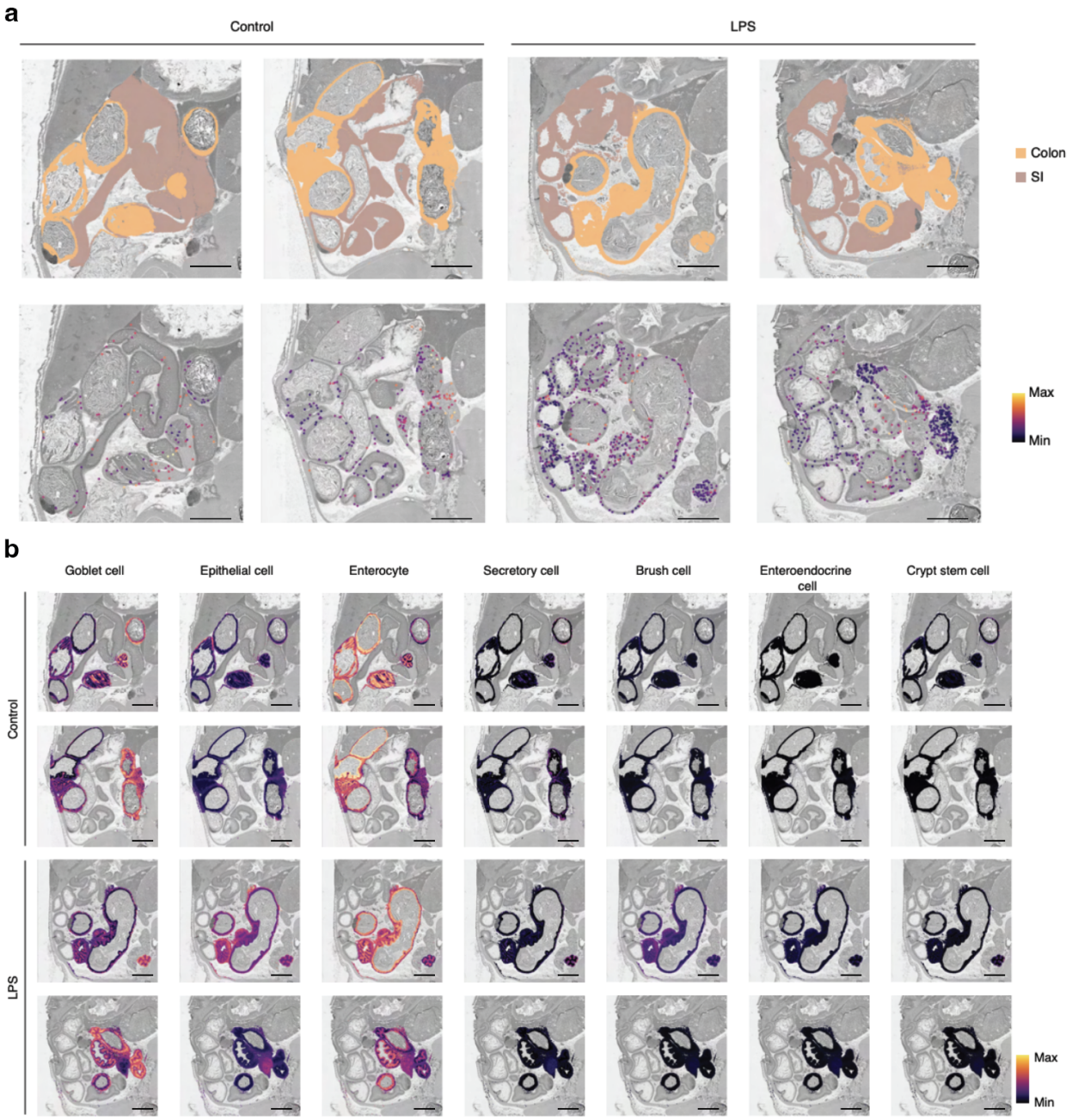


Figure 3.14: Spatial transcriptomics analysis of *Pla2g5* in the gut. a, Whole-mouse spatial transcriptomics data from control and LPS conditions (columns) were magnified to only show colon (brown) and small intestine (SI, yellow) tissues (top) and *Pla2g5* normalized expression (bottom) overlaid on a greyscale H&E image. **b,** Cell type deconvolution analysis of each ST spot data for indicated colon cell types (top) across control and LPS conditions (rows). Scale bars, 2.5 mm.

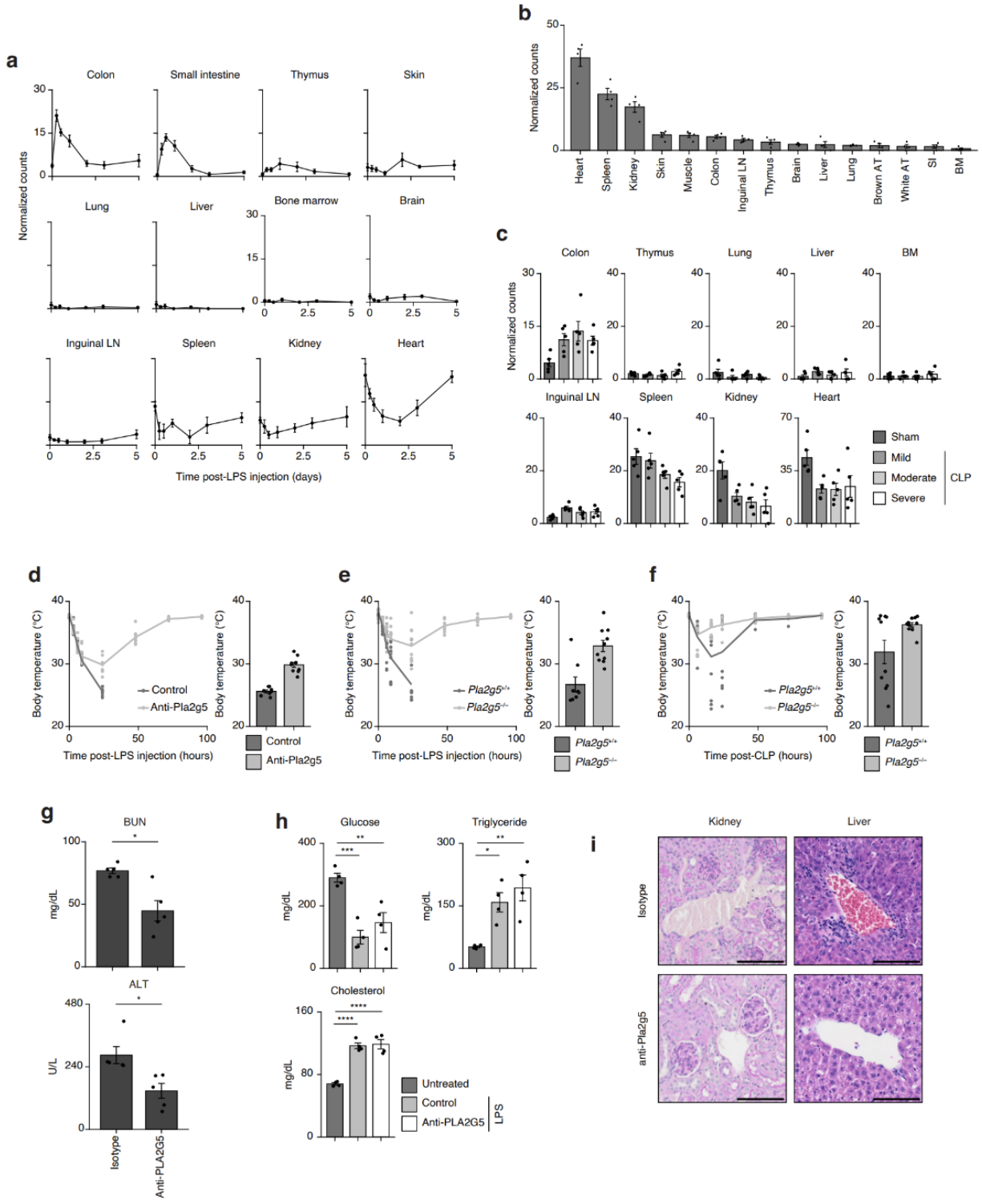


Figure 3.15: Blocking PLA2G5 rescues mice from sepsis. a, Normalized counts for *Pla2g5* from indicated organs in LPS sepsis. LN, lymph node. Means ± SEM are shown (n = 3-4).

Figure 3.15: **b,** Basal whole-tissue gene expression of Pla2g5 mRNAs across 15 tissues. Shown are normalized counts for Pla2g5 from indicated organs in naive mice. LN, lymph node; AT, adipose tissue; SI, small intestine; BM, bone marrow. Data are shown as means ± SEM (n = 4). **c,** Normalized counts for Pla2g5 from indicated organs at 16 hours post-surgery across the three indicated severity grades (mild, moderate, severe) of cecal ligation and puncture (CLP) sepsis. LN, lymph node. Means ± SEM are shown (n = 5). **d-f,** Measurements of rectal temperature in mice upon LPS (**d-e**) or cecal ligation and puncture (CLP, **f**) sepsis using anti-PLA2G5 neutralizing antibodies (**d**) or indicated mouse genotypes (**e-f**). Data are representative of three independent experiments. **g,** Serum levels of indicated organ injury markers at 24 hours post-injection of LPS in the presence PLA2G5 neutralizing or mouse IgG1 isotype control antibodies (Isotype). Means ± SEM are shown (n = 4-5). **h,** Serum levels of indicated metabolites before (untreated) and 24 hours post-injection with a sublethal LPS dose in the presence or absence of Pla2g5 blockade. Data are representative of two independent experiments and shown as means ± SEM (n = 4). *, $P < 0.05$; **, $P < 0.01$; ***, $P < 0.001$; and ****, $P < 0.0001$ by one-way ANOVA with Tukey-Kramer test. i, Histological analysis of kidney (PAS staining) and lungs (H&E staining) at 24 hours post-sublethal LPS injection from mice treated with PLA2G5 neutralizing (bottom) or mouse IgG1 isotype control (top) antibodies. Scale bars, 100 µm. The experiments shown in **a-i** were conducted, and the figures were generated, by Michihiro Takahama.

3.13h and Fig 3.15i). Thus, our results suggested that PLA2G5 regulates tissue damage and survival during LPS and CLP sepsis.

3.4.6 Organism-wide analysis reveals PLA2G5's role red blood cell homeostasis during sepsis

To investigate the mechanisms underlying the net, harmful effects of PLA2G5 during sepsis, we first measured the serum levels of TNF-α, IL-6, IL-12, IL-18, and IL-10 during LPS sepsis and found no difference between PLA2G5-deficient and wild-type mice (Fig 3.16a). Second, using lipidomics on colon tissues, we found that the levels of all the lipid metabolites tested showed little to no changes upon PLA2G5 blockade except for resolvin D2 (RvD2), which was downregulated upon PLA2G5 blockade in LPS-treated mice Fig 3.16b-l). Therefore, the role of PLA2G5 in sepsis appeared to be independent of systemic cytokine dysregulation or the lipolytic activities of the enzyme in colon tissue where it is induced during LPS and CLP sepsis. To yield clues about PLA2G5's mechanism of action in sepsis, we measured changes in whole-tissue gene expression levels in mice upon LPS injection with or without PLA2G5 antibody neutralization across 12 organs (bone marrow, brain, colon, heart, inguinal lymph node, kidney liver, lung, skin, small intestine, spleen, and thymus) (Fig 3.17a). By performing pathway enrichment analysis on these whole tissue expression profiles, we observed a link between PLA2G5 blockade and changes in pathways related to splenic macrophages and iron homeostasis (Fig 3.17). Since it is well-established that splenic red pulp macrophages play a role in red blood cell recycling and iron homeostasis (Muñoz et al., 2000), it prompted us to explore the potential effects of PLA2G5 on these processes. By mining our whole-tissue gene expression profiles, we found that several genes linked to splenic red pulp macrophages, such as *Spic*, *Hmox1*, and *Vcam1* (Kohyama et al., 2009), were upregulated upon PLA2G5 blockade in LPS-injected mice (Fig 3.17b), suggesting that PLA2G5 impacts the abundance of these splenic cells. Furthermore, the increase in splenic red pulp macrophages during

sepsis upon PLA2G5 blockade was associated with a decrease in Prussian blue staining of ferric iron in the spleen (Fig 3.17c).

These observations led us to hypothesize that PLA2G5 may impact red blood cells because of the effects of PLA2G5 blockade on splenic red pulp macrophages and iron stores. To test this, we first asked if PLA2G5 could directly lyse red blood cells (RBCs) using an in vitro assay whereby recombinant PLA2G5 protein (rPLA2G5) was mixed with mouse RBCs. rPLA2G5 led to increased RBC lysis in a dose-dependent manner in vitro upon treatment with $Ca2^{+}$ and a calcium ionophore, which damages the plasma membrane of RBCs by disrupting the distribution of phospholipids (Fig 3.17a-b). Furthermore, the hemolytic effects of rPLA2G5 were dependent on its phospholipase activity as shown by adding varespladib, a broad inhibitor of secreted PLA2 enzymes, in our in vitro hemolytic assay (Fig 3.17c). Next, we examined the effect of osmotic pressure on the hemolysis induced by rPLA2G5. The exposure of RBCs to hypertonic conditions inhibited hemolysis mediated by rPLA2G5 while the exposure to hypotonic conditions promoted hemolysis, indicating that osmotic pressure affected the hemolytic activity of rPLA2G5 (Fig 3.17d). To elucidate how PLA2G5 affected RBC membranes at the molecular level during hemolysis, we performed lipidomics on erythrocytes in the presence or absence of rPLA2G5 in vitro. We found that rPLA2G5 led to the release of lysophospholipids with saturation and lower degrees of unsaturation and fatty acids from RBC membranes in our in vitro hemolysis assay (Fig 3.17e-f). Taken together, our data suggested that PLA2G5 hydrolyzed several phospholipids of damaged erythrocyte membranes, which led to hemolysis through osmotic pressure changes in RBCs.

3.4.7 PLA2G5 acts as a self-venom during sepsis by mediating intravascular hemolysis

Next, we sought to test if PLA2G5 impacted red blood cells in vivo during sepsis. We measured the plasma levels of heme, a degradation product of cell-free hemoglobin, in $Pla2g5^{+/+}$

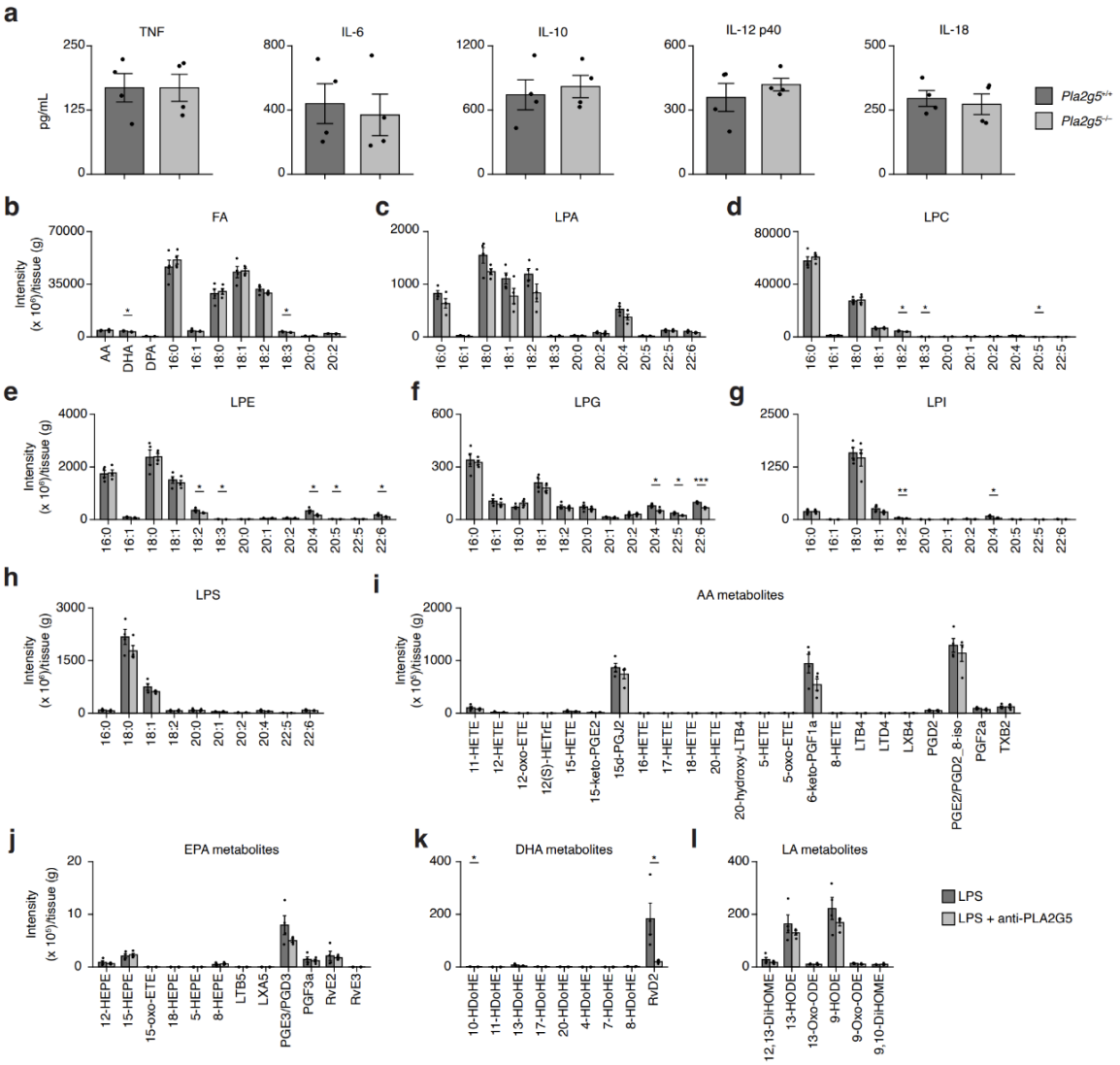


Figure 3.16: Impact of PLA2G5 on serum cytokine and lipid levels during sepsis. a, Serum levels of indicated cytokines in Pla2g5$^{+/+}$ or Pla2g5$^{-/-}$ mice at 24 hours after LPS injection. Data are shown as means ± SEM (n = 4) and representative of two independent experiments. **b-l**, Lipidomics profiling in colon tissues from mice after 12 hours post-sublethal LPS injection and pre-treated with anti-Pla2g5 neutralizing antibodies or left untreated. Shown are mass spectrometry intensities for indicated lipid metabolites: FA, fatty acid; LPA, lysophosphatidic acid; LPC, lysophosphatidylcholine; LPE, lysophosphatidylethanolamine; LPG, lysophosphatidylglycerol; LPI, lysophosphatidylinositol; LPS, lysophosphatidylserine; AA, arachidonic acid; DPA, docosapentaenoic acid; EPA, eicosapentaenoic acid; DHA, docosahexaenoic acid; LA, linoleic acid, metabolites; AA, arachidonic acid; PGE2/PGD2_8-iso, PGE2/PGD2_8-iso-PGA2. Means ± SEM are shown (n = 4). *, $P < 0.05$; **, $P < 0.01$; ***, $P < 0.001$ by Student's t test. The experiments shown in **a-l** were conducted, and the figures were generated, by Michihiro Takahama.

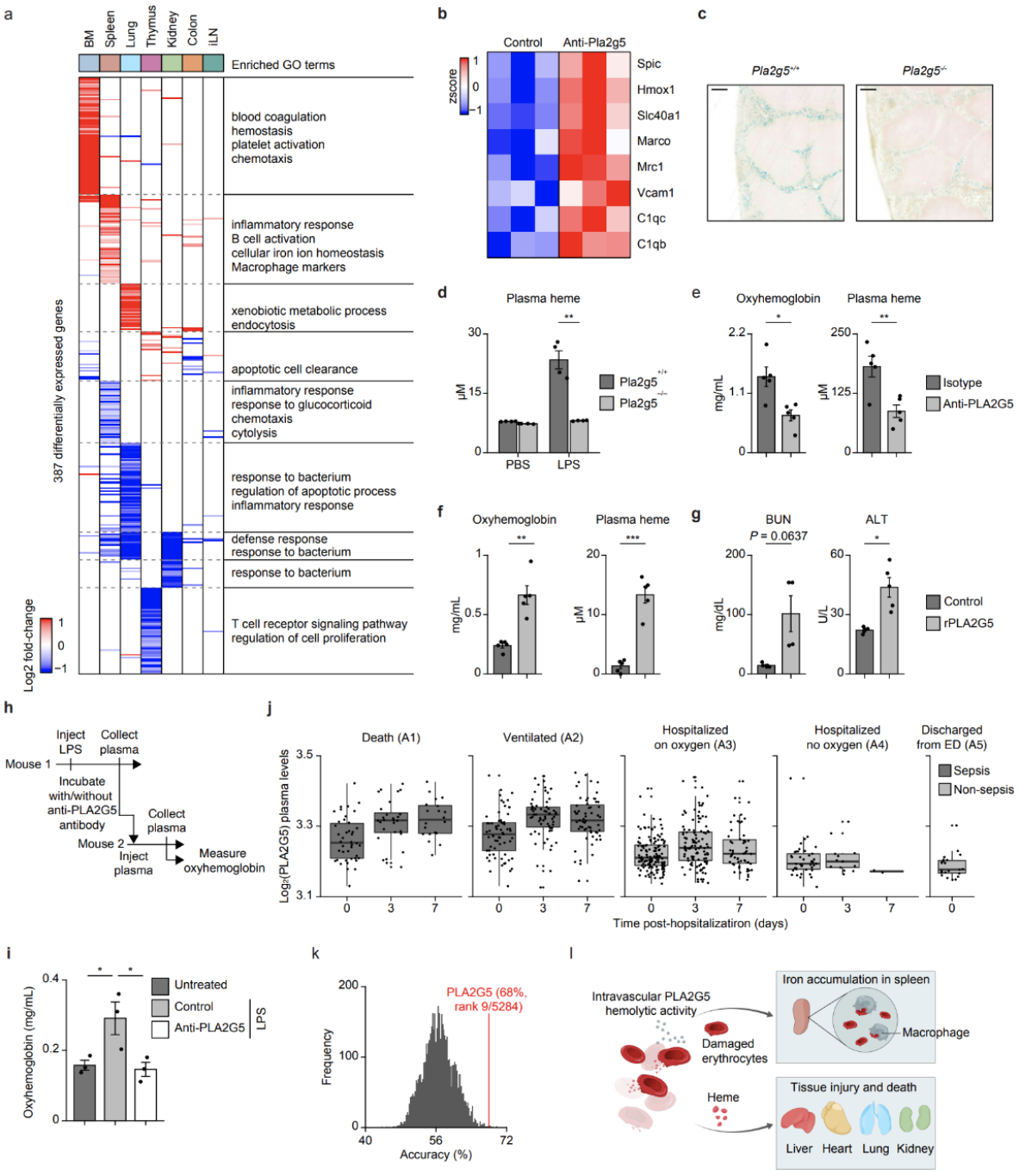


Figure 3.17: PLA2G5 induces intravascular hemolysis during sepsis. a, Heatmap of differentially expressed genes (rows) from whole-tissue mRNA profiles ordered by k-means clustering (dashed lines) and organ types (top, colors) at 12 hours after sublethal LPS injection and anti-PLA2G5 antibody pre-treatment. Values are log2 fold-changes relative to matching tissues from LPS-treated mice without antibody blockade (FDR-adjusted p-value < 0.01; n = 3-4). Representative enriched Gene Ontology (GO) terms within each cluster are indicated on the right (p-value < 0.05).

Figure 3.17: **b,** Heatmap of gene expression levels for genes related to splenic red pulp macrophage (rows) from whole-spleen mRNA profiles at 12 hours after sublethal LPS injection with or without anti-PLA2G5 antibody pre-treatment (columns). Values are normalized counts scaled by row (n = 3). **c,** Images of Prussian blue staining for ferric iron on spleen histological sections from LPSinjected Pla2g5$^{+/+}$ (top) or Pla2g5$^{-/-}$ (bottom) mice. Images are representative of two independent experiments. **d,** Plasma heme concentrations in Pla2g5$^{+/+}$ or Pla2g5$^{-/-}$ mice 24 hours post-sub-lethal LPS or PBS (control) injections. Means ± SEM are shown (n = 4). **e,** Plasma concentration of oxyhemoglobin and heme in mice 12 hours post-lethal LPS injection and pre-treated with anti-PLA2G5 neutralizing antibodies or isotype control. Means ± SEM are shown (n = 5). **f-g,** Plasma concentration of oxyhemoglobin and heme (**f**) and serum levels of BUN and ALT (**g**) in mice injected with recombinant PLA2G5 (rPLA2G5) or saline only (Control). Means ± SEM are shown (n = 4-5). **h-i,** Plasma oxyhemoglobin levels in mice injected with plasma which were collected from LPS or PBS (Control)-injected mice and incubated in vitro with anti-PLA2G5 neutralizing antibodies for 4 hours at 4°C prior to transfer into naive mice. Means ± SEM are shown (n = 3). **j,** Box plots depicting Log2 relative fluorescence units of PLA2G5 level in plasma of patients with COVID-19 by severity over time (Methods). Patients were classified by acuity levels based on the World Health Organization (WHO) Ordinal Outcomes Scale. Acuity levels were determined by their severity condition within 28 days post-enrollment as follows: A1, death within 28 days; A2, intubation, mechanical ventilation; A3, hospitalized and requiring supplemental oxygen; A4, hospitalized without requiring supplemental oxygen; and A5, discharged directly from the Emergency Department without subsequently returning and requiring admission within 28 days. Median and interquartile range (IQR) of Sequential Organ Failure Assessment (SOFA) score for each acuity levels are 8 and 5-10 (A1); 7 and 6-9 (A2); 1 and 0-3 (A3); 0 and 0-1 (A4); 1 and 0-1 (A5). A1 and A2 were classified as sepsis (dark grey) and A3-A5 as non-sepsis (light grey). **k,** Distribution of accuracy values from a decision tree classifier analysis using PLA2G5 plasma levels at day 0 from sepsis and non-sepsis patient groups (data from panel H). Data are representative of two to three independent experiments (A-D, F, and H). *, $P < 0.05$; **, $P < 0.01$; ***, $P < 0.001$ by one-way ANOVA with Tukey-Kramer test or Student's t test. **l,** PLA2G5 causes intravascular hemolysis through its lipolytic activity on select phospholipids of erythrocyte membranes. Damaged erythrocytes are captured by splenic macrophages, leading to iron accumulation in spleen, and the degradation products from erythrocytes, such as heme, lead to toxic effects for tissues. Scale bars, 200 µm. The experiments shown in **a-l** were conducted, and the figures were generated, by Michihiro Takahama.

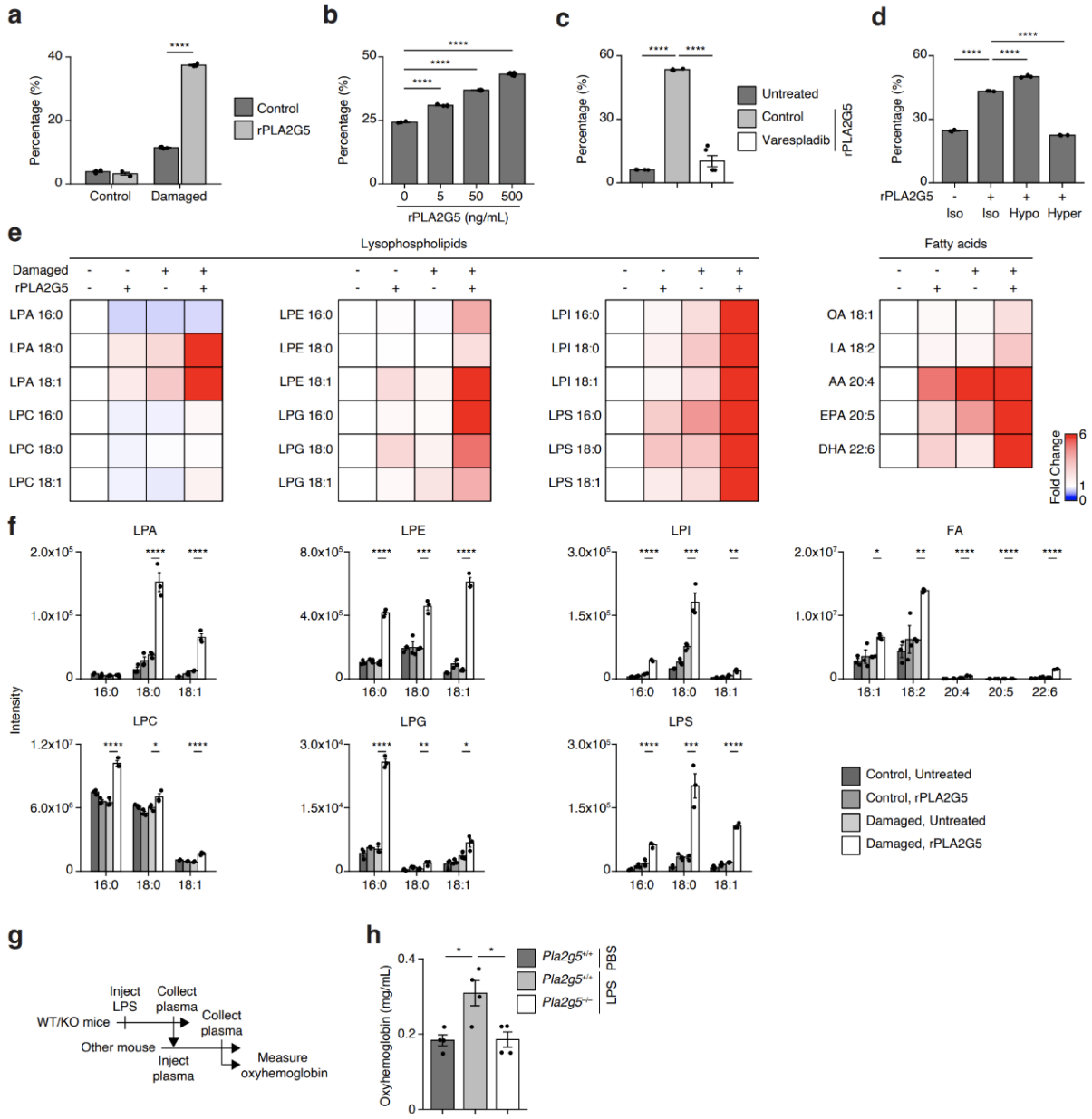


Figure 3.18: PLA2G5 hydrolyzes phospholipids of damaged erythrocyte membranes. a-d, In vitro hemolysis assay. Shown are percentages of cell-free oxyhemoglobin (relative to an equal volume of chemically lysed erythrocytes) in cell lysates from normal (Control) or phosphatidylserine (PS)-exposing (Damaged) erythrocytes incubated with recombinant PLA2G5 (rPLA2G5) or BSA for 1 hour at 37°C (**a**), PS-exposing erythrocytes incubated with indicated concentrations of rPLA2G5 for 1 hour at 37°C (**b**), PS-exposing erythrocytes incubated with rPLA2G5 in the presence or absence of the secreted phospholipase A2 inhibitor Varespladib or left untreated (control) (**c**), or PS-exposing erythrocytes incubated with rPLA2G5 in isotonic, hypotonic, or hypertonic solution (**d**). Means ± SEM are shown (n = 4). Data are representative of three independent experiments.

Figure 3.18: e-f, Lipidomics profiling of normal or PS-exposing erythrocytes incubated with rPLA2G5 for 1 hour at 37°C. Shown are fold-changes relative to normal erythrocytes (**e**) and mass spectrometry intensities (**f**) for indicated lipid metabolites. LPA, lysophosphatidic acid; LPC, lysophosphatidylcholine; LPE, lysophosphatidylethanolamine; LPG, lysophosphatidylglycerol; LPI, lysophosphatidylinositol; LPS, lysophosphatidylserine; OA, oleic acid; LA, linoleic acid; AA, arachidonic acid; EPA, eicosapentaenoic acid; DHA, docosahexaenoic acid. Means ± SEM are shown (n = 3). **g-h,** Plasma oxyhemoglobin levels in mice injected with plasma collected from LPS-injected $Pla2g5^{+/+}$ or $Pla2g5^{-/-}$ mice or PBS-injected $Pla2g5^{+/+}$ mice as control. Means ± SEM are shown (n = 4). *, $P < 0.05$; **, $P < 0.01$; ***, $P < 0.001$; ****, $P < 0.0001$ by one-way ANOVA with Tukey-Kramer test or Student's t test. The experiments shown in **a-h** were conducted, and the figures were generated, by Michihiro Takahama.

and Pla2g5$^{-/-}$ mice challenged with LPS. We found a significant decrease in the plasma levels of heme in Pla2g5-deficient mice compared to wild type (Fig 3.17d). Moreover, PLA2G5 neutralization also inhibited the elevation of the plasma levels of oxyhemoglobin and heme in mice injected with lethal dose of LPS (Fig 3.17e). We next asked if PLA2G5 would be sufficient to induce intravascular hemolysis in vivo by injecting rPLA2G5 in naïve mice. We found that the intravenous injection of rPLA2G5 in mice was sufficient to elevate the plasma levels of oxyhemoglobin and heme (Fig 3.17f) and the serum levels of BUN and ALT (Fig 3.17g) well above their physiological range of expression. Going further, to test if PLA2G5 was present in the blood circulation and led to intravascular hemolysis in vivo during sepsis, we performed plasma transfer experiments using donor plasma from wild-type and Pla2g5$^{-/-}$ mice treated with LPS. Donor plasma samples from wild-type mice injected with LPS were incubated with anti-PLA2G5 or isotype control antibodies ex vivo prior to plasma transfer into naive mice. Donor plasma samples from Pla2g5$^{-/-}$ mice injected with LPS were directly injected into naive, wild-type mice. We found that plasma from LPS-injected, wild-type mice led an increase in hemolysis in naive mice, whereas plasma from PLA2G5 knockout or blockade did not (Fig 3.17h-i and Fig 3.17g-h). Lastly, we asked if PLA2G5 could be found in the blood circulation of sepsis patients by mining publicly available plasma proteomic data from patients that match the clinical definition of sepsis (Singer et al., 2016). Using published blood proteomics data from COVID-19 patients35, we found that the plasma levels of PLA2G5 were significantly upregulated in patients with COVID-19-induced sepsis compared to milder, non-sepsis cases (Fig 3.17j), which was predictive of patient survival with high accuracy compared to all other analytes measured in plasma (rank 9 in prediction accuracy for PLA2G5 out of a total of 5,284 proteins measured) (Fig 3.17k). Overall, our results support a model whereby the release of PLA2G5 into the systemic circulation during sepsis leads to intravascular hemolysis and a concurrent increase in the blood levels of heme, a known inducer of multi-tissue injury (Fig 3.17l).

3.5 Discussion

While the mouse is a key research model to study biology and disease, our knowledge about the spatial expression of mouse genes across all cell types and tissue regions of the body is lacking. To address this fundamental challenge, we created tools enabling the body-wide phenotyping of mice at the molecular and cellular levels. Specifically, we obtained spatiotranscriptomics maps of whole-mouse sections of 10 µm in diameter covering ~5M nuclei across more than 16 organ types. Using a mouse model of endotoxemia, we generated organism-wide spatial transcriptomics data upon LPS injection, which revealed the spatio-molecular and -cellular effects of systemic inflammation on the body. Moreover, by mining these spatial datasets, we uncovered an interorgan axis whereby bloodborne PLA2G5, a secreted phospholipase, led to hemolysis and multi-organ injury with lethal consequences for the host during sepsis. In humans with bacterial and viral sepsis, the plasma level of PLA2G5 were predictive of disease severity and mortality (Ackermann et al., 2020; Singer et al., 2016).

What is the impact of body-wide, spatial profiling in mice for biomedical research at large? Our work demonstrated the power of using spatial profiling tools that bridge the molecular, cellular, tissue, and whole-body scales in mice to produce high-resolution information about the molecular and cellular makeup of the body of mice. Such data, which were previously unattainable, will fuel new discoveries in disease mechanisms and therapeutic targets (Chen et al., 2015; Ståhl et al., 2016; Rodriques et al., 2019). Moreover, we showed the utility of body-wide spatial phenotyping to study disease processes using systemic inflammation during endotoxemia as a model system. This approach can uncover critical pathophysiological pathways and identify biomarkers for disease progression and treatment response (Lubeck et al., 2014; Crosetto et al., 2015). Beyond these initial applications, we foresee numerous applications across biomedical fields of inquiry for the spatiomolecular analysis of whole-mouse sections to study biological processes spanning genes, cells, tissues, and the whole

organism.

Third, whole-mouse section profiling enhances our understanding of organismal biology and physiology in both health and disease models. By capturing the spatial context of cellular and molecular changes, these maps can reveal critical insights into how different tissues and organs respond to genetic perturbations, environmental changes, and disease processes (Chen et al., 2022; Tian et al., 2023). Our results demonstrated that whole-body profiling enables the detailed spatial analysis of the molecular and cellular changes driving systemic inflammatory processes. Moreover, organismal toxicology can greatly benefit from this approach by measuring the impact of known or candidate drugs – small molecules, biologics, cells, or otherwise – on all tissues of the body simultaneously. This comprehensive profiling will deepen our understanding of biodistribution and its relation to the impact of therapies on desired and undesired targets across the body (Wang et al., 2009; Mortazavi et al., 2008).

Lastly, moving beyond the mouse, these emerging tools can be applied to other mammalian and non-mammalian model systems of interest. For example, human organ systems at scale, body- or organ-wide phenotyping of bats for their unique immune systems, rats for neurobiological studies, and zebrafish developmental studies (Baid et al., 2024; Ellenbroek and Youn, 2016; Veldman and Lin, 2008).

CHAPTER 4

DISCUSSION

4.1 Array-seq overcomes hurdles of current spatial transcriptomics methods

Spatial transcriptomics technologies have revolutionized our ability to analyze gene expression within the spatial context of tissues. However, these methods face significant challenges that limit their utility and broader adoption. Key issues include limited capture area sizes, complex implementation protocols, high costs, and incompatibility with traditional histological techniques like H&E staining. Addressing these challenges is crucial for advancing ST technologies and making them more accessible and practical for a wide range of research and clinical applications.

Limited capture area size remains a significant challenge for many ST methods. For example, larger tissues often require data stitching. In one study using Visium, researchers constructed a human embryonic limb cell atlas by stitching together data from multiple Visium arrays (Zhang et al., 2023a). In addition to requiring additional computation steps for data alignment, this method requires the use of different tissue sections for each capture area, preventing a true single-plane representation of tissues. However, Visium's 6.5 x 6.5 mm^2 capture area is insufficient for capturing a full longitudinally sectioned mouse kidney or a complete mouse brain. Only whole-mouse studies on embryos have been performed using methods like DBiT-seq and Stereo-seq. While these studies are crucial for developmental insights, they do not provide a platform for understanding diseases affecting developed mice or the possibility of studying difficult-to-dissect adult mouse organs, diseases, and response to therapies (Liu et al., 2023b; Chen et al., 2022). Additionally, current methods do not enable high-throughput experiments. For instance, a study examining spatial mechanisms during mouse heart development using Visium likely required dozens of arrays, significantly

extending the time needed to complete the study (Mantri et al., 2021). Each slide's separate library preparation introduces batch effects during sequencing, complicating data analysis despite computational tools designed to mitigate this issue (Stuart et al., 2019; Haghverdi et al., 2018). However, some data artifacts may still remain after batch correction. In contrast, Array-seq can perform experiments on large tissue sections without the need for stitching histology or ST data. The large capture area size of 11.31 cm^2 enables experiments on large-format tissues, particularly human samples, providing a significant leap in the field by scaling from embryos to whole mouse sections (Takahama et al., 2024). This capability is crucial for high-throughput experiments, as it can avoid batch effects altogether by limiting experiments to a single Array-seq slide. The large capture area size also enables comprehensive studies of tissue-level perturbations and functional spatiomolecular studies, making it a versatile tool for both basic and clinical research.

Implementing ST technologies also poses significant challenges due to the need for custom instrumentation and complex protocols. Techniques like XYZeq and sci-Space, for example, require the dissociation of single cells or nuclei within spatially barcoded spots for scRNA-seq, which provides single-cell transcriptomic data but lacks high spatial resolution (Lee et al., 2021; Srivatsan et al., 2021). These methods necessitate specialized instrumentation for spotting oligonucleotides, adding layers of complexity and potential points of failure (Moses and Pachter, 2022). Slide-seq, HDST, and Pixel-seq demand fluorescent imaging on microscopes, which involves custom microfluidic devices for flowing fluorescently labeled nucleotides or primers. This requirement adds significant technical hurdles, including the need for precise control of fluid dynamics and the integration of imaging systems capable of high-resolution fluorescence detection (Rodriques et al., 2019; Vickovic et al., 2019; Fu et al., 2022). Furthermore, Pixel-seq specifically requires the use of a custom-built robotic arm for precise gel stamping. The original paper detailing Pixel-seq does not sufficiently describe the fabrication of this robotic arm, making it challenging for other labs to reproduce the

method reliably (Fu et al., 2022). Similarly, Seq-Scope, Nova-ST, and Open-ST necessitate the disassembly of Illumina flow cells, a process that can be both costly and technically demanding. Errors during disassembly can lead to substantial financial losses due to the cost of flow cells (Cho et al., 2021; Poovathingal et al., 2024; Schott et al., 2024). While Open-ST has the most detailed protocol and simple workflow, it still requires custom 3D-printed apparatus for flow cell processing, adding another layer of complexity and potential technical barriers (Schott et al., 2024). In contrast, Array-seq offers a simpler and more accessible solution by not requiring custom instrumentation for oligonucleotide spotting. The high-quality arrays are purchased from Agilent, with each spatially barcoded oligonucleotide spot's location pre-determined, eliminating the need for fluorescent sequencing for spatial feature localization. Array-seq does not involve any custom instrumentation for array-probe synthesis, requiring only a straightforward hybridization and extension-ligation reaction. Additionally, no custom parts are needed for library preparation and sequencing. The use of commercially available ProPlate gaskets facilitates simple pipetting at each step, similar to Visium, making the method more user-friendly and easier to adopt in various research settings (Moses and Pachter, 2022).

The high costs associated with many ST methods present a significant barrier to widespread adoption, particularly for smaller labs and extensive studies in larger labs (You et al., 2024). Despite advancements in the field, commercialized ST platforms remain expensive. The original method for spatial transcriptomics was licensed to 10x Genomics and commercialized as Visium. Slide-seq, another notable method, is offered through Curio Biosciences as Seeker. Similarly, DBiT-seq is available via AtlasXomics, though it does not offer mRNA capture. Stereo-seq, provided by STOmics, offers limited sizes, with non-histology-compatible solutions available up to 2x3 cm^2 and H&E-compatible solutions up to 1x1 cm^2. The commercialization of these technologies has undoubtedly increased accessibility; however, the high costs associated with these platforms limit their availability and application scope.

Many other methods have not been commercialized and have seen limited use since their inception. For instance, HDST and sci-Space are methods that have not transitioned into commercial products, making their adoption challenging for labs without direct consultation from the originating institutions (Moses and Pachter, 2022). This dichotomy between commercialized, expensive platforms and non-commercialized, inaccessible methods presents a significant challenge within the field of spatial transcriptomics. The high cost of commercially available products restricts their use to well-funded labs and precludes smaller labs from conducting comprehensive studies, thus limiting the overall progress and innovation in the field. Array-seq offers a promising solution to these cost-related challenges. By leveraging Agilent microarrays, researchers can create a large-format spatial transcriptomics array at a significantly lower cost. The conversion of an Agilent microarray into a spatial transcriptomics array involves a straightforward workflow that utilizes low-cost, commercially available products. This results in arrays that are at least 30-fold cheaper per mm^2 than any other commercially available ST product, and >100-fold cheaper per mm^2 than Visium, the most widely used ST method. Consequently, Array-seq expands the availability of spatial transcriptomics to a broader range of scientists, facilitating more extensive and cost-effective research (Takahama et al., 2024). This affordability can democratize access to spatial transcriptomics technology, enabling smaller labs to participate in high-throughput spatial transcriptomics research and large labs to conduct more extensive studies without being hindered by prohibitive costs.

Some methods in spatial transcriptomics are limited in their ability to integrate with traditional histological techniques such as H&E staining, which significantly hinders their application and utility in comprehensive tissue analysis. Slide-seq (Seeker), larger format Stereo-seq (STOmics), and Pixel-seq are not compatible with the imaging of H&E-stained tissue sections. This limitation poses a significant problem, as the integration of spatial transcriptomics with H&E imaging can unlock a plethora of analytical opportunities. H&E

staining is a cornerstone of histopathology, widely used for identifying disease phenotypes, providing a general reference for tissue orientation, and facilitating manual cell type annotation based on histological features (Gurcan et al., 2009; Korzynska et al., 2021). Moreover, advanced deep learning tools can be employed to analyze H&E images to predict molecular profiles and disease outcomes (Campanella et al., 2019; Lu et al., 2021; Kiemen et al., 2022). Visium and small format Stereo-seq (STOmics) are currently the only widely adopted methods that allow for the imaging of H&E-stained tissues alongside spatial transcriptomic data. However, their capture area sizes are limited, restricting their applicability for larger tissue sections or high-throughput experiments. Visium, for instance, has a capture area of 6.5 x 6.5 mm^2, which is suboptimal for extensive tissue profiling (Moses and Pachter, 2022). Array-seq addresses these challenges by combining compatibility with H&E staining, ease of adoption, and a large capture area. This combination significantly expands the potential applications of spatial transcriptomics experiments, making it feasible to analyze large tumors from human tissues, perform organism-scale experiments, and conduct high-throughput studies. The integration of spatial transcriptomics with H&E imaging in Array-seq facilitates the simultaneous visualization of histological architecture and molecular data, enhancing the understanding of tissue heterogeneity and disease mechanisms (Ståhl et al., 2016; Chen et al., 2022). Additionally, Array-seq's compatibility with H&E staining allows researchers to leverage existing histopathological knowledge and tools, thereby providing a comprehensive approach to spatial and molecular tissue analysis (Gurcan et al., 2009; Korzynska et al., 2021).

The limitations of current ST methods, including restricted capture areas, complex technical requirements, and high costs, pose significant barriers to comprehensive tissue analysis and high-throughput experiments. These challenges hinder the study of large and complex tissues, introduce batch effects, and limit the accessibility of ST technologies to well-funded labs. Array-seq offers a promising solution by providing a larger capture area, simplifying

the implementation process, and reducing costs, thereby democratizing access to spatial transcriptomics. By overcoming these limitations, Array-seq enables more extensive and cost-effective research, paving the way for significant advancements in both basic and clinical research.

4.2 Application of spatial transcriptomics to multi-omics and targeting of non-polyadenylated RNA species

The integration of multi-omics and the targeting of non-polyadenylated RNA species are pivotal advancements in genomics, significantly enhancing our understanding of cellular processes and regulatory mechanisms. These approaches aim to provide a more comprehensive and detailed picture of gene expression and regulation (Deng et al., 2019; Zhu et al., 2020). Traditional RNA sequencing methods predominantly focus on polyadenylated RNA, which represents only a portion of the entire transcriptome. By also targeting non-polyadenylated RNA species through methods such as ribosomal RNA (rRNA) depletion or random priming during cDNA synthesis, researchers have identified novel regulatory RNAs, such as non-coding RNAs, enhancer RNAs, and other transcripts that are essential for cellular function and implicated in various diseases (Fan et al., 2015; Heumos et al., 2023).

Single-cell multi-omics approaches, such as CITE-seq (Cellular Indexing of Transcriptomes and Epitopes by sequencing), combine transcriptomic and proteomic data from individual cells, providing insights into both gene expression and protein abundance. CITE-seq uses oligonucleotide-labeled antibodies to tag surface proteins, which are then sequenced along with RNA to give a multi-dimensional view of cellular states (Stoeckius et al., 2017; Mimitou et al., 2021). Similarly, single-cell ATAC-seq (Assay for Transposase-Accessible Chromatin using sequencing) profiles chromatin accessibility, revealing regulatory regions of the genome that are open and potentially active (Buenrostro et al., 2015; Mimitou et al., 2021). Furthermore, methods to map DNA methylation at single-cell resolution have been

developed, such as single-cell bisulfite sequencing (scBS-seq), which provides insights into epigenetic modifications and their role in gene regulation (Smallwood et al., 2014). These advancements enable multiple layers of omics data to gain a holistic understanding of cellular functions.

Recent spatial transcriptomics methods have been able to translate the ability to target non-polyadenylated RNA species and integrations with multi-omics originally pioneered in older NGS modalities. Spatial total RNA-sequencing (STRS) enabled the capture of both polyadenylated and non-polyadenylated RNA species, by incubating tissue sections with E. *coli* poly(A) polymerase to add poly(A) tails to RNAs *in situ* prior to capture (McKellar et al., 2023). STRS otherwise follows conventional protocols to capture, spatially barcode and sequence RNAs. Spatial multi-omics approaches, such as spatial CITE-seq, Spatial Multi-Omics (SM-Omics), and DBit-seq combines oligonucleotide-labeled antibodies with spatial transcriptomics techniques to profile cell surface proteins and RNA in the same tissue sections (Liu et al., 2023b; Vickovic et al., 2022; Liu et al., 2020). Spatial epigenetic methods build from the DBiT-seq platform have been developed to map chromatin accessibility and histone modifications within spatial contexts (Deng et al., 2022; Zhang et al., 2023b).

Array-seq can be made compatible with targeting on non-polyadenylated species and spatial multi-omics. The anchor 2 oligonucleotide of Array-seq can be ordered as any sequence, including mixed bases. This results in straightforward modification of which RNAs Array-seq targets without changing the design of the printed array. Furthermore, multiple anchor 2 oligonucleotides can be added simultaneously during the hybridization step, enabling a mixture of probes targeting sets of sequence-specific RNA species. This can include the small and large subunits of rRNA species (Noller, 1991), tRNA species which have homology in the 3' acceptor stem sequence despite some discriminator bases (Jahn et al., 1991), snRNA species contain a 3-box sequence element required for proper 3 end formation located 9–19 nt downstream of the snRNA-coding region (Hernandez, 1985), and lncRNA species which have

conserved exon structures (Derrien et al., 2012). Furthermore, oligonucleotide-barcoded antibodies and Array-seq poly(A) polymerase can be implemented into the Array-seq workflow for proteomics and pan-transcriptomic functionalities.

4.3 Conclusion

In this work, we describe a method, Array-seq, to repurpose classical oligonucleotide microarrays for spatial transcriptomics profiling. This platform, characterized by a large capture area of 11.31 cm^2, offers substantial improvements over existing methods such as Visium, including increased spot density and dramatically reduced costs. The flexibility and scalability of Array-seq enable comprehensive high-throughput studies, such as simultaneous profiling of multiple tissue samples, 3D data generation, and large-scale tissue sections which were previously unattainable with smaller capture areas. To address the difficulty of generating high quality sections with heterogeneous cell type and tissue composition, we developed a novel sectioning method involving the transfer of tissue section on an adhesive film. Using this transfer method on Array-seq slides enabled spatial transcriptomics profiling of whole adult mouse sections. This data generated an extensive spatial gene expression atlas for the adult mouse, a critical model for biological and disease research. The spot level annotation of whole mouse sections with 17 organs, 45 tissue subregions, and 333 cell types, and transcriptome-wide gene expression enables a comprehensive view of the cellular architecture and patterns of gene expression. Inhibiting PLA2G5 mitigated these effects, highlighting its potential as a therapeutic target. Using Array-seq we also identified PLA2G5 as a critical mediator in the pathogenesis of the disease, operating as a "self-venom" that disrupts red blood cell integrity and iron metabolism. This discovery elucidates a novel mechanism where PLA2G5 acts as a "self-venom," disrupting red blood cell integrity and iron metabolism, thus advancing our understanding of the role of non-immune related factors in the pathophysiology of sepsis.

We also demonstrated the utility of body-wide spatial transcriptomics in disease research

using an endotoxemia model of sepsis, revealing key transcription factor-mediated pathways, measuring changes cell type composition, and identifying biomarkers for disease progression across the mouse organism. Using Array-seq we also identified PLA2G5 as a critical mediator in the pathogenesis of the disease, operating as a "self-venom" that disrupts red blood cell integrity and iron metabolism. The inhibition of PLA2G5 via genetic and antibody approaches mitigated the deleterious effects of sepsis in mice, highlighted by restored splenic red pulp macrophage counts and iron homeostasis. This work marks a significant step in the convergence of molecular biology and spatial genomics, providing an in-depth understanding of systemic inflammation and opening new avenues for research into other complex diseases.

4.4 Future Questions

Array-seq presents opportunities for further enhancement in performance. For instance, the sensitivity of Array-seq could be increased by optimizing protocols to minimize RNA degradation before tissue permeabilization. Increased sensitivity would enhance the reliability of unsupervised clustering for identifying tissue subregions and integrating with scRNA-seq for cell type annotation. Additionally, utilizing a multiplexed padlock ligation (MPLA)-like approach, as employed in other methods, has shown to increase sensitivity in high RNA integrity number (RIN) fresh-frozen tissues (Mirzazadeh et al., 2023). Additionally, the current design of Anchor 2, which results in 16 bases of sequencing in read 1 separating the spatial barcode and UMI, could be optimized to yield more informative sequencing data. Reducing the length of read 2 while maintaining its effectiveness might be achieved by increasing the GC content of the Anchor 2 binding motif and decreasing its length.

Expanding the application of Array-seq to formalin-fixed paraffin-embedded (FFPE) tissues is desirable due to the prevalence of archived FFPE samples. This adaptation could be achieved using an MPLA-based approach without altering the current oligonucleotide sequence design of Array-seq slides. The ability to process FFPE tissues would signifi-

cantly broaden the potential applications of Array-seq in both clinical and research settings (Stoeckius et al., 2017; Moses and Pachter, 2022).

The integration of multi-omics approaches with Array-seq also holds significant promise. Incorporating oligonucleotide-barcoded antibodies, such as those available from Total-seq antibody panels, into the Array-seq workflow could provide deeper insights into cell states and potential therapeutic targets. However, antibody staining generally performs better on paraformaldehyde (PFA)-fixed tissues compared to methanol-fixed tissues, suggesting that MPLA-based approaches might improve the data quality when implemented (Stoeckius et al., 2017; Han et al., 2018). Additionally, Array-seq could be adapted to target non-polyadenylated RNA species by using poly(A) polymerase or modifying the 3' capture sequence of Anchor 2.

Further opportunities exist for organism-wide profiling using Array-seq. Current whole-mouse data generated on a single z-plane limits the heterogeneity of tissue subregions and cell types captured, potentially biasing measured proportions. Generating a three-dimensional mouse atlas would provide a more robust dataset for investigating gene expression patterns in biological structures. Various organism-wide disease models, such as fungal and viral sepsis, could yield insights into shared gene expression modules during systemic infections. Because pathogens like C. *albicans* and viruses produce polyadenylated transcripts, their RNA species can be spatially mapped to visualize infection sites. It has been shown that spatial transcriptomics is capable of concurrently visualizing the host and virus transcriptomics (Jang et al., 2023). Additionally, generating a time-course dataset for sepsis would help elucidate the temporal dynamics of spatial gene expression and cell type organization (Farrell et al., 2018).

Array-seq could also be employed to generate high-throughput spatial transcriptomics data on human organs, potentially creating a comprehensive human spatial gene expression atlas. This atlas would be invaluable for understanding human biology, as it would capture

the full structural characteristics of large organs. Additionally, Array-seq can be applied to other model organisms, such as bats, zebrafish, and rats, providing important references for researchers studying disease processes in these species (Chen et al., 2022; Zhang et al., 2023a).

REFERENCES

Soman N Abraham and Ashley L St. John. Mast cell-orchestrated immunity to pathogens. *Nature Reviews Immunology*, 10(6):440–452, 2010.

Maximilian Ackermann, Stijn E Verleden, Mark Kuehnel, Axel Haverich, Tobias Welte, Florian Laenger, Arno Vanstapel, Christopher Werlein, Helge Stark, Alexandar Tzankov, et al. Pulmonary vascular endothelialitis, thrombosis, and angiogenesis in covid-19. *New England Journal of Medicine*, 383(2):120–128, 2020.

Michael Adamzik, Tim Hamburger, Frank Petrat, Jürgen Peters, Herbert de Groot, and Matthias Hartmann. Free hemoglobin concentration in severe sepsis: methods of measurement and prediction of outcome. *Critical care*, 16:1–10, 2012.

Mir S Adil, S Priya Narayanan, and Payaningal R Somanath. Cell-cell junctions: structure and regulation in physiology and pathology. *Tissue Barriers*, 9(1):1848212, 2021.

Shizuo Akira and Kiyoshi Takeda. Toll-like receptor signalling. *Nature reviews immunology*, 4(7):499–511, 2004.

Yannick O Alexandre and Scott N Mueller. Splenic stromal niches in homeostasis and immunity. *Nature Reviews Immunology*, 23(11):705–719, 2023.

Alma Andersson, Joseph Bergenstråhle, Michaela Asp, Ludvig Bergenstråhle, Aleksandra Jurek, José Fernández Navarro, and Joakim Lundeberg. Single-cell and spatial transcriptomics enables probabilistic inference of cell type topography. *Communications biology*, 3 (1):565, 2020.

Robin Andersson, Claudia Gebhard, Irene Miguel-Escalada, Ilka Hoof, Jette Bornholdt, Mette Boyd, Yun Chen, Xiaobei Zhao, Christian Schmidl, Takahiro Suzuki, et al. An atlas of active enhancers across human cell types and tissues. *Nature*, 507(7493):455–461, 2014.

Michael Angelo, Sean C Bendall, Rachel Finck, Matthew B Hale, Chuck Hitzman, Alexander D Borowsky, Richard M Levenson, John B Lowe, Scot D Liu, Shuchun Zhao, et al. Multiplexed ion beam imaging of human breast tumors. *Nature medicine*, 20(4):436–442, 2014.

Stefano Angiari, Marah C Runtsch, Caroline E Sutton, Eva M Palsson-McDermott, Beth Kelly, Nisha Rana, Harry Kane, Gina Papadopoulou, Erika L Pearce, Kingston HG Mills, et al. Pharmacological activation of pyruvate kinase m2 inhibits cd4+ t cell pathogenicity and suppresses autoimmunity. *Cell metabolism*, 31(2):391–405, 2020.

Derek C Angus and Tom Van der Poll. Severe sepsis and septic shock. *New England journal of medicine*, 369(9):840–851, 2013.

Rohit Arora, Christian Cao, Mehul Kumar, Sarthak Sinha, Ayan Chanda, Reid McNeil, Divya Samuel, Rahul K Arora, T Wayne Matthews, Shamir Chandarana, et al. Spatial transcriptomics reveals distinct and conserved tumor core and edge architectures that predict survival and targeted therapy response. *Nature Communications*, 14(1):5029, 2023.

Andre Bafica, Carl G Feng, Helton C Santiago, Julio Aliberti, Allen Cheever, Karen E Thomas, Gregory A Taylor, Stefanie N Vogel, and Alan Sher. The ifn-inducible gtpase lrg47 (irgm1) negatively regulates tlr4-triggered proinflammatory cytokine production and prevents endotoxemia. *The Journal of Immunology*, 179(8):5514–5522, 2007.

Kaushal Baid, Aaron T Irving, Nolwenn Jouvenet, and Arinjay Banerjee. The translational potential of studying bat immunity. *Trends in Immunology*, 2024.

Robert A Balk. Severe sepsis and septic shock: definitions, epidemiology, and clinical manifestations. *Critical care clinics*, 16(2):179–192, 2000.

SL Beaucage and Marvin H Caruthers. Deoxynucleoside phosphoramidites—a new class of key intermediates for deoxypolynucleotide synthesis. *Tetrahedron letters*, 22(20):1859–1862, 1981.

Rinaldo Bellomo, John A Kellum, and Claudio Ronco. Acute kidney injury. *The Lancet*, 380(9843):756–766, 2012.

Shani Ben-Moshe, Yonatan Shapira, Andreas E Moor, Rita Manco, Tamar Veg, Keren Bahar Halpern, and Shalev Itzkovitz. Spatial sorting enables comprehensive characterization of liver zonation. *Nature metabolism*, 1(9):899–911, 2019.

B Beutler and A Cerami. Tumor necrosis, cachexia, shock, and inflammation: a common mediator. *Annual review of biochemistry*, 57(1):505–518, 1988.

Kasprzyk Arkadiusz Mongin Emmanuel Rust Alistair Slater Guy Birney Ewan, Goldman Nick et al. Initial sequencing and comparative analysis of the mouse genome. *Nature*, 420(6915):520–562, 2002.

Andries Blokzijl, Mikaela Friedman, Fredrik Pontén, and Ulf Landegren. Profiling protein expression and interactions: proximity ligation as a tool for personalized medicine. *Journal of internal medicine*, 268(3):232–245, 2010.

Ernesto Bockamp, Marko Maringer, Christian Spangenberg, Stephan Fees, Stuart Fraser, Leonid Eshkind, Franz Oesch, and Bernhard Zabel. Of mice and models: improved animal models for biomedical research. *Physiological genomics*, 11(3):115–132, 2002.

Roger C Bone, Robert A Balk, Frank B Cerra, R Phillip Dellinger, Alan M Fein, William A Knaus, Roland MH Schein, and William J Sibbald. Definitions for sepsis and organ failure and guidelines for the use of innovative therapies in sepsis. *Chest*, 101(6):1644–1655, 1992.

Michael Bonelli, Karolina Dalwigk, Alexander Platzer, Isabel Olmos Calvo, Silvia Hayer, Birgit Niederreiter, Johannes Holinka, Florian Sevelda, Thomas Pap, Günter Steiner, et al. Irf1 is critical for the tnf-driven interferon response in rheumatoid fibroblast-like synoviocytes: Jakinibs suppress the interferon response in ra-flss. *Experimental & molecular medicine*, 51(7):1–11, 2019.

Giuseppina Bonizzi and Michael Karin. The two nf-κb activation pathways and their role in innate and adaptive immunity. *Trends in immunology*, 25(6):280–288, 2004.

Audrey Bonnan, Matthew MJ Rowan, Christopher A Baker, M McLean Bolton, and Jason M Christie. Autonomous purkinje cell activation instructs bidirectional motor learning through evoked dendritic calcium signaling. *Nature communications*, 12(1):2153, 2021.

Jonathan S Boomer, Kathleen To, Kathy C Chang, Osamu Takasu, Dale F Osborne, Andrew H Walton, Traci L Bricker, Stephen D Jarman, Daniel Kreisel, Alexander S Krupnick, et al. Immunosuppression in patients who die of sepsis and multiple organ failure. *Jama*, 306(23):2594–2605, 2011.

Lars E Borm, Alejandro Mossi Albiach, Camiel CA Mannens, Jokubas Janusauskas, Ceren Özgün, David Fernández-García, Rebecca Hodge, Francisca Castillo, Charlotte RH Hedin, Eduardo J Villablanca, et al. Scalable in situ single-cell profiling by electrophoretic capture of mrna using eel fish. *Nature biotechnology*, 41(2):222–231, 2023.

Hicham Bouabe and Klaus Okkenhaug. Gene targeting in mice: a review. *Virus-Host Interactions: Methods and Protocols*, pages 315–336, 2013.

Volker Brinkmann, Ulrike Reichard, Christian Goosmann, Beatrix Fauler, Yvonne Uhlemann, David S Weiss, Yvette Weinrauch, and Arturo Zychlinsky. Neutrophil extracellular traps kill bacteria. *science*, 303(5663):1532–1535, 2004.

Pierre Bruhns. Properties of mouse and human igg receptors and their contribution to disease models. *Blood, The Journal of the American Society of Hematology*, 119(24):5640–5649, 2012.

Jason D Buenrostro, Beijing Wu, Ulrike M Litzenburger, Dave Ruff, Michael L Gonzales, Michael P Snyder, Howard Y Chang, and William J Greenleaf. Single-cell chromatin accessibility reveals principles of regulatory variation. *Nature*, 523(7561):486–490, 2015.

Tilo Buschmann. Dnabarcodes: an r package for the systematic construction of dna sample tags. *Bioinformatics*, 33(6):920–922, 2017.

Dylan M Cable, Evan Murray, Luli S Zou, Aleksandrina Goeva, Evan Z Macosko, Fei Chen, and Rafael A Irizarry. Robust decomposition of cell type mixtures in spatial transcriptomics. *Nature biotechnology*, 40(4):517–526, 2022.

Changchun Cai, Zongxian Cao, Patricia A Loughran, Sodam Kim, Sophie Darwiche, Sebastian Korff, and Timothy R Billiar. Mast cells play a critical role in the systemic inflammatory response and end-organ injury resulting from trauma. *Journal of the American College of Surgeons*, 213(5):604–615, 2011.

Stuart K Calderwood, Salamatu S Mambula, and Phillip J Gray Jr. Extracellular heat shock proteins in cell signaling and immunity. *Annals of the New York Academy of Sciences*, 1113(1):28–39, 2007.

Gabriela Camicia, Roberto Pozner, and Gabriela de Larrañaga. Neutrophil extracellular traps in sepsis. *Shock*, 42(4):286–294, 2014.

Gabriele Campanella, Matthew G Hanna, Luke Geneslaw, Allen Miraflor, Vitor Werneck Krauss Silva, Klaus J Busam, Edi Brogi, Victor E Reuter, David S Klimstra, and Thomas J Fuchs. Clinical-grade computational pathology using weakly supervised deep learning on whole slide images. *Nature medicine*, 25(8):1301–1309, 2019.

Cesar P Canales and Katherina Walz. The mouse, a model organism for biomedical research. In *Cellular and animal models in human genomics research*, pages 119–140. Elsevier, 2019.

Zixuan Cang, Yanxiang Zhao, Axel A Almet, Adam Stabell, Raul Ramos, Maksim V Plikus, Scott X Atwood, and Qing Nie. Screening cell–cell communication in spatial transcriptomics via collective optimal transport. *Nature methods*, 20(2):218–228, 2023.

Richard M Caprioli, Terry B Farmer, and Jocelyn Gile. Molecular imaging of biological samples: localization of peptides and proteins using maldi-tof ms. *Analytical chemistry*, 69(23):4751–4760, 1997.

MH Caruthers, AD Barone, SL Beaucage, DR Dodds, EF Fisher, LJ McBride, M Matteucci, Z Stabinsky, and J-Y Tang. [15] chemical synthesis of deoxyoligonucleotides by the phosphoramidite method. In *Methods in enzymology*, volume 154, pages 287–313. Elsevier, 1987.

Axelle Caudrillier, Kai Kessenbrock, Brian M Gilliss, John X Nguyen, Marisa B Marques, Marc Monestier, Pearl Toy, Zena Werb, Mark R Looney, et al. Platelets induce neutrophil extracellular traps in transfusion-related acute lung injury. *The Journal of clinical investigation*, 122(7):2661–2671, 2012.

Maurizio Cecconi, Laura Evans, Mitchell Levy, and Andrew Rhodes. Sepsis and septic shock. *The Lancet*, 392(10141):75–87, 2018.

Mark Chee, Robert Yang, Earl Hubbell, Anthony Berno, Xiaohua C Huang, David Stern, Jim Winkler, David J Lockhart, Macdonald S Morris, and Stephen PA Fodor. Accessing genetic information with high-density dna arrays. *Science*, 274(5287):610–614, 1996.

Ao Chen, Sha Liao, Mengnan Cheng, Kailong Ma, Liang Wu, Yiwei Lai, Xiaojie Qiu, Jin Yang, Jiangshan Xu, Shijie Hao, et al. Spatiotemporal transcriptomic atlas of mouse organogenesis using dna nanoball-patterned arrays. *Cell*, 185(10):1777–1792, 2022.

Ao Chen, Yidi Sun, Ying Lei, Chao Li, Sha Liao, Juan Meng, Yiqin Bai, Zhen Liu, Zhifeng Liang, Zhiyong Zhu, et al. Single-cell spatial transcriptome reveals cell-type organization in the macaque cortex. *Cell*, 186(17):3726–3743, 2023a.

Fei Chen, Asmamaw T Wassie, Allison J Cote, Anubhav Sinha, Shahar Alon, Shoh Asano, Evan R Daugharthy, Jae-Byum Chang, Adam Marblestone, George M Church, et al. Nanoscale imaging of rna with expansion microscopy. *Nature methods*, 13(8):679–684, 2016.

Feng Chen, Katharina Schönberger, and Jan S Tchorz. Distinct hepatocyte identities in liver homeostasis and regeneration. *JHEP Reports*, 5(8):100779, 2023b.

Kok Hao Chen, Alistair N Boettiger, Jeffrey R Moffitt, Siyuan Wang, and Xiaowei Zhuang. Spatially resolved, highly multiplexed rna profiling in single cells. *Science*, 348(6233): aaa6090, 2015.

Shanze Chen, Abdullah FUH Saeed, Quan Liu, Qiong Jiang, Haizhao Xu, Gary Guishan Xiao, Lang Rao, and Yanhong Duo. Macrophages in immunoregulation and therapeutics. *Signal Transduction and Targeted Therapy*, 8(1):207, 2023c.

Xiaoyin Chen, Yu-Chi Sun, George M Church, Je Hyuk Lee, and Anthony M Zador. Efficient in situ barcode sequencing using padlock probe-based baristaseq. *Nucleic acids research*, 46(4):e22–e22, 2018.

Chun-Seok Cho, Jingyue Xi, Yichen Si, Sung-Rye Park, Jer-En Hsu, Myungjin Kim, Goo Jun, Hyun Min Kang, and Jun Hee Lee. Microscopic examination of spatial transcriptome using seq-scope. *Cell*, 184(13):3559–3572, 2021.

Josie A Christopher, Aikaterini Geladaki, Charlotte S Dawson, Owen L Vennard, and Kathryn S Lilley. Subcellular transcriptomics and proteomics: a comparative methods review. *Molecular & Cellular Proteomics*, 21(2), 2022.

Kamila Chughtai and Ron MA Heeren. Mass spectrometric imaging for biomedical tissue analysis. *Chemical reviews*, 110(5):3237–3277, 2010.

Hans Clevers. Modeling development and disease with organoids. *Cell*, 165(7):1586–1597, 2016.

Simone Codeluppi, Lars E Borm, Amit Zeisel, Gioele La Manno, Josina A van Lunteren, Camilla I Svensson, and Sten Linnarsson. Spatial organization of the somatosensory cortex revealed by osmfish. *Nature methods*, 15(11):932–935, 2018.

Jonathan Cohen. The immunopathogenesis of sepsis. *Nature*, 420(6917):885–891, 2002.

Tabula Muris Consortium. A single-cell transcriptomic atlas characterizes ageing tissues in the mouse. *Nature*, 583(7817):590–595, 2020.

Nina S Corsini and Juergen A Knoblich. Human organoids: New strategies and methods for analyzing human development and disease. *Cell*, 185(15):2756–2769, 2022.

Kevin N Couper, Daniel G Blount, and Eleanor M Riley. Il-10: the master regulator of immunity to infection. *The Journal of Immunology*, 180(9):5771–5777, 2008.

Courtney B Crayne, Sabrin Albeituni, Kim E Nichols, and Randy Q Cron. The immunology of macrophage activation syndrome. *Frontiers in immunology*, 10:119, 2019.

Ian Nicholas Crispe. Hepatic t cells and liver tolerance. *Nature Reviews Immunology*, 3(1): 51–62, 2003.

Ian Nicholas Crispe. The liver as a lymphoid organ. *Annual review of immunology*, 27(1): 147–163, 2009.

Nicola Crosetto, Magda Bienko, and Alexander Van Oudenaarden. Spatially resolved transcriptomics and beyond. *Nature Reviews Genetics*, 16(1):57–66, 2015.

Rory P Cunningham and Natalie Porat-Shliom. Liver zonation–revisiting old questions with new technologies. *Frontiers in physiology*, 12:732929, 2021.

James E Darnell Jr, lan M Kerr, and George R Stark. Jak-stat pathways and transcriptional activation in response to ifns and other extracellular signaling proteins. *Science*, 264(5164): 1415–1421, 1994.

Muriel T Davisson. The jackson laboratory mouse mutant resource. In *Handbook of Mouse Mutations with Skin and Hair Abnormalities*, pages 21–28. CRC Press, 2020.

Consuelo M López de Padilla and Timothy B Niewold. The type i interferons: Basic concepts and clinical relevance in immune-mediated inflammatory diseases. *Gene*, 576(1):14–21, 2016.

R Phillip Dellinger, Mitchell M Levy, Jean M Carlet, Julian Bion, Margaret M Parker, Roman Jaeschke, Konrad Reinhart, Derek C Angus, Christian Brun-Buisson, Richard Beale, et al. Surviving sepsis campaign: international guidelines for management of severe sepsis and septic shock: 2008. *Critical care medicine*, 36(1):296–327, 2008.

Yanxiang Deng, Amanda Finck, and Rong Fan. Single-cell omics analyses enabled by microchip technologies. *Annual review of biomedical engineering*, 21(1):365–393, 2019.

Yanxiang Deng, Marek Bartosovic, Sai Ma, Di Zhang, Petra Kukanja, Yang Xiao, Graham Su, Yang Liu, Xiaoyu Qin, Gorazd B Rosoklija, et al. Spatial profiling of chromatin accessibility in mouse and human tissues. *Nature*, 609(7926):375–383, 2022.

Thomas Derrien, Rory Johnson, Giovanni Bussotti, Andrea Tanzer, Sarah Djebali, Hagen Tilgner, Gregory Guernec, David Martin, Angelika Merkel, David G Knowles, et al. The gencode v7 catalog of human long noncoding rnas: analysis of their gene structure, evolution, and expression. *Genome research*, 22(9):1775–1789, 2012.

William F Dietrich, Joyce Miller, Robert Steen, Mark A Merchant, Deborah Damron-Boles, Zeeshan Husain, Robert Dredge, Mark J Daly, Kimberly A Ingalls, Tara J O'Connor, et al. A comprehensive genetic map of the mouse genome. *Nature*, 380(6570):149–152, 1996.

Charles A Dinarello. Interleukin-1 in the pathogenesis and treatment of inflammatory diseases. *Blood, The Journal of the American Society of Hematology*, 117(14):3720–3732, 2011.

James M Dolezal, Andrew Srisuwananukorn, Dmitry Karpeyev, Siddhi Ramesh, Sara Kochanny, Brittany Cody, Aaron S Mansfield, Sagar Rakshit, Radhika Bansal, Melanie C Bois, et al. Uncertainty-informed deep learning models enable high-confidence predictions for digital histopathology. *Nature communications*, 13(1):6572, 2022.

Bart Ellenbroek and Jiun Youn. Rodent models in neuroscience research: is it a rat race? *Disease models & mechanisms*, 9(10):1079–1087, 2016.

Cecilia Eriksson, Noritaka Masaki, Ikuko Yao, Takahiro Hayasaka, and Mitsutoshi Setou. Maldi imaging mass spectrometry—a mini review of methods and recent developments. *Mass Spectrometry*, 2(Special_Issue):S0022–S0022, 2013.

Charles T Esmon. The interactions between inflammation and coagulation. *British journal of haematology*, 131(4):417–430, 2005.

Laura Evans, Andrew Rhodes, Waleed Alhazzani, Massimo Antonelli, Craig M Coopersmith, Craig French, Flávia R Machado, Lauralyn Mcintyre, Marlies Ostermann, Hallie C Prescott, et al. Surviving sepsis campaign: international guidelines for management of sepsis and septic shock 2021. *Critical care medicine*, 49(11):e1063–e1143, 2021.

H Christina Fan, Glenn K Fu, and Stephen PA Fodor. Combinatorial labeling of single cells for gene expression cytometry. *Science*, 347(6222):1258367, 2015.

Yuhang Fan, Žaneta Andrusivová, Yunming Wu, Chew Chai, Ludvig Larsson, Mengxiao He, Liqun Luo, Joakim Lundeberg, and Bo Wang. Expansion spatial transcriptomics. *Nature methods*, 20(8):1179–1182, 2023.

Zhuoqing Fang, Xinyuan Liu, and Gary Peltz. Gseapy: a comprehensive package for performing gene set enrichment analysis in python. *Bioinformatics*, 39(1):btac757, 2023.

Giamila Fantuzzi. Adipose tissue, adipokines, and inflammation. *Journal of Allergy and clinical immunology*, 115(5):911–919, 2005.

Jeffrey A Farrell, Yiqun Wang, Samantha J Riesenfeld, Karthik Shekhar, Aviv Regev, and Alexander F Schier. Single-cell reconstruction of developmental trajectories during zebrafish embryogenesis. *Science*, 360(6392):eaar3131, 2018.

Tobias Fehlmann, Stefanie Reinheimer, Chunyu Geng, Xiaoshan Su, Snezana Drmanac, Andrei Alexeev, Chunyan Zhang, Christina Backes, Nicole Ludwig, Martin Hart, et al. cpas-based sequencing on the bgiseq-500 to explore small non-coding rnas. *Clinical Epigenetics*, 8:1–11, 2016.

Eva Fischer, Michael A Marano, Kimberly J Van Zee, Craig S Rock, Arthur S Hawes, William A Thompson, Laura DeForge, John S Kenney, Daniel G Remick, Duane C Bloedow, et al. Interleukin-1 receptor blockade improves survival and hemodynamic performance in escherichia coli septic shock, but fails to alter host responses to sublethal endotoxemia. *The Journal of clinical investigation*, 89(5):1551–1557, 1992.

Stephen PA Fodor, J Leighton Read, Michael C Pirrung, Lubert Stryer, Amy Tsai Lu, and Dennis Solas. Light-directed, spatially addressable parallel chemical synthesis. *science*, 251(4995):767–773, 1991.

Xiaonan Fu, Li Sun, Runze Dong, Jane Y Chen, Runglawan Silakit, Logan F Condon, Yiing Lin, Shin Lin, Richard D Palmiter, and Liangcai Gu. Polony gels enable amplifiable dna stamping and spatial transcriptomics of chronic pain. *Cell*, 185(24):4621–4633, 2022.

Xu-zhe Fu and Yu Wang. Interferon-γ regulates immunosuppression in septic mice by promoting the warburg effect through the pi3k/akt/mtor pathway. *Molecular Medicine*, 29 (1):95, 2023.

Cem Gabay and Irving Kushner. Acute-phase proteins and other systemic responses to inflammation. *New England journal of medicine*, 340(6):448–454, 1999.

Stephen J Galli, Mindy Tsai, and Adrian M Piliponsky. The development of allergic inflammation. *Nature*, 454(7203):445–454, 2008.

Alba Garrido-Trigo, Ana M Corraliza, Marisol Veny, Isabella Dotti, Elisa Melón-Ardanaz, Aina Rill, Helena L Crowell, Ángel Corbí, Victoria Gudiño, Miriam Esteller, et al. Macrophage and neutrophil heterogeneity at single-cell spatial resolution in human inflammatory bowel disease. *Nature Communications*, 14(1):4506, 2023.

Charlotte Giesen, Hao AO Wang, Denis Schapiro, Nevena Zivanovic, Andrea Jacobs, Bodo Hattendorf, Peter J Schüffler, Daniel Grolimund, Joachim M Buhmann, Simone Brandt, et al. Highly multiplexed imaging of tumor tissues with subcellular resolution by mass cytometry. *Nature methods*, 11(4):417–422, 2014.

Yury Goltsev, Nikolay Samusik, Julia Kennedy-Darling, Salil Bhate, Matthew Hale, Gustavo Vazquez, Sarah Black, and Garry P Nolan. Deep profiling of mouse splenic architecture with codex multiplexed imaging. *Cell*, 174(4):968–981, 2018.

Raffaella Gozzelino, Viktoria Jeney, and Miguel P Soares. Mechanisms of cell protection by heme oxygenase-1. *Annual review of pharmacology and toxicology*, 50(1):323–354, 2010.

Dominic Grün and Alexander van Oudenaarden. Design and analysis of single-cell sequencing experiments. *Cell*, 163(4):799–810, 2015.

F Peter Guengerich. Cytochrome p450 and chemical toxicology. *Chemical research in toxicology*, 21(1):70–83, 2008.

Metin N Gurcan, Laura E Boucheron, Ali Can, Anant Madabhushi, Nasir M Rajpoot, and Bulent Yener. Histopathological image analysis: A review. *IEEE reviews in biomedical engineering*, 2:147–171, 2009.

C Erik Hack, Els R De Groot, RJ Felt-Bersma, Jan H Nuijens, RJ Strack Van Schijndel, AJ Eerenberg-Belmer, Lambertus G Thijs, and Lucien A Aarden. Increased plasma levels of interleukin-6 in sepsis. *Blood*, 1989.

Laleh Haghverdi, Aaron TL Lun, Michael D Morgan, and John C Marioni. Batch effects in single-cell rna-sequencing data are corrected by matching mutual nearest neighbors. *Nature biotechnology*, 36(5):421–427, 2018.

Keren Bahar Halpern, Rom Shenhav, Orit Matcovitch-Natan, Beata Toth, Doron Lemze, Matan Golan, Efi E Massasa, Shaked Baydatch, Shanie Landen, Andreas E Moor, et al. Single-cell spatial reconstruction reveals global division of labour in the mammalian liver. *Nature*, 542(7641):352–356, 2017.

Xiaoping Han, Renying Wang, Yincong Zhou, Lijiang Fei, Huiyu Sun, Shujing Lai, Assieh Saadatpour, Ziming Zhou, Haide Chen, Fang Ye, et al. Mapping the mouse cell atlas by microwell-seq. *Cell*, 172(5):1091–1107, 2018.

Douglas Hanahan and Robert A Weinberg. Hallmarks of cancer: the next generation. *cell*, 144(5):646–674, 2011.

PR Harrison, D Conkie, J Paul, and K Jones. Localisation of cellular globin messenger rna by in situ hybridisation to complementary dna. *FEBS letters*, 32(1):109–112, 1973.

Stefan Haug, Selvaraj Muthusamy, Yong Li, Galen Stewart, Xianwu Li, Martin Treppner, Anna Köttgen, and Shreeram Akilesh. Multi-omic analysis of human kidney tissue identified medulla-specific gene expression patterns. *Kidney International*, 105(2):293–311, 2024.

Matthew S Hayden and Sankar Ghosh. Nf-κb, the first quarter-century: remarkable progress and outstanding questions. *Genes & development*, 26(3):203–234, 2012.

Nouria Hernandez. Formation of the 3 end of u1 snrna is directed by a conserved sequence located downstream of the coding region. *The EMBO journal*, 4(7):1827–1837, 1985.

Stephan Herzig, Fanxin Long, Ulupi S Jhala, Susan Hedrick, Rebecca Quinn, Anton Bauer, Dorothea Rudolph, Gunther Schutz, Cliff Yoon, Pere Puigserver, et al. Creb regulates hepatic gluconeogenesis through the coactivator pgc-1. *Nature*, 413(6852):179–183, 2001.

Jochen Hess, Peter Angel, and Marina Schorpp-Kistner. Ap-1 subunits: quarrel and harmony among siblings. *Journal of cell science*, 117(25):5965–5973, 2004.

Lukas Heumos, Anna C Schaar, Christopher Lance, Anastasia Litinetskaya, Felix Drost, Luke Zappia, Malte D Lücken, Daniel C Strobl, Juan Henao, Fabiola Curion, et al. Best practices for single-cell analysis across modalities. *Nature Reviews Genetics*, 24(8):550–572, 2023.

Christian Hinze, Nikos Karaiskos, Anastasiya Boltengagen, Katharina Walentin, Klea Redo, Nina Himmerkus, Markus Bleich, S Steven Potter, Andrew S Potter, Kai-Uwe Eckardt, et al. Kidney single-cell transcriptomes predict spatial corticomedullary gene expression and tissue osmolality gradients. *Journal of the American Society of Nephrology*, 32(2): 291–306, 2021.

Richard S Hotchkiss, Paul E Swanson, Bradley D Freeman, Kevin W Tinsley, J Perren Cobb, George M Matuschak, Timothy G Buchman, and Irene E Karl. Apoptotic cell death in patients with sepsis, shock, and multiple organ dysfunction. *Critical care medicine*, 27(7): 1230–1251, 1999.

Richard S Hotchkiss, Kevin W Tinsley, Paul E Swanson, Robert E Schmieg, Jia Ji Hui, Katherine C Chang, Dale F Osborne, Bradley D Freeman, J Perren Cobb, Timothy G Buchman, et al. Sepsis-induced apoptosis causes progressive profound depletion of b and cd4+ t lymphocytes in humans. *The Journal of Immunology*, 166(11):6952–6963, 2001.

Richard S Hotchkiss, Guillaume Monneret, and Didier Payen. Sepsis-induced immunosuppression: from cellular dysfunctions to immunotherapy. *Nature Reviews Immunology*, 13 (12):862–874, 2013.

Richard S Hotchkiss, Lyle L Moldawer, Steven M Opal, Konrad Reinhart, Isaiah R Turnbull, and Jean-Louis Vincent. Sepsis and septic shock. *Nature reviews Disease primers*, 2(1): 1–21, 2016.

Kenneth H Hu, John P Eichorst, Chris S McGinnis, David M Patterson, Eric D Chow, Kelly Kersten, Stephen C Jameson, Zev J Gartner, Arjun A Rao, and Matthew F Krummel. Zipseq: barcoding for real-time mapping of single cell transcriptomes. *Nature methods*, 17 (8):833–843, 2020.

Xiaoyi Hu, Jing Li, Maorong Fu, Xia Zhao, and Wei Wang. The jak/stat signaling pathway: from bench to clinic. *Signal transduction and targeted therapy*, 6(1):402, 2021.

Timothy R Hughes, Mao Mao, Allan R Jones, Julja Burchard, Matthew J Marton, Karen W Shannon, Steven M Lefkowitz, Michael Ziman, Janell M Schelter, Michael R Meyer, et al. Expression profiling using microarrays fabricated by an ink-jet oligonucleotide synthesizer. *Nature biotechnology*, 19(4):342–347, 2001.

Christopher A Hunter and Simon A Jones. Il-6 as a keystone cytokine in health and disease. *Nature immunology*, 16(5):448–457, 2015.

Saiful Islam, Amit Zeisel, Simon Joost, Gioele La Manno, Pawel Zajac, Maria Kasper, Peter Lönnerberg, and Sten Linnarsson. Quantitative single-cell rna-seq with unique molecular identifiers. *Nature methods*, 11(2):163–166, 2014.

Lionel B Ivashkiv and Laura T Donlin. Regulation of type i interferon responses. *Nature Reviews Immunology*, 14(1):36–49, 2014.

Martina Jahn, M John Rogers, and Dieter Söll. Anticodon and acceptor stem nucleotides in trnagln are major recognition elements for e. coli glutaminyl-trna synthetase. *Nature*, 352 (6332):258–260, 1991.

Sanjay Jain and Michael T Eadon. Spatial transcriptomics in health and disease. *Nature Reviews Nephrology*, pages 1–13, 2024.

Charles A Janeway Jr and Ruslan Medzhitov. Innate immune recognition. *Annual review of immunology*, 20(1):197–216, 2002.

Min J Jang, Gerard M Coughlin, Cameron R Jackson, Xinhong Chen, Miguel R Chuapoco, Julia L Vendemiatti, Alexander Z Wang, and Viviana Gradinaru. Spatial transcriptomics for profiling the tropism of viral vectors in tissues. *Nature biotechnology*, 41(9):1272–1286, 2023.

Qi Jiang, Xin Wang, Enyu Huang, Qiao Wang, Chengping Wen, Guocan Yang, Liwei Lu, and Dawei Cui. Inflammasome and its therapeutic targeting in rheumatoid arthritis. *Frontiers in immunology*, 12:816839, 2022.

Eun-Kyeong Jo, Jin Kyung Kim, Dong-Min Shin, and Chihiro Sasakawa. Molecular mechanisms regulating nlrp3 inflammasome activation. *Cellular & molecular immunology*, 13 (2):148–159, 2016.

Melissa R Junttila and Frederic J De Sauvage. Influence of tumour micro-environment heterogeneity on therapeutic response. *Nature*, 501(7467):346–354, 2013.

Motohiko Kadoki, Ashwini Patil, Cornelius C Thaiss, Donald J Brooks, Surya Pandey, Deeksha Deep, David Alvarez, Ulrich H von Andrian, Amy J Wagers, Kenta Nakai, et al. Organism-level analysis of vaccination reveals networks of protection across tissues. *Cell*, 171(2):398–413, 2017.

Tugrul T Kararli. Comparison of the gastrointestinal anatomy, physiology, and biochemistry of humans and commonly used laboratory animals. *Biopharmaceutics & drug disposition*, 16(5):351–380, 1995.

Rajendra Karki, Bhesh Raj Sharma, Shraddha Tuladhar, Evan Peter Williams, Lillian Zalduondo, Parimal Samir, Min Zheng, Balamurugan Sundaram, Balaji Banoth, RK Subbarao Malireddi, et al. Synergism of tnf-α and ifn-γ triggers inflammatory cell death, tissue damage, and mortality in sars-cov-2 infection and cytokine shock syndromes. *Cell*, 184(1):149–168, 2021.

Moujtaba Y Kasmani, Paytsar Topchyan, Ashley K Brown, Ryan J Brown, Xiaopeng Wu, Yao Chen, Achia Khatun, Donia Alson, Yue Wu, Robert Burns, et al. A spatial sequencing atlas of age-induced changes in the lung during influenza infection. *Nature communications*, 14(1):6597, 2023.

Jakob Nikolas Kather, Alexander T Pearson, Niels Halama, Dirk Jäger, Jeremias Krause, Sven H Loosen, Alexander Marx, Peter Boor, Frank Tacke, Ulf Peter Neumann, et al. Deep learning can predict microsatellite instability directly from histology in gastrointestinal cancer. *Nature medicine*, 25(7):1054–1056, 2019.

Jakob Nikolas Kather, Lara R Heij, Heike I Grabsch, Chiara Loeffler, Amelie Echle, Hannah Sophie Muti, Jeremias Krause, Jan M Niehues, Kai AJ Sommer, Peter Bankhead, et al. Pan-cancer image-based detection of clinically actionable genetic alterations. *Nature cancer*, 1(8):789–799, 2020.

Taro Kawai and Shizuo Akira. The role of pattern-recognition receptors in innate immunity: update on toll-like receptors. *Nature immunology*, 11(5):373–384, 2010.

Tadafumi Kawamoto and Komei Kawamoto. Preparation of thin frozen sections from nonfixed and undecalcified hard tissues using kawamot's film method (2012). *Skeletal development and repair: methods and protocols*, pages 149–164, 2014.

Tadafumi Kawamoto and Komei Kawamoto. Preparation of thin frozen sections from nonfixed and undecalcified hard tissues using kawamoto's film method (2020). *Skeletal development and repair: Methods and protocols*, pages 259–281, 2021.

Rongqin Ke, Marco Mignardi, Alexandra Pacureanu, Jessica Svedlund, Johan Botling, Carolina Wählby, and Mats Nilsson. In situ sequencing for rna analysis in preserved tissue and cells. *Nature methods*, 10(9):857–860, 2013.

Gavin Kelsey, Oliver Stegle, and Wolf Reik. Single-cell epigenomics: Recording the past and predicting the future. *Science*, 358(6359):69–75, 2017.

Ashley L Kiemen, Alicia M Braxton, Mia P Grahn, Kyu Sang Han, Jaanvi Mahesh Babu, Rebecca Reichel, Ann C Jiang, Bridgette Kim, Jocelyn Hsu, Falone Amoa, et al. Coda: quantitative 3d reconstruction of large tissues at cellular resolution. *Nature Methods*, 19 (11):1490–1499, 2022.

Yuhei Kirita, Haojia Wu, Kohei Uchimura, Parker C Wilson, and Benjamin D Humphreys. Cell profiling of mouse acute kidney injury reveals conserved cellular responses to injury. *Proceedings of the National Academy of Sciences*, 117(27):15874–15883, 2020.

Ludger Klein, Bruno Kyewski, Paul M Allen, and Kristin A Hogquist. Positive and negative selection of the t cell repertoire: what thymocytes see (and don't see). *Nature Reviews Immunology*, 14(6):377–391, 2014.

Vitalii Kleshchevnikov, Artem Shmatko, Emma Dann, Alexander Aivazidis, Hamish W King, Tong Li, Rasa Elmentaite, Artem Lomakin, Veronika Kedlian, Adam Gayoso, et al. Cell2location maps fine-grained cell types in spatial transcriptomics. *Nature biotechnology*, 40(5):661–671, 2022.

Johannes Klopf, Christine Brostjan, Wolf Eilenberg, and Christoph Neumayer. Neutrophil extracellular traps and their implications in cardiovascular and inflammatory disease. *International journal of molecular sciences*, 22(2):559, 2021.

Mark A Knepper, Tae-Hwan Kwon, and Soren Nielsen. Molecular physiology of water balance. *New England Journal of Medicine*, 372(14):1349–1358, 2015.

Masako Kohyama, Wataru Ise, Brian T Edelson, Peter R Wilker, Kai Hildner, Carlo Mejia, William A Frazier, Theresa L Murphy, and Kenneth M Murphy. Role for spi-c in the development of red pulp macrophages and splenic iron homeostasis. *Nature*, 457(7227): 318–321, 2009.

Aleksandra A Kolodziejczyk, Jong Kyoung Kim, Valentine Svensson, John C Marioni, and Sarah A Teichmann. The technology and biology of single-cell rna sequencing. *Molecular cell*, 58(4):610–620, 2015.

Björn Koos, Linda Andersson, Carl-Magnus Clausson, Karin Grannas, Axel Klaesson, Gaëlle Cane, and Ola Söderberg. Analysis of protein interactions in situ by proximity ligation assays. *High-Dimensional Single Cell Analysis: Mass Cytometry, Multi-parametric Flow Cytometry and Bioinformatic Techniques*, pages 111–126, 2014.

Anna Korzynska, Lukasz Roszkowiak, Jakub Zak, and Krzysztof Siemion. A review of current systems for annotation of cell and tissue images in digital pathology. *Biocybernetics and Biomedical Engineering*, 41(4):1436–1453, 2021.

Mina Kozai, Yuki Kubo, Tomoya Katakai, Hiroyuki Kondo, Hiroshi Kiyonari, Karin Schaeuble, Sanjiv A Luther, Naozumi Ishimaru, Izumi Ohigashi, and Yousuke Takahama. Essential role of ccl21 in establishment of central self-tolerance in t cells. *Journal of Experimental Medicine*, 214(7):1925–1935, 2017.

Satoshi Kozuki, Mio Kabata, Satoko Sakurai, Keiko Iwaisako, Tomomi Nishimura, Masakazu Toi, Takuya Yamamoto, and Fumiko Toyoshima. Periportal hepatocyte proliferation at midgestation governs maternal glucose homeostasis in mice. *Communications Biology*, 6 (1):1226, 2023.

Gérard Lambeau and Michael H Gelb. Biochemistry and physiology of mammalian secreted phospholipases a2. *Annu. Rev. Biochem.*, 77(1):495–520, 2008.

Mohamed Lamkanfi and Vishva M Dixit. Inflammasomes and their roles in health and disease. *Annual review of cell and developmental biology*, 28(1):137–161, 2012.

Mohamed Lamkanfi and Vishva M Dixit. Mechanisms and functions of inflammasomes. *Cell*, 157(5):1013–1022, 2014.

Rasmus Larsen, Raffaella Gozzelino, Viktória Jeney, László Tokaji, Fernando A Bozza, André M Japiassú, Dolores Bonaparte, Moisés Marinho Cavalcante, Ângelo Chora, Ana Ferreira, et al. A central role for free heme in the pathogenesis of severe sepsis. *Science translational medicine*, 2(51):51ra71–51ra71, 2010.

Toby Lawrence. The nuclear factor nf-κb pathway in inflammation. *Cold Spring Harbor perspectives in biology*, 1(6):a001651, 2009.

Helen M Lazear, John W Schoggins, and Michael S Diamond. Shared and distinct functions of type i and type iii interferons. *Immunity*, 50(4):907–923, 2019.

Je Hyuk Lee, Evan R Daugharthy, Jonathan Scheiman, Reza Kalhor, Joyce L Yang, Thomas C Ferrante, Richard Terry, Sauveur SF Jeanty, Chao Li, Ryoji Amamoto, et al. Highly multiplexed subcellular rna sequencing in situ. *science*, 343(6177):1360–1363, 2014.

Youjin Lee, Derek Bogdanoff, Yutong Wang, George C Hartoularos, Jonathan M Woo, Cody T Mowery, Hunter M Nisonoff, David S Lee, Yang Sun, James Lee, et al. Xyzeq: Spatially resolved single-cell rna sequencing reveals expression heterogeneity in the tumor microenvironment. *Science advances*, 7(17):eabg4755, 2021.

Jenneke Leentjens, Matthijs Kox, Johannes G van der Hoeven, Mihai G Netea, and Peter Pickkers. Immunotherapy for the adjunctive treatment of sepsis: from immunosuppression to immunostimulation. time for a paradigm change? *American journal of respiratory and critical care medicine*, 187(12):1287–1293, 2013.

Ed Lein, Lars E Borm, and Sten Linnarsson. The promise of spatial transcriptomics for neuroscience in the era of molecular cell typing. *Science*, 358(6359):64–69, 2017.

Ed S Lein, Michael J Hawrylycz, Nancy Ao, Mikael Ayres, Amy Bensinger, Amy Bernard, Andrew F Boe, Mark S Boguski, Kevin S Brockway, Emi J Byrnes, et al. Genome-wide atlas of gene expression in the adult mouse brain. *Nature*, 445(7124):168–176, 2007.

Marcel Levi. Inflammation and coagulation. *Inflammation: From Molecular and Cellular Mechanisms to the Clinic*, pages 833–860, 2017.

Marcel Levi and Tom van der Poll. Disseminated intravascular coagulation: a review for the internist. *Internal and emergency medicine*, 8:23–32, 2013.

Jeffrey M Levsky, Shailesh M Shenoy, Rossanna C Pezo, and Robert H Singer. Single-cell gene expression profiling. *Science*, 297(5582):836–840, 2002.

Mitchell M Levy, Mitchell P Fink, John C Marshall, Edward Abraham, Derek Angus, Deborah Cook, Jonathan Cohen, Steven M Opal, Jean-Louis Vincent, Graham Ramsay, et al. 2001 sccm/esicm/accp/ats/sis international sepsis definitions conference. *Critical care medicine*, 31(4):1250–1256, 2003.

Steven M Lewis, Adam Williams, and Stephanie C Eisenbarth. Structure and function of the immune system in the spleen. *Science immunology*, 4(33):eaau6085, 2019.

Jonathan Liu, Vanessa Tran, Venkata Naga Pranathi Vemuri, Ashley Byrne, Michael Borja, Yang Joon Kim, Snigdha Agarwal, Ruofan Wang, Kyle Awayan, Abhishek Murti, et al. Concordance of merfish spatial transcriptomics with bulk and single-cell rna sequencing. *Life science alliance*, 6(1), 2023a.

Yang Liu, Mingyu Yang, Yanxiang Deng, Graham Su, Archibald Enninful, Cindy C Guo, Toma Tebaldi, Di Zhang, Dongjoo Kim, Zhiliang Bai, et al. High-spatial-resolution multi-omics sequencing via deterministic barcoding in tissue. *Cell*, 183(6):1665–1681, 2020.

Yang Liu, Marcello DiStasio, Graham Su, Hiromitsu Asashima, Archibald Enninful, Xiaoyu Qin, Yanxiang Deng, Jungmin Nam, Fu Gao, Pino Bordignon, et al. High-plex protein and whole transcriptome co-mapping at cellular resolution with spatial cite-seq. *Nature Biotechnology*, 41(10):1405–1409, 2023b.

Yansheng Liu, Andreas Beyer, and Ruedi Aebersold. On the dependency of cellular protein levels on mrna abundance. *Cell*, 165(3):535–550, 2016.

Yahui Long, Kok Siong Ang, Mengwei Li, Kian Long Kelvin Chong, Raman Sethi, Chengwei Zhong, Hang Xu, Zhiwei Ong, Karishma Sachaphibulkij, Ao Chen, et al. Spatially informed clustering, integration, and deconvolution of spatial transcriptomics with graphst. *Nature Communications*, 14(1):1155, 2023.

Ming Y Lu, Drew FK Williamson, Tiffany Y Chen, Richard J Chen, Matteo Barbieri, and Faisal Mahmood. Data-efficient and weakly supervised computational pathology on whole-slide images. *Nature biomedical engineering*, 5(6):555–570, 2021.

Eric Lubeck and Long Cai. Single-cell systems biology by super-resolution imaging and combinatorial labeling. *Nature methods*, 9(7):743–748, 2012.

Eric Lubeck, Ahmet F Coskun, Timur Zhiyentayev, Mubhij Ahmad, and Long Cai. Single-cell in situ rna profiling by sequential hybridization. *Nature methods*, 11(4):360–361, 2014.

Malte D Luecken and Fabian J Theis. Current best practices in single-cell rna-seq analysis: a tutorial. *Molecular systems biology*, 15(6):e8746, 2019.

Emma Lundberg and Georg HH Borner. Spatial proteomics: a powerful discovery tool for cell biology. *Nature Reviews Molecular Cell Biology*, 20(5):285–302, 2019.

Andrew D Luster. The role of chemokines in linking innate and adaptive immunity. *Current opinion in immunology*, 14(1):129–135, 2002.

Ying Ma and Xiang Zhou. Spatially informed cell-type deconvolution for spatial transcriptomics. *Nature biotechnology*, 40(9):1349–1359, 2022.

Evan Z Macosko, Anindita Basu, Rahul Satija, James Nemesh, Karthik Shekhar, Melissa Goldman, Itay Tirosh, Allison R Bialas, Nolan Kamitaki, Emily M Martersteck, et al. Highly parallel genome-wide expression profiling of individual cells using nanoliter droplets. *Cell*, 161(5):1202–1214, 2015.

Florencia Paula Madorsky Rowdo, Antonela Baron, Mariela Urrutia, and José Mordoh. Immunotherapy in cancer: a combat between tumors and the immune system; you win some, you lose some. *Frontiers in Immunology*, 6:127, 2015.

Alison Maloney and Paul Workman. Hsp90 as a new therapeutic target for cancer therapy: the story unfolds. *Expert opinion on biological therapy*, 2(1):3–24, 2002.

Alberto Mantovani, Federica Marchesi, Alberto Malesci, Luigi Laghi, and Paola Allavena. Tumour-associated macrophages as treatment targets in oncology. *Nature reviews Clinical oncology*, 14(7):399–416, 2017.

Madhav Mantri, Gaetano J Scuderi, Roozbeh Abedini-Nassab, Michael FZ Wang, David McKellar, Hao Shi, Benjamin Grodner, Jonathan T Butcher, and Iwijn De Vlaminck. Spatiotemporal single-cell rna sequencing of developing chicken hearts identifies interplay between cellular differentiation and morphogenesis. *Nature communications*, 12(1):1771, 2021.

John C Marioni, Christopher E Mason, Shrikant M Mane, Matthew Stephens, and Yoav Gilad. Rna-seq: an assessment of technical reproducibility and comparison with gene expression arrays. *Genome research*, 18(9):1509–1517, 2008.

Greg S Martin, David M Mannino, and Marc Moss. The effect of age on the development and outcome of adult sepsis. *Critical care medicine*, 34(1):15–21, 2006.

Michael A Matthay, Rachel L Zemans, Guy A Zimmerman, Yaseen M Arabi, Jeremy R Beitler, Alain Mercat, Margaret Herridge, Adrienne G Randolph, and Carolyn S Calfee. Acute respiratory distress syndrome. *Nature reviews Disease primers*, 5(1):18, 2019.

Florian B Mayr, Sachin Yende, and Derek C Angus. Epidemiology of severe sepsis. *Virulence*, 5(1):4–11, 2014.

David W McKellar, Madhav Mantri, Meleana M Hinchman, John SL Parker, Praveen Sethupathy, Benjamin D Cosgrove, and Iwijn De Vlaminck. Spatial mapping of the total transcriptome by in situ polyadenylation. *Nature biotechnology*, 41(4):513–520, 2023.

Christopher R Merritt, Giang T Ong, Sarah E Church, Kristi Barker, Patrick Danaher, Gary Geiss, Margaret Hoang, Jaemyeong Jung, Yan Liang, Jill McKay-Fleisch, et al. Multiplex digital spatial profiling of proteins and rna in fixed tissue. *Nature biotechnology*, 38(5): 586–599, 2020.

Javier Mestas and Christopher CW Hughes. Of mice and not men: differences between mouse and human immunology. *The Journal of Immunology*, 172(5):2731–2738, 2004.

Eleni P Mimitou, Caleb A Lareau, Kelvin Y Chen, Andre L Zorzetto-Fernandes, Yuhan Hao, Yusuke Takeshima, Wendy Luo, Tse-Shun Huang, Bertrand Z Yeung, Efthymia Papalexi, et al. Scalable, multimodal profiling of chromatin accessibility, gene expression and protein levels in single cells. *Nature biotechnology*, 39(10):1246–1258, 2021.

Reza Mirzazadeh, Zaneta Andrusivova, Ludvig Larsson, Phillip T Newton, Leire Alonso Galicia, Xesús M Abalo, Mahtab Avijgan, Linda Kvastad, Alexandre Denadai-Souza, Nathalie Stakenborg, et al. Spatially resolved transcriptomic profiling of degraded and challenging fresh frozen samples. *Nature Communications*, 14(1):509, 2023.

Jeffrey R Moffitt, Dhananjay Bambah-Mukku, Stephen W Eichhorn, Eric Vaughn, Karthik Shekhar, Julio D Perez, Nimrod D Rubinstein, Junjie Hao, Aviv Regev, Catherine Dulac, et al. Molecular, spatial, and functional single-cell profiling of the hypothalamic preoptic region. *Science*, 362(6416):eaau5324, 2018.

Reuben Moncada, Dalia Barkley, Florian Wagner, Marta Chiodin, Joseph C Devlin, Maayan Baron, Cristina H Hajdu, Diane M Simeone, and Itai Yanai. Integrating microarray-based spatial transcriptomics and single-cell rna-seq reveals tissue architecture in pancreatic ductal adenocarcinomas. *Nature biotechnology*, 38(3):333–342, 2020.

SRMJ Moncada, RML Palmer, and EA_ Higgs. Nitric oxide: physiology, pathophysiology, and pharmacology. *Pharmacological reviews*, 43(2):109–142, 1991.

Kevin W Moore, Rene de Waal Malefyt, Robert L Coffman, and Anne O'Garra. Interleukin-10 and the interleukin-10 receptor. *Annual review of immunology*, 19(1):683–765, 2001.

Y Morodomi, S Kanaji, E Won, et al. Modified application of kawamoto's film method for super resolution imaging of megakaryocytes in undecalcified bone marrow. *Res Pract Thromb Haemost*, (4):86–91, 2019.

Herbert C Morse III. Building a better mouse: One hundred years of genetics and biology. In *The mouse in biomedical research*, pages 1–11. Elsevier, 2007.

Ali Mortazavi, Brian A Williams, Kenneth McCue, Lorian Schaeffer, and Barbara Wold. Mapping and quantifying mammalian transcriptomes by rna-seq. *Nature methods*, 5(7): 621–628, 2008.

Lambda Moses and Lior Pachter. Museum of spatial transcriptomics. *Nature methods*, 19 (5):534–546, 2022.

P Mukherjee, S Roy, D Ghosh, and SK Nandi. Role of animal models in biomedical research: a review. *Laboratory Animal Research*, 38(1):18, 2022.

Nilda M Muñoz, Kwang Pyo Kim, Sang Kyo Han, Evan Boetticher, Anne I Sperling, Hiroyuki Sano, Kyou Han, Xiangdong Zhu, Alan R Leff, and Wonhwa Cho. Characterization of monoclonal antibodies specific for 14-kda human group v secretory phospholipase a2 (hvpla2). *Hybridoma*, 19(2):171–176, 2000.

Nilda M Muñoz, Angelo Y Meliton, Lucille N Meliton, Steven M Dudek, and Alan R Leff. Secretory group v phospholipase a2 regulates acute lung injury and neutrophilic inflammation caused by lps in mice. *American Journal of Physiology-Lung Cellular and Molecular Physiology*, 296(6):L879–L887, 2009.

Makoto Murakami, Hiroyasu Sato, and Yoshitaka Taketomi. Updating phospholipase a2 biology. *Biomolecules*, 10(10):1457, 2020.

Heini Murer, Nati Hernando, Ian Forster, and Jurg Biber. Proximal tubular phosphate reabsorption: molecular mechanisms. *Physiological reviews*, 80(4):1373–1409, 2000.

Caitlin Naylor and William A Petri. Leptin regulation of immune responses. *Trends in molecular medicine*, 22(2):88–98, 2016.

Harry F Noller. Ribosomal rna and translation. *Annual review of biochemistry*, 60(1):191–227, 1991.

Seljlro Okusawa, JA Gelfand, T Ikejima, RJ Connolly, ChA Dinarello, et al. Interleukin 1 induces a shock-like state in rabbits. synergism with tumor necrosis factor and the effect of cyclooxygenase inhibition. *The Journal of clinical investigation*, 81(4):1162–1172, 1988.

Steven M Opal and Vera A DePalo. Anti-inflammatory cytokines. *Chest*, 117(4):1162–1172, 2000.

Surya Pandey, Michihiro Takahama, Adam Gruenbaum, Makda Zewde, Katerina Cheronis, and Nicolas Chevrier. A whole-tissue rna-seq toolkit for organism-wide studies of gene expression with pme-seq. *Nature protocols*, 15(4):1459–1483, 2020.

Sara M Parigi, Ludvig Larsson, Srustidhar Das, Ricardo O Ramirez Flores, Annika Frede, Kumar P Tripathi, Oscar E Diaz, Katja Selin, Rodrigo A Morales, Xinxin Luo, et al. The spatial transcriptomic landscape of the healing mouse intestine following damage. *Nature communications*, 13(1):828, 2022.

Joseph E Parrillo, Margaret M Parker, Charles Natanson, Anthony F Suffredini, Robert L Danner, Robert E Cunnion, and Frederick P Ognibene. Septic shock in humans: advances in the understanding of pathogenesis, cardiovascular dysfunction, and therapy. *Annals of internal medicine*, 113(3):227–242, 1990.

Ajay Patil and Ashwini Patil. Cellkb immune: a manually curated database of hematopoietic marker gene sets from 7 species for rapid cell type identification. *biorxiv*, pages 2020–12, 2020.

A Paun and PM Pitha. The irf family, revisited. *Biochimie*, 89(6-7):744–753, 2007.

A Caviani Pease, Dennis Solas, Edward J Sullivan, Maureen T Cronin, Christopher P Holmes, and SP Fodor. Light-generated oligonucleotide arrays for rapid dna sequence analysis. *Proceedings of the National Academy of Sciences*, 91(11):5022–5026, 1994.

James Edward Pease and Timothy John Williams. Chemokines and their receptors in allergic disease. *Journal of allergy and clinical immunology*, 118(2):305–318, 2006.

Robert L Perlman. Mouse models of human disease: an evolutionary perspective. *Evolution, medicine, and public health*, 2016(1):170–176, 2016.

Simone Picelli, Åsa K Björklund, Omid R Faridani, Sven Sagasser, Gösta Winberg, and Rickard Sandberg. Smart-seq2 for sensitive full-length transcriptome profiling in single cells. *Nature methods*, 10(11):1096–1098, 2013.

Simone Picelli, Omid R Faridani, Åsa K Björklund, Gösta Winberg, Sven Sagasser, and Rickard Sandberg. Full-length rna-seq from single cells using smart-seq2. *Nature protocols*, 9(1):171–181, 2014.

Adrian Pickar-Oliver and Charles A Gersbach. The next generation of crispr–cas technologies and applications. *Nature reviews Molecular cell biology*, 20(8):490–507, 2019.

Suresh Poovathingal, Kristofer Davie, Roel Vandepoel, Nicholas Poulvellarie, Annelien Verfaillie, Nikky Corthout, and Stein Aerts. Nova-st: Nano-patterned ultra-dense platform for spatial transcriptomics. *bioRxiv*, pages 2024–02, 2024.

Tiffany Porta Siegel, Gregory Hamm, Josephine Bunch, Jo Cappell, John S Fletcher, and Kristina Schwamborn. Mass spectrometry imaging and integration with other imaging modalities for greater molecular understanding of biological tissues. *Molecular imaging and biology*, 20:888–901, 2018.

Bin-Zhi Qian and Jeffrey W Pollard. Macrophage diversity enhances tumor progression and metastasis. *Cell*, 141(1):39–51, 2010.

Nhat D Quach, Robert D Arnold, and Brian S Cummings. Secretory phospholipase a2 enzymes as pharmacological targets for treatment of disease. *Biochemical pharmacology*, 90(4):338–348, 2014.

Anjali Rao, Dalia Barkley, Gustavo S França, and Itai Yanai. Exploring tissue architecture using spatial transcriptomics. *Nature*, 596(7871):211–220, 2021.

Radhakrishna Rao. Endotoxemia and gut barrier dysfunction in alcoholic liver disease. *Hepatology*, 50(2):638–644, 2009.

C Redit, S Cha, and N Ai. Single-cell proteomics: challenges and prospects. *Nat Methods*, 20(3):317–8, 2023.

Bing Ren, François Robert, John J Wyrick, Oscar Aparicio, Ezra G Jennings, Itamar Simon, Julia Zeitlinger, Jorg Schreiber, Nancy Hannett, Elenita Kanin, et al. Genome-wide location and function of dna binding proteins. *Science*, 290(5500):2306–2309, 2000.

Yanming Ren, Zongyao Huang, Lingling Zhou, Peng Xiao, Junwei Song, Ping He, Chuanxing Xie, Ran Zhou, Menghan Li, Xiangqun Dong, et al. Spatial transcriptomics reveals niche-specific enrichment and vulnerabilities of radial glial stem-like cells in malignant gliomas. *Nature Communications*, 14(1):1028, 2023.

Daniel Rittirsch, Markus S Huber-Lang, Michael A Flierl, and Peter A Ward. Immunodesign of experimental sepsis by cecal ligation and puncture. *Nature protocols*, 4(1):31–36, 2009.

Samuel G Rodriques, Robert R Stickels, Aleksandrina Goeva, Carly A Martin, Evan Murray, Charles R Vanderburg, Joshua Welch, Linlin M Chen, Fei Chen, and Evan Z Macosko. Slide-seq: A scalable technology for measuring genome-wide expression at high spatial resolution. *Science*, 363(6434):1463–1467, 2019.

Russell P Rother, Leonard Bell, Peter Hillmen, and Mark T Gladwin. The clinical sequelae of intravascular hemolysis and extracellular plasma hemoglobin: a novel mechanism of human disease. *Jama*, 293(13):1653–1662, 2005.

Kristina E Rudd, Sarah Charlotte Johnson, Kareha M Agesa, Katya Anne Shackelford, Derrick Tsoi, Daniel Rhodes Kievlan, Danny V Colombara, Kevin S Ikuta, Niranjan Kissoon, Simon Finfer, et al. Global, regional, and national sepsis incidence and mortality, 1990–2017: analysis for the global burden of disease study. *The Lancet*, 395(10219):200–211, 2020.

Alain Rudiger and Mervyn Singer. The heart in sepsis: from basic mechanisms to clinical management. *Current vascular pharmacology*, 11(2):187–195, 2013.

George T Rudkin and BD Stollar. High resolution detection of dna–rna hybrids in situ by indirect immunofluorescence. *Nature*, 265(5593):472–473, 1977.

José B Sáenz and Jason C Mills. Acid and the basis for cellular plasticity and reprogramming in gastric repair and cancer. *Nature Reviews Gastroenterology & Hepatology*, 15(5):257–273, 2018.

Antoine-Emmanuel Saliba, Alexander J Westermann, Stanislaw A Gorski, and Jörg Vogel. Single-cell rna-seq: advances and future challenges. *Nucleic acids research*, 42(14):8845–8860, 2014.

Fredrik Salmén, Patrik L Ståhl, Annelie Mollbrink, Jose Fernandez Navarro, Sanja Vickovic, Jonas Frisen, and Joakim Lundeberg. Barcoded solid-phase rna capture for spatial transcriptomics profiling in mammalian tissue sections. *Nature protocols*, 13(11):2501–2534, 2018.

Sachin K Samuchiwal and Barbara Balestrieri. Harmful and protective roles of group v phospholipase a2: Current perspectives and future directions. *Biochimica et Biophysica Acta (BBA)-Molecular and Cell Biology of Lipids*, 1864(6):819–826, 2019.

Rickard Sandberg. Entering the era of single-cell transcriptomics in biology and medicine. *Nature methods*, 11(1):22–24, 2014.

Francisco Kerr Saraiva and Andrei C Sposito. Cardiovascular effects of glucagon-like peptide 1 (glp-1) receptor agonists. *Cardiovascular Diabetology*, 13:1–11, 2014.

Hiroyasu Sato, Yoshitaka Taketomi, Ayako Ushida, Yuki Isogai, Takumi Kojima, Tetsuya Hirabayashi, Yoshimi Miki, Kei Yamamoto, Yasumasa Nishito, Tetsuyuki Kobayashi, et al. The adipocyte-inducible secreted phospholipases pla2g5 and pla2g2e play distinct roles in obesity. *Cell metabolism*, 20(1):119–132, 2014.

Dominik J Schaer, Paul W Buehler, Abdu I Alayash, John D Belcher, and Gregory M Vercellotti. Hemolysis and free hemoglobin revisited: exploring hemoglobin and hemin scavengers as a novel class of therapeutic proteins. *Blood, The Journal of the American Society of Hematology*, 121(8):1276–1284, 2013.

Nicholas Schaum, Jim Karkanias, Norma F Neff, Andrew P May, Stephen R Quake, Tony Wyss-Coray, Spyros Darmanis, Joshua Batson, Olga Botvinnik, Michelle B Chen, et al. Single-cell transcriptomics of 20 mouse organs creates a tabula muris: The tabula muris consortium. *Nature*, 562(7727):367, 2018.

Mark Schena, Dari Shalon, Ronald W Davis, and Patrick O Brown. Quantitative monitoring of gene expression patterns with a complementary dna microarray. *Science*, 270(5235): 467–470, 1995.

Christian Schindler, David E Levy, and Thomas Decker. Jak-stat signaling: from interferons to cytokines. *Journal of Biological Chemistry*, 282(28):20059–20063, 2007.

William M Schneider, Meike Dittmann Chevillotte, and Charles M Rice. Interferon-stimulated genes: a complex web of host defenses. *Annual review of immunology*, 32 (1):513–545, 2014.

Marie Schott, Daniel León-Periñán, Elena Splendiani, Leon Strenger, Jan Robin Licha, Tancredi Massimo Pentimalli, Simon Schallenberg, Jonathan Alles, Sarah Samut Tagliaferro, Anastasiya Boltengagen, et al. Open-st: High-resolution spatial transcriptomics in 3d. *Cell*, 2024.

Kate Schroder, Paul J Hertzog, Timothy Ravasi, and David A Hume. Interferon-γ: an overview of signals, mechanisms and functions. *Journal of Leucocyte Biology*, 75(2):163–189, 2004.

Daniel Schulz, Vito Riccardo Tomaso Zanotelli, Jana Raja Fischer, Denis Schapiro, Stefanie Engler, Xiao-Kang Lun, Hartland Warren Jackson, and Bernd Bodenmiller. Simultaneous multiplexed imaging of mrna and proteins with subcellular resolution in breast cancer tissue samples by mass cytometry. *Cell systems*, 6(1):25–36, 2018.

Gregg L Semenza. Hypoxia-inducible factors in physiology and medicine. *Cell*, 148(3): 399–408, 2012.

Christopher W Seymour, Vincent X Liu, Theodore J Iwashyna, Frank M Brunkhorst, Thomas D Rea, André Scherag, Gordon Rubenfeld, Jeremy M Kahn, Manu Shankar-Hari, Mervyn Singer, et al. Assessment of clinical criteria for sepsis: for the third international consensus definitions for sepsis and septic shock (sepsis-3). *Jama*, 315(8):762–774, 2016.

Bita Shakoory, Joseph A Carcillo, W Winn Chatham, Richard L Amdur, Huaqing Zhao, Charles A Dinarello, Randall Q Cron, and Steven M Opal. Interleukin-1 receptor blockade is associated with reduced mortality in sepsis patients with features of macrophage activation syndrome: reanalysis of a prior phase iii trial. *Critical care medicine*, 44(2): 275–281, 2016.

Hailing Shi, Yichun He, Yiming Zhou, Jiahao Huang, Kamal Maher, Brandon Wang, Zefang Tang, Shuchen Luo, Peng Tan, Morgan Wu, et al. Spatial atlas of the mouse central nervous system at molecular resolution. *Nature*, 622(7983):552–561, 2023.

Vincent Feng-Sheng Shih, Rachel Tsui, Andrew Caldwell, and Alexander Hoffmann. A single nfκb system for both canonical and non-canonical signaling. *Cell research*, 21(1):86–102, 2011.

Junji Shimizu, Atsushi Murao, Yongchan Lee, Monowar Aziz, and Ping Wang. Extracellular cirp promotes kupffer cell inflammatory polarization in sepsis. *Frontiers in Immunology*, 15:1411930, 2024.

Mervyn Singer, Clifford S Deutschman, Christopher Warren Seymour, Manu Shankar-Hari, Djillali Annane, Michael Bauer, Rinaldo Bellomo, Gordon R Bernard, Jean-Daniel Chiche, Craig M Coopersmith, et al. The third international consensus definitions for sepsis and septic shock (sepsis-3). *Jama*, 315(8):801–810, 2016.

Frances V Sjaastad, Isaac J Jensen, Roger R Berton, Vladimir P Badovinac, and Thomas S Griffith. Inducing experimental polymicrobial sepsis by cecal ligation and puncture. *Current Protocols in Immunology*, 131(1):e110, 2020.

William C Skarnes, Barry Rosen, Anthony P West, Manousos Koutsourakis, Wendy Bushell, Vivek Iyer, Alejandro O Mujica, Mark Thomas, Jennifer Harrow, Tony Cox, et al. A conditional knockout resource for the genome-wide study of mouse gene function. *Nature*, 474(7351):337–342, 2011.

Sébastien A Smallwood, Heather J Lee, Christof Angermueller, Felix Krueger, Heba Saadeh, Julian Peat, Simon R Andrews, Oliver Stegle, Wolf Reik, and Gavin Kelsey. Single-cell genome-wide bisulfite sequencing for assessing epigenetic heterogeneity. *Nature methods*, 11(8):817–820, 2014.

Homer William Smith. *The kidney: structure and function in health and disease*. Oxford University Press, 1951.

Ola Söderberg, Karl-Johan Leuchowius, Mats Gullberg, Malin Jarvius, Irene Weibrecht, Lars-Gunnar Larsson, and Ulf Landegren. Characterizing proteins and their interactions in cells and tissues using the in situ proximity ligation assay. *Methods*, 45(3):227–232, 2008.

Magali Soumillon, Davide Cacchiarelli, Stefan Semrau, Alexander van Oudenaarden, and Tarjei S Mikkelsen. Characterization of directed differentiation by high-throughput single-cell rna-seq. *BioRxiv*, page 003236, 2014.

Peter E Spronk, Durk F Zandstra, and Can Ince. Bench-to-bedside review: sepsis is a disease of the microcirculation. *Critical care*, 8:1–7, 2004.

Sanjay R Srivatsan, Mary C Regier, Eliza Barkan, Jennifer M Franks, Jonathan S Packer, Parker Grosjean, Madeleine Duran, Sarah Saxton, Jon J Ladd, Malte Spielmann, et al. Embryo-scale, single-cell spatial transcriptomics. *Science*, 373(6550):111–117, 2021.

Edward C Stack, Chichung Wang, Kristin A Roman, and Clifford C Hoyt. Multiplexed immunohistochemistry, imaging, and quantitation: a review, with an assessment of tyramide signal amplification, multispectral imaging and multiplex analysis. *Methods*, 70(1):46–58, 2014.

Patrik L Ståhl, Fredrik Salmén, Sanja Vickovic, Anna Lundmark, José Fernández Navarro, Jens Magnusson, Stefania Giacomello, Michaela Asp, Jakub O Westholm, Mikael Huss, et al. Visualization and analysis of gene expression in tissue sections by spatial transcriptomics. *Science*, 353(6294):78–82, 2016.

Daniel B Stetson and Ruslan Medzhitov. Type i interferons in host defense. *Immunity*, 25 (3):373–381, 2006.

Robert R Stickels, Evan Murray, Pawan Kumar, Jilong Li, Jamie L Marshall, Daniela J Di Bella, Paola Arlotta, Evan Z Macosko, and Fei Chen. Highly sensitive spatial transcriptomics at near-cellular resolution with slide-seqv2. *Nature biotechnology*, 39(3):313–319, 2021.

Marlon Stoeckius, Christoph Hafemeister, William Stephenson, Brian Houck-Loomis, Pratip K Chattopadhyay, Harold Swerdlow, Rahul Satija, and Peter Smibert. Simultaneous epitope and transcriptome measurement in single cells. *Nature methods*, 14(9): 865–868, 2017.

Tim Stuart, Andrew Butler, Paul Hoffman, Christoph Hafemeister, Efthymia Papalexi, William M Mauck, Yuhan Hao, Marlon Stoeckius, Peter Smibert, and Rahul Satija. Comprehensive integration of single-cell data. *cell*, 177(7):1888–1902, 2019.

Donghui Su, Robert I Roth, and Jack Levin. Hemoglobin infusion augments the tumor necrosis factor response to bacterial endotoxin (lipopolysaccharide) in mice. *Critical care medicine*, 27(4):771–778, 1999.

Michihiro Takahama, Ashwini Patil, Gabriella Richey, Denis Cipurko, Katherine Johnson, Peter Carbonetto, Madison Plaster, Surya Pandey, Katerina Cheronis, Tatsuki Ueda, et al. A pairwise cytokine code explains the organism-wide response to sepsis. *Nature Immunology*, 25(2):226–239, 2024.

Kiyoshi Takeda and Shizuo Akira. Toll receptors and pathogen resistance. *Cellular microbiology*, 5(3):143–153, 2003.

James E Talmadge, Rakesh K Singh, Isaiah J Fidler, and Avraham Raz. Murine models to evaluate novel and conventional therapeutic strategies for cancer. *The American journal of pathology*, 170(3):793–804, 2007.

Tadatsugu Taniguchi and Akinori Takaoka. A weak signal for strong responses: interferon-alpha/beta revisited. *Nature reviews Molecular cell biology*, 2(5):378–386, 2001.

Burak Tepe, Matthew C Hill, Brandon T Pekarek, Patrick J Hunt, Thomas J Martin, James F Martin, and Benjamin R Arenkiel. Single-cell rna-seq of mouse olfactory bulb reveals cellular heterogeneity and activity-dependent molecular census of adult-born neurons. *Cell reports*, 25(10):2689–2703, 2018.

Luyi Tian, Fei Chen, and Evan Z Macosko. The expanding vistas of spatial transcriptomics. *Nature Biotechnology*, 41(6):773–782, 2023.

Vincent A Traag, Ludo Waltman, and Nees Jan Van Eck. From louvain to leiden: guaranteeing well-connected communities. *Scientific reports*, 9(1):1–12, 2019.

Kevin J Tracey, Yuman Fong, David G Hesse, Kirk R Manogue, Annette T Lee, George C Kuo, Stephen F Lowry, and Anthony Cerami. Anti-cachectin/tnf monoclonal antibodies prevent septic shock during lethal bacteraemia. *Nature*, 330(6149):662–664, 1987.

Cole Trapnell, Davide Cacchiarelli, Jonna Grimsby, Prapti Pokharel, Shuqiang Li, Michael Morse, Niall J Lennon, Kenneth J Livak, Tarjei S Mikkelsen, and John L Rinn. The dynamics and regulators of cell fate decisions are revealed by pseudotemporal ordering of single cells. *Nature biotechnology*, 32(4):381–386, 2014.

Tom van der Poll and Steven M Opal. Host–pathogen interactions in sepsis. *The Lancet infectious diseases*, 8(1):32–43, 2008.

Stefan Van der Walt, Johannes L Schönberger, Juan Nunez-Iglesias, François Boulogne, Joshua D Warner, Neil Yager, Emmanuelle Gouillart, and Tony Yu. scikit-image: image processing in python. *PeerJ*, 2:e453, 2014.

Peter Vaupel and Arnulf Mayer. Hypoxia in cancer: significance and impact on clinical outcome. *Cancer and Metastasis Reviews*, 26:225–239, 2007.

Matthew B Veldman and Shuo Lin. Zebrafish as a developmental model organism for pediatric research. *Pediatric research*, 64(5):470–476, 2008.

Fabienne Venet, Chun-Shiang Chung, Guillaume Monneret, Xin Huang, Brian Horner, Megan Garber, and Alfred Ayala. Regulatory t cell populations in sepsis and trauma. *Journal of Leucocyte Biology*, 83(3):523–535, 2008.

Andrea Ventura, Alexander Meissner, Christopher P Dillon, Michael McManus, Phillip A Sharp, Luk Van Parijs, Rudolf Jaenisch, and Tyler Jacks. Cre-lox-regulated conditional rna interference from transgenes. *Proceedings of the National Academy of Sciences*, 101 (28):10380–10385, 2004.

Sanja Vickovic, Gökcen Eraslan, Fredrik Salmén, Johanna Klughammer, Linnea Stenbeck, Denis Schapiro, Tarmo Äijö, Richard Bonneau, Ludvig Bergenstråhle, José Fernandéz Navarro, et al. High-definition spatial transcriptomics for in situ tissue profiling. *Nature methods*, 16(10):987–990, 2019.

Sanja Vickovic, Britta Lötstedt, Johanna Klughammer, S Mages, Å Segerstolpe, O Rozenblatt-Rosen, and A Regev. Sm-omics is an automated platform for high-throughput spatial multi-omics. *Nature communications*, 13(1):795, 2022.

Kyle H Vining and David J Mooney. Mechanical forces direct stem cell behaviour in development and regeneration. *Nature reviews Molecular cell biology*, 18(12):728–742, 2017.

Guiping Wang, Jeffrey R Moffitt, and Xiaowei Zhuang. Multiplexed imaging of high-density libraries of rnas with merfish and expansion microscopy. *Scientific reports*, 8(1):4847, 2018a.

Haichao Wang, Mary F Ward, and Andrew E Sama. Targeting hmgb1 in the treatment of sepsis. *Expert opinion on therapeutic targets*, 18(3):257–268, 2014.

Haifeng Wang, Marie La Russa, and Lei S Qi. Crispr/cas9 in genome editing and beyond. *Annual review of biochemistry*, 85(1):227–264, 2016.

Xiao Wang, William E Allen, Matthew A Wright, Emily L Sylwestrak, Nikolay Samusik, Sam Vesuna, Kathryn Evans, Cindy Liu, Charu Ramakrishnan, Jia Liu, et al. Three-dimensional intact-tissue sequencing of single-cell transcriptional states. *Science*, 361 (6400):eaat5691, 2018b.

Zhong Wang, Mark Gerstein, and Michael Snyder. Rna-seq: a revolutionary tool for transcriptomics. *Nature reviews genetics*, 10(1):57–63, 2009.

Kazuhiro Watanabe, Yoshitaka Taketomi, Yoshimi Miki, Kiyotaka Kugiyama, and Makoto Murakami. Group v secreted phospholipase a2 plays a protective role against aortic dissection. *Journal of Biological Chemistry*, 295(30):10092–10111, 2020.

Irene Weibrecht, Karl-Johan Leuchowius, Carl-Magnus Clausson, Tim Conze, Malin Jarvius, W Mathias Howell, Masood Kamali-Moghaddam, and Ola Söderberg. Proximity ligation assays: a recent addition to the proteomics toolbox. *Expert review of proteomics*, 7(3): 401–409, 2010.

F Alexander Wolf, Philipp Angerer, and Fabian J Theis. Scanpy: large-scale single-cell gene expression data analysis. *Genome biology*, 19:1–5, 2018.

Haojia Wu, Eryn E Dixon, Qiao Xuanyuan, Juanru Guo, Yasuhiro Yoshimura, Chitnis Debashish, Anezka Niesnerova, Hao Xu, Morgane Rouault, and Benjamin D Humphreys. High resolution spatial profiling of kidney injury and repair using rna hybridization-based in situ sequencing. *Nature communications*, 15(1):1396, 2024.

Younan Xia and George M Whitesides. Soft lithography. *Angewandte Chemie International Edition*, 37(5):550–575, 1998.

A Xiaowei. Method of the year 2020: Spatially resolved transcriptomics. *Nat. Methods*, 18 (1), 2021.

Wei Xu, Rita G Domingues, Diogo Fonseca-Pereira, Manuela Ferreira, Helder Ribeiro, Silvia Lopez-Lastra, Yasutaka Motomura, Lara Moreira-Santos, Franck Bihl, Veronique Braud, et al. Nfil3 orchestrates the emergence of common helper innate lymphoid cell precursors. *Cell reports*, 10(12):2043–2054, 2015.

Munehiro Yamaguchi, Sachin K Samuchiwal, Oswald Quehenberger, Joshua A Boyce, and Barbara Balestrieri. Macrophages regulate lung ilc2 activation via pla2g5-dependent mechanisms. *Mucosal immunology*, 11(3):615–626, 2018.

K Yamamoto, Y Miki, H Sato, R Murase, Y Taketomi, and M Murakami. Secreted phospholipase a2 specificity on natural membrane phospholipids. In *Methods in Enzymology*, volume 583, pages 101–117. Elsevier, 2017.

Kei Yamamoto, Yoshimi Miki, Mariko Sato, Yoshitaka Taketomi, Yasumasa Nishito, Choji Taya, Kazuaki Muramatsu, Kazutaka Ikeda, Hiroki Nakanishi, Ryo Taguchi, et al. The role of group iif-secreted phospholipase a2 in epidermal homeostasis and hyperplasia. *Journal of Experimental Medicine*, 212(11):1901–1919, 2015.

María Yáñez-Mó, Pia R-M Siljander, Zoraida Andreu, Apolonija Bedina Zavec, Francesc E Borràs, Edit I Buzas, Krisztina Buzas, Enriqueta Casal, Francesco Cappello, Joana Carvalho, et al. Biological properties of extracellular vesicles and their physiological functions. *Journal of extracellular vesicles*, 4(1):27066, 2015.

Huan Yang, Daniel J Antoine, Ulf Andersson, and Kevin J Tracey. The many faces of hmgb1: molecular structure-functional activity in inflammation, apoptosis, and chemotaxis. *Journal of leukocyte biology*, 93(6):865–873, 2013.

Toshiaki Yano, Daisuke Fujioka, Yukio Saito, Tsuyoshi Kobayashi, Takamitsu Nakamura, Jun-ei Obata, Kenichi Kawabata, Kazuhiro Watanabe, Yosuke Watanabe, Hideto Mishina, et al. Group v secretory phospholipase a2 plays a pathogenic role in myocardial ischaemia–reperfusion injury. *Cardiovascular research*, 90(2):335–343, 2011.

Hao Yin, Wen Xue, Sidi Chen, Roman L Bogorad, Eric Benedetti, Markus Grompe, Victor Koteliansky, Phillip A Sharp, Tyler Jacks, and Daniel G Anderson. Genome editing with cas9 in adult mice corrects a disease mutation and phenotype. *Nature biotechnology*, 32 (6):551–553, 2014.

Yue You, Yuting Fu, Lanxiang Li, Zhongmin Zhang, Shikai Jia, Shihong Lu, Wenle Ren, Yifang Liu, Yang Xu, Xiaojing Liu, et al. Systematic comparison of sequencing-based spatial transcriptomic methods. *Nature Methods*, pages 1–12, 2024.

L Zappia and A Oshlack. Clustering trees: a visualization for evaluating clusterings at multiple resolutions. gigascience 7, giy083, 2018.

Bao Zhang, Peng He, John EG Lawrence, Shuaiyu Wang, Elizabeth Tuck, Brian A Williams, Kenny Roberts, Vitalii Kleshchevnikov, Lira Mamanova, Liam Bolt, et al. A human embryonic limb cell atlas resolved in space and time. *Nature*, pages 1–11, 2023a.

Di Zhang, Yanxiang Deng, Petra Kukanja, Eneritz Agirre, Marek Bartosovic, Mingze Dong, Cong Ma, Sai Ma, Graham Su, Shuozhen Bao, et al. Spatial epigenome–transcriptome co-profiling of mammalian tissues. *Nature*, 616(7955):113–122, 2023b.

Xiaoting Zhang, Wentao Ji, Xiaoming Deng, and Lulong Bo. High-dose ascorbic acid potentiates immune modulation through stat1 phosphorylation inhibition and negative regulation of pd-l1 in experimental sepsis. *Inflammopharmacology*, 32(1):537–550, 2024.

Edward Zhao, Matthew R Stone, Xing Ren, Jamie Guenthoer, Kimberly S Smythe, Thomas Pulliam, Stephen R Williams, Cedric R Uytingco, Sarah EB Taylor, Paul Nghiem, et al. Spatial transcriptomics at subspot resolution with bayesspace. *Nature biotechnology*, 39 (11):1375–1384, 2021.

Grace XY Zheng, Jessica M Terry, Phillip Belgrader, Paul Ryvkin, Zachary W Bent, Ryan Wilson, Solongo B Ziraldo, Tobias D Wheeler, Geoff P McDermott, Junjie Zhu, et al. Massively parallel digital transcriptional profiling of single cells. *Nature communications*, 8(1):14049, 2017.

Chenxu Zhu, Sebastian Preissl, and Bing Ren. Single-cell multimodal omics: the power of many. *Nature methods*, 17(1):11–14, 2020.

Josefin Zschaler, Denise Schlorke, and Juergen Arnhold. Differences in innate immune response between man and mouse. *Critical Reviews in Immunology*, 34(5), 2014.